Modelling and Stability Analysis of Aircraft Power Systems

Kongpan Areerak (M.Eng)

Thesis submitted to the University of Nottingham for the degree of Doctor of Philosophy, October 2009

Acknowledgements

I would like to express my deepest and sincere gratitude to both of my supervisors, Prof. Greg Asher and Dr. Dave Thomas for their guidance and invaluable help throughout the course of this research. I would like to thank Dr. Serhiy Bozhko for his valuable assistance to my project. I would also like to thank Dr. Chris Gerada for acting as internal examiner and Dr. Jiabin Wang, from the University of Sheffield, for acting as external examiner.

Thanks are also due to all my friends and colleagues in the PEMC group for their continuous support and valuable discussions during my time in the school. Special thanks to Dr. Lee Empringham and Dr. Liliana de Lillo for making the testing rig available to support my work.

Thanks to Thai people who have given me the study opportunity by granting me a Royal Thai Government Scholarship. Thanks also to all who have educated me: my primary and secondary school teachers, and my colleagues at Suranaree University of Technology, Thailand. A million thanks to my mum, dad, aunt, Areerak's family, and my girlfriend. They have raised and taught me. Without their encouragement, understanding and love, it would be impossible to finish my study.

Kongpan Areerak

Nottingham, UK 2009

Abstract

The more-electric aircraft concept is a major trend in aircraft electrical power system engineering and results in an increase in electrical loads based on power electronic converters and motor drive systems. Unfortunately, power electronic driven loads often behave as constant power loads having the small-signal negative impedance that can significantly degrade the power system stability margin. Therefore, the stability issue of aircraft power systems is of great importance. The research of the thesis deals with the modelling and stability analysis of an aircraft power system. The aircraft power system architecture considered in the thesis is based on the More Open Electrical Technologies (MOET) aircraft power system with one generator as only a single generator can be connected to a system at any one time. The small-signal stability analysis is used with the system dynamic model derived from the dq modelling method under the assumption that the aircraft power system operating point does not change rapidly during normal operation mode. The linearization technique using the first order terms of a Taylor expansion is used so as to achieve a set of linear models around an equilibrium point for a small-signal stability study. The thesis presents the development of effective models capable of representing the electrical power system dynamic behaviour for stability studies. The proposed model can be used to predict the instability point for variations in operating points and/or system parameters. Agreement between the theoretical estimation, simulation, and experimental results for a simple system are achieved that ranges from acceptable to very good. Finally, the subsystem models described in the thesis can be interconnected in an algorithmic way that is representative of a more generalized aircraft power system model. The generalized model is also applied to a more complex and realistic aircraft power system with simulation validations for thorough investigations of aircraft power system stability. This model may be considered as a powerful and flexible stability analysis tool to analyse the complex multi-converter electrical power systems.

Contents

Appendices

Appendix A: Transformation Conventions

Appendix B: DQ Transformations of Line Elements

Appendix C: Linearization Approach

Appendix D: The SABER Benchmark Models

Appendix E: The Details of the Element Matrices of the Generalized Model

List of Figures

List of Tables

Chapter 1

Introduction

1.1 Aircraft Electrical Power Systems

More Electric Aircraft (MEA) [1]-[7] concept is a major trend in aircraft electrical power system (EPS) engineering and results in an increase in electrical loads based on power electronic converters and motor drive systems. The trend of using electromechanical actuators (EMAs) instead of hydraulic actuators is increased [4]. This is because the power electronic converters driving various loads and actuation systems can improve the performance of aircraft power system and their reliability [1],[2],[4]-[6]. In addition, increasing the use of the EPS in the aircraft can reduce fuel consumption, weight, and maintenance costs [3]-[6]. New EPS architectures may take many forms: AC, DC, hybrid, frequency-wild, variable voltage, together with the possibility of novel connectivity topologies. The existing electric aircraft architecture is based on the constant frequency AC power system. The power is provided by a constant frequency three-phase AC power at 400 Hz and 115Vrms [1],[3],[6],[7]. The constant-speed-regulated generator (CSRG) [1][3][7] is used to provide the power with constant frequency. Transformer rectifier units (TRUs) are used to transform the AC power into DC for feeding DC loads. Although approximately 95% of all in-service aircraft [7] use the constant frequency power system, the CSRG system is complex and has low efficiency of power conversion [6],[7]. Hence, the next generation of aircraft power system architecture is introduced based on a variable frequency AC distribution system [1]-[7] (e.g. B787 [8] and A350 [6]). The power is distributed from three-phase AC power at 230 Vrms with variable frequency between 360 Hz-720 Hz [7]. The increasing of the voltage level (from 115V to

230V) can reduce conduction losses and weight. Moreover, the variable frequency system is less complex with easier maintenance compared with the constant frequency system. The rectifier unit is used to produce +/-270V (540V) for a high power DC bus feeding DC environmental control system or other DC loads.

In this research, the large aircraft power system architecture considered is based on the More Open Electrical Technologies (MOET) Large Aircraft Electrical System Architecture from Airbus France (document WP3.11 Architecture V0 [9]) . This architecture in the simplified form is shown in Figure 1.1. More details of the principle operations under both normal and abnormal conditions can be found in [9]. In this thesis, we consider only those details that are important for development of models suitable for stability studies. The architecture assumes that there are two turbine engines (ENG1/ENG2), each driving two 250 kVA generators (SG1-SG4). The generators are operated with a generator control unit (GCU) to control 230Vac at the main power system high-voltage AC buses (HVAC1-1, HVAC1-2, HVAC2-3, HVAC2-4). The power system is frequency-wild 360-900 Hz depending on engines rotational speed. In Figure 1.1, there are three primary electrical power centres (PEPDC1-PEPDC3) and two emergency electrical power centres (EEPDC1, EEPDC2).

For the primary electrical power centres, the PEPDC1 consists of a 230Vac bus (HVAC1-1), a +/-270Vdc bus (HVDC1-1) produced by an auto-transformer rectifier unit (ATRU1), and a 28Vdc bus (DC1) fed from a buck-boost converter unit (BBCU1). Similarly, the PEPDC2 consists of a 230Vac bus (HVAC2-4), a +/-270Vdc bus (HVDC2-4) produced by ATRU4, and a 28Vdc bus (DC2) fed from BBCU2, while the PEPDC3 consists of a 230Vac buses (HVAC1-2, HVAC2-3), a +/-270Vdc buses (HVDC1-2, HVDC2-3) produced by ATRU2 and ATRU3, and 115Vac buses (AC1, AC2) fed from auto-transformer units (ATU1,ATU2).

For emergency electrical power centres, the EEPDC1 contains a 230Vac essential bus (AC ESS1), and a 28Vdc essential bus (DC ESS1) fed from a battery charger rectifier unit (BCRU1), while the EEPDC2 contains 230Vac essential bus (AC ESS2), and 28Vdc essential bus (DC ESS2) fed from BCRU2.

The system is generally symmetrical in which each component is operated in parallel with an identical component or is used as a back up by having redundant secondary devices for when the primary device fails. For normal operation, SG1 supplies the electricity to PEPDC1, EEPDC1, electrical wing ice protection system (WIPS1), and electrical environmental conditioning system (ECSM1). Similarly, SG4 supplies the electricity to PEPDC2, EEPDC2, electrical wing ice protection system (WIPS2), and electrical environmental conditioning system (ECSM4). SG2 and SG3 supply the electrical power to PEPDC3 including the electrical environmental conditioning system (ECSM2, ECSM3). In addition, EEPDC1 is supplied by HVAC1-1 and EMA1 is fed from AC ESS1. Similarly, EEPDC2 is supplied by HVAC2-4 and EMA2 is fed from AC ESS2. Four batteries (BAT1, BAT ESS1, BAT2, BAT ESS2) are charged during the normal mode.

It is important to note that two or more generators cannot supply the power to the same bus at the same time. For this reason, the generalized electrical aircraft power systems based on the MOET system in Figure 1.1 for 'one generator' can be used as shown in Figure 1.2. This system diagram is used as a basis for the studies in this research. The 250 kVA generator feeds 230Vac three-phase power with variable frequency 300-900 Hz onto the HVAC1 bus. The autotransformer rectifier unit (ATRU1) produces the DC link bus voltage (HVDC1) +/-270V feeding the electromechanical actuator for an electrical environmental conditioning system (ECSM1), and other DC loads through the HVDC1 bus. The generator also supplies electricity to an electrical wing ice protection system (WIPS1) and the AC ESS1 bus. The AC ESS1 bus supplies

a controlled PWM rectifier unit feeding the electromechanical actuators (EMA) for aileron, rudder, flaps, spoilers, and elevator.

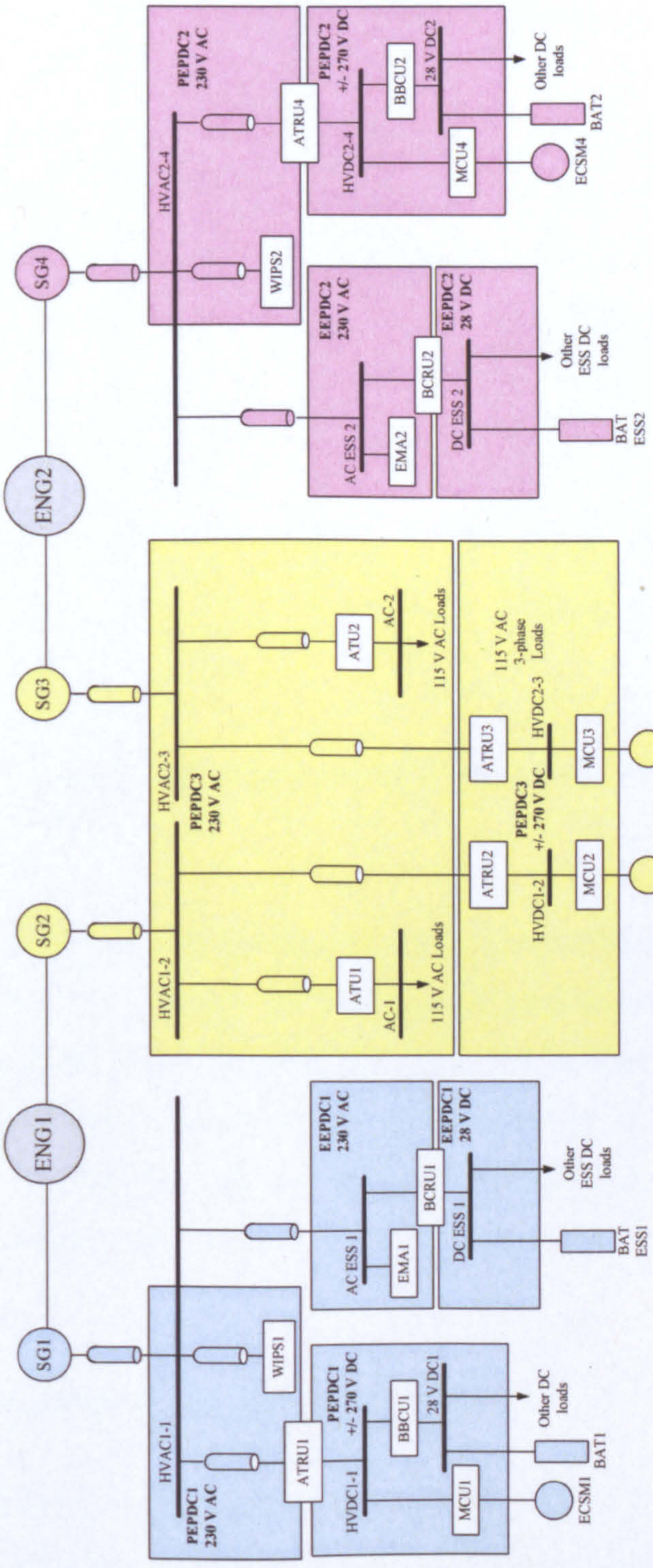

Figure 1.1: MOET large aircraft power system architecture

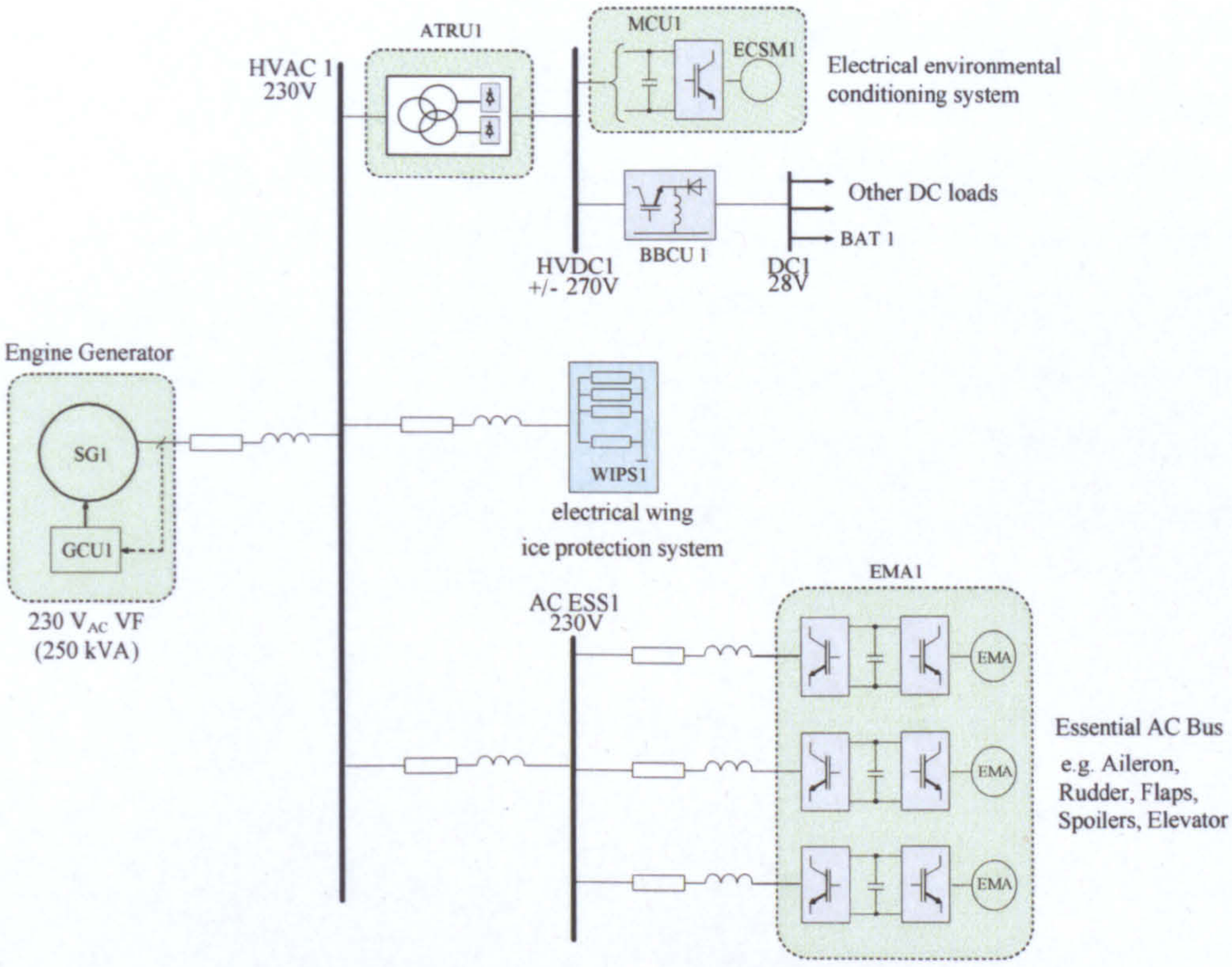

Figure 1.2: The generalized aircraft power system based on MOET system for one engine generator

It can be seen in Figure 1.2 that there are many electrical loads based on power electronic converters (AC/DC, DC/DC, DC/AC converters) driving various loads and actuation systems. It will be described in the next section that these loads can significantly degrade power system stability margins. Hence, the development of effective models capable of representing EPS dynamic behaviour is of great importance.

1.2 Literature Review and Background

As mentioned before, the more-electric aircraft concept is a major trend in aircraft electrical power system (EPS) engineering and results in an increase in electrical loads based on power electronic converters and motor drive systems. Therefore, the aircraft power systems become more complex electrical

distribution systems with a multiplicity of actuators, aircraft loads and bus geometries [2]. Unfortunately, it is well known that regulated power electronic driven loads often behave as constant power loads (CPLs) having small-signal negative impedance that can significantly degrade power system stability margins [10]-[14]. To fully understand the impact of constant power loads, there are two concepts to keep in mind; constant power load definitions and negative impedance instability. These concepts including the literature review for the modelling and stability analysis of power electronic based system (PEBS) are addressed in this section.

1.2.1 Constant Power Loads and Negative Impedance Instability

The power converters with their controls normally behave as constant power loads [11]-[14] in steady state operation. There can be a large number of these loads in aircraft power systems [2],[3]. An example of CPLs, as shown in Figure 1.3, is a DC/AC inverter feeding a machine or actuator drive under tight current and speed servo control. Therefore, in steady state the speed (ω_r) is almost constant. For each operational point, the torque (T_L) is constant, and the output power (P_{out}) which is the multiplication between torque and speed is also constant. If we assume for each operating point that the machine losses are constant and there are no losses in the DC/AC inverter, the input power (P_{inv}) of this inverter will be constant. Therefore, the DC/AC inverter feeding a regulated drive presents CPL behaviour to the aircraft power systems. For the EPS topology of Figure 1.1, these CPL drives include critical flight actuators and environmental controls.

Another example of CPLs, as shown in Figure 1.4, is a DC/DC converter feeding electrical loads under tight voltage control. The simple load for this case is the resistive loads in which the relationship between voltage and current is linear. Therefore, as for the actuator drive systems, the output voltage (V_{out}) is regulated for each operating point. Due to regulation, the input power of DC/DC converter (P_{conv}) is constant. As a result, this converter with

a regulated load also behaves with a CPL characteristic to the power system. Examples include battery charge and other DC loads (e.g. avionics).

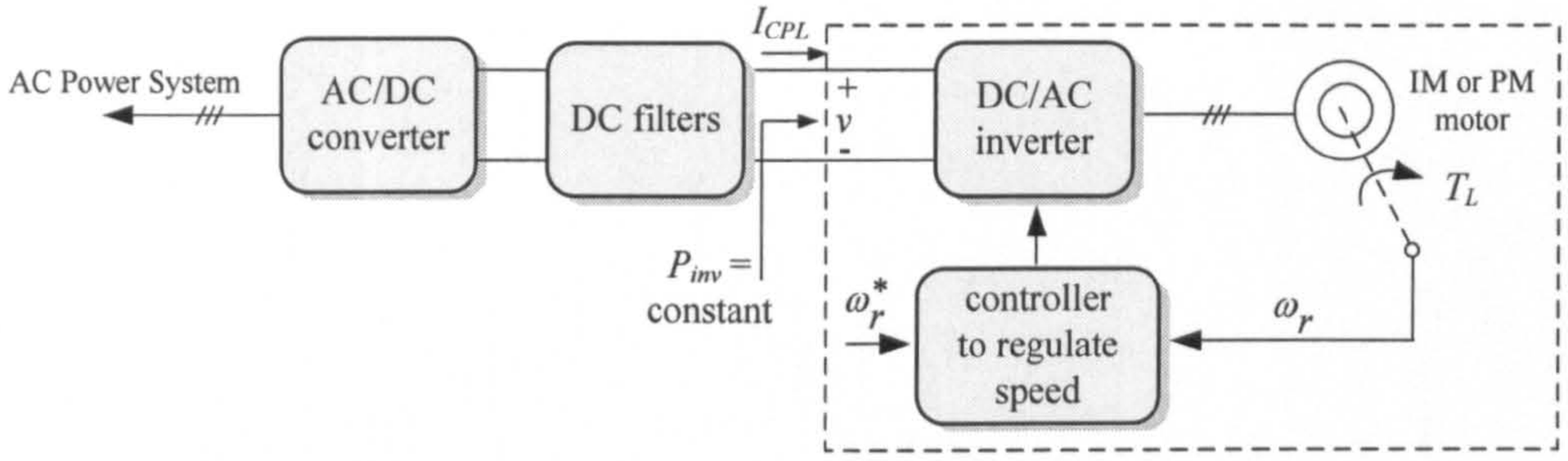

Figure 1.3: An actuator drive system behaving as a CPL to the AC power system

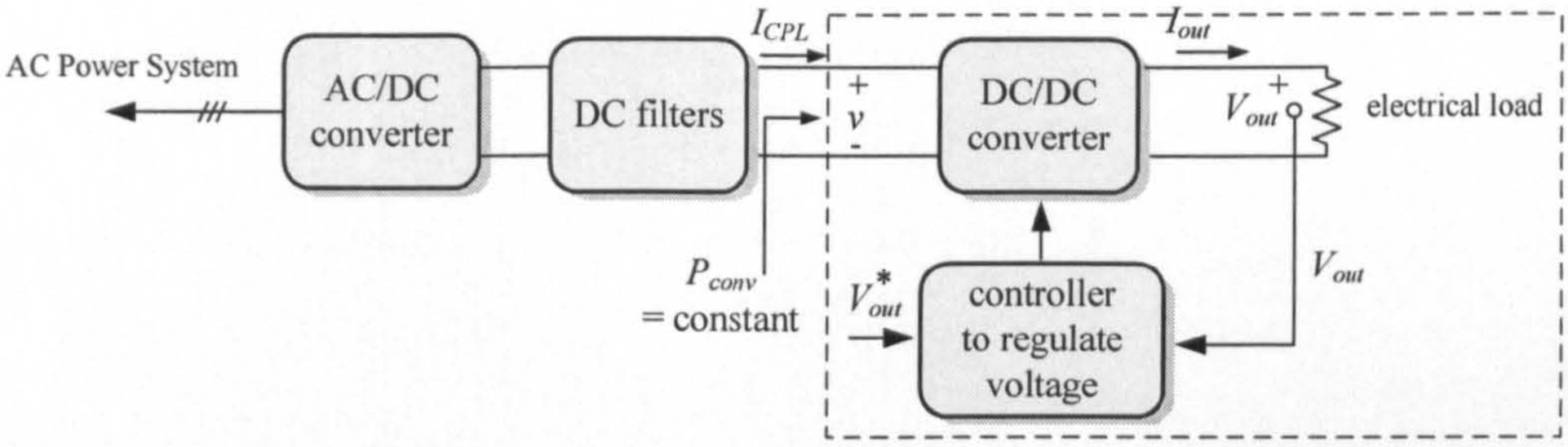

Figure 1.4: A DC voltage regulator presenting a CPL to the AC power system

A controlled power converter can be made to achieve nearly an ideal constant power regulation under the fast controller actions. Hence, these converters can behave as an ideal CPL in which the current into a CPL can be defined as:

$$I_{CPL} = \frac{P_{CPL}}{v} \tag{1-1}$$

where P_{CPL} is the command power depending on the system operating point and v is the voltage across the CPL as shown in Figure 1.3 and Figure 1.4. Taking the partial differential of (1-1), we have:

$$\partial I_{CPL} = -\frac{P_{CPLo}}{v_o^2}\partial v + \frac{1}{v_o}\partial P_{CPL} \tag{1-2}$$

The P_{CPL} is constant for each operating point. Hence, ∂P_{CPL} in (1-2) is set to zero to yield:

$$\frac{\partial v}{\partial I_{CPL}} = -\frac{v_o^2}{P_{CPLo}} \tag{1-3}$$

The characteristic of an ideal CPL is depicted in Figure 1.5. If v decreases, I_{CPL} has to increase to keep the constant power P_{CPL} at the input terminal. The global impedance value of CPL is positive, while the incremental impedance is always negative as shown in (1-3). Therefore, the CPL has a small-signal negative impedance to the system.

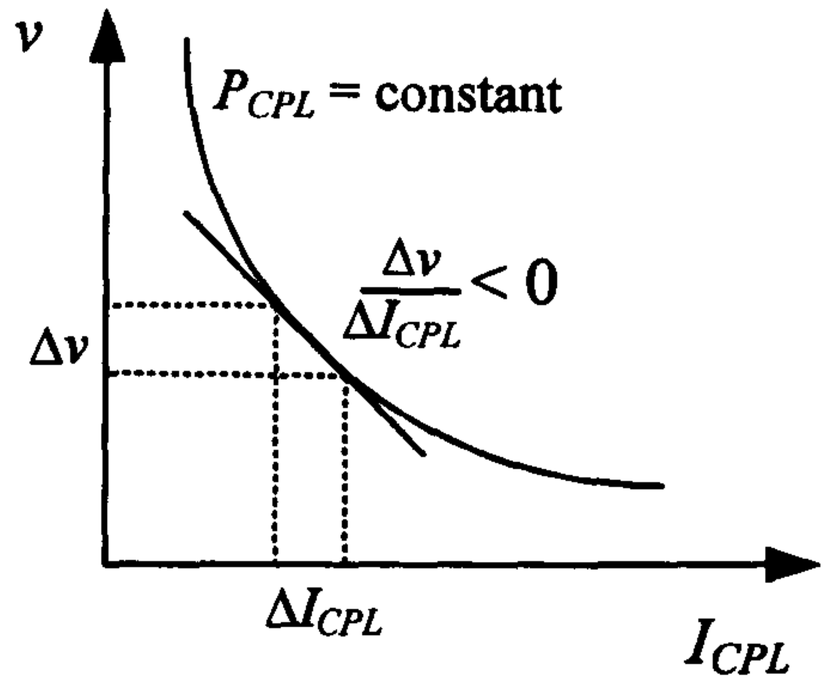

Figure 1.5: The negative impedance behaviour of CPL

The CPLs are normally fed through power converters via DC-link low pass filters as shown in Figure 1.3 and Figure 1.4. The negative impedance of the CPL may reduce the low filter resistance that is normally positive. Reducing the filter resistance can produce oscillatory behaviour. Therefore, if the system has a sufficiently large CPL, the system can become unstable. The CPL can significantly degrade the system performance and stability [10]-[14].

Hence, development of effective models capable of representing power electronic based system (PEBS) dynamic behaviour is of great importance. The dynamic model can be used to predict the system operating point at which instability occurs. There is a lot of previous work for power system models and stability studies. The literature review for modelling of power converters and stability study of the power system with CPL is described below.

1.2.2 The Modelling and Stability Analysis of PEBSs

It is well known that the power converter model is time-varying because of the switching behaviour. Several approaches are commonly used for eliminating the switching actions to achieve time-invariant model. Then, the classical eigenvalue and frequency domain approaches can be used for stability analysis. The first is the generalized state-space averaging (SSA) modelling method. This will be described in Section 2.3. This method has been used to analyse many power converters in DC distribution systems [12],[13],[15]-[17], as well as uncontrolled and controlled rectifiers in single-phase AC distribution systems [18], and 6- and 12- pulse diode rectifiers in three phase systems [19].

The second is an average-value modelling method, which has been used for 6- and 12- pulse diode rectifiers in many publications [20]-[22], as well as generators with line-commutated rectifiers [23]-[27]. These rectifiers can be modelled with good accuracy as a constant DC voltage source. Moreover, [28] reported a new average-value model of three-phase and nine-phase diode rectifiers to improve AC current and DC voltage dynamics. However this method is not easily applicable to the analysis of the stability of the general AC power system with multi-converter power electronic systems.

Another technique widely used for AC system analysis is that of dq-transformation theory [29]-[31], in which power converters can be treated as time-varying transformers. The dq modelling method can also be easily

applied for modelling a power system comprising vector-controlled converters where the SSA model and the average-value model are not easily applicable. Moreover, the resulting converter models can be easily combined with models of other power elements expressed in terms of synchronously rotating frames such as generators, front-end converters, and vector-controlled drives. Hence, the dq modelling method is selected for modelling the aircraft power system in this research. The dq models of three-phase AC-DC power systems have been reported in the previous works [29]-[31]. But these do not include CPL. Applying the dq modelling approach for stability studies of the power system including a CPL has been addressed in our publications [32]-[34].

On obtaining the non-linear dynamic model, the stability analysis can proceed either through large-signal or small-signal linearization methods. Large-signal stability analysis has been applied in [35],[36] using the Lyapunov's theorem. However, this method may provide some difficulties for a complex power system. Normally, the stability analysis of power systems with power electronic loads uses the small-signal method. The linearized model can be easily analyzed by the classical stability study methods. However, the stability results from the linearized model are valid only small perturbations in the system operation point. The more details of large-signal stability analysis can be found in [35],[36]. In this thesis, the stability analysis focuses on small-signal method only, similar to reported in [17], [32]-[34], [37]-[48] assuming the converter is operated around the equilibrium point. Two approaches can be used for investigating stability of linearized models. The first is the eigenvalue theorem in which the system eigenvalues can be calculated from the Jacobian matrix [17],[32]-[34], [37]-[40]. Another method is an impedance/admittance method based on the Middlebrook criterion [10] which has been successfully used to analyse the stability of DC distributed power systems [41]-[48]. For AC distribution systems, many publications reported the input and output impedance of AC-DC converters. References [49]-[51] described the input impedance of boost single-phase PFC converters, as well as three-phase PWM rectifiers [52],[53]. Although, the application of boost single-phase PFC

converter models for stability analysis based on the impedance/admittance method was described in [54], the output impedance of the AC source was defined from measurements. For diode rectifiers, most existing work describes the output impedance derived from their average-value models [20]-[27]. This is because the average-value models easily allow establishing the output impedance of the source subsystem for stability analysis using the impedance/admittance method as described in [55]. However, as mentioned before, this model is not easily applicable to analyse the stability of the general AC power system with multi-converter power electronic systems. Therefore, references [56]-[58] report the input impedance modelling and analysis of line-commutated rectifiers. However, the application of these models for stability analysis has not been reported. It can be seen that one problem of the impedance/admittance method is the difficulty in deriving source impedance and load admittances for complex AC systems having parallel power converter connections. Therefore, the eigenvalue approach is selected for stability analysis in this research with the dq model.

Generally, most research work for stability studies focuses on only individual converters for its stand-alone operation [17], [32]-[55]. The dynamic models of multi-converter systems have been studied for DC distribution system in [59]. Studies for AC system have not been reported. In addition, the interconnection of the converters can affect power quality and system stability [43],[59]. Therefore, the derivation of the dynamic model of frequency-wild power systems with the multiplicity of actuators, aircraft loads and bus geometries is in need of study.

In order to avoid negative impedance instability, there are two possible ways. The first is a passive damping. The passive damping can be added into the DC-link filter in series or parallel with the DC-link capacitor [60]. In addition, a large DC-link capacitor can also be used to mitigate the instability problem caused by a CPL [61]. However, the passive technique may increase the power losses and the large capacitor causes higher weight and cost. The second way

is by an active technique. Reducing the regulation bandwidth of the load can improve the system stability [60]. Moreover, [61]-[63] represented the nonlinear control strategy to mitigate this instability problem. Recently, a simple linear compensation technique using active damping to damp the filter is used to overcome the negative impedance instability [64],[65].

If we have a more accurate model for stability studies, a dynamic model can be used to predict the instability point for possible variations in system operating points and system parameters. Hence, the dynamic model of the power system with CPLs is of importance. If the model can ensure that the system is always stable, then we do not need to add any passive damping into the system. In addition, we can find out how to make the system more stable from the dynamic model. Moreover, the accurate dynamic model can also be used for the design of stabilization controllers.

1.3 The Scope and Structure of the Thesis

The research of the thesis deals with the modelling and stability analysis of the aircraft power system. The aircraft power system architecture considered in the thesis is based on the MOET aircraft power system for one engine generator as shown in Figure 1.2. The small-signal stability analysis is used in this research under the assumption that the aircraft power system operating point is not changed rapidly during normal operation mode. Hence, the linearization technique using the first order terms of a Taylor expansion [70],[71] is used so as to achieve a set of linear models around an equilibrium point for a small-signal stability study. The power flow equation [72] is used to determine the steady-state values of the system. The thesis presents the development of effective models capable of representing EPS dynamic behaviour for stability studies. The proposed model can be used to predict the instability point for variations in system operating points or system parameters. The model can be also used for thorough investigations of aircraft

power system stability for representative architectures and worst-case operational modes. In order to accomplish the research objectives set out above, the thesis is organised into eight chapters. The structure of the thesis is described as follows:

Chapter 1 is the introduction to the thesis which describes the aircraft power system architecture used in the thesis. This chapter describes the effect of the negative impedance instability caused by constant power loads. The literature review for modelling of power converters and stability study of the power system with constant power loads are also described. The thesis layout is also outlined.

Chapter 2. The application of a dq modelling method for the stability analysis of a system consisting of CPLs has not been reported in previous publications. Chapter 2 derived the dq model of a six-pulse diode rectifier for stability studies of such systems. To compare with other modelling approaches, the six-pulse diode rectifier model is derived by three different approaches that are; state-space averaging (SSA) method, average-value modelling method, and dq modelling method. The system dynamic models from the three approaches are then used for stability analysis with the eigenvalue theorem. The comparisons of the stability results from the different power converter models are described. In addition, the impedance/admittance method based on Middlebrook criterion is used for stability analysis and the results from this method are compared with those from the eigenvalue theorem. According to the results, the dq modelling method is selected for modelling the power converter in the thesis. Stability analysis uses the eigenvalue theorem with the linearized dq models. This chapter also show how the dq models of the six-pulse diode rectifier can be used to represent the twelve-pulse autotransformer rectifier unit. The SABER time-domain simulation is used to support the theoretical results.

Chapter 3 derives the dq model of a controlled PWM rectifier. This model is used for stability studies of power systems with PWM rectifiers which have not been reported in previous publications. Chapter 3 also shows that the dq modelling method is easily applicable to model a converter controlled in terms of a rotating dq-frame aligned with the grid voltage vector. The dynamic model of the system can predict the instability point for variations of system operating point and system parameters. The SABER simulation is used as a benchmark model to support the theoretical results.

Chapter 4. In Chapter 2 and 3, an ideal CPL was used to represent the controlled electromechanical actuators (EMAs). In Chapter 4 however, we investigate the effect of the dynamics of EMA and their impact on stability. The effects of actuator dynamics have been considered in [73]. However, these effects have not been widely discussed in previous publications in which the CPL is generally defined as an ideal current source without dynamic behaviour. This chapter also represents how to combine the dynamic of CPL into the power system with a diode rectifier or a PWM rectifier for stability studies using the dq modelling method with the eigenvalue theorem. The stability margins are assessed and compared against those for the power system with the ideal CPLs. The study is supported by intensive time domain simulations. This chapter also considers EMAs using a surface mount permanent magnet (SMPM) machine. As far as the mathematical formulation is concerned, the SMPM machine is considered a special case of the more general equation of the induction machine. The initial formulations are derived neglecting the internal resistance of the DC-link capacitor (r_c). This is a reasonable assumption for normal C_{dc} and r_c values. However, in experimental work in Chapter 5, it is found useful to put many capacitors in series (to obtain low values) and hence r_c is usually high. The power system with the PM machine and r_c is also described in this chapter.

Chapter 5 describes experiments undertaken to practically ascertain the effect of the CPL dynamics as explained in Chapter 4 and hence verify the dq

modelling approach described in Chapters 2-4. In particular the experimental results are aimed towards showing the impact on system dynamics of variations in AC supply frequency, actuator speed loop dynamics, and DC link voltage measurement filtering. The comparisons between theoretical and experimental results are made. After this the dq models will be applied to more complex power systems.

Chapter 6 describes how the dq modelling method is used to create a nonlinear dynamic model for a more realistic power system that includes the output voltage dynamics of the synchronous generator (SG) and generator control unit (GCU), as well as the dynamics of electromechanical actuators (non-ideal CPL) as described in Chapter 4. These effects have not been addressed in previous publications in which the constant power load (CPL) is generally defined as an ideal current source without dynamic behaviour (ideal CPL), and the generator with GCU is regarded as an ideal voltage source with an infinitely fast controller action. The details of how to combine the dynamics of a GCU and an electromechanical actuator into a power system with a diode rectifier for stability studies is described in this chapter. The impact of using the dynamic models for the SG-GCU and non-ideal CPL in comparison with the models using an ideal voltage source and ideal CPL is also shown. The SABER time-domain simulation is used to support the predicted results from the model.

Chapter 7 extends the work from the previous chapters to create the dynamic model of the generalized aircraft power system representing real architectures with multiplicity of actuators, aircraft loads and bus geometries using the dq modelling approach. Three example systems including the real aircraft power system as described in Chapter 1 are used to illustrate how to apply the generalized model for a stability study. It is also shown how the theory can be used to predict instability due to possible variations in operating points and system parameters. It will be shown how the elements described in the thesis can be interconnected in an algorithmic way resulting in a powerful and

flexible stability analysis tool. The SABER time-domain simulation is used to support the theoretical results.

Chapter 8 contains the conclusion of the thesis. It summarises the work and the main outcome of the PhD research work. It also provides possible future researches that can be developed from the work of the thesis. The publications from the research are also given.

Chapter 2

Power Systems with a Diode Rectifier and an Ideal Constant Power Load

2.1 Introduction

Chapter 1 discussed the main elements of aircraft power system architecture as shown in Figure 2.1. This consists of an engine generator with a generator control unit (GCU), transmission line, uncontrolled rectifier or autotransformer rectifier unit (ATRU) feeding the electromechanical actuator (EMA) for a DC bus environmental control or other DC loads through a HVDC bus. These loads behave as a CPL. Moreover, the engine generator also supplies electricity to wing de-icing loads and the essential AC bus (AC ESS). The AC ESS bus supplies a controlled PWM rectifier unit feeding the electromechanical actuators for aileron, rudder, flaps, spoilers, and elevator. However, this chapter focuses on only the system consisting of 3-phase voltage source, ATRU1, DC-link filters, and ideal CPL. Although the six-pulse diode rectifier are generally not acceptable in the aircraft power system application according to the aerospace power quality standard requirements [74], the six-pulse diode rectifier can be used to represent the twelve-pulse autotransformer rectifier unit (ATRU1) as shown in Figure 2.1 (dashdot line). This is because of the symmetry of two six-pulse diode rectifiers in the ATRU. Therefore, the twelve-pulse diode rectifier can be approximately represented by an equivalent six-pulse diode rectifier [75] that will be shown in Section 2.6. An ideal CPL is also used to represent an EMA for the electrical environmental conditioning system. An ideal 3-phase voltage source is used to represent an engine generator with a GCU by assuming an infinitely fast

infinitely fast controller action of the GCU. Similarly, the ideal CPL is used to represent actuator drive systems under the same assumption.

Generally, there are two methods to analyse the stability of the AC-DC power system feeding CPLs via a six-pulse diode rectifier. The first approach is to analyse the system stability on the DC distribution system only [37]. This excludes the line parameters on the AC side under the assumption that the AC subsystem is always stable, and the DC voltage of the output rectifier is constant. However, considering the stability of AC and DC subsystems individually cannot provide precise results [18]. Hence, the second method considers a stability study for hybrid AC and DC distribution system connected together via a power converter [18], [38]. This can provide stability prediction with good accuracy.

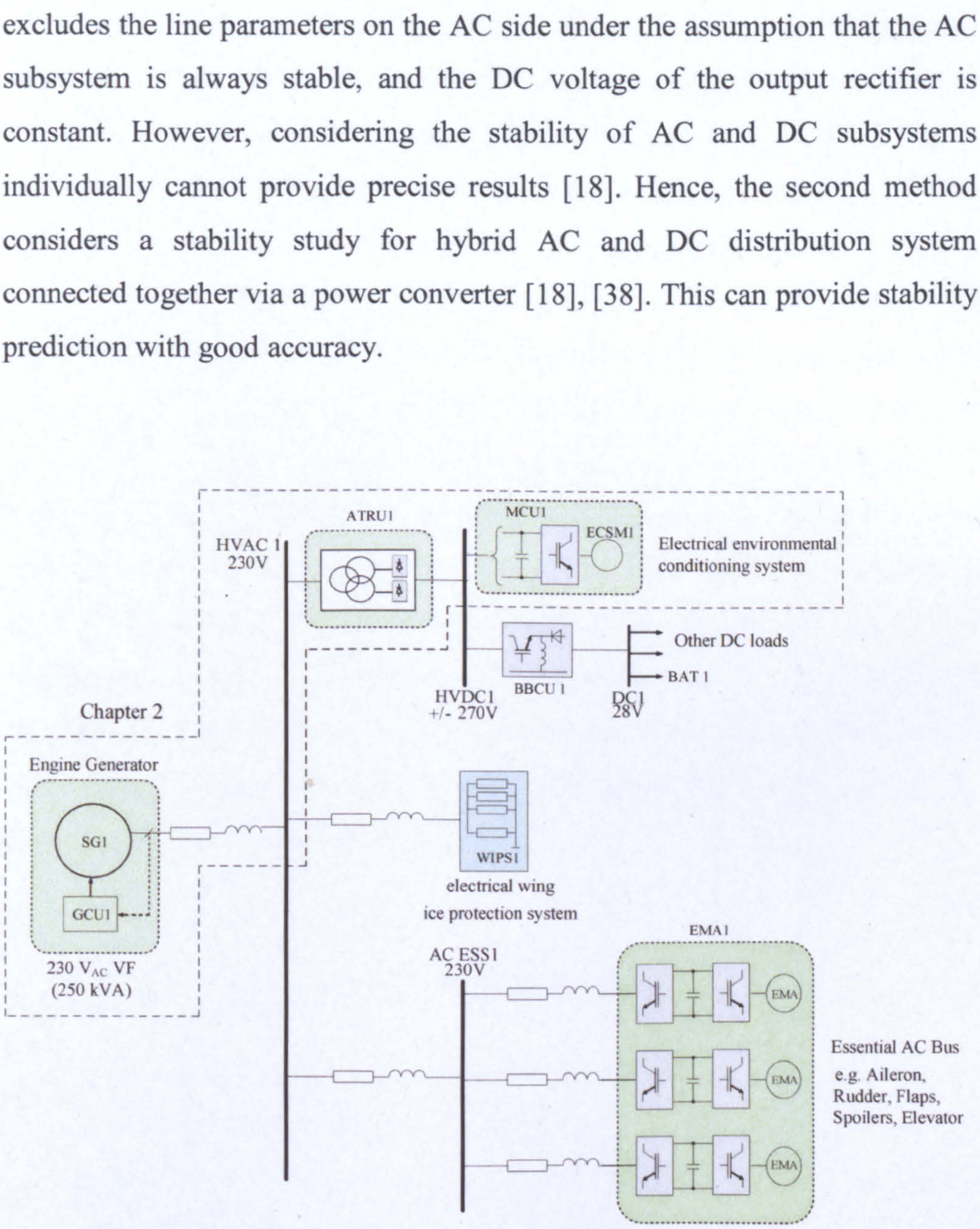

Figure 2.1: The main elements of aircraft power system architecture

This chapter presents the stability analysis of AC-DC power systems by considering both AC and DC sides. The dq modelling approach [29]-[31] is used to model the power converter treated as a time-varying transformer ratio. The results from dq modelling method are explained in Section 2.2. The dq models of three-phase AC-DC power systems feeding an ideal CPL have not been reported in the pervious works [29]-[31]. Our work from this section was published in [32]. In addition, the stability results using the dq modelling approach are also compared against those of other methods. These include the state space averaging (SSA) modelling approach [12],[13],[15]-[19] as described in Section 2.3, and the average-value modelling method [20]-[28] as described in Section 2.4. The SSA modelling approach has been used to analyse many power converters in DC and AC distribution systems. This approach uses the complex Fourier coefficients of the switching signal waveform as the system state variables. The average-value models for the six-pulse diode rectifier have also been derived in many publications [23]-[26],[66] in which the rectifier can be modelled as a DC voltage source with a particular internal impedance. In Section 2.5, the impedance/admittance stability methods based on Middlebrook criterion are introduced. This method analyses the system stability in the frequency domain. Finally, Section 2.6 shows how the dq models of the six-pulse diode rectifier from Section 2.2 can be used to represent the twelve-pulse autotransformer rectifier unit. The chapter summary is addressed in Section 2.7.

2.2 Analysis using dq modelling Approach

This section deals with stability analysis of a three-phase frequency-wild AC power system with an ideal CPL fed through a six-pulse diode rectifier. The mathematical model of the power system suitable for stability analysis is derived using the dq modelling approach. Simulation results are used to support the theoretical results. It is also shown how the theory can be used to predict instability due to possible variations in the system parameters.

2.2.1. Power System Definition and Assumptions

The power system studied in this section is shown in Figure 2.2. It consists of a 3-phase voltage source, transmission line, six-pulse diode rectifier, DC-link filters, and an ideal CPL connected to the DC bus. Note that the ideal voltage source may be used to represent an engine generator with GCU by assuming an infinitely fast controller action of the GCU. Similarly, the ideal CPL is used to represent actuator drive systems under the same assumption.

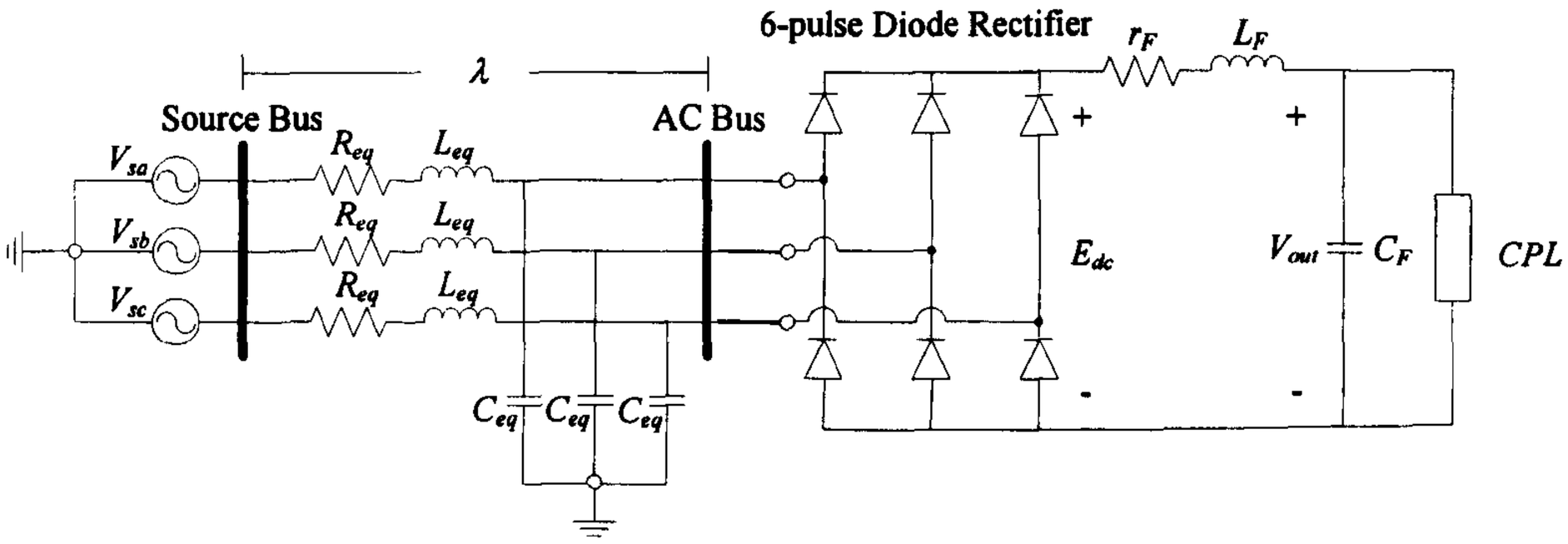

Figure 2.2: The power system studied

It is assumed that the 3-phase voltage source is balanced. R_{eq}, L_{eq}, and C_{eq} are the equivalent parameters of a transmission line. Note that if there are no C_{eq} in the system, they can be set to 2nF to represent the cable parasitic capacitance in the mathematical model. This is because the dq mathematical model for the diode rectifier requires a voltage source which can be provided by these capacitances. The small value of capacitance cannot affect to the stability results of the system as it will be shown in Chapter 5. The DC link filters are shown by elements r_F, L_F and C_F. E_{dc} and V_{out} are the output terminal voltage of the rectifier and the voltage across the DC link capacitor C_F, respectively. A phase shift between the source bus and the AC bus is shown in Figure 2.2 as λ. The effect of L_{eq} on the AC side causes an overlap angle μ in the output waveforms that causes as a commutation voltage drop. This drop can be represented as a variable resistance r_μ depending on the system frequency ω, and located on the DC side as shown in Figure 2.3

[66],[67]. Since the commutation voltage drop has been moved on to the DC side, the switching signals for 3-phase bridge rectifier can be applied without considering the effect of overlap angle. This is shown in Figure 2.4. From Figure 2.3, E_{dcl} represents the output voltage from the switching signal without an overlap angle, while E_{dc} represents the voltage at the rectifier output terminal taking onto account the voltage drop due to the commutation resistance r_{μ}.

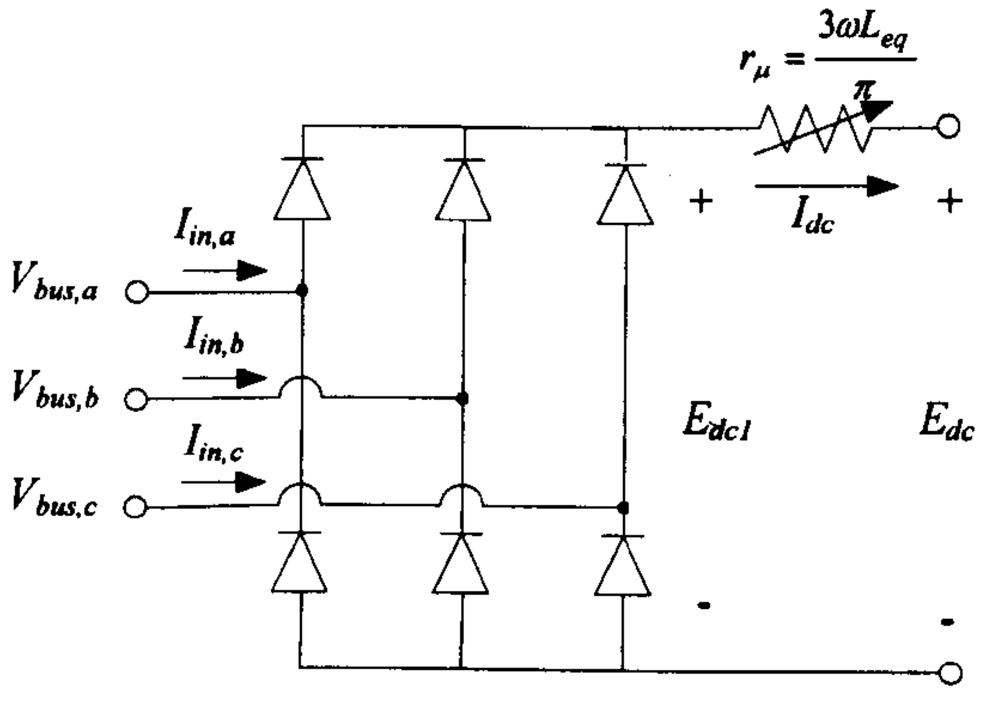

Figure 2.3: Three-phase diode rectifier with overlap angle resistance

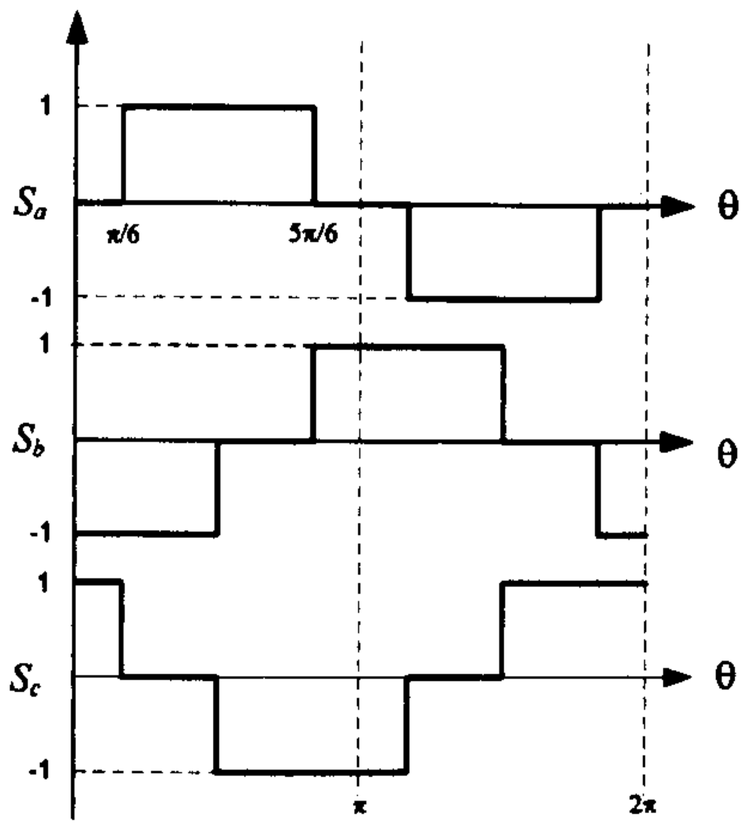

Figure 2.4: The rectifier switching signal

The dq modelling approach is now applied to derive a mathematical model of the power system depicted in Figure 2.2. The details of how to model the six-pulse diode rectifier as a time-varying transformer ratio by using dq modelling method is as follows:

The switching function of S_a in Figure 2.4 can be expressed by a Fourier series [68]:

$$S_a = \sum_{k=1,5,7,....}^{\infty} \frac{\sqrt{3}}{\pi} \cdot \frac{(-1)^{L+1}}{k} \times (-2\sin k\omega t) \tag{2-1}$$

where $k = 6L \pm 1$ (L = 0, 1, 2,....., $k > 0$). Expressions for S_b and S_c are obtained by replacing ωt in (2-1) by $\left(\omega t - \frac{2\pi}{3}\right)$ and $\left(\omega t - \frac{4\pi}{3}\right)$, respectively. Neglecting the stability effects arising from higher harmonics of the fundamental [18], the switching functions in (2-1) can be written for three phases as [68]:

$$\mathbf{S_{abc}} = \frac{2\sqrt{3}}{\pi}\left[\sin(\omega t + \phi) \quad \sin(\omega t - \frac{2\pi}{3} + \phi) \quad \sin(\omega t - \frac{4\pi}{3} + \phi)\right]^T \tag{2-2}$$

where ϕ is a phase angle of the rectifier AC bus voltage. The relationship between input and output terminal of rectifier is given by [68],[69]:

$$\mathbf{I_{in,abc}} = \mathbf{S_{abc}} I_{dc} \tag{2-3}$$

$$E_{dc1} = \mathbf{S_{abc}^T V_{bus,abc}} \tag{2-4}$$

For a diode rectifier, the fundamental input current is in phase with the input voltage assuming that the output DC current of the rectifier I_{dc} is constant [18]. With (2-3), this means that the input rectifier voltage, the switching signals, and the input rectifier current are all in phase. The diode rectifier is then transformed into a two axis frame rotating at the system frequency ω by means of:

$$\mathbf{T}[\theta(t)]=\sqrt{\frac{2}{3}}\begin{bmatrix}\cos(\theta(t)) & \cos(\theta(t)-\frac{2\pi}{3}) & \cos(\theta(t)+\frac{2\pi}{3})\\ -\sin(\theta(t)) & -\sin(\theta(t)-\frac{2\pi}{3}) & -\sin(\theta(t)+\frac{2\pi}{3})\end{bmatrix} \quad (2\text{-}5)$$

where $\theta(t)=\omega t-\frac{\pi}{2}+\phi_1$.

The basic concept of dq-transformation is addressed in Appendix A.

This is the common dq-axis frame which can be fixed to any chosen bus. Fixing the d-axis to a bus means that V_q at that bus is zero by definition.

Combining (2-3), (2-4) and (2-5) results in:

$$\mathbf{I}_{\mathbf{in,dq}}=\mathbf{S}_{\mathbf{dq}}I_{dc} \quad (2\text{-}6)$$

$$E_{dc1}=\mathbf{S}_{\mathbf{dq}}^{T}\mathbf{V}_{\mathbf{bus,dq}} \quad (2\text{-}7)$$

$$\mathbf{S}_{\mathbf{dq}}=\sqrt{\frac{3}{2}}\cdot\frac{2\sqrt{3}}{\pi}\begin{bmatrix}\cos(\phi_1-\phi) & -\sin(\phi_1-\phi)\end{bmatrix}^{T} \quad (2\text{-}8)$$

From (2-6), (2-7), and (2-8) the rectifier is represented as a transformer having d and q-axis transformer ratios S_d, S_q that depend on the phase shift between the dq-frame (ϕ_1) and the rectifier terminal voltage frame (ϕ). The vector diagram for the dq transformation is as shown in Figure 2.5 where V_s is the peak amplitude phase voltage, I_{in} is the peak amplitude current, and S is the peak amplitude of the switching signal equal to $2\sqrt{3}/\pi$. The equivalent circuit of the six-pulse diode rectifier in the dq-frame derived by using dq modelling approach is shown in Figure 2.6. In addition, the dq model of six-pulse diode rectifier is derived under the assumptions that the DC load current is constant, only one commutation occurs at a time ($\mu<60^{\circ}$), and the diode rectifier is operated in the continuous conduction mode (CCM).

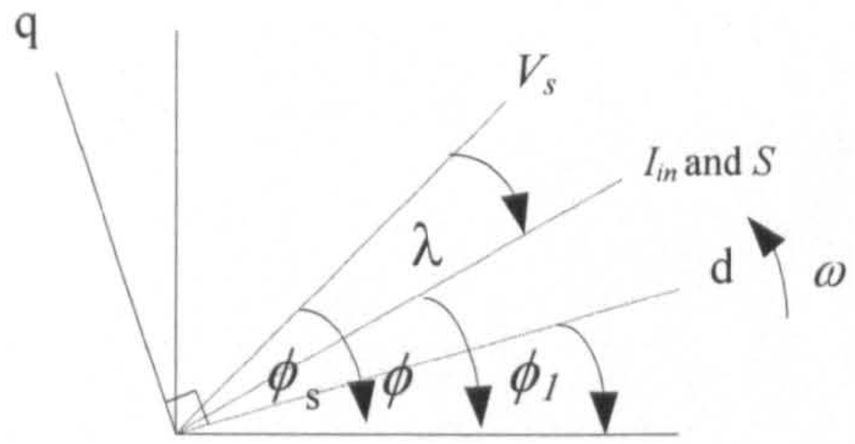

Figure 2.5: The vector diagram for DQ transformation

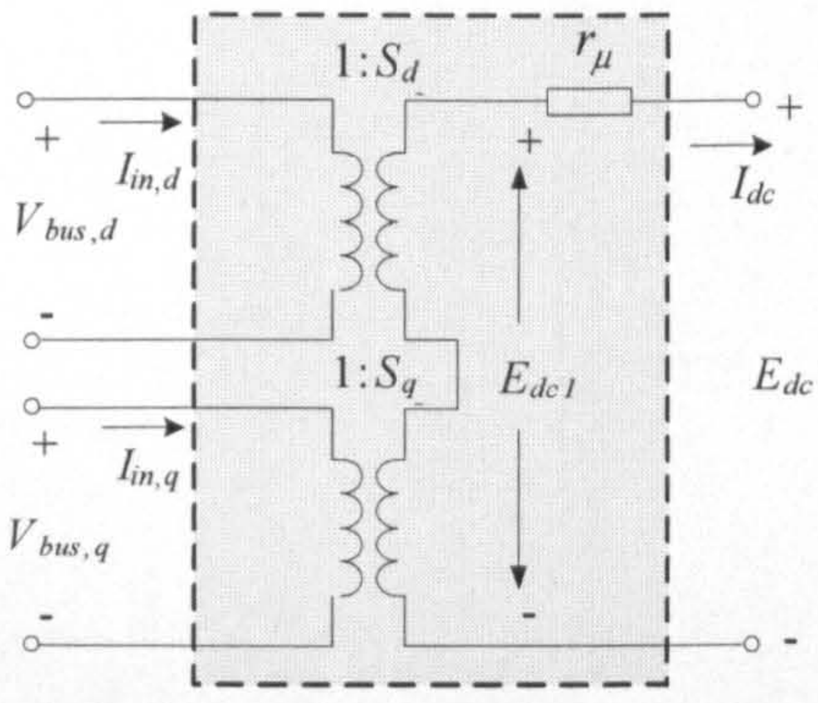

Figure 2.6: The uncontrolled rectifier equivalent circuit in the dq frame

Using (2-5), the cable section can be transformed into the dq-frame. The transformation of the series RL and shunt C circuits into the dq-frame are addressed in Appendix B. The dq representation of the cable is then combined with the diode rectifier model as shown in Figure 2.6. As a result, the equivalent circuit of the power system of Figure 2.2 can be represented in the synchronously rotating dq-frame is shown in Figure 2.7, where the 3-phase diode bridge rectifier is represented as a transformer. The equivalent circuit in Figure 2.7 can be simplified by fixing the rotating frame on the bus at the input terminal of the diode rectifier frame $(\phi_1 = \phi)$. This results in circuit shown in Figure 2.8.

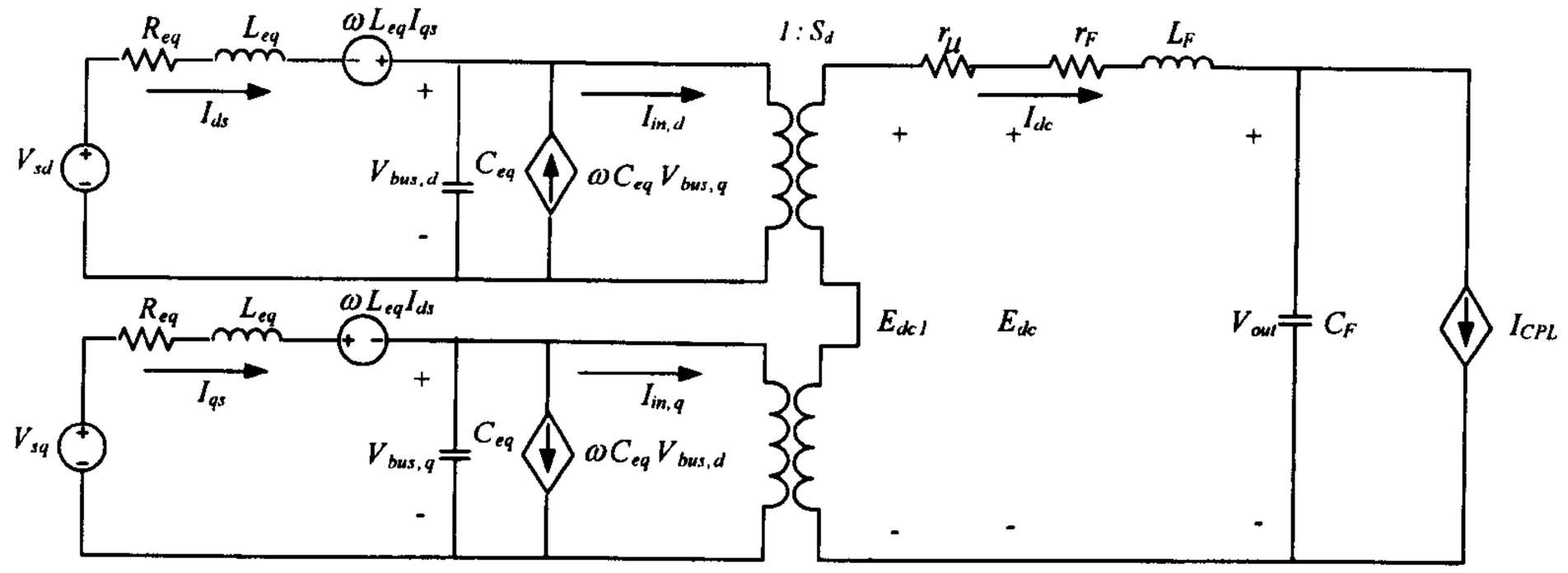

Figure 2.7: The equivalent circuit of the system considered on dq frame

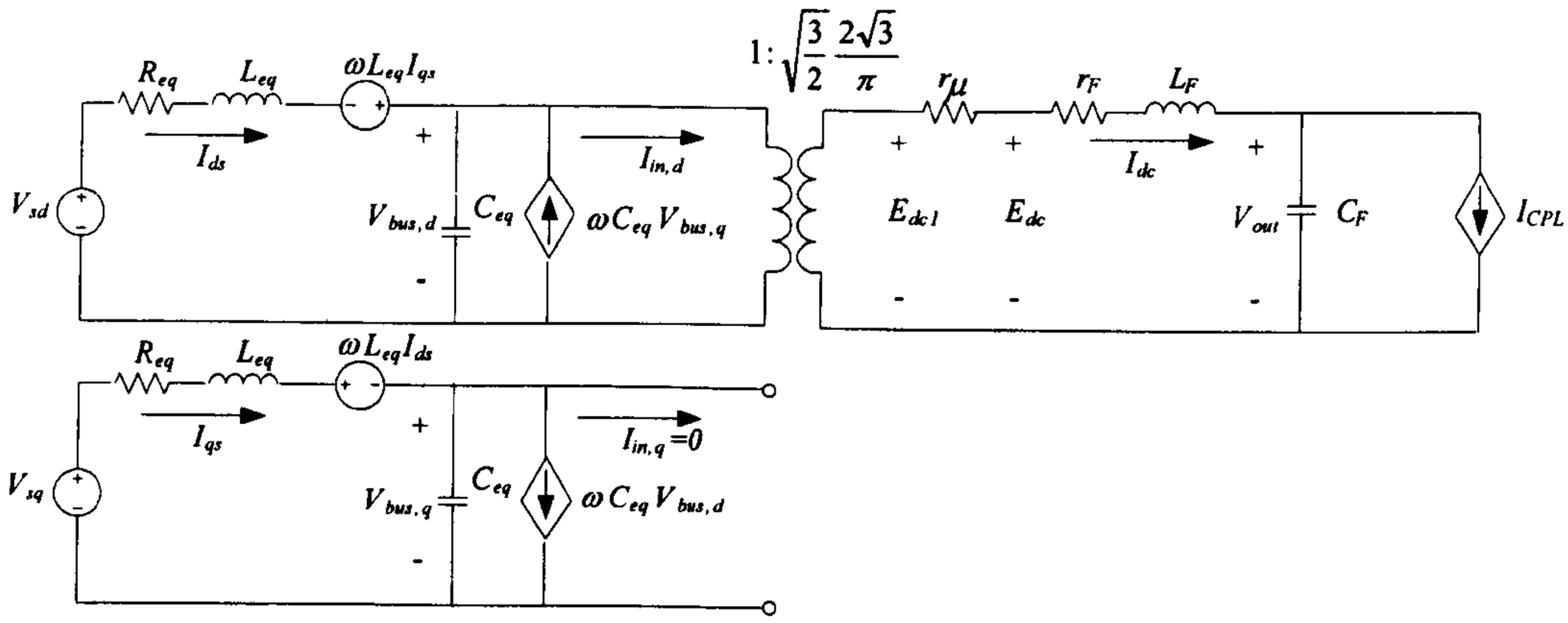

Figure 2.8: The simplified equivalent circuit of the power system

It can be seen from Figure 2.8 that $I_{in,q} = 0$ and transformer in the q-axis is eliminated. Therefore, the equivalent circuit given in Figure 2.8 is easier to analyse. In addition, the ideal CPL can be considered as a voltage-dependent current source given by

$$I_{CPL} = \frac{P_{CPL}}{V_{out}} \tag{2-9}$$

2.2.2. Deriving the Non-Linear Dynamic Model and Linearized Model

Applying the Kirchhoff's voltage law (KVL) and Kirchhoff's current law (KCL) to the circuit in Figure 2.8 determines the set of nonlinear differential equations. We define:

State variables:$\mathbf{x} = [\, I_{ds}\ I_{qs}\ V_{bus,d}\ V_{bus,q}\ I_{dc}\ V_{out}]$

Input:$\mathbf{u} = [\, V_m\ P_{CPL}\,]$ (2-10)

Output:$\mathbf{y} = [V_{out}]$

The set of nonlinear differential equations is given as follows:

$$
\begin{aligned}
\dot{I}_{ds} &= -\frac{R_{eq}}{L_{eq}} I_{ds} + \omega I_{qs} - \frac{1}{L_{eq}} V_{bus,d} + \frac{1}{L_{eq}} V_{sd} \\
\dot{I}_{qs} &= -\omega I_{ds} - \frac{R_{eq}}{L_{eq}} I_{qs} - \frac{1}{L_{eq}} V_{bus,q} + \frac{1}{L_{eq}} V_{sq} \\
\dot{V}_{bus,d} &= \frac{1}{C_{eq}} I_{ds} + \omega V_{bus,q} - \sqrt{\frac{3}{2}} \frac{2\sqrt{3}}{\pi C_{eq}} I_{dc} \\
\dot{V}_{bus,q} &= -\omega V_{bus,d} + \frac{1}{C_{eq}} I_{qs} \\
\dot{I}_{dc} &= \sqrt{\frac{3}{2}} \frac{2\sqrt{3}}{\pi L_F} V_{bus,d} - \left(\frac{r_F}{L_F} + \frac{r_\mu}{L_F} \right) I_{dc} - \frac{1}{L_F} V_{out} \\
\dot{V}_{out} &= \frac{1}{C_F} I_{dc} - \frac{1}{C_F} \frac{P_{CPL}}{V_{out}}
\end{aligned}
\qquad (2\text{-}11)
$$

As mentioned in Chapter 1, the linearized model can be used to analyse the small-signal stability of aircraft power systems under the assumption that the system operating points are not changed rapidly. This assumption is the normal behaviour of the aircraft power systems. Therefore, equation (2-11) is linearized using the first order terms of the Taylor expansion [70],[71] (Appendix C) so as to achieve a set of linear differential equations around an

equilibrium point. The dq linearized model of (2-11) is then of the following form:

$$\begin{aligned} \delta\dot{\mathbf{x}} &= \mathbf{A}(\mathbf{x_0},\mathbf{u_0})\delta\mathbf{x} + \mathbf{B}(\mathbf{x_0},\mathbf{u_0})\delta\mathbf{u} \\ \delta\mathbf{y} &= \mathbf{C}(\mathbf{x_0},\mathbf{u_0})\delta\mathbf{x} + \mathbf{D}(\mathbf{x_0},\mathbf{u_0})\delta\mathbf{u} \end{aligned} \tag{2-12}$$

where

$$\delta\mathbf{x} = [\delta I_{ds} \quad \delta I_{qs} \quad \delta V_{bus,d} \quad \delta V_{bus,q} \quad \delta I_{dc} \quad \delta V_{out}]^T$$

$$\delta\mathbf{u} = [\delta V_m \quad \delta P_{CPL}]^T, \qquad \delta\mathbf{y} = [\delta V_{out}]$$

The form of $\mathbf{A(x_0,u_0)}$, $\mathbf{B(x_0,u_0)}$, $\mathbf{C(x_0,u_0)}$, and $\mathbf{D(x_0,u_0)}$ are given in (2-13).

$$\mathbf{A}(\mathbf{x_0},\mathbf{u_0}) = \begin{bmatrix} -\frac{R_{eq}}{L_{eq}} & \omega & -\frac{1}{L_{eq}} & 0 & 0 & 0 \\ -\omega & -\frac{R_{eq}}{L_{eq}} & 0 & -\frac{1}{L_{eq}} & 0 & 0 \\ \frac{1}{C_{eq}} & 0 & 0 & \omega & -\sqrt{\frac{3}{2}}\cdot\frac{2\sqrt{3}}{\pi C_{eq}} & 0 \\ 0 & \frac{1}{C_{eq}} & -\omega & 0 & 0 & 0 \\ 0 & 0 & \sqrt{\frac{3}{2}}\cdot\frac{2\sqrt{3}}{\pi L_F} & 0 & -\left(\frac{r_F}{L_F}+\frac{r_\mu}{L_F}\right) & -\frac{1}{L_F} \\ 0 & 0 & 0 & 0 & \frac{1}{C_F} & \frac{P_{CPLo}}{C_F V_{out,o}^2} \end{bmatrix}_{6\times 6}$$

$$\mathbf{B}(\mathbf{x_0},\mathbf{u_0}) = \begin{bmatrix} \sqrt{\frac{3}{2}}\cdot\frac{\cos(\lambda_o)}{L_{eq}} & 0 \\ \sqrt{\frac{3}{2}}\cdot\frac{\sin(\lambda_o)}{L_{eq}} & 0 \\ 0 & 0 \\ 0 & 0 \\ 0 & 0 \\ 0 & -\frac{1}{C_F V_{out,o}} \end{bmatrix}_{6\times 2}$$

$$\mathbf{C}(\mathbf{x_o},\mathbf{u_o}) = [0\ 0\ 0\ 0\ 0\ 1]_{1\times 6}$$
$$\mathbf{D}(\mathbf{x_o},\mathbf{u_o}) = [0\ 0]_{1\times 2} \qquad (2\text{-}13)$$

2.2.3. Calculating the Steady-State Equilibrium Value

The dq linearized model from Section 2.2.2 is derived through the linearization technique around the operating point (or steady state value). According to (2-13), the linearized model needs to define $V_{out,o}$ and λ_o for the small-signal simulation and stability study. The power flow equation [72] can be applied to determine the steady state values at the AC side. The single line power flow diagram of the power system in Figure 2.2 is depicted in Figure 2.9 in which the line capacitors are ignored assuming C_{eq} is very small.

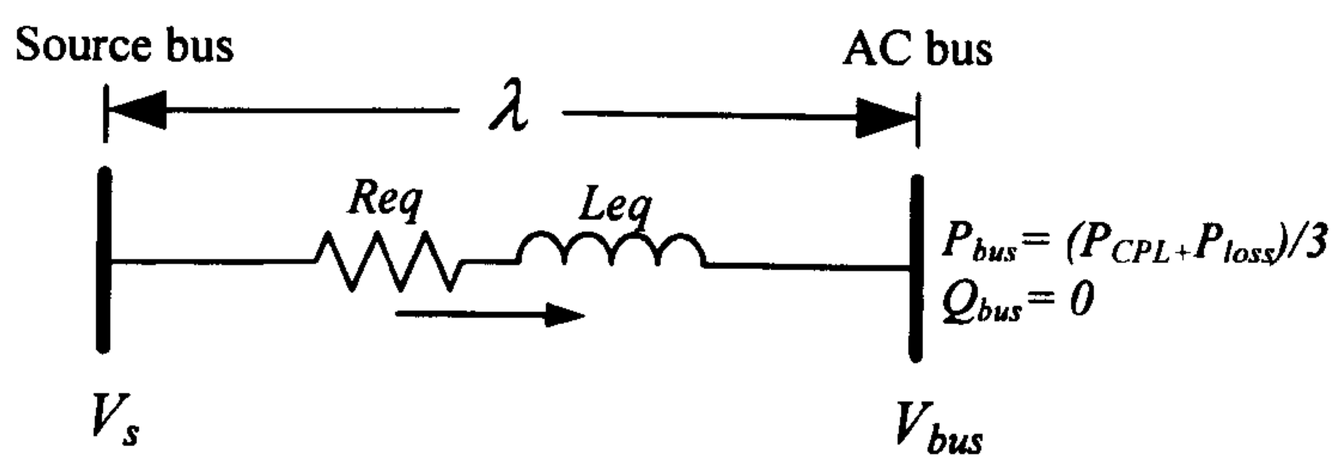

Figure 2.9: The single line diagram for steady state power calculations

Figure 2.9 leads to a system of two nonlinear equations:

$$+\frac{V_{bus}V_s}{Z}\cos(\gamma_Z-\lambda)-\frac{V_{bus}^2}{Z}\cos(\gamma_Z)=(P_{CPL}+P_{loss})/3$$
$$+\frac{V_{bus}V_s}{Z}\sin(\gamma_Z-\lambda)-\frac{V_{bus}^2}{Z}\sin(\gamma_Z)=Q_{bus}=0 \qquad (2\text{-}14)$$

where V_{bus} is the steady state phase voltage at the AC bus or input terminal of the diode rectifier (rms), and λ the phase shift between V_s and V_{bus}. In addition, $Z\angle\gamma_Z$ is the transmission line impedance, while the active and reactive power (per phase) at the AC bus is given by:

$$\begin{aligned} P_{bus} &= (P_{CPL} + P_{loss})/3 \\ Q_{bus} &= 0 \end{aligned} \tag{2-15}$$

where P_{CPL} is the constant power load value and P_{loss} is the power loss due to r_F. Q_{bus} is set to zero because of the diode rectifier assumption that the fundamental input current is in phase with the input voltage. Equation (2-14) can be solved by using a numerical method such as Newton Raphson so as to get $V_{bus,o}$ and λ_o at the steady-state conditions. Consequently, $V_{out,o}$ for dq linearized model in (2-13) can then be calculated using:

$$V_{out,o} = \frac{3\sqrt{3}}{\pi}\left(\sqrt{2}V_{bus,o}\right) - \frac{3L_{eq}\omega}{\pi}I_{dco} - r_F I_{dco} \tag{2-16}$$

where

$$I_{dco} = \frac{\sqrt{3}\left|\dfrac{V_s e^{j0} - V_{bus,o}e^{-j\lambda_o}}{Ze^{j\gamma_Z}}\right|}{\sqrt{\dfrac{3}{2}}\left(\dfrac{2\sqrt{3}}{\pi}\right)}, Z = \sqrt{R_{eq}^2 + (\omega L_{eq})^2}, \gamma_Z = \tan^{-1}\left(\frac{\omega L_{eq}}{R_{eq}}\right)$$

According to (2-14), (2-15), and (2-16), the steady-state values change when the system operating point, defined from P_{CPL}, change. Therefore, we can get different linearized models of the system in Figure 2.2 for each operating point. The steady-state values from the solutions of (2-14) and (2-16) with the set of parameters in Table 2.1 are depicted in Figure 2.10.

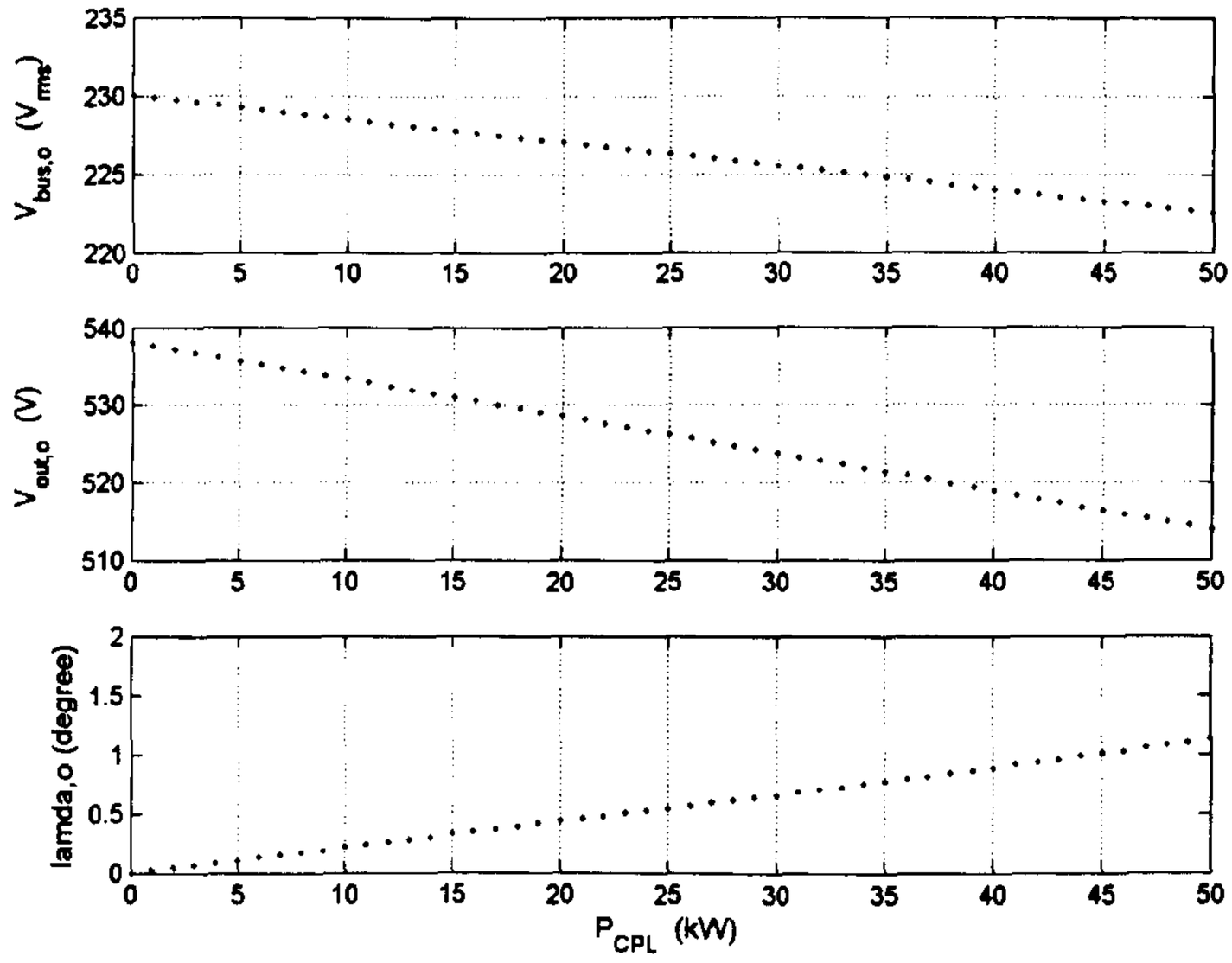

Figure 2.10: The steady-state values for V_{bus}, V_{out} and λ as P_{CPL} varies

2.2.4. Small-Signal Simulation and Stability Analysis

The linearized model (2-12) was simulated for small-signal transients against a corresponding 3-phase benchmark circuit model simulated in SABER. The details of SABER model for the system in Figure 2.2 are explained in Appendix D.1. The example system parameters are given in Table 2.1. Figure 2.11 for example shows the V_{out} response of the system of Figure 2.2 to a step change of P_{CPL} from 2 to 3 kW that occurs at t = 1s. Similarly, Figure 2.12 is the response to a step change in P_{CPL} from 10 to 11 kW. An excellent agreement between both models is achieved under small-signal simulation.

Table 2.1: The set of parameters for the example system

Parameter	Value	Description
V_s	230 $V_{rms/phase}$	phase source voltage
ω	$2\pi\times400$ rad/s	source frequency
R_{eq}	0.1 Ω	transmission line resistance
L_{eq}	24 μH	transmission line inductance
C_{eq}	2 nF	transmission line capacitance
r_F	0.01 Ω	DC link inductor resistance
L_F	2 mH	DC link inductance
C_F	500 μF	DC link capacitance

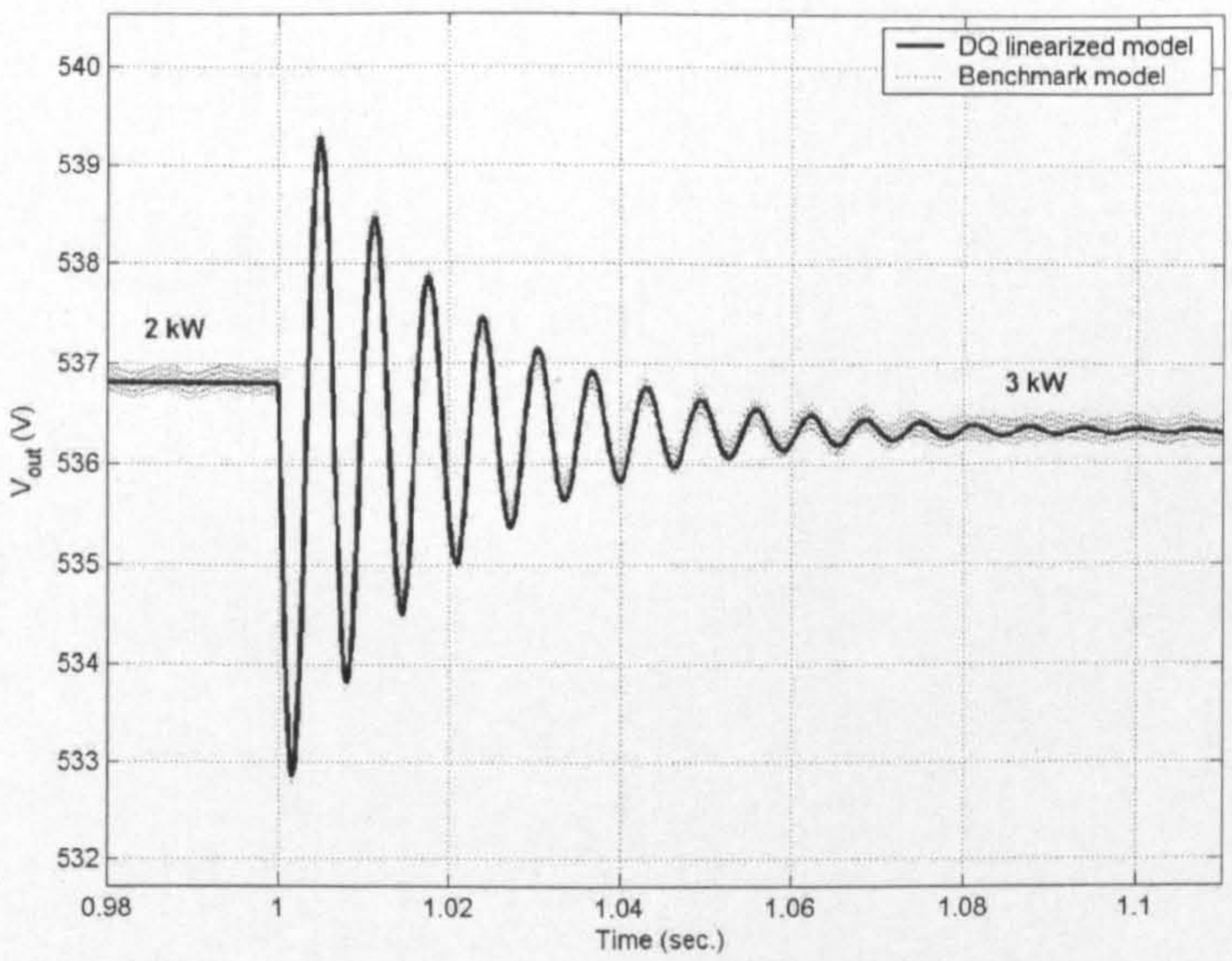

Figure 2.11: Verification for changing P_{CPL} from 2 to 3 kW

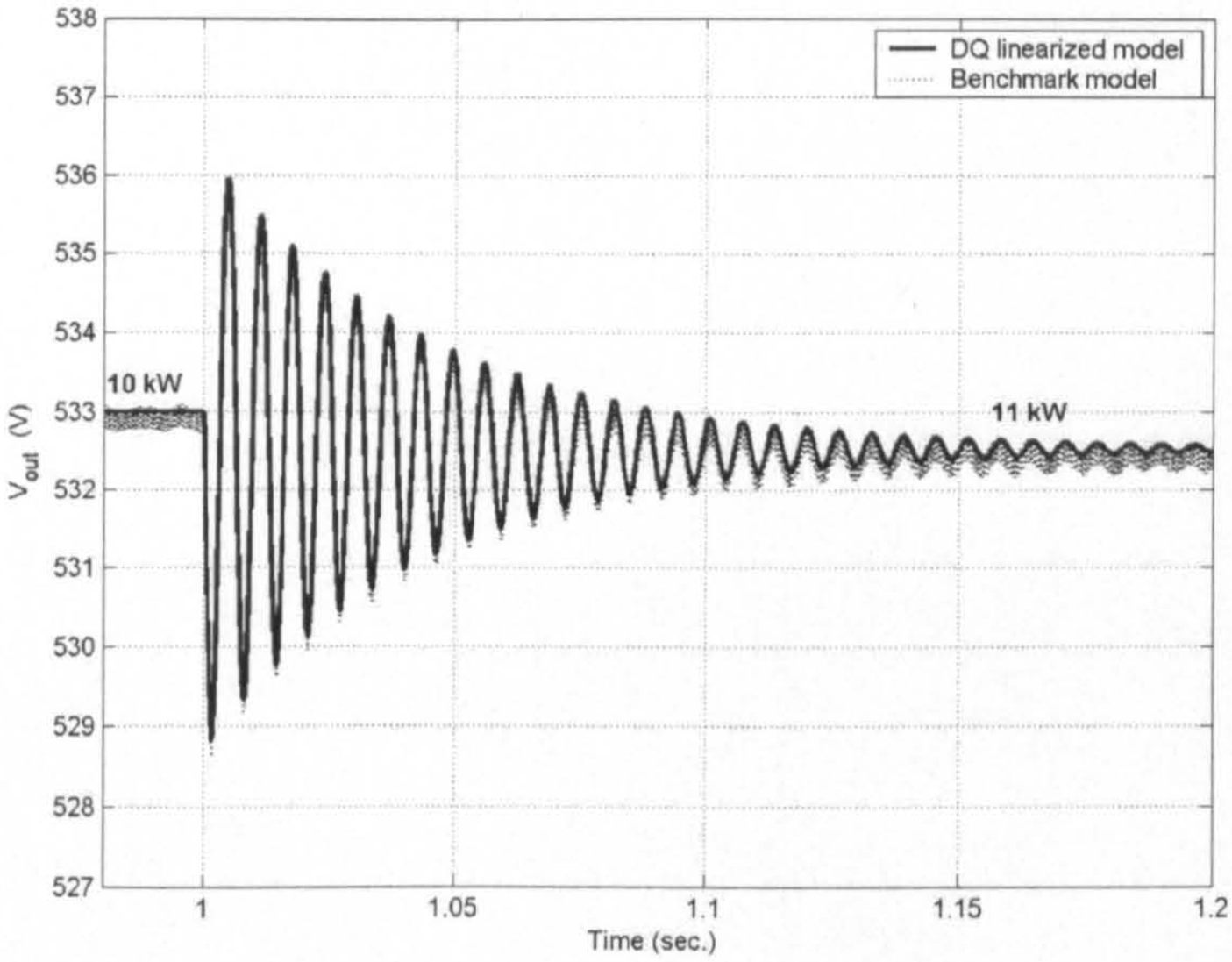

Figure 2.12: Verification for changing P_{CPL} from 10 to 11 kW

In respect of stability analysis, the linearized model from the dq modelling approach is used with the eigenvalue theorem. The eigenvalues can be calculated from the Jacobian matrix $\mathbf{A}(\mathbf{x_o}, \mathbf{u_o})$ in (2-13) by

$$\det[\lambda \mathbf{I} - \mathbf{A}] = 0 \tag{2-17}$$

and the system is stable if

$$real\ \lambda_i < 0 \tag{2-18}$$

where i = 1, 2, 3,….., n (n – the number of state variables)

The eigenvalues of the linearized **A** matrix for the example power system with parameters in Table 2.1 were analyzed for the case when the P_{CPL} varies from 0 kW to 50 kW. This root locus is shown in Figure 2.13 and some eigenvalues (λ_5 and λ_6) cross in to the right hand plane. Figure 2.14 shows zoomed area of interest: as one can see, the system becomes unstable when the P_{CPL} exceeds 17 kW for the studied case.

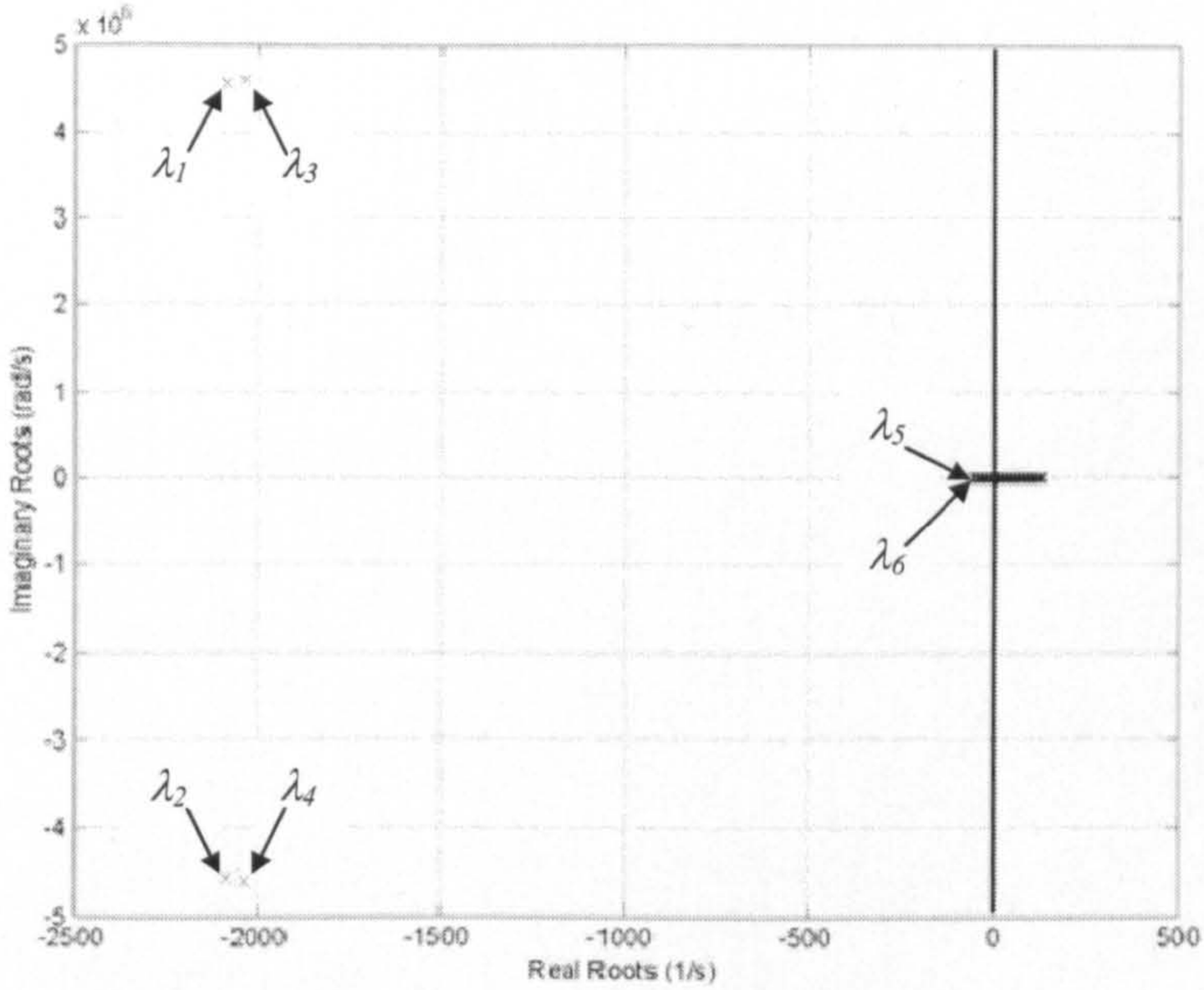

Figure 2.13: Eigenvalue plot from dq linearized model

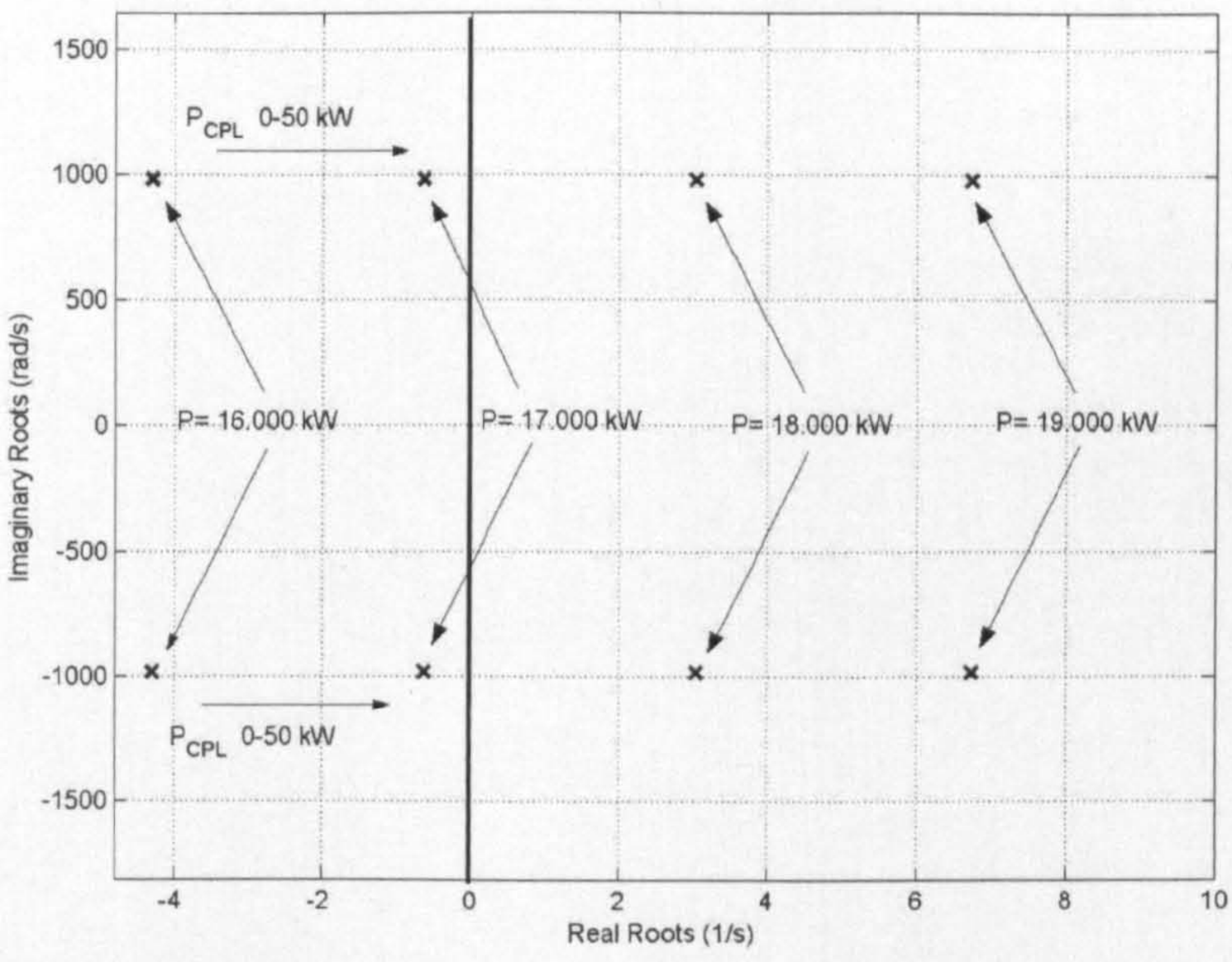

Figure 2.14: Zoomed area of interest from Figure 2.13 (λ_5 and λ_6)

The eigenvalues λ_1-λ_4 in Figure 2.13 are related to the system parameters L_{eq} and C_{eq} since they are located close to the resonant frequency $1/\sqrt{L_{eq}C_{eq}}$ (~4.56e^{06} rad/s according to the system parameters given in Table 2.1).

Similarly, the dominant eigenvalues λ_5 and λ_6 are related to L_F and C_F since they are located close to $1/\sqrt{L_F C_F}$ (~1000 rad/s). Therefore, the DC link filter parameters are significant for the system stability. This will be supported by the results in Section 2.2.5.

Figure 2.15 shows the SABER time-domain benchmark simulations that confirm the theoretical result with the instability occurring at a constant power load value of 18 kW. This is greater than the 17 kW value for the unstable condition.

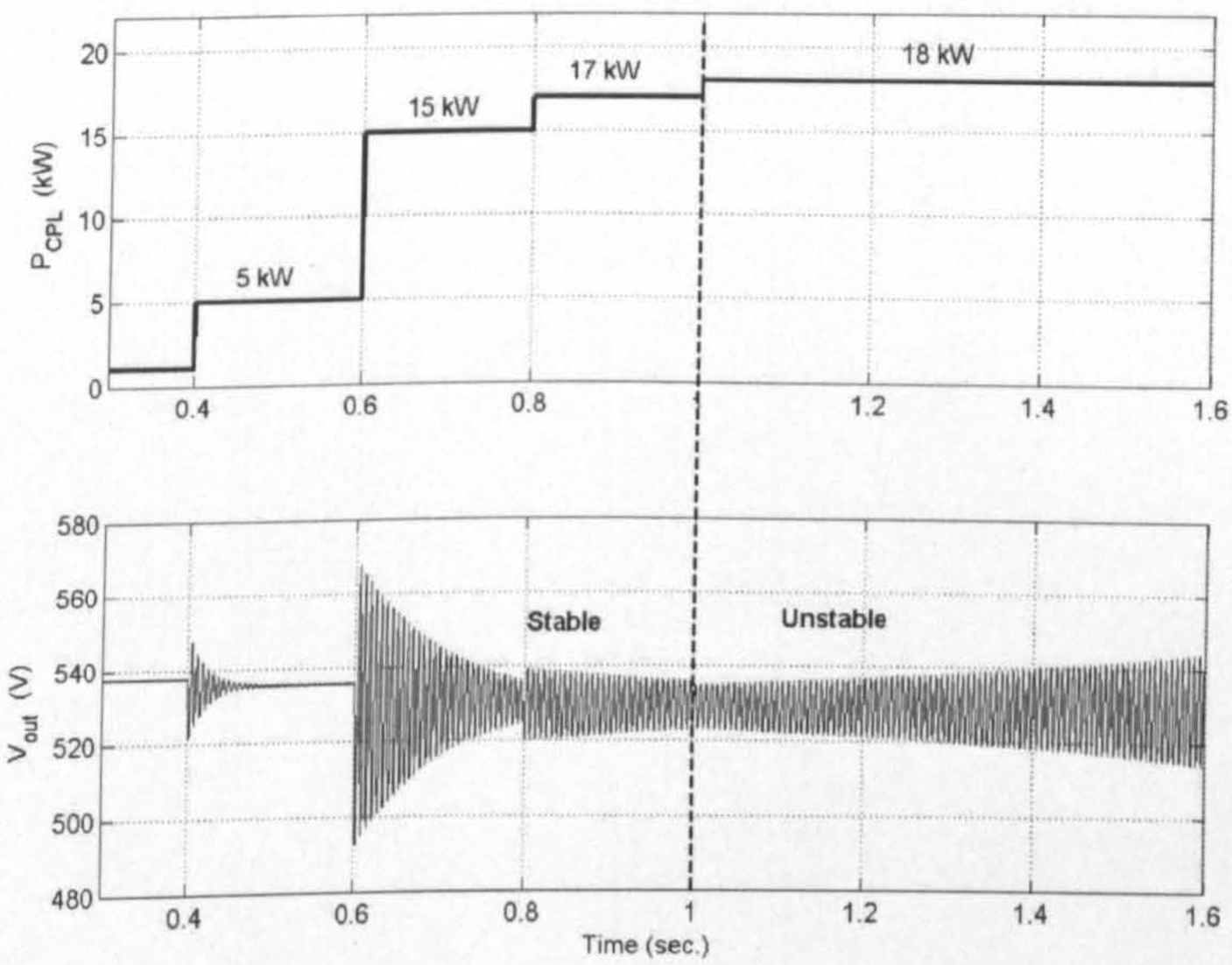

Figure 2.15: Step response for operating point (P_{CPL}) variations

2.2.5. Investigating Stability due to Variations in System Parameters

In this section, the dynamic model is used to predict instability for variations in system parameters of the power system in Figure 2.2. Since the considered aircraft power system is frequency-wild, it is very important to study stability variation with changes in system frequency. Moreover, L_F and C_F can be imposed by the engineering designers. Therefore, it is very interesting to study

the variations in L_F and C_F on stability as well. Note that the model is derived under the assumption that only one commutation occurs at a time ($\mu<60^o$). Therefore, if the L_{eq} is large enough to provide the overlap angle $\mu>60^o$, the model is no longer applicable.

Figure 2.16 shows the P_{CPL} values at which the instability occurs when the system frequency is set to 200, 400, 600, and 800 Hz, while other parameters are fixed as shown in Table 2.1.

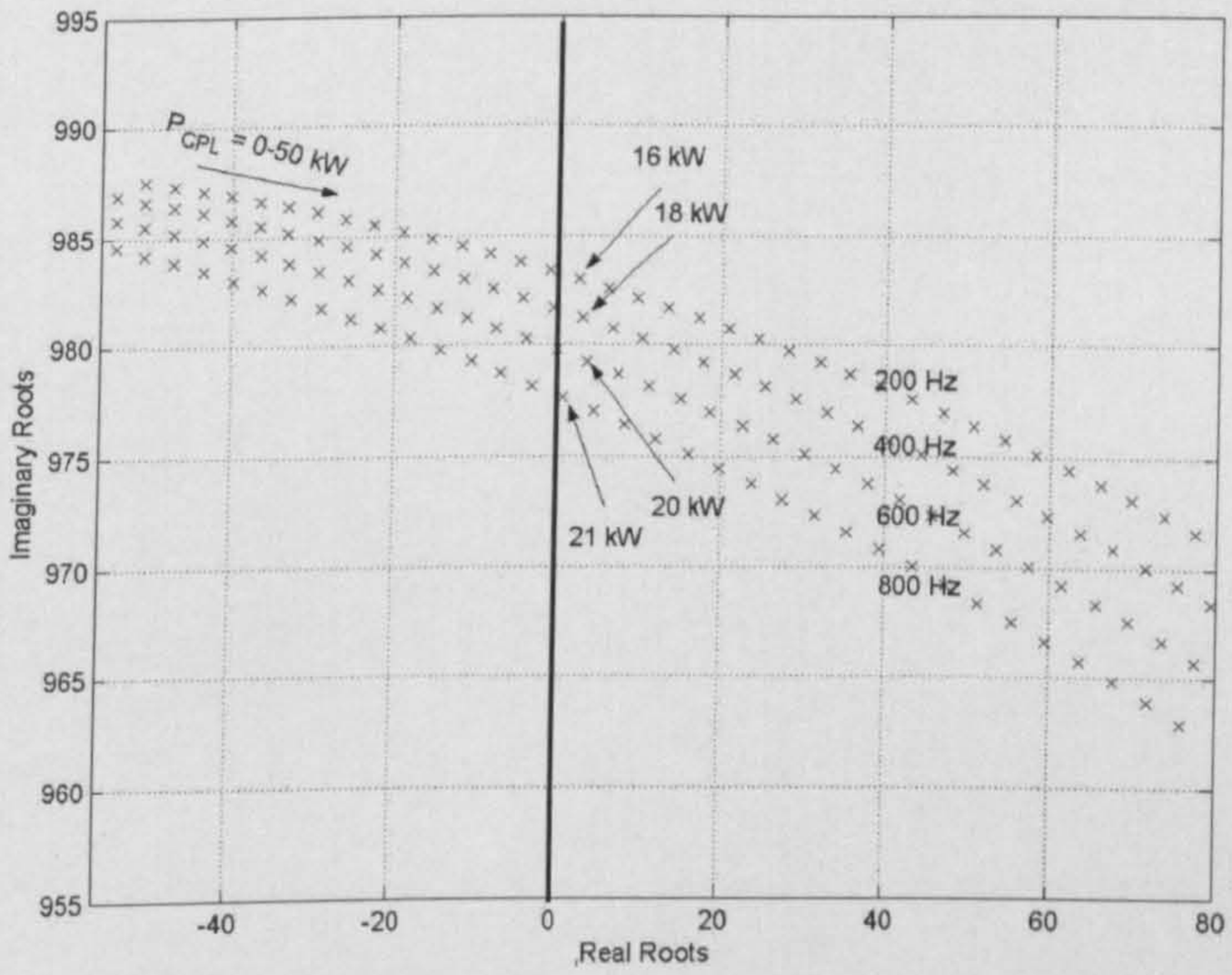

Figure 2.16: Eigenvalue plot for system frequency variations

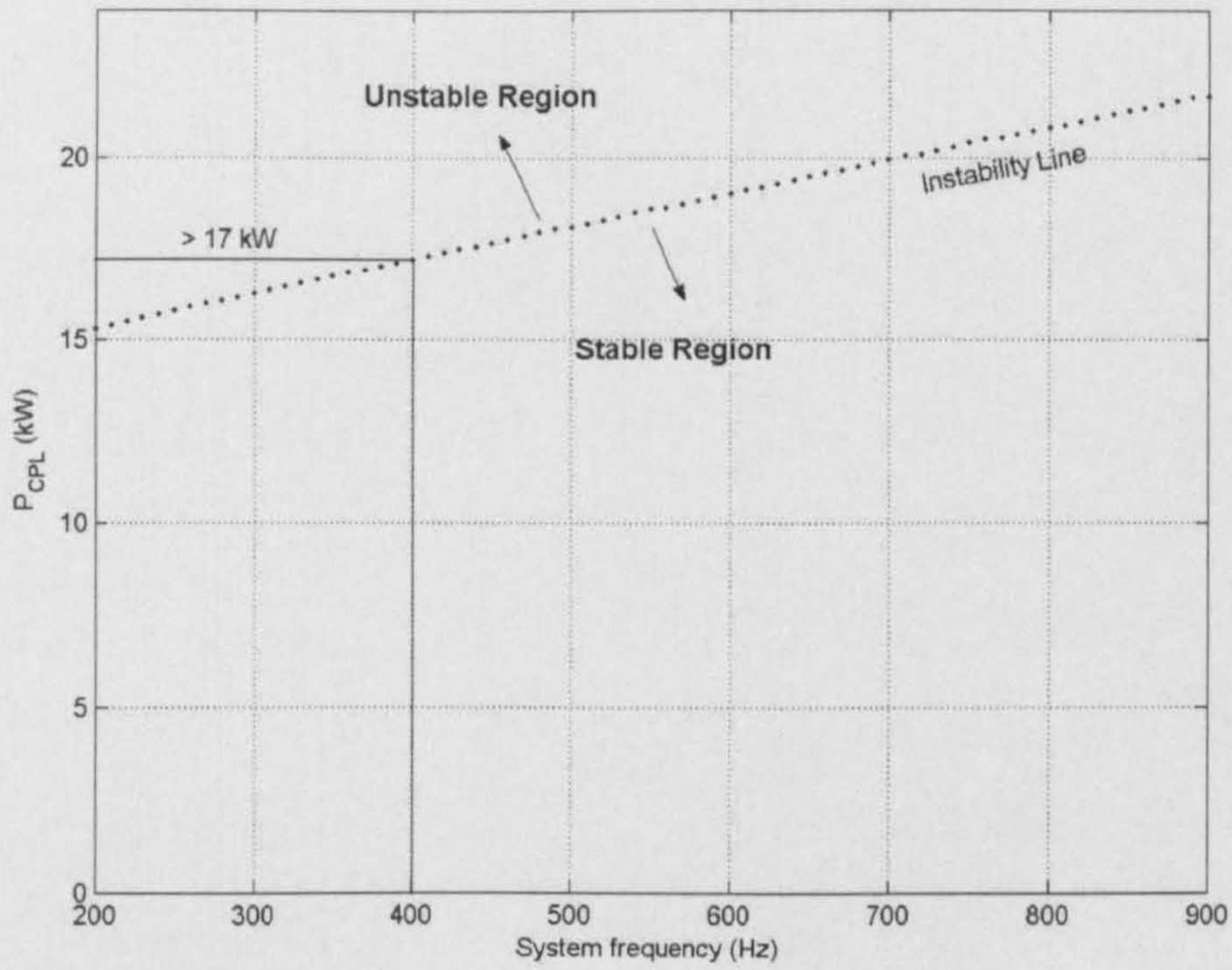

Figure 2.17: Instability power for system frequency variations

Figure 2.17 displays the instability conditions for the full operational frequency range. Again, these analytical results are supported by SABER benchmark simulation shown in Figure 2.18.

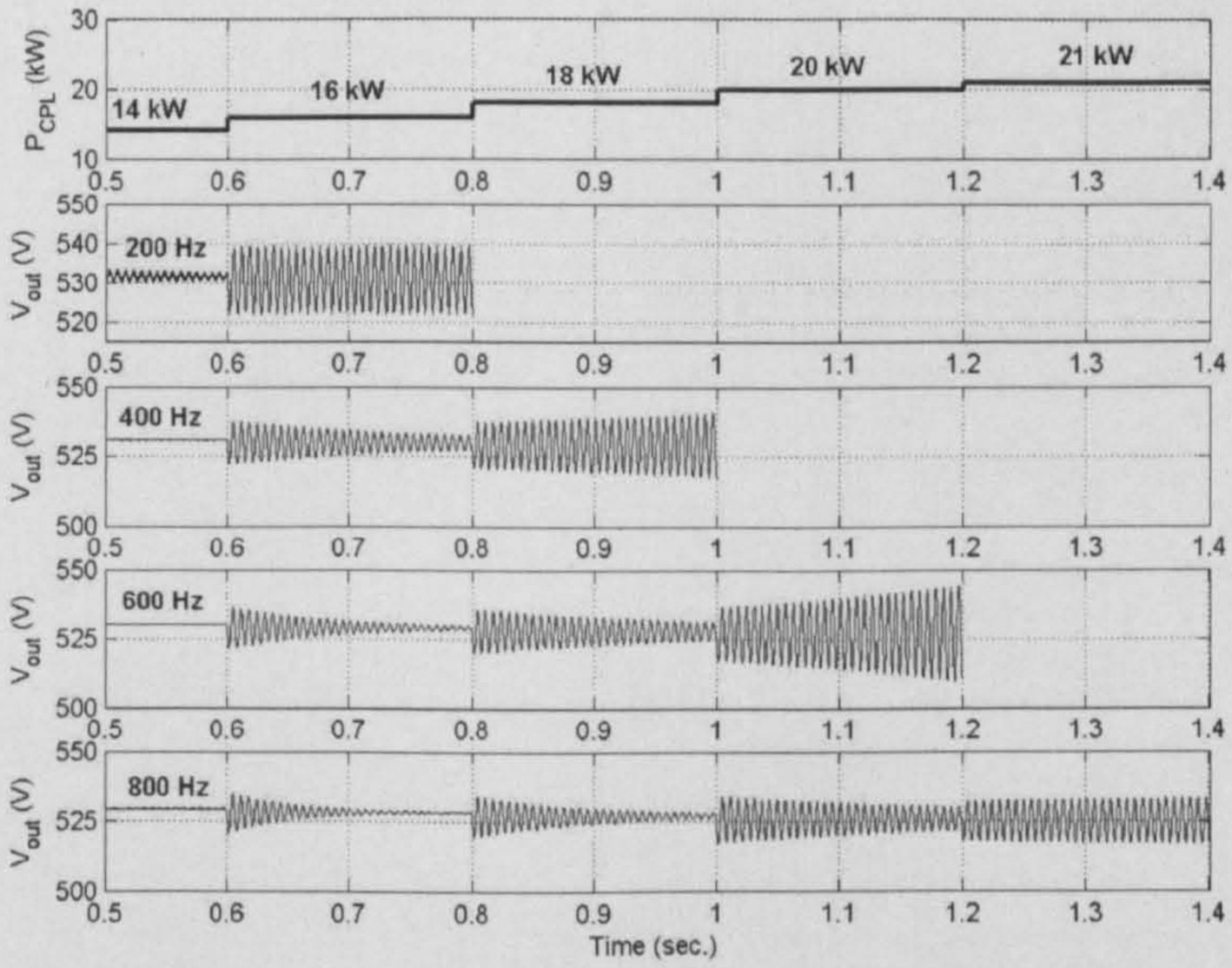

Figure 2.18: Verification of analytical results for system frequency variations

In Figure 2.18, the top graph shows stepwise changes in P_{CPL}, and the graphs below show the corresponding responses of the DC link voltage for different system frequencies. The analytical results delivered by the dq linearized system in (2-12) predict the unstable behaviour with high degree of accuracy.

The main outcome of this parameter study is that increasing system frequency expands the stability range. For example, the P_{CPL} produces instability at 16 kW at 200 Hz, but is stable at 20 kW at 800 Hz. This is because the resistance r_μ in the equivalent circuit as shown in Figure 2.6 will be increased when the system frequency increases. This is because r_μ depends on the system frequency. According to Middlebrook criterion [10], the power level at which instability occurs will be increased when the filter is designed to achieve lower Q-factor. The filter Q-factor is given by:

$$Q = \frac{1}{R_F}\sqrt{\frac{L_F}{C_F}} \tag{2-19}$$

where $R_F = r_\mu + r_F$

Note that r_μ is the commutation resistance and r_F is DC link inductor resistance. Therefore, it is expected that increasing system frequency (increasing r_μ) can reduce the DC-link filter Q-factor. As a result, the stability range can be expanded because of lower Q-factor. However, in some particular cases, for example [76], increasing grid frequency can degrade the system stability because the reduction in DC-link voltage becomes more dominant (voltage drop is increased). Therefore, the results depend on the system parameters and on the system operating points.

Figure 2.19 shows the stable and unstable regions for L_F variations with the other parameters fixed as given in Table 2.1.

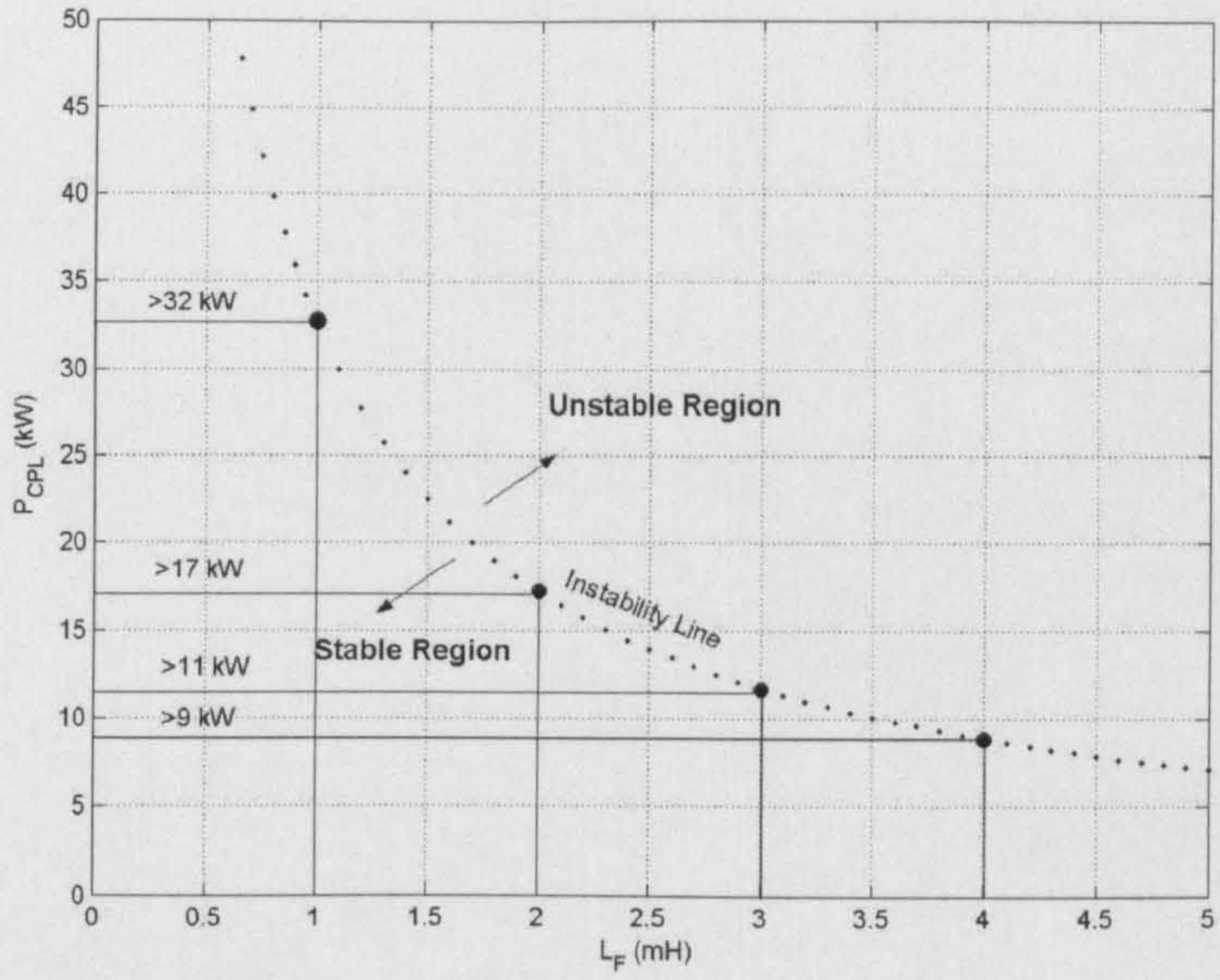

Figure 2.19: Instability power for L_F variations

These analytical results in Figure 2.19 are compared to the SABER benchmark simulation shown in Figure 2.20 in which the top graph shows stepwise changes in P_{CPL}, and the graphs below show the V_{out} responses for different L_F: 4mH, 3mH, 2mH and 1mH. The model can predict the instability point with high accuracy for variations in L_F. Smaller value of L_F increases the power level at which instability occurs. This is because smaller L_F causes lower Q-factor. However, we have to compromise between current ripple and stability margin because smaller L_F provides better stability condition but also results in higher ripple currents.

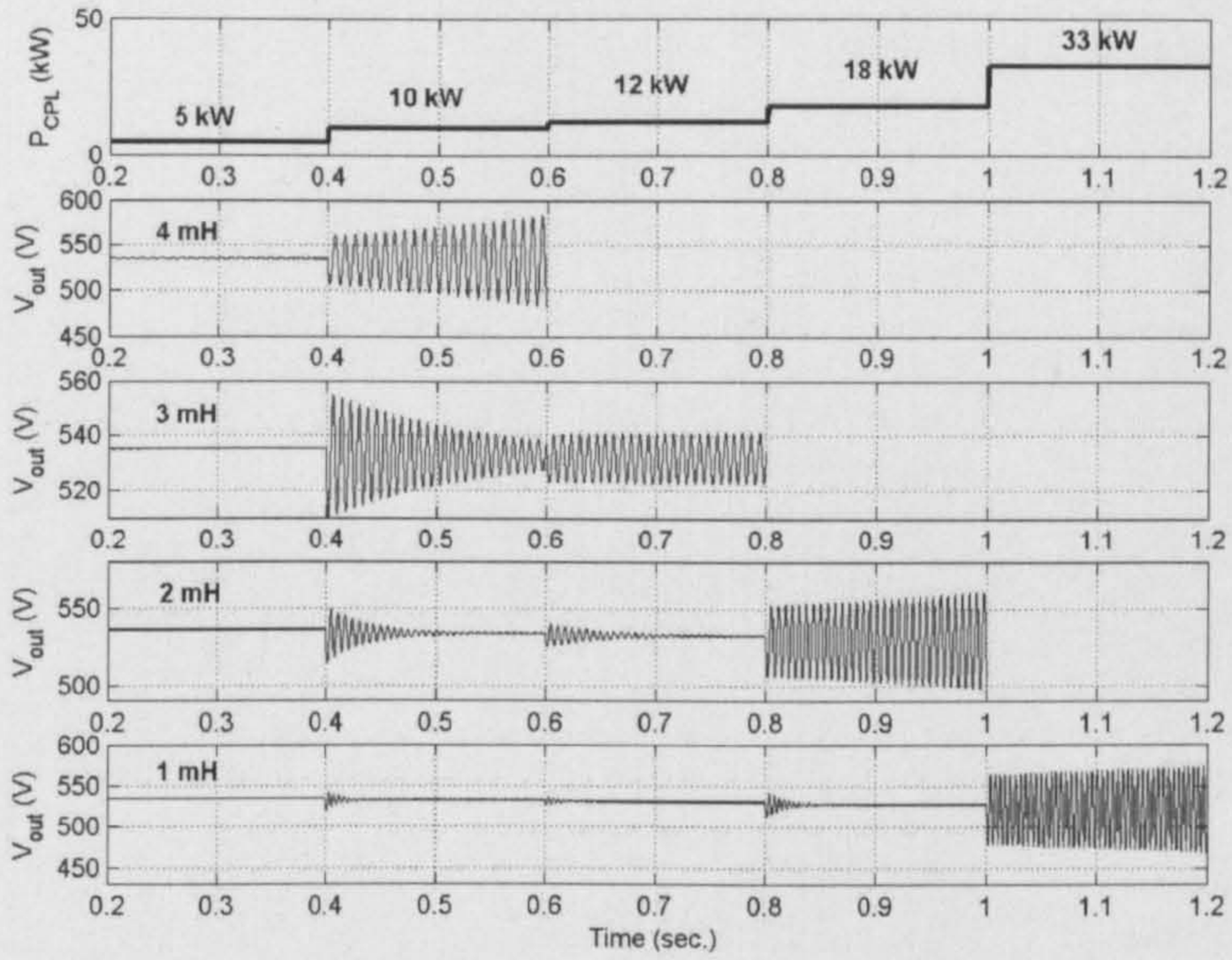

Figure 2.20: Verification of analytical results for L_F variations

Figure 2.21 shows the stable and unstable region for variations in C_F with other parameters fixed as given in Table 2.1. In this Figure, the bold points are for the specific C_F value, here equal to 300 μF, 500μF, 700 μH, and 1000μF. These analytical results of Figure 2.21 are also compared to SABER benchmark simulation shown in Figure 2.22 in which the top graph shows stepwise changes in P_{CPL}, and the graphs below show the V_{out} responses for different C_F. From the results; the proposed model can predict the instability point with high accuracy. It can be seen that greater value of C_F can increase the power level at which instability occurs. This is because greater value of C_F causes lower Q-factor. However, higher C_F can provide smooth voltage, but also causes higher weight and cost.

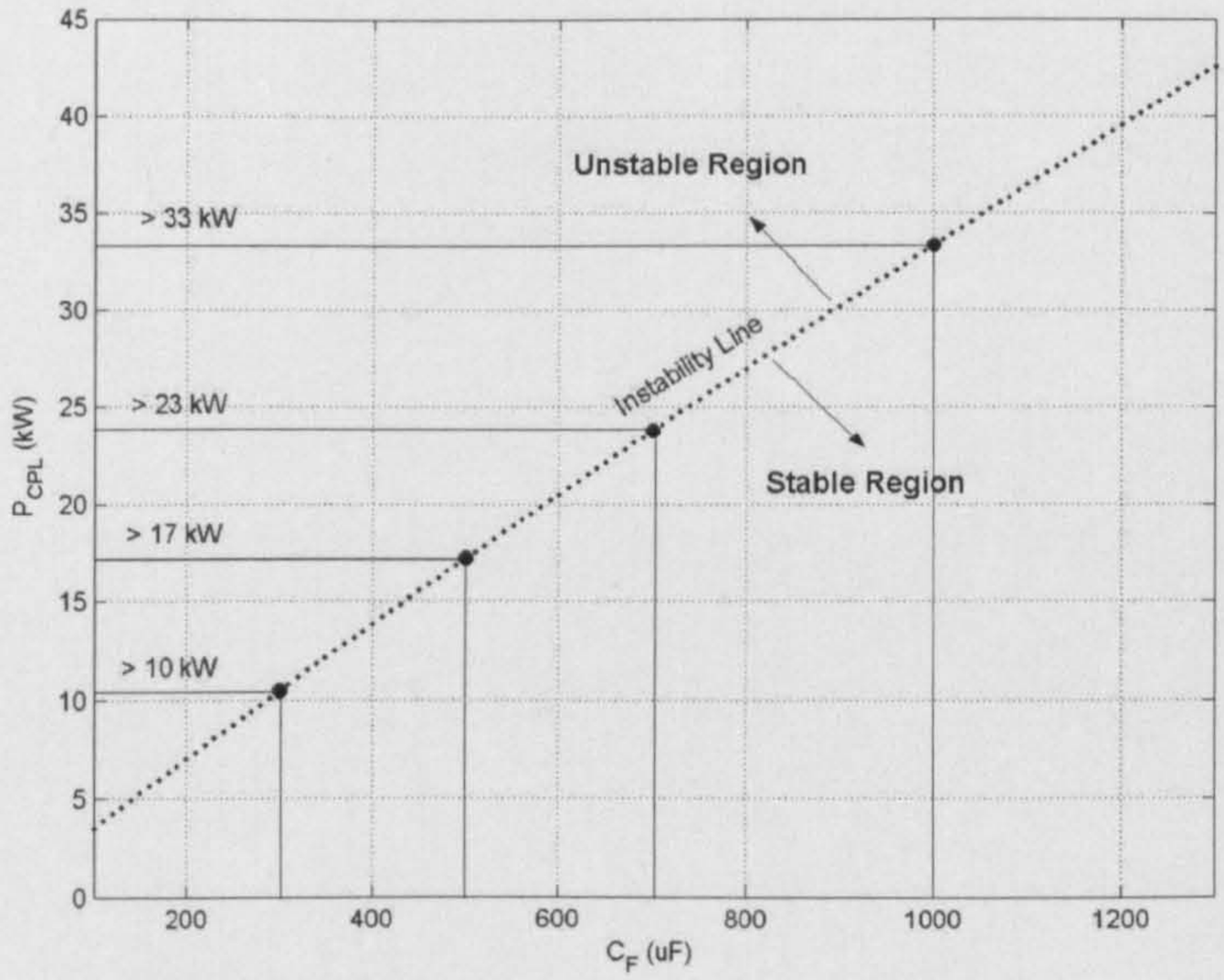

Figure 2.21: Instability power for C_F variations

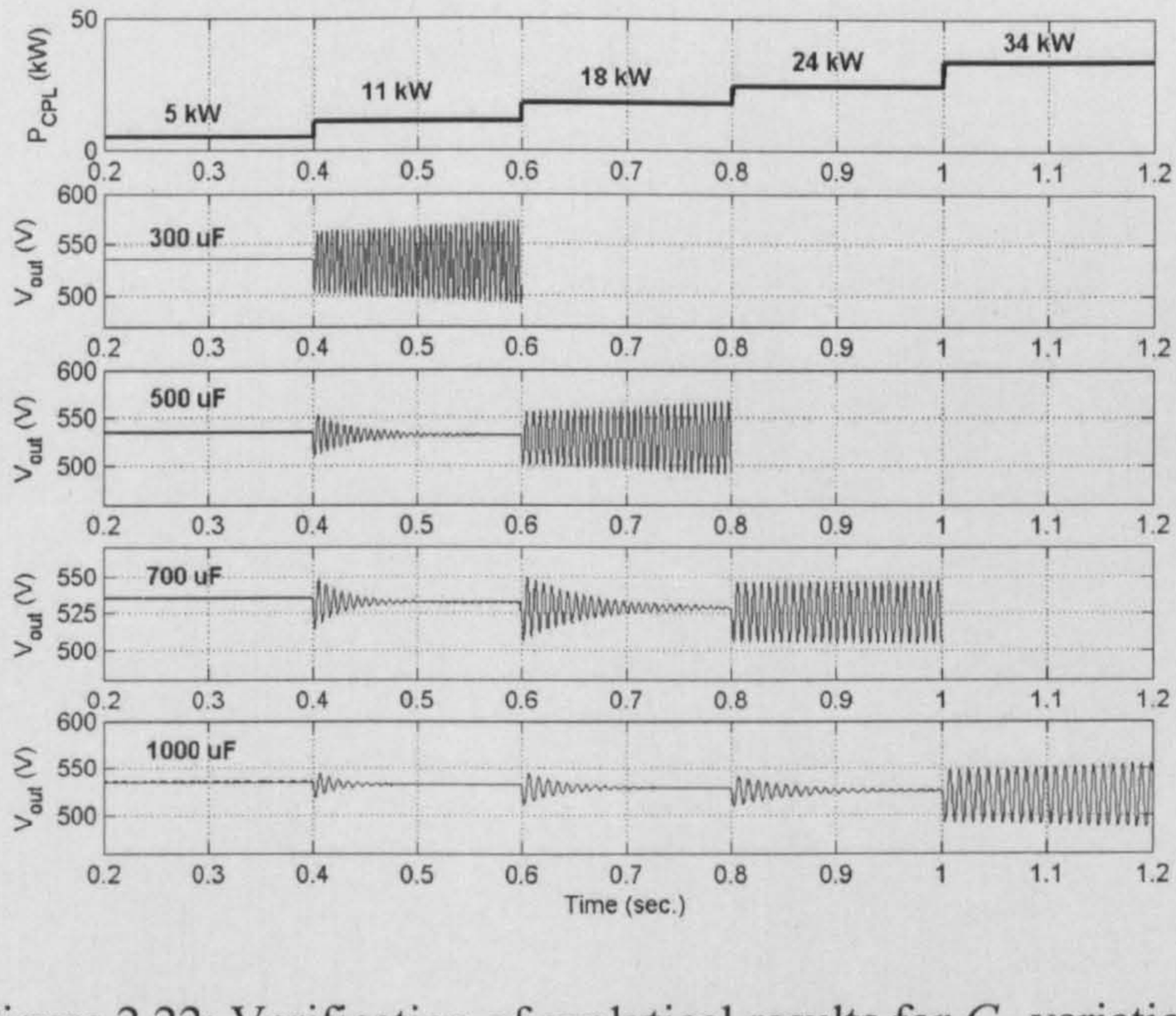

Figure 2.22: Verification of analytical results for C_F variations

The results in this section confirms that the dq modelling approach can be used to create the mathematical model of the six-pulse diode rectifier feeding an ideal CPL with good accuracy. This section has shown how the power system stability can be investigated with variations in operating points defined

by varying P_{CPL}, and system parameters. In the next section, the comparison between the proposed method with other stability analysis methods, the SSA and the average-value modelling methods, is discussed.

2.3 System Modelling and Stability Analysis using the State Space Averaging (SSA) Modelling Approach

The state space averaging modelling method is an alternative method to finding the large-signal nonlinear model of the AC-DC rectifier system. Similarly to the dq modelling method, the SSA approach is also used for eliminating the time-varying switching functions to achieve time-invariant power converter model. Whereas the dq modelling method assumed a transformation between the fundamental 2-phase AC quantities and DC quantities, the SSA modelling approach specifies the 3-phase switching function relationship and derives the relationship of fundamental switching function using time-dependent coefficients of the complex Fourier series. The large-signal model can be linearized for analysing the small-signal stability in the same manner as the dq modelling approach. The detail of how to model the power system in Figure 2.2 by using the SSA modelling method is explained in this section.

2.3.1. Derivation of Non-Linear and Linearized Models

In general, a periodic waveform with period T can be represented by the complex Fourier series [17],[79] of the form

$$f(t) = \sum_{k=-\infty}^{\infty} \langle x \rangle_k (t) e^{jk\omega_s t} \tag{2-20}$$

where $\omega_s = \frac{2\pi}{T}$ and $\langle x \rangle_k (t)$ are the complex Fourier coefficients

The SSA modelling approach uses the $\langle x \rangle_k(t)$ of the waveform as the state variables of the system. These coefficients can be determined by

$$< x >_k (t) = \frac{1}{T} \int_{t-T}^{t} f(t) e^{-jk\omega_s t} dt \tag{2-21}$$

The necessary properties of the $\langle x \rangle_k(t)$ for modelling the system using SSA modelling method are given in [17],[79]:

1) Differentiation with respect to time:

$$\frac{d}{dt}\langle x \rangle_k(t) = \left\langle \frac{d}{dt} x \right\rangle_k (t) - jk\omega_s \langle x \rangle_k (t) \tag{2-22}$$

2) The convolution relationship:

$$\langle xy \rangle_k = \sum_i \langle x \rangle_{k-i} \langle y \rangle_i \tag{2-23}$$

3) If $f(t)$ is real (real-valued periodic waveform),

$$\langle x \rangle_{-k} = \overline{\langle x \rangle_k} \tag{2-24}$$

4) The coefficient of the periodic waveforms $f(t-\tau)$ is

$$\langle x \rangle_k e^{-\left(\frac{j2\pi k\tau}{T}\right)} \tag{2-25}$$

In equation (2-20) and (2-21), the value of k depends on the accuracy level. If k approaches infinity, the approximation error approaches zero. If the waveform can be assumed to have no ripple, it can be set to $k = 0$. On the

other hand, if the waveform is similar to a sinusoidal signal, k can normally be set to -1,1. This method is called the first harmonic approximation [15]-[18]. In order to use the SSA modelling method, the AC side of the equivalent circuit requires a 3-phase representation. Hence, the circuit of Figure 2.7 becomes that of Figure 2.23. The relationship between the input and output terminal of the rectifier is given in (2-3) and (2-4)

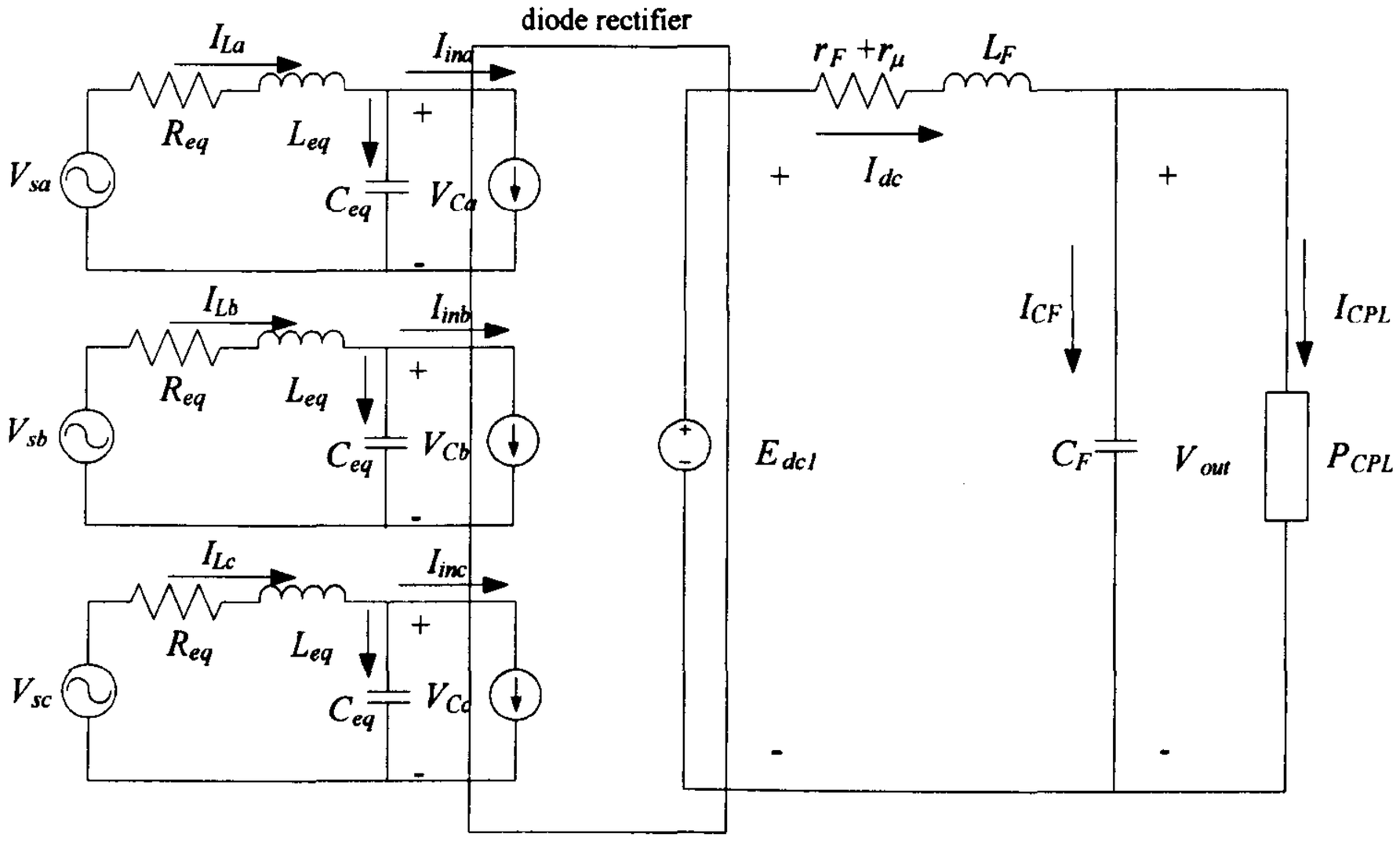

Figure 2.23: The equivalent circuit of the power system in Figure 2.2 for SSA method

The sets of nonlinear differential equation from the equivalent circuit in Figure 2.23 are given by:

$$
\begin{aligned}
V_{sa} &= R_{eq} I_{La} + L_{eq} \frac{dI_{La}}{dt} + V_{Ca} \\
V_{sb} &= R_{eq} I_{Lb} + L_{eq} \frac{dI_{Lb}}{dt} + V_{Cb} \\
V_{sc} &= R_{eq} I_{Lc} + L_{eq} \frac{dI_{Lc}}{dt} + V_{Cc} \\
I_{La} &= C_{eq} \frac{dV_{Ca}}{dt} + I_{ina} \\
I_{Lb} &= C_{eq} \frac{dV_{Cb}}{dt} + I_{inb} \\
I_{Lc} &= C_{eq} \frac{dV_{Cc}}{dt} + I_{inc} \\
E_{dc1} &= (r_F + r_\mu) I_{dc} + L_F \frac{dI_{dc}}{dt} + V_{out} \\
I_{dc} &= C_F \frac{dV_{out}}{dt} + \frac{P_{CPL}}{V_{out}}
\end{aligned}
\tag{2-26}
$$

From the equivalent circuit in Figure 2.23, the state variables of system are the Fourier coefficients of $V_{out}, I_{La}, I_{Lb}, I_{Lc}, V_{Ca}, V_{Cb}, V_{Cc}$, and I_{dc}. Using the first harmonic approximation in the AC variables, and neglecting ripples on the DC side, we can define 14 state variables:

$$
\begin{aligned}
\langle V_{out} \rangle_0 &= x_1 \\
\langle I_{La} \rangle_1 &= x_2 + jx_3 \\
\langle I_{Lb} \rangle_1 &= x_4 + jx_5 \\
\langle I_{Lc} \rangle_1 &= x_6 + jx_7 \\
\langle V_{Ca} \rangle_1 &= x_8 + jx_9 \\
\langle V_{Cb} \rangle_1 &= x_{10} + jx_{11} \\
\langle V_{Cc} \rangle_1 &= x_{12} + jx_{13} \\
\langle I_{dc} \rangle_0 &= x_{14}
\end{aligned}
\tag{2-27}
$$

Using the Equation (2-21) and (2-25) to obtain the zero and first harmonics of the input sinusoidal voltages and the commutation functions of Figure 2.4, the complex Fourier coefficients can be determined as:

$$\langle V_{sa}\rangle_0 = \langle V_{sb}\rangle_0 = \langle V_{sc}\rangle_0 = 0$$

$$\langle V_{sa}\rangle_1 = -\frac{jV_m}{2}, \langle V_{sb}\rangle_1 = -\frac{jV_m}{2}\left(-\frac{1}{2}-\frac{j\sqrt{3}}{2}\right), \langle V_{sc}\rangle_1 = -\frac{jV_m}{2}\left(-\frac{1}{2}+\frac{j\sqrt{3}}{2}\right)$$

$$\langle S_a\rangle_0 = \langle S_b\rangle_0 = \langle S_c\rangle_0 = 0$$

$$\langle S_a\rangle_1 = -\frac{j\sqrt{3}}{\pi}(\cos\lambda - j\sin\lambda), \tag{2-28}$$

$$\langle S_b\rangle_1 = -\frac{j\sqrt{3}}{\pi}\left(\cos\left(\frac{2\pi}{3}+\lambda\right) - j\sin\left(\frac{2\pi}{3}+\lambda\right)\right),$$

$$\langle S_c\rangle_1 = -\frac{j\sqrt{3}}{\pi}\left(\cos\left(\frac{4\pi}{3}+\lambda\right) - j\sin\left(\frac{4\pi}{3}+\lambda\right)\right)$$

where V_m is the peak voltage of the supply.

Then, applying (2-22)-(2-24) in (2-26) with the relationship (2-3) and (2-4) and substituting the Fourier coefficients of the three phase sources and the commutation functions as given in (2-28), the dynamic model of the system by using SSA modelling method can be expressed as:

$$\dot{x}_1 = -\frac{P_{CPL}}{C_F x_1} + \frac{1}{C_F} x_{14}$$

$$\dot{x}_2 = -\frac{R_{eq}}{L_{eq}} x_2 + \omega x_3 - \frac{1}{L_{eq}} x_8$$

$$\dot{x}_3 = -\omega x_2 - \frac{R_{eq}}{L_{eq}} x_3 - \frac{1}{L_{eq}} x_9 - \frac{V_m}{2L_{eq}}$$

$$\dot{x}_4 = -\frac{R_{eq}}{L_{eq}} x_4 + \omega x_5 - \frac{1}{L_{eq}} x_{10} - \frac{\sqrt{3}}{4L_{eq}} V_m$$

$$\dot{x}_5 = -\omega x_4 - \frac{R_{eq}}{L_{eq}} x_5 - \frac{1}{L_{eq}} x_{11} + \frac{V_m}{4L_{eq}}$$

$$\dot{x}_6 = -\frac{R_{eq}}{L_{eq}} x_6 + \omega x_7 - \frac{1}{L_{eq}} x_{12} + \frac{\sqrt{3}}{4L_{eq}} V_m$$

$$\dot{x}_7 = -\omega x_6 - \frac{R_{eq}}{L_{eq}} x_7 - \frac{1}{L_{eq}} x_{13} + \frac{V_m}{4L_{eq}}$$

$$\dot{x}_8 = \frac{1}{C_{eq}} x_2 + \omega x_9 + \frac{\sqrt{3}}{\pi C_{eq}} \sin\lambda \, x_{14}$$

$$\dot{x}_9 = \frac{1}{C_{eq}} x_3 - \omega x_8 + \frac{\sqrt{3}}{\pi C_{eq}} \cos\lambda \, x_{14}$$

$$\dot{x}_{10} = \frac{1}{C_{eq}} x_4 + \omega x_{11} + \frac{\sqrt{3}}{\pi C_{eq}} \sin\left(\frac{2\pi}{3} + \lambda\right) x_{14}$$

$$\dot{x}_{11} = \frac{1}{C_{eq}} x_5 - \omega x_{10} + \frac{\sqrt{3}}{\pi C_{eq}} \cos\left(\frac{2\pi}{3} + \lambda\right) x_{14}$$

$$\dot{x}_{12} = \frac{1}{C_{eq}} x_6 + \omega x_{13} + \frac{\sqrt{3}}{\pi C_{eq}} \sin\left(\frac{4\pi}{3} + \lambda\right) x_{14}$$

$$\dot{x}_{13} = \frac{1}{C_{eq}} x_7 - \omega x_{12} + \frac{\sqrt{3}}{\pi C_{eq}} \cos\left(\frac{4\pi}{3} + \lambda\right) x_{14}$$

$$\begin{aligned} \dot{x}_{14} = & -\frac{1}{L_F} x_1 - \frac{2\sqrt{3}}{\pi L_F} \sin\lambda \, x_8 - \frac{2\sqrt{3}}{\pi L_F} \cos\lambda \, x_9 \\ & - \frac{2\sqrt{3}}{\pi L_F} \sin\left(\frac{2\pi}{3} + \lambda\right) x_{10} - \frac{2\sqrt{3}}{\pi L_F} \cos\left(\frac{2\pi}{3} + \lambda\right) x_{11} \\ & - \frac{2\sqrt{3}}{\pi L_F} \sin\left(\frac{4\pi}{3} + \lambda\right) x_{12} - \frac{2\sqrt{3}}{\pi L_F} \cos\left(\frac{4\pi}{3} + \lambda\right) x_{13} - \frac{(r_\mu + r_F)}{L_F} x_{14} \end{aligned} \tag{2-29}$$

Again, (2-29) is linearlized using the first order terms of Taylor expansion so as to achieve a set of linear differential equations around an equilibrium point. The SSA linearized model of (2-29) is then of the form as given in (2-12) in which the Jacobian matrix $\mathbf{A}(\mathbf{x_0},\mathbf{u_0})$ is:

$$\mathbf{A}(\mathbf{x_0},\mathbf{u_0}) = \begin{bmatrix}
\frac{P_{CPLo}}{C_F V_{out,o}^2} & 0 & 0 & 0 & 0 & 0 & 0 & 0 & 0 & 0 & 0 & 0 & 0 & \frac{1}{C_F} \\
0 & -\frac{R_{eq}}{L_{eq}} & \omega & 0 & 0 & 0 & 0 & -\frac{1}{L_{eq}} & 0 & 0 & 0 & 0 & 0 & 0 \\
0 & -\omega & -\frac{R_{eq}}{L_{eq}} & 0 & 0 & 0 & 0 & 0 & -\frac{1}{L_{eq}} & 0 & 0 & 0 & 0 & 0 \\
0 & 0 & 0 & -\frac{R_{eq}}{L_{eq}} & \omega & 0 & 0 & 0 & 0 & -\frac{1}{L_{eq}} & 0 & 0 & 0 & 0 \\
0 & 0 & 0 & -\omega & -\frac{R_{eq}}{L_{eq}} & 0 & 0 & 0 & 0 & 0 & -\frac{1}{L_{eq}} & 0 & 0 & 0 \\
0 & 0 & 0 & 0 & 0 & -\frac{R_{eq}}{L_{eq}} & \omega & 0 & 0 & 0 & 0 & -\frac{1}{L_{eq}} & 0 & 0 \\
0 & 0 & 0 & 0 & 0 & -\omega & -\frac{R_{eq}}{L_{eq}} & 0 & 0 & 0 & 0 & 0 & -\frac{1}{L_{eq}} & 0 \\
0 & \frac{1}{C_{eq}} & 0 & 0 & 0 & 0 & 0 & 0 & \omega & 0 & 0 & 0 & 0 & 0 \\
0 & 0 & \frac{1}{C_{eq}} & 0 & 0 & 0 & 0 & -\omega & 0 & 0 & 0 & 0 & 0 & \frac{2}{\pi C_{eq}} \\
0 & 0 & 0 & \frac{1}{C_{eq}} & 0 & 0 & 0 & 0 & 0 & 0 & \omega & 0 & 0 & \frac{\sqrt{3}}{\pi C_{eq}} \\
0 & 0 & 0 & 0 & \frac{1}{C_{eq}} & 0 & 0 & 0 & 0 & -\omega & 0 & 0 & 0 & -\frac{1}{\pi C_{eq}} \\
0 & 0 & 0 & 0 & 0 & \frac{1}{C_{eq}} & 0 & 0 & 0 & 0 & 0 & 0 & \omega & -\frac{\sqrt{3}}{\pi C_{eq}} \\
0 & 0 & 0 & 0 & 0 & 0 & \frac{1}{C_{eq}} & 0 & 0 & 0 & 0 & -\omega & 0 & -\frac{1}{\pi C_{eq}} \\
-\frac{1}{L_F} & 0 & 0 & 0 & 0 & 0 & 0 & 0 & -\frac{4}{\pi L_F} & -\frac{2\sqrt{3}}{\pi L_F} & \frac{2}{\pi L_F} & \frac{2\sqrt{3}}{\pi L_F} & \frac{2}{\pi L_F} & -\frac{(r_\mu + r_F)}{L_F}
\end{bmatrix}_{14\times 14} \tag{2-30}$$

Equation (2-30) contains the steady-state value $V_{out,o}$, and this is obtained in the same manner as that described in Section 2.2. The steady-state value $V_{out,o}$ depends on the operating point set by P_{CPL}.

2.3.2. Small-Signal Stability Analysis

In respect of stability analysis, the linearized model from SSA modelling approach is used with the eigenvalue theorem. The eigenvalues can be calculated from the Jacobian matrix $\mathbf{A}(\mathbf{x_0},\mathbf{u_0})$ in (2-30). Results will not be given in detail since they are very similar to those obtained by the dq modelling approach. This is seen in Figure 2.24 which shows the eigenvalues: as one can see, the system becomes unstable when the P_{CPL} exceeds 17 kW for

the studied case. The dominant eigenvalues shown in Figure 2.24 are numerically the same as those of Figure 2.14 (dq modelling approach).

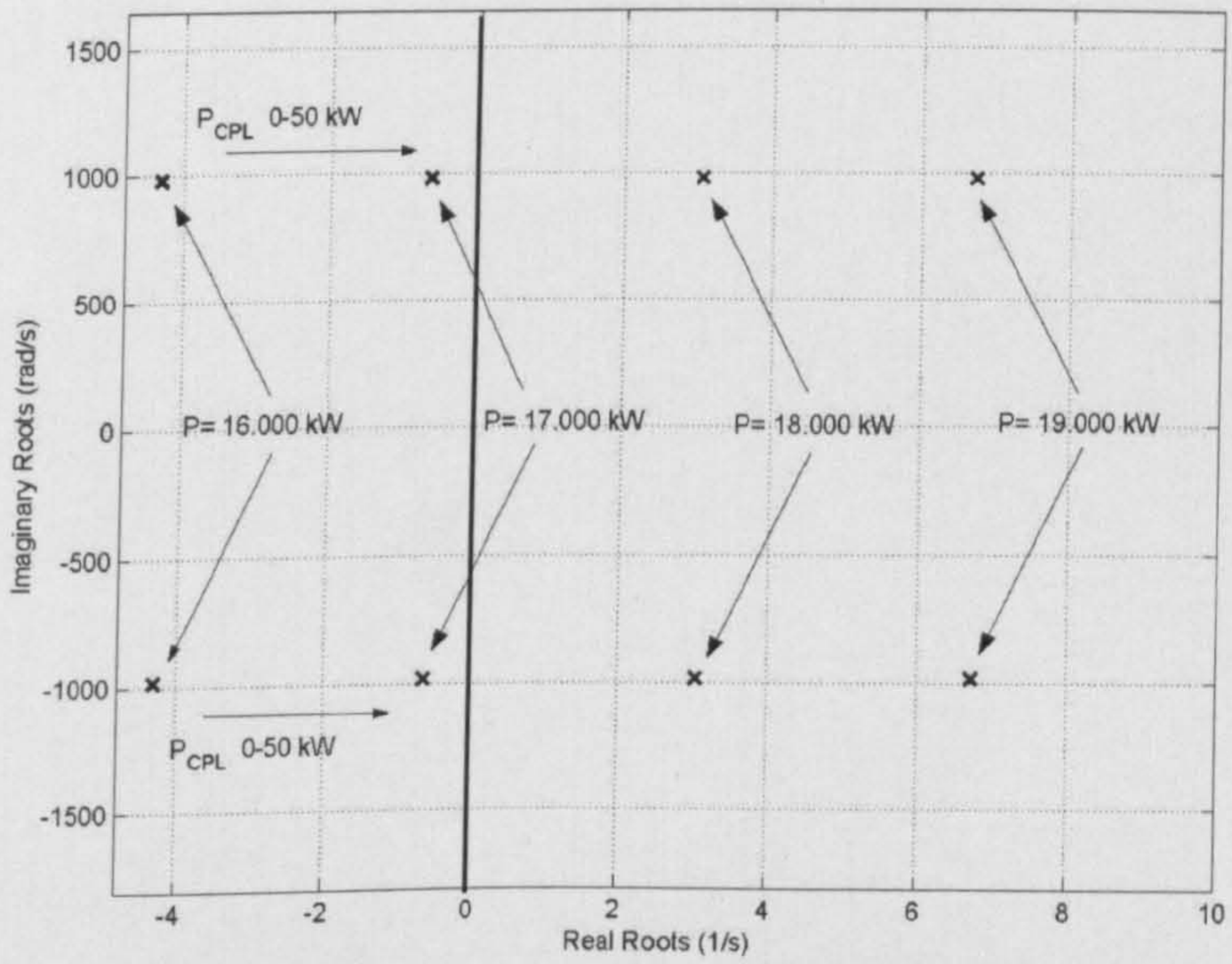

Figure 2.24: Zoomed area of eigenvalue plot from SSA model

2.4 System Modelling and Stability Analysis using Average-Value Modelling Method

In this section, the average-value modelling method is used to model the power system in Figure 2.2. This model is derived under the assumptions [66] that the amplitude of the AC supply is constant, the DC load current is constant, and only one commutation occurs at a time. The detail of this model is explained below:

2.4.1. Derivation of Non-Linear and Linearized Models

The average-value model for a six-pulse diode rectifier is depicted in Figure 2.25. This model has been derived in many publications [23]-[26]. Figure 2.25 shows that the six-pulse diode rectifier can be modelled as a DC bus voltage. This circuit provides the approximation of the average DC voltage.

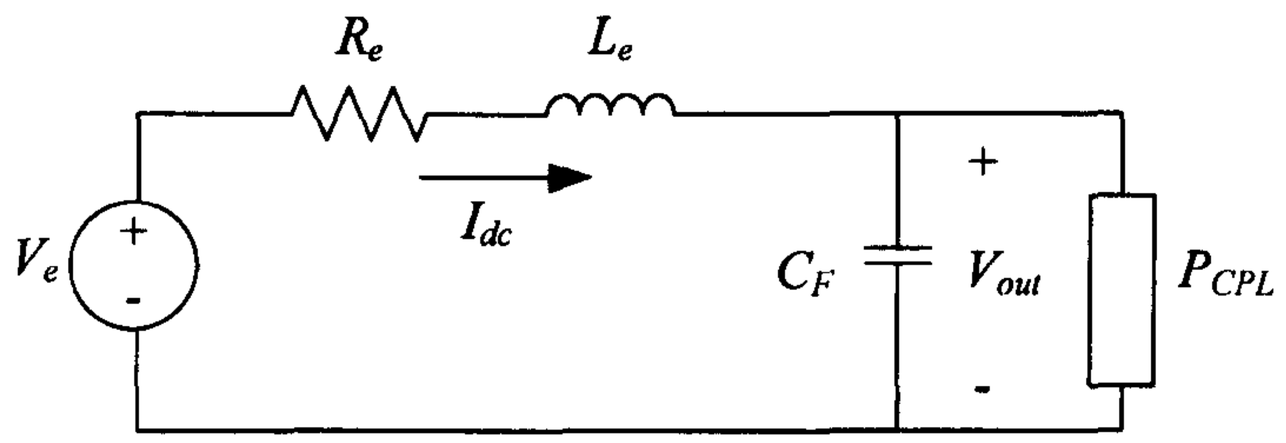

Figure 2.25: The equivalent circuit for average-value modelling method

The DC source voltage V_e, the equivalent resistance R_e, and inductance L_e are expressed in (2-31), (2-32), and (2-33), respectively.

$$V_e = \frac{3\sqrt{3}}{\pi} V_m \tag{2-31}$$

$$R_e = 2R_{eq} + r_F + r_\mu \tag{2-32}$$

$$L_e = 2L_{eq} + L_F \tag{2-33}$$

where V_m is the peak of phase voltage for AC supply.

The sets of nonlinear differential equation from the equivalent circuit in Figure 2.25 are given in (2-34) in which I_{dc} and V_{out} are set as state-variables.

$$\begin{aligned} \frac{dI_{dc}}{dt} &= -R_e L_e^{-1} I_{dc} - L_e^{-1} V_{out} + L_e^{-1} V_e \\ \frac{dV_{out}}{dt} &= C_F^{-1} I_{dc} - \frac{P_{CPL}}{C_F V_{out}} \end{aligned} \tag{2-34}$$

Again, (2-34) is linearized using the first order terms of Taylor expansion to achieve a set of linear differential equations around an equilibrium point. The average-value linearized model of (2-34) is then of the form as given in (2-12) in which the Jacobian matrix $\mathbf{A}(\mathbf{x_o}, \mathbf{u_o})$ is

$$\mathbf{A}(\mathbf{x_o},\mathbf{u_o}) = \begin{bmatrix} -\frac{R_e}{L_e} & -\frac{1}{L_e} \\ \frac{1}{C_F} & \frac{P_{CPLo}}{C_F V_{out,o}^2} \end{bmatrix}_{2\times 2} \tag{2-35}$$

We can derive the steady-state value $V_{out,o}$ in the same manner as for the other methods (see Section 2.2.3). This steady-state value depends on the operating point defined by P_{CPL}. However, for this method, the steady-state value can easily be determined by setting (2-34) equal to zero. Both methods can obtain nearly the same value of $V_{out,o}$.

To compare the average-value model with the one from the dq modelling method, the equivalent circuit in Figure 2.7 can be simplified by transferring all elements from the AC side to the DC side via transformer ratios. The circuit of Figure 2.7 becomes that of Figure 2.26. The DC voltage source $V_{e,dq}$, the equivalent resistance $R_{e,dq}$, and inductance $L_{e,dq}$ are expressed in (2-36), (2-37), and (2-38), respectively.

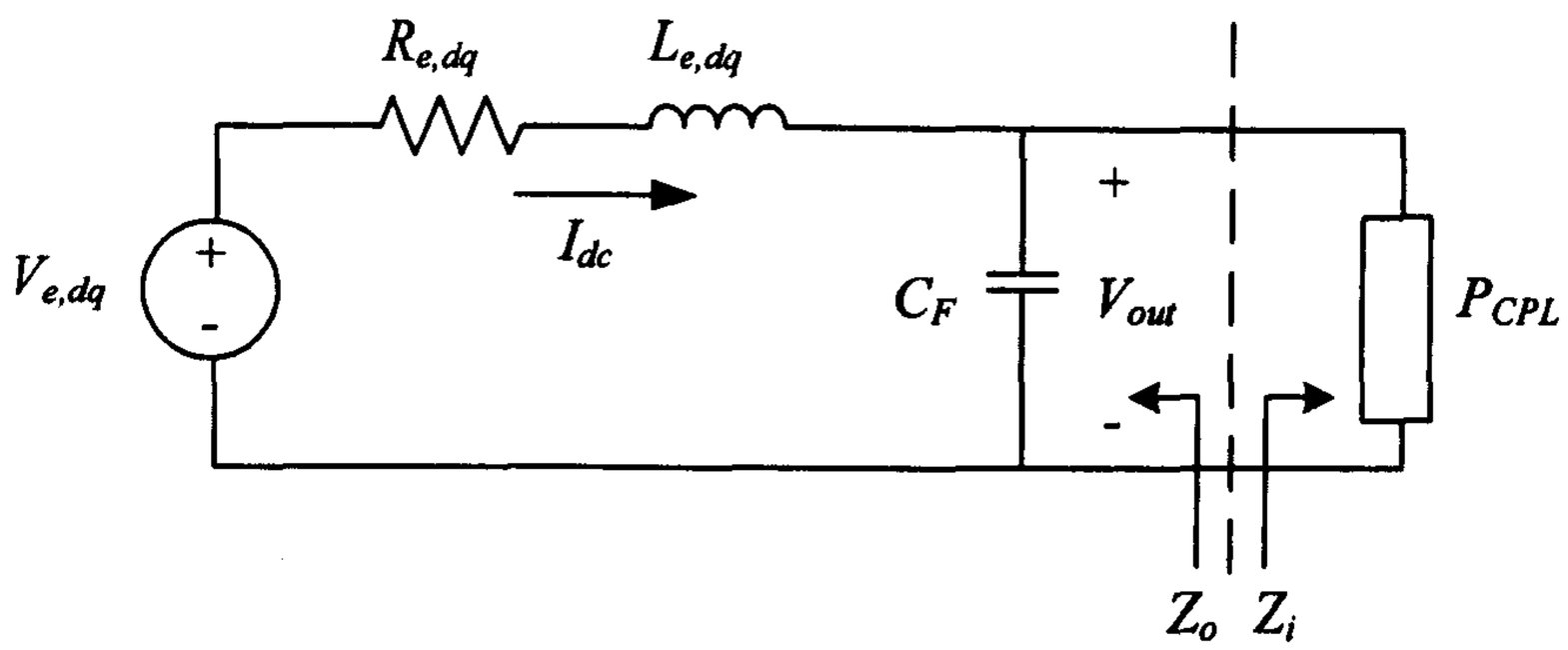

Figure 2.26: The simplified equivalent circuit from the dq modelling method

$$\begin{aligned} V_{e,dq} &= S_d V_{sd} + S_q V_{sq} \ \left(V_{sq} \approx 0\right) \\ &= S_d V_{sd} = \sqrt{\frac{3}{2}}\frac{2\sqrt{3}}{\pi} V_{LL,rms} \end{aligned} \tag{2-36}$$

$$R_{e,dq} = r_\mu + r_F + \left[\sqrt{\frac{3}{2}}\frac{2\sqrt{3}}{\pi}\right]^2 \left[\cos^2(\phi_1 - \phi) + \sin^2(\phi_1 - \phi)\right] R_{eq} \qquad (2\text{-}37)$$
$$= r_\mu + r_F + 1.824 R_{eq}$$

$$L_{e,dq} = L_F + \left[\sqrt{\frac{3}{2}}\frac{2\sqrt{3}}{\pi}\right]^2 \left[\cos^2(\phi_1 - \phi) + \sin^2(\phi_1 - \phi)\right] L_{eq} \qquad (2\text{-}38)$$
$$= L_F + 1.824 L_{eq}$$

Note that the equivalent circuit in Figure 2.26 with (2-36)-(2-38) assumes that V_{sq} and C_{eq} are neglected because they are very small. In addition, the nonlinearity terms, dependent voltage sources and current sources, are ignored. The average-value model in Figure 2.25 and the simplified dq model are nearly the same. However, simplifying the dq model is not applicable for more complex systems. The simplification of the dq model in Figure 2.26 is only possible for the simple power system in Figure 2.2. It would be very difficult to apply for the complex systems of Chapter 7.

2.4.2. Small-Signal Stability Analysis

In respect of stability analysis, the average-value linearized model is used with the eigenvalue theorem. The eigenvalues can be calculated from the Jacobian matrix $\mathbf{A}(\mathbf{x_0}, \mathbf{u_0})$ in (2-35). Figure 2.27 shows the zoomed area of interest. As one can see, the system becomes unstable when P_{CPL} exceeds 18 kW for the studied case. For the simplified dq model in Figure 2.26, the system becomes unstable when P_{CPL} exceeds 17 kW. The dominant eigenvalues are numerically the same as those from the dq modelling approach. For the average-value model, the stability results are close to the results obtained from the dq and SSA modelling methods. According to the benchmark simulation results, the system is unstable for P_{CPL} of 18 kW. Therefore, the results from average-value model for this case provide some error compared with other methods.

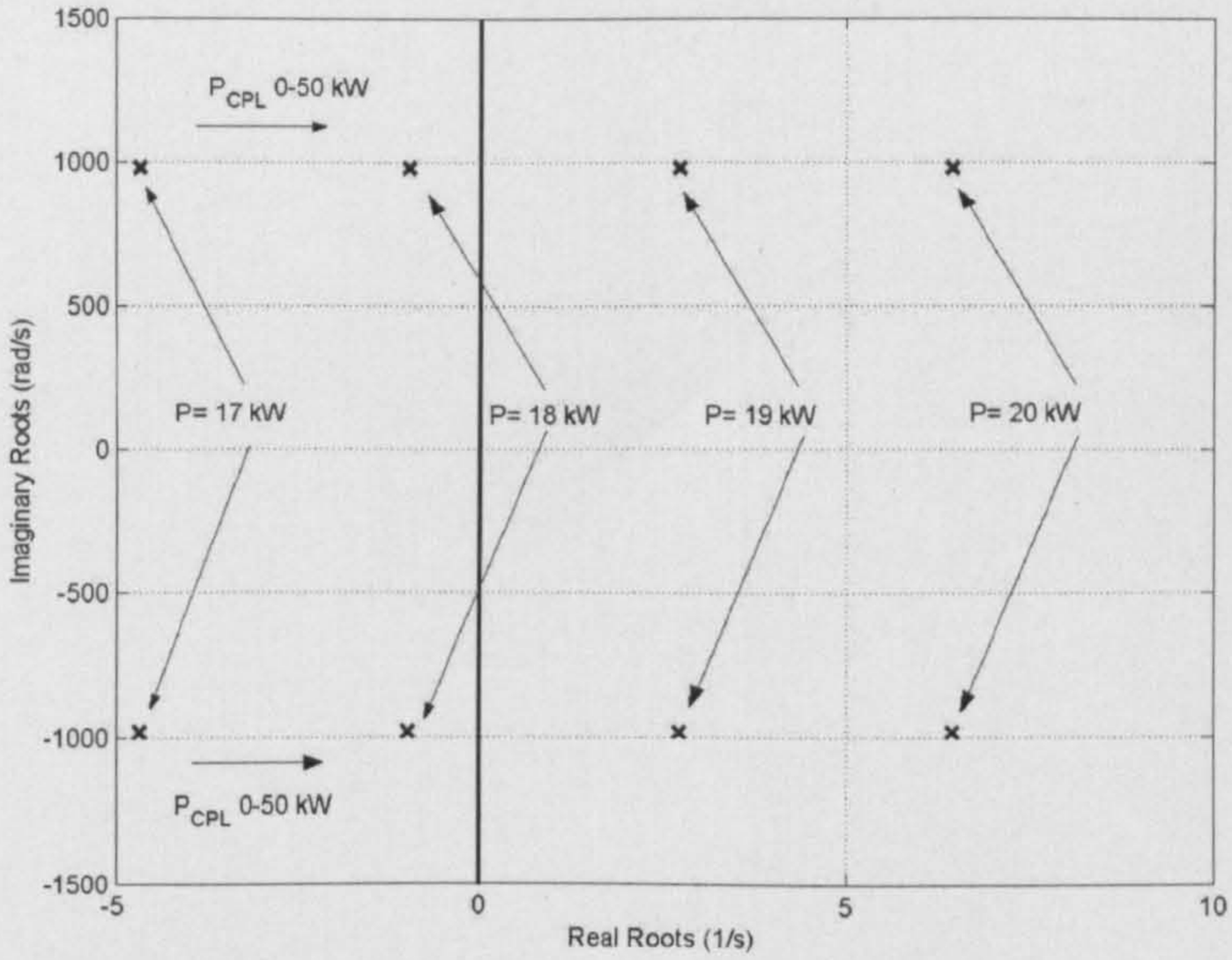

Figure 2.27: Zoomed area of eigenvalue plot from average-value model

Section 2.2, 2.3 and 2.4 has discussed the dq model (6 state variables), the SSA model (14 state variables), the simplified dq model (2-state-variables) and the average-value model (2 state-variables). In addition, the comparison of eigenvalues from the different methods for P_{CPL} equal to 17 kW is shown in Table 2.2 The results show that the dominant eigenvalues of the dq , SSA, and simplified dq models are almost the same. For the average-value model, the eigenvalues are not quite the same as for other models. Hence, the stability results provide some error compared with others.

Table 2.2: The comparison of eigenvalues for P_{CPL} equal to 17 kW

eigenvalues	dq (6 state variables)	SSA (14 state variables)	simplified dq (2 state variables)	average-value (2 state variables)
$\lambda_{1,2}$	-2039.19 ± j 4.614e6	**-0.6349 ± j 981.72**	**-0.6350 ± j 981.72**	**-4.6745 ± j 980.15**
$\lambda_{3,4}$	-2083.22 ± j 4.564e6	-2039.19 ± j 4.614e6	-	-
$\lambda_{5,6}$	**-0.6349 ± j 981.72**	-2083.22 ± j 4.564e6	-	-
$\lambda_{7,8}$	-	-2083.33 ± j 4.562e6	-	-
$\lambda_{9,10}$	-	-2083.33 ± j 4.562e6	-	-
$\lambda_{11,12}$	-	-2083.33 ± j 4.567e6	-	-
$\lambda_{13,14}$	-	-2083.33 ± j 4.567e6	-	-

2.5 Stability Analysis using the Impedance/Admittance Method

Hitherto, we have considered eigenvalue analysis for analysing the small signal stability of a linearized system. Another approach is to analyse the linearized system in the frequency-domain. The output impedance of the source subsystem (Z_o) and input impedance of the load subsystem (Z_i) of the power system in Figure 2.2 need to be identified for the frequency domain approach. According to the Nyquist criterion, the system is stable if the Nyquist contour of Z_o/Z_i does not circle (-1,0) point in the *S*-plane. This criterion is necessary and sufficient conditions for stability study. Many works that deal with impedance/admittance stability methods for power electronic systems are based on Middlebrook criterion [10], [41]-[48] defined in Middlebrook in 1976 [10] as follows:

$$|Z_o| < |Z_i| \tag{2-39}$$

The system is stable if the condition in (2-39) is satisfied for all frequencies. This is equivalent to the Nyquist contour of Z_o/Z_i to be within the unit circle (for the stable condition). The Middlebrook's criterion is the sufficient

condition for the stability analysis. Therefore, the impedance derivations are very important for the stability analysis using this approach. However, it is difficult to derive Z_o and Z_i for three phase power systems such as that Figure 2.2. Although reference [56]-[58] reported the input impedance modelling and analysis of line-commutated rectifiers, the application of these models for stability analysis has not been reported. To handle the stability problem, we can derive the impedances from the equivalent circuit using the simplified dq model or the average-value model. For the SSA model, it is difficult to derive Z_o from the equivalent circuit. It means that the SSA modelling method does not lend itself to using the impedance/admittance methods for stability study.

2.5.1. Applying Impedance/Admittance Method to the dq model

The stability analysis of the power system in Figure 2.2 based on the Middlebrook criterion using the dq modelling approach must use the simplified dq model equivalent circuit in Figure 2.26. For the small-signal stability study, Z_o and Z_i can be easily defined from the equivalent circuit in Figure 2.26 in which

$$Z_o = \frac{L_{e,dq}\, s + R_{e,dq}}{L_{e,dq}C_{e,dq}\, \mathrm{s}^2 + R_{e,dq}C_{e,dq}\, \mathrm{s} + 1} \tag{2-40}$$

and for an ideal CPL

$$Z_i = -\frac{V_{out,o}^2}{P_{CPLo}} \tag{2-41}$$

The magnitude of Z_o by using the system parameters in Table 2.1 is shown in Figure 2.28 in which $|Z_o|_{\max} = 24.32$ dB.

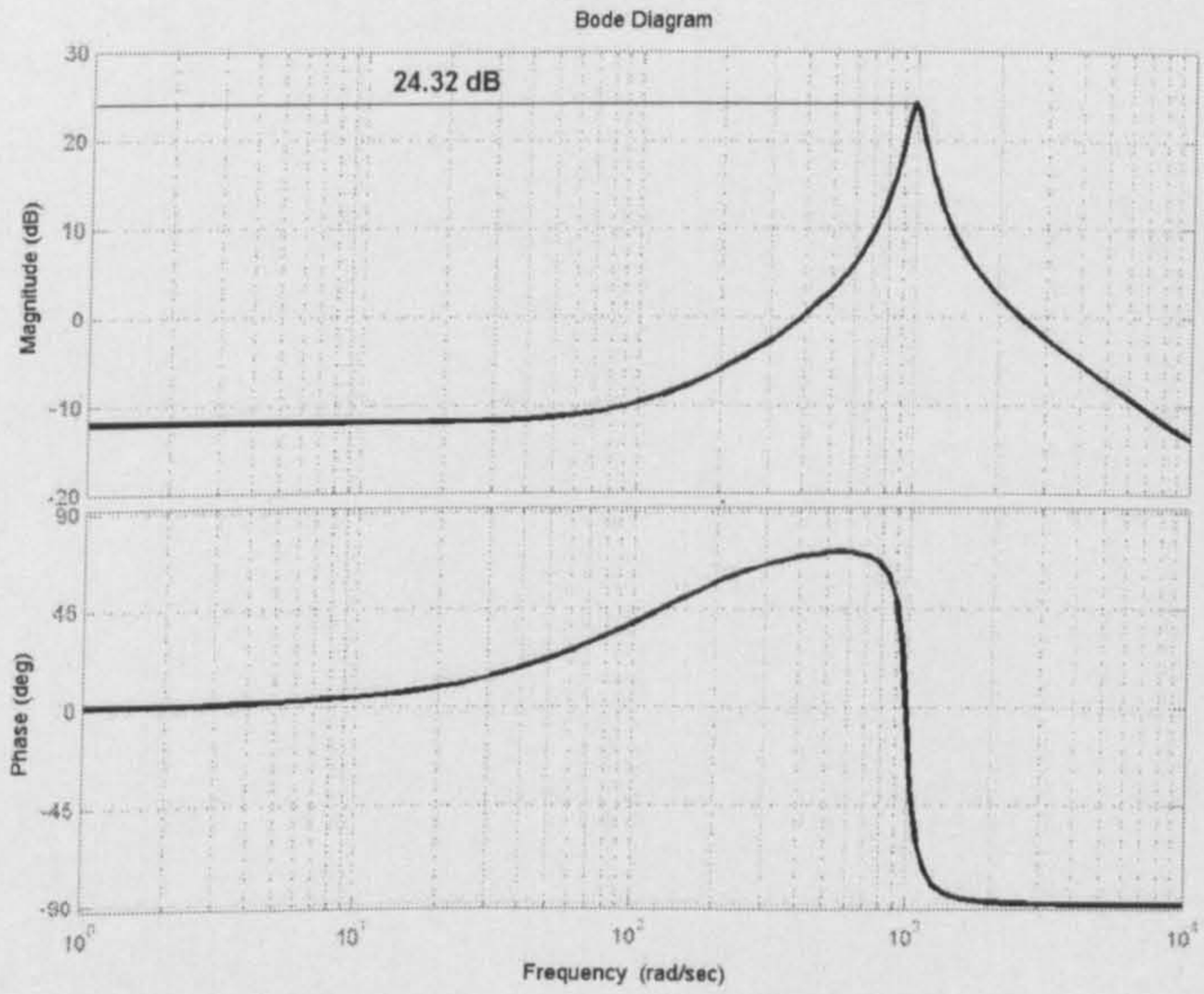

Figure 2.28: The output impedance bode diagram from simplified dq model

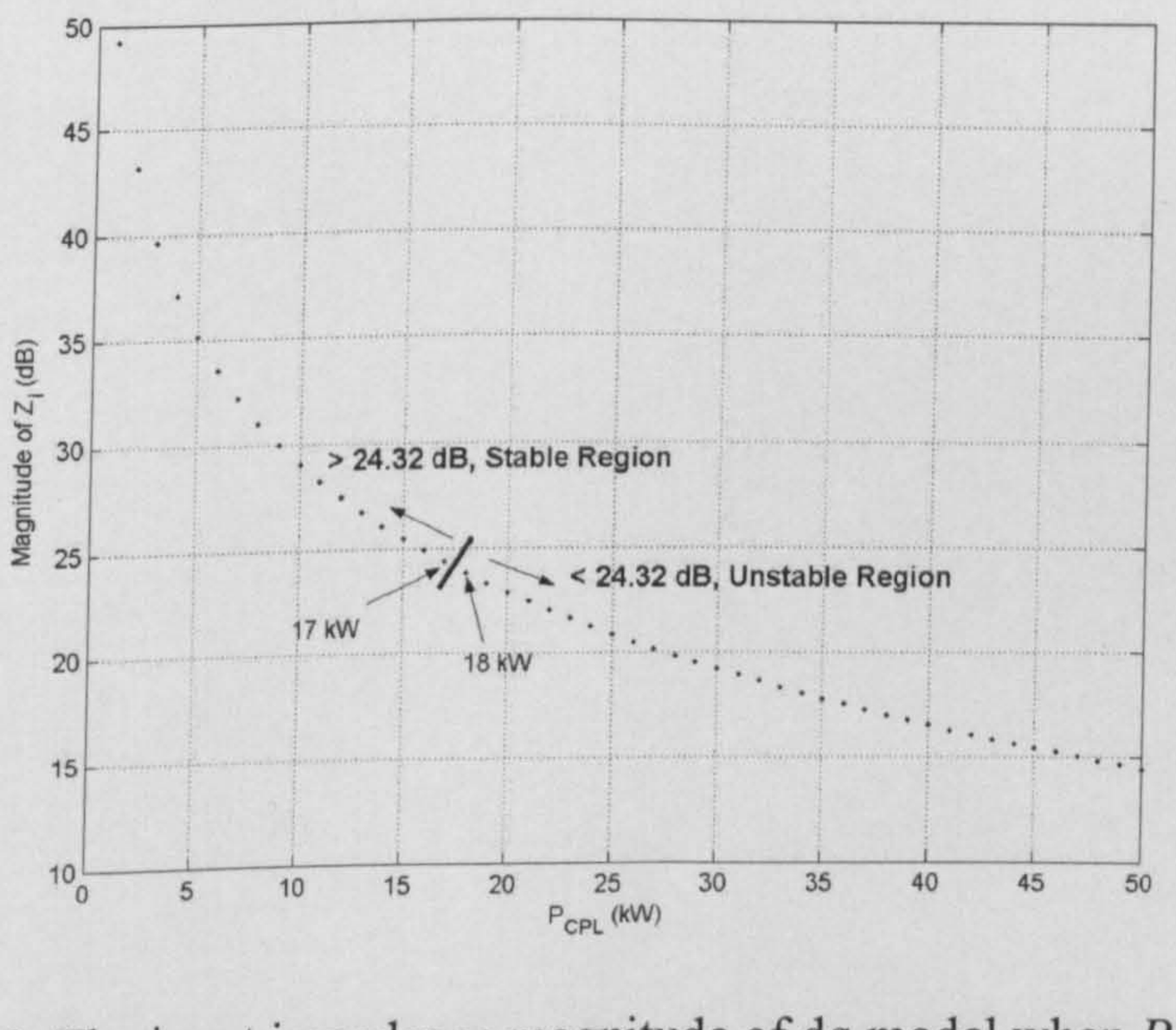

Figure 2.29: The input impedance magnitude of dq model when P_{CPL} varies

The magnitude of Z_i is independent of frequency, but is a function of P_{CPL}. The system becomes unstable when P_{CPL} exceeds 17 kW ($|Z_o| > |Z_i|$ and the condition in (2-39) is not satisfied). It can be seen that the stability derived

from dq modelling approach using the impedance/admittance method are the same as the one based on eigenvalue theorem.

2.5.2. Applying Impedance/Admittance Method to the average-value model

The stability analysis of the power system in Figure 2.2 based on Middlebrook criterion can also use the average-value model. One has to derive Z_o and Z_i from the equivalent circuit in Figure 2.25 where the DC voltage source V_e, the equivalent resistance R_e, and the inductance L_e are expressed in (2-31), (2-32), and (2-33), respectively. For the small-signal stability study, Z_o and Z_i can be easily derived from the equivalent circuit in Figure 2.25:

$$Z_o = \frac{L_e\, s + R_e}{L_e C_e\, \mathrm{s}^2 + R_e C_e\, \mathrm{s} + 1} \tag{2-42}$$

and the input impedance is the same as that of (2-41). The magnitude of Z_o is shown in Figure 2.30 in which $|Z_o|_{\max} = 23.76$ dB.

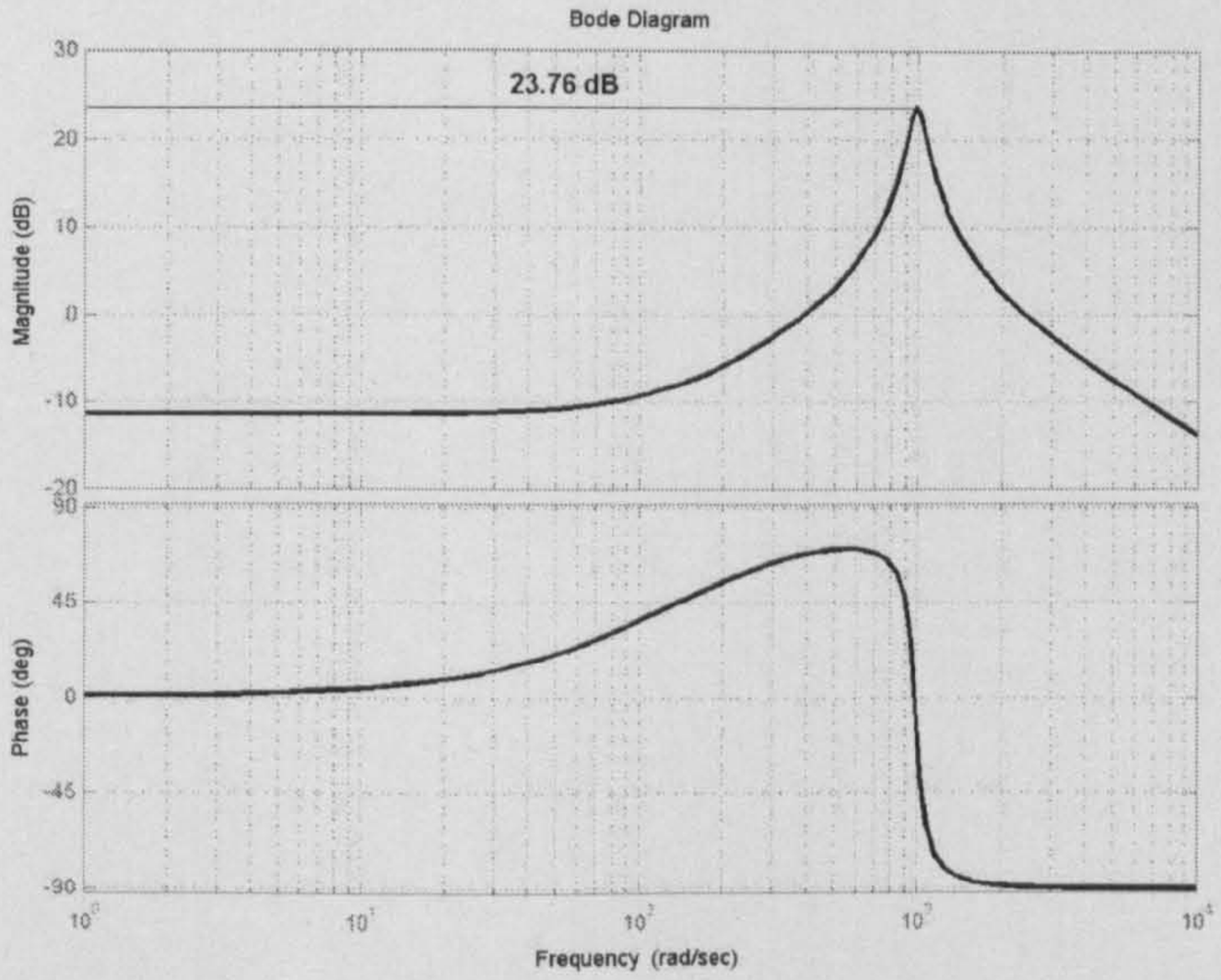

Figure 2.30: The output impedance bode diagram from the average-value model

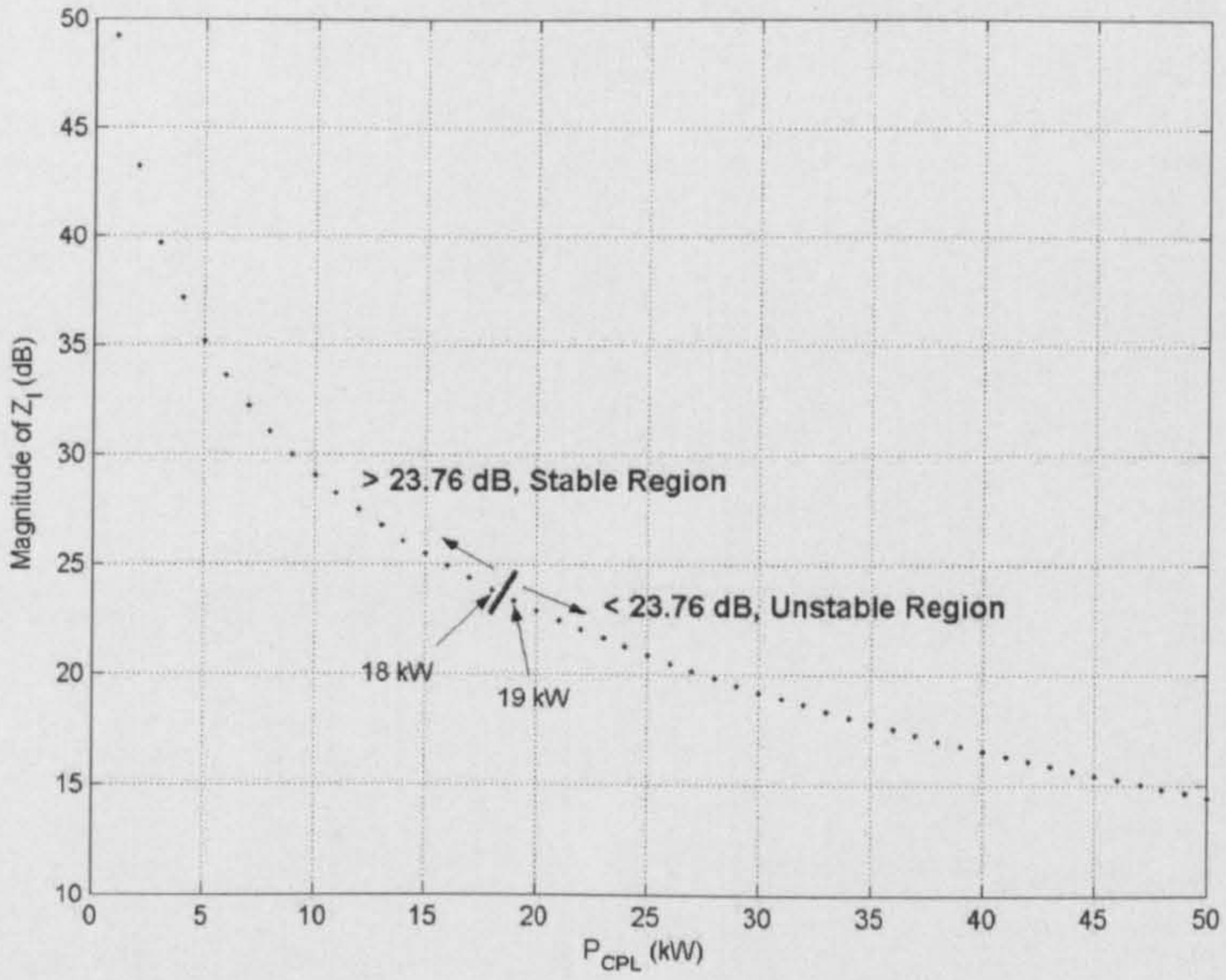

Figure 2.31: The input impedance of the average-value model when P_{CPL} varies

The magnitude of Z_i is also shown in Figure 2.31 where the system becomes unstable when P_{CPL} exceeds 18 kW ($|Z_o| > |Z_i|$).It can be seen that the stability results using the average-value model based on the impedance/admittance approach are the same as the one based on the eigenvalue theorem.

According to the results from Section 2.2-2.5, the dq, SSA, and average-value models can provide equivalent circuits of the power system in Figure 2.2. These equivalent circuits can be used for stability study. In respect to stability analysis, the eigenvalue theorem can be applied to all methods. The average-value model has some error and it is not easily applicable for the complex power systems with multiplicity of actuators, aircraft loads, and bus geometries. The impedance/admittance method can be easily used on the dq and average-value models. In addition, the dq modelling method can also be applied for modelling power systems comprising vector-controlled converters where the SSA and average-value models are not easily derived. Moreover, the resulting converter models can be easily combined with models of other

power elements expressed in terms of synchronously rotating frames such as generators, front-end converters, and vector-controlled drives. Hence, the dq approaches will be used for modelling the power system in this research. For stability studies, the eigenvalue theorem is used in this research. However, the impedance/admittance method can be used for stability study as well.

2.6 Twelve-Pulse Autotransformer Rectifier Unit and CPLs

As mentioned in Chapter 1, the aircraft power systems for this research are based on an AC distribution system. There is a twelve-pulse autotransformer rectifier unit (ATRU) to provide a high voltage DC (HVDC) bus. This HVDC bus is to supply energy for an environmental control and other DC loads. The ATRU is used to reduce the harmonics arising from the diode rectifier. In this section, the detail of how the six-pulse diode rectifier model using the dq modelling approach can represent the ATRU will be illustrated. This model is then used for stability analysis.

2.6.1. Power System Definition and Assumptions

The twelve-pulse autotransformer rectifier unit (ATRU) is shown in Figure 2.32 in which the autotransformer turns-ratio n:1:1 is set to 6.464:1:1 to provide the phase shifted outputs $\pm 15^{o}$ with respect to the supply [21],[80]. The symmetry of two six-pulse diode rectifiers are connected in parallel to feed the ideal CPL through DC link filters. The elements R_T and L_T represent the resistance and the inductance of the cable, while R_s and L_s represent the equivalent resistance and leakage inductance of the autotransformer for each of the two rectifiers, both referred to the secondary side.

The power system in Figure 2.2 for the six-pulse diode rectifier can be approximately used to represent the ATRU in Figure 2.32 [75],[80] by setting:

$$R_{eq} \approx \frac{R_s}{2} + R_T \tag{2-43}$$

where $R_s = \left[\frac{r_p}{n^2} + r_s\right]$

$$L_{eq} \approx \frac{L_s}{2} + L_T \tag{2-44}$$

where $L_s = \left[\frac{l_p}{n^2} + l_s\right]$

$$r_\mu = \frac{3\omega}{\pi}\left[\left(1 - \frac{3}{n}\right)L_T + \frac{L_s}{2}\right] \tag{2-45}$$

The inter-phase reactor (IPR) is used to balance the output voltages of paralleled diode rectifier. The equivalent circuit of IPR is represented by the leakage inductance L_{ipr} as shown in Figure 2.32.

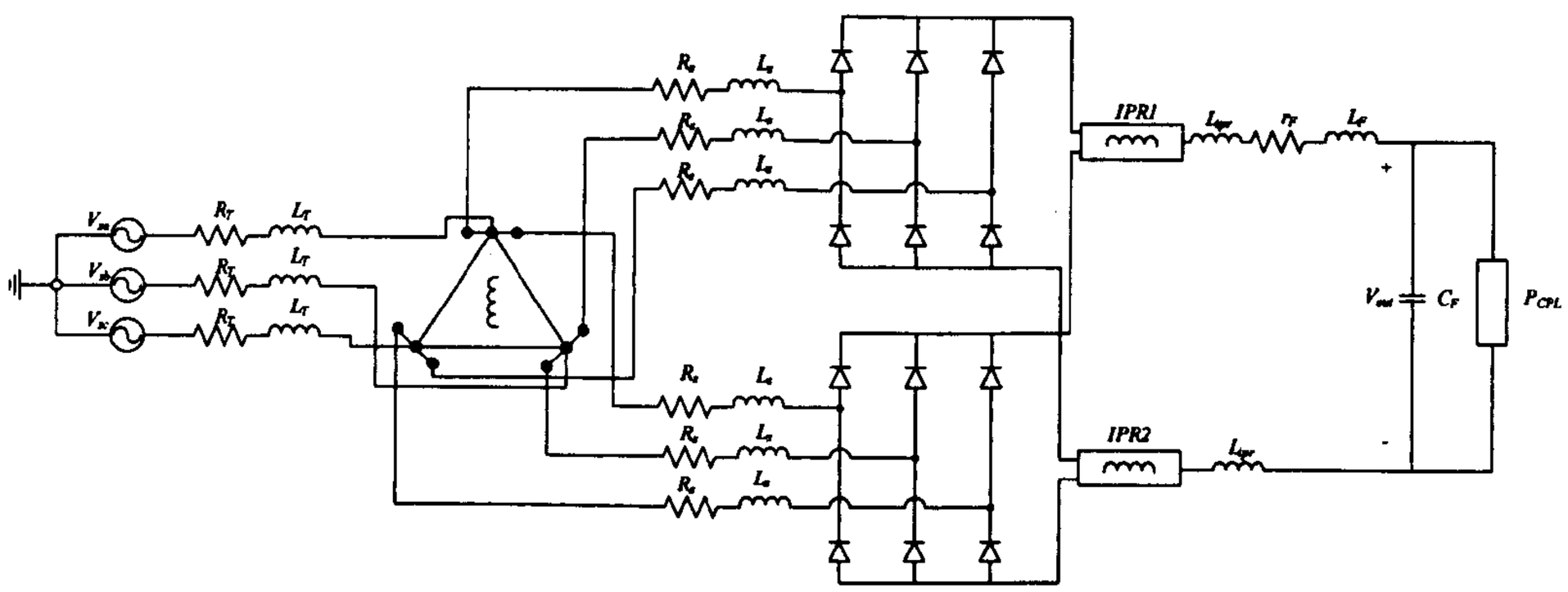

Figure 2.32: The power system with ATRU and an ideal CPL

The dq modelling method of Section 2.2 is applied for approximate analysis of the system in Figure 2.32 taking into account (2-43), (2-44), and (2-45).

Moreover, the steady state value $V_{outo,12\,pulse}$ for ATRU system can be calculated by [21]:

$$V_{outo,12\,pulse} = 1.035 V_{outo,6\,pulse} \tag{2-46}$$

where $V_{outo,6\,pulse}$ can be calculated by using power flow equations as addressed in Section 2.2.3.

2.6.2. Small-Signal Stability Analysis

The dq linearized model is used with the eigenvalue theorem for stability study. The eigenvalues can be calculated from the Jacobian matrix $\mathbf{A}(\mathbf{x_o}, \mathbf{u_o})$ in (2-13). The example system parameters are given in Table 2.3. Note that the leakage inductance of IPR is set to zero because the coupling factor of IPR in the benchmark model is set to 1. However, the IPR equivalent leakage inductance can be set to any value depending on the coupling factor. The parameters shown are for an ATRU feed supplying a load of typically 20-30 kW.

R_{eq} and L_{eq} can be calculated by using (2-43) and (2-44) respectively, with the system parameters in Table 2.3. Therefore, the power system in Figure 2.32 can be represented by the system in Figure 2.2 with R_{eq} = 0.29 Ω and L_{eq}= 101.11 μH. The eigenvalues of the linearized **A** matrix (see (2-13) in Section 2.2) with parameters in Table 2.3 and the new equivalent parameters from (2-43)-(2-46) were analyzed for the case when the P_{CPL} varies from 0 kW to 50 kW. The zoomed area of the root locus is shown in Figure 2.33 where the system becomes unstable when the P_{CPL} exceeds 23 kW. Figure 2.34 shows the SABER time-domain benchmark simulation for the power system in Figure 2.32 (see Appendix D.2) to compare with the theoretical results. As expected the instability occurs at a constant power load value of 24 kW which agrees with the analysis of Figure 2.33.

Table 2.3: The set of parameters for the ATRU

parameter	Value	description
V_s	230 $V_{rms/phase}$	phase source voltage
ω	2π×400 rad/s	source frequency
R_T	0.1 Ω	transmission line resistance
L_T	40 μH	transmission line inductance
r_p	1 Ω	the primary resistance of autotransformer
l_p	2.55 mH	the primary leakage inductance of autotransformer
r_s	0.36 Ω	the secondary resistance of autotransformer
l_s	61 μH	the secondary leakage inductance of autotransformer
r_F	0.01 Ω	DC link inductor resistance
L_F	4 mH	DC link inductance
C_F	500 μF	DC link capacitance
n	6.464	turn ratio of autotransformer
L_{ipr}	0 μH	leakage inductance of inter-phase reactor

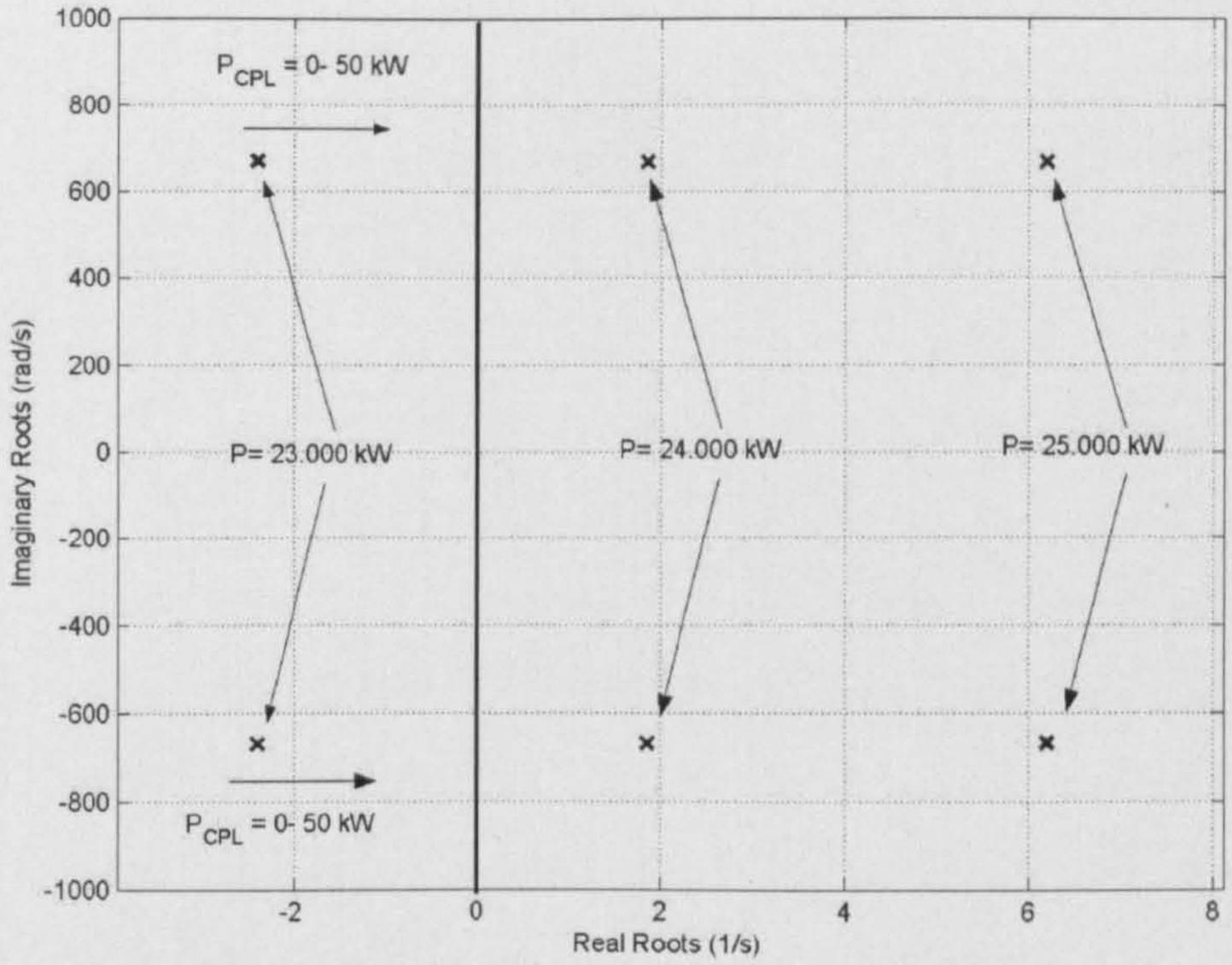

Figure 2.33: Eigenvalue plot of the system in Figure 2.32

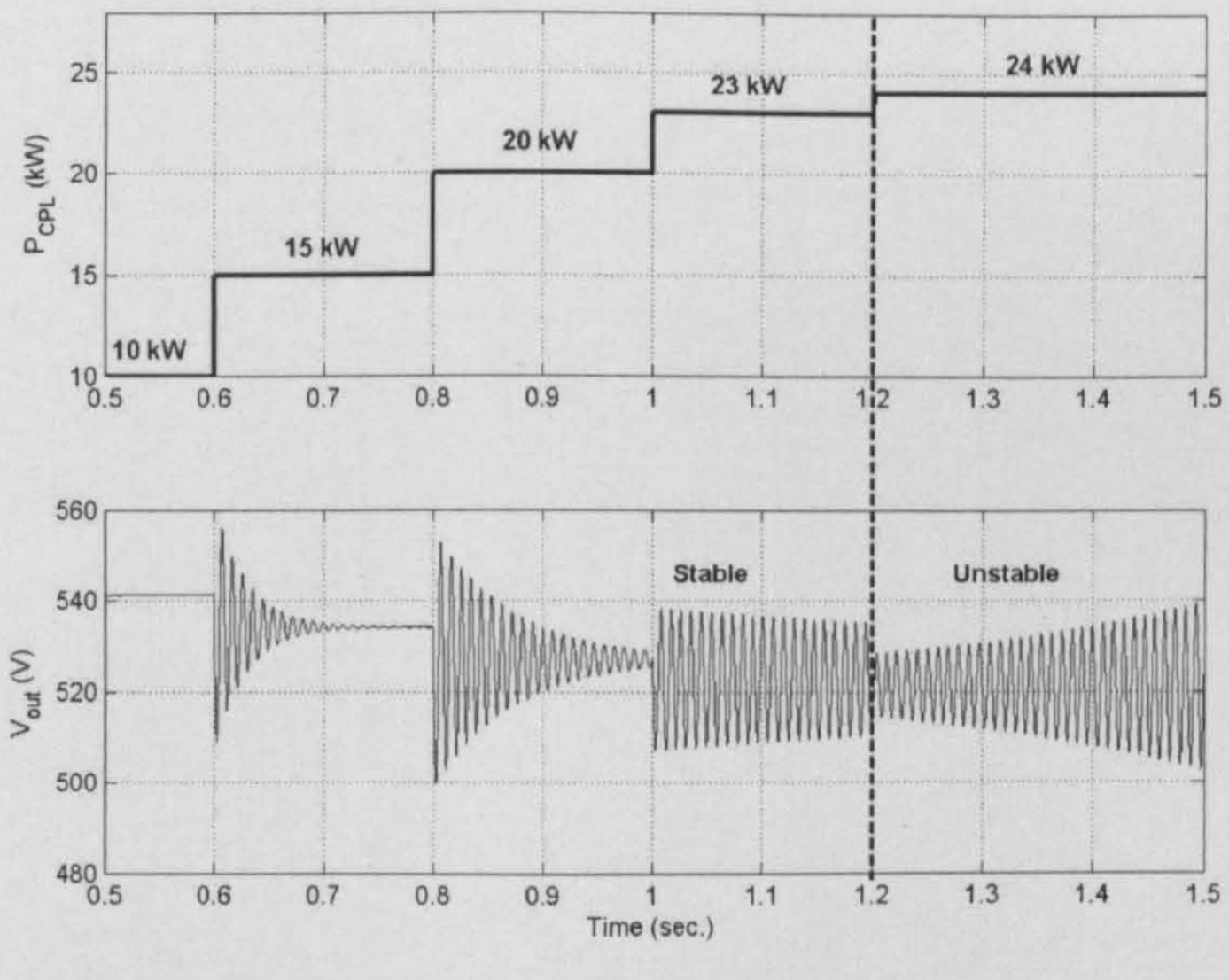

Figure 2.34: Step response for P_{CPL} variations (ATRU)

2.7 Chapter Summary

This chapter deals with the stability analysis of AC-DC power system with an ideal CPL fed through both six-pulse and twelve-pulse diode rectifiers (or

ATRU). The results show that dq, SSA, and average-value modelling approaches can provide the equivalent circuit for the power system to create the mathematical model for stability study. The SABER time-domain simulation is used for comparison with the theoretical results. Good agreement between them is achieved.

The average-value model is not easily applicable for the complex power systems with the multiplicity of actuators, aircraft loads, and bus geometries. In addition, the stability results from SSA and dq modelling approach are the same. The dq modelling method can also be applied for modelling power systems comprising vector-controlled converters where the SSA and average-value models are not easily derived. Moreover, the resulting converter models can be easily combined with models of other power elements expressed in terms of synchronously rotating frames such as generators, front-end converters, and vector-controlled drives. Hence, the dq modelling approach is selected for modelling the aircraft power systems in this research. For stability studies, the eigenvalue theorem is used in this research. This chapter also shows how the six-pulse diode rectifier model can approximately represent the twelve-pulse diode rectifier with autotransformer. In the next chapter, the dq modelling approach is used to model the power system with an ideal CPL fed through a controlled PWM rectifier. Since the controlled PWM rectifier uses dq structures, the dq modelling method is straightforward and appropriate. Stability analysis will use the eigenvalue approach.

Chapter 3

Power Systems with a Controlled PWM Rectifier and an Ideal CPL

3.1 Introduction

Chapter 1 discussed the main elements of an aircraft power system architecture as shown in Figure 3.1. The engine generator with a generator control unit (GCU), transmission line, six-pulse diode rectifier feeding an ideal CPL through HVDC bus was discussed in Chapter 2. This chapter deals with the stability analysis of an AC-DC power system with a CPL fed through a controlled PWM rectifier. The part of the aircraft power system is shown as a dashdot line in Figure 3.1. The ideal voltage source is used to represent an engine generator with a GCU by assuming an infinitely fast controller action of the GCU. Similarly, the ideal CPL is used to represent actuator drive systems under the same assumption. The effect of actuator dynamics (dynamic CPL) will be considered in Chapter 4, while the effect of GCU dynamics will be considered in Chapter 6. The more complex power system having parallel power converter connections will be considered in Chapter 7.

In this Chapter, the dq modelling approach is applied to create the equivalent circuit to represent the power system shown as a dashdot line in Figure 3.1. The dq approach is more applicable to a converter controlled in terms of a rotating dq-frame aligned with the grid voltage vector. In respect to stability analysis, the eigenvalue theorem is used. It will be shown that the natural frequency of the DC-link voltage control loop has a substantial effect on

system stability. Therefore, this is considered in the study and reported in this chapter. The work from this chapter was published in [33].

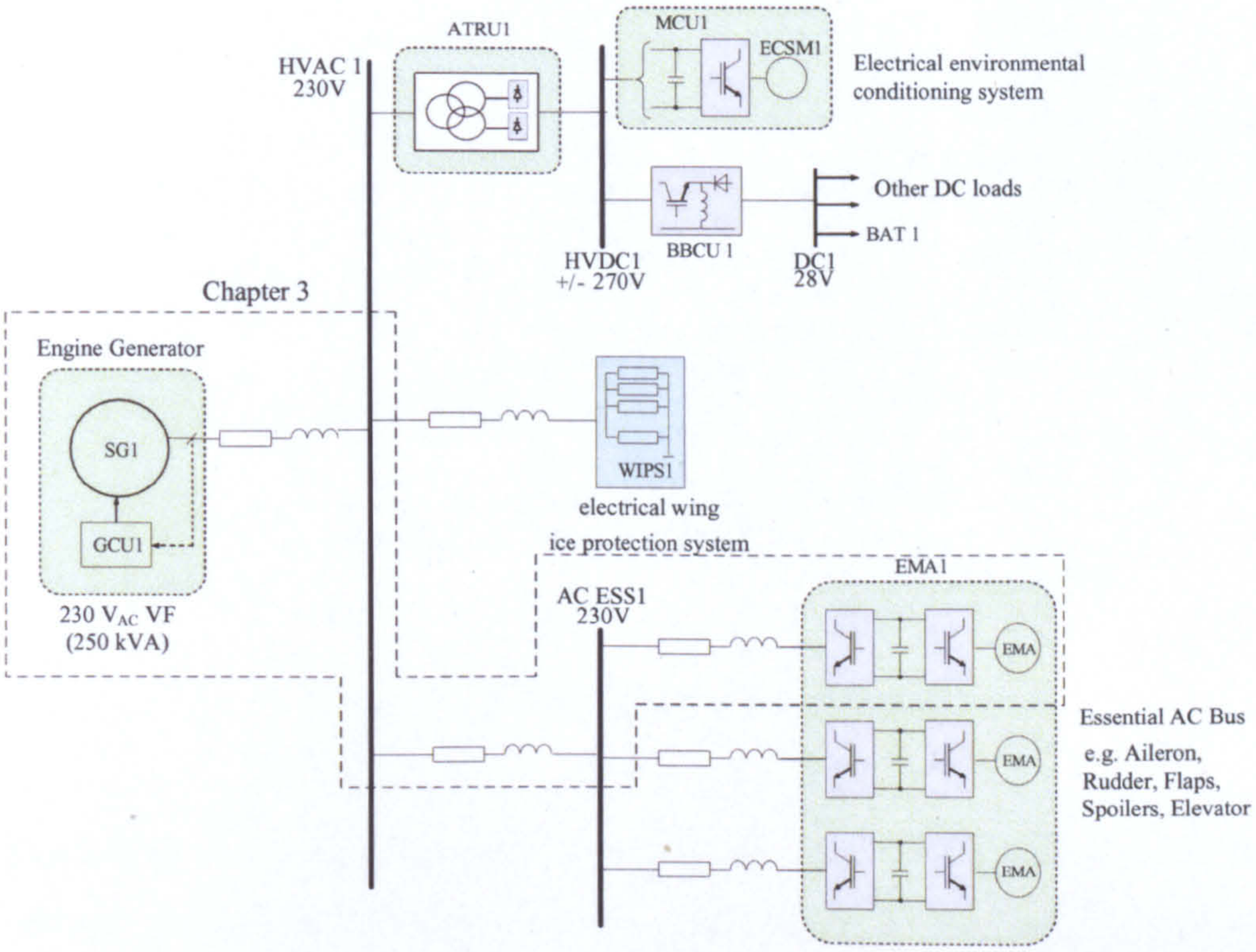

Figure 3.1: The main elements of aircraft power system architecture

3.2 Power System Definitions and Assumptions

The power system studied is shown in Figure 3.2. It consists of a three-phase source, transmission line, filters and a front-end PWM converter under standard close-loop control [81]. The CPL is fed through a DC bus. It is assumed that the three-phase source is balanced. R_{eq}, L_{eq}, and C_{eq} are the equivalent parameters of a transmission line, r_F and L_F are AC filter parameters, and C_F is a DC-link capacitor. The PWM converter considered uses six ideal switches as IGBTs. It is assumed that there are no loss and no system harmonics.

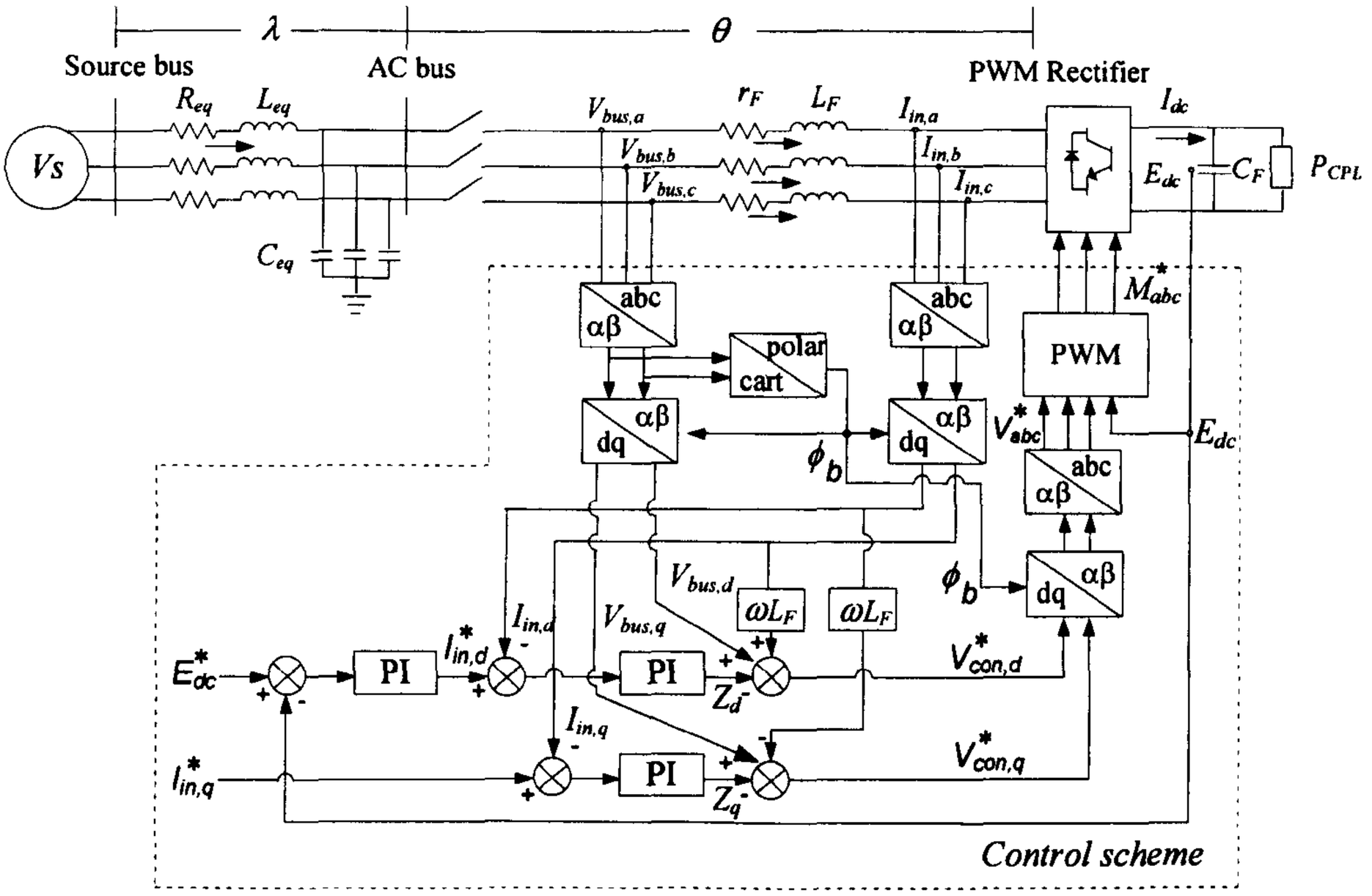

Figure 3.2: The power system studied

The PWM converter considered consists of vector-controllers to keep the voltage across the DC-link constant, here regulated to the E^*_{dc} voltage command, and to keep a unity power factor at the AC bus by setting $I^*_{in,q}$ equal to zero. The vector-control is in terms of the reference frame aligned to the AC bus voltage vector. The schematic of the controllers on the direct axis used to regulate the DC-link voltage and the quadrature axis used to regulate the reactive power is shown in Figure 3.3. The parameters K_{pe}, K_{ie}, K_{pd}, K_{id}, K_{pq}, K_{iq} are the proportional and integral gains of voltage and current PI controllers. The design for the voltage loop and current loop in Figure 3.3 can be found in [81].

The dq modelling approach is applied to derive a mathematical model for the power system in Figure 3.2 including vector-controllers. The PWM converter is modelled in the dq frame represented as a transformer. The vector diagram for the dq-transformation is depicted in Figure 3.4. Note that the input terminal voltage V_{con} lags the bus voltage V_{bus} by an angle θ, while the bus voltage V_{bus} lags the source voltage V_s by an angle λ as shown in Figure 3.2.

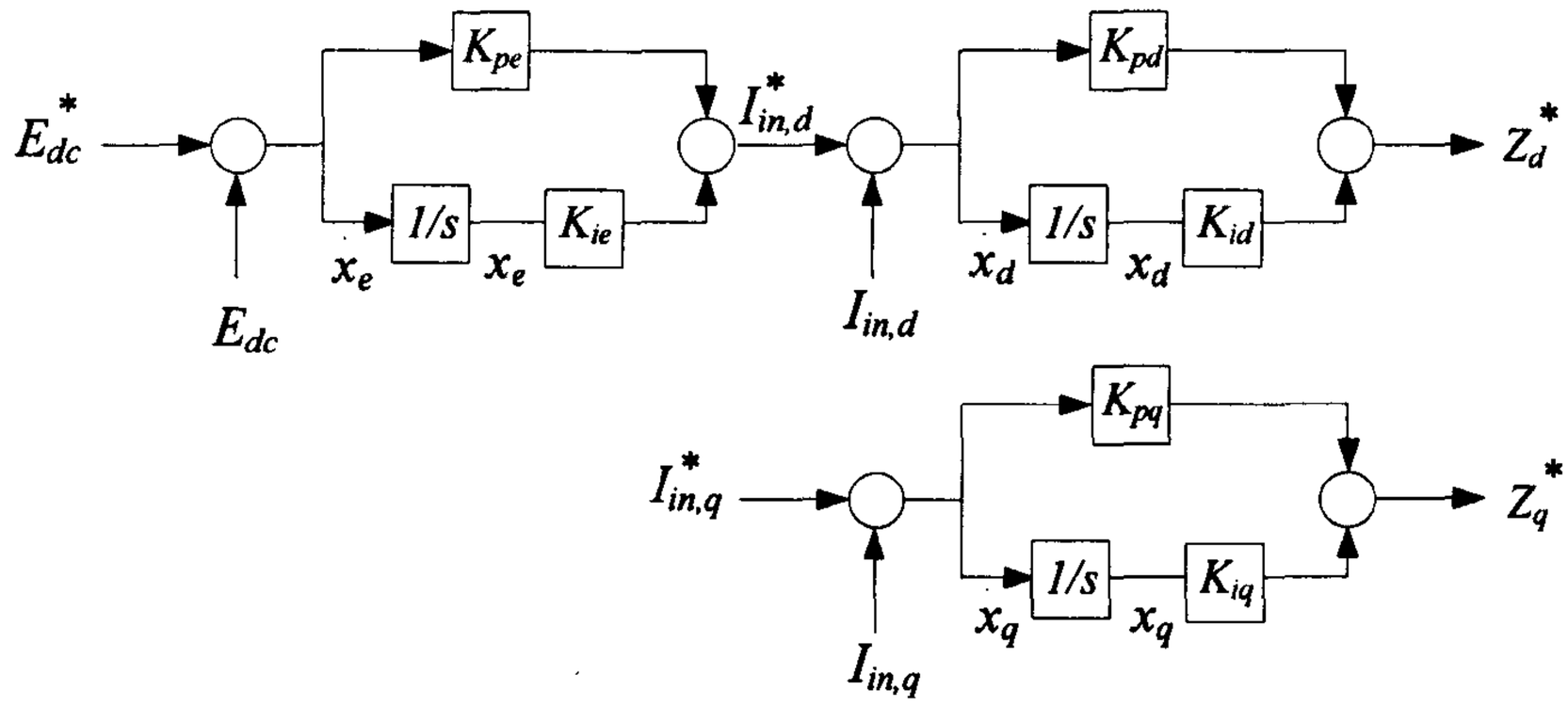

Figure 3.3: The schematic of controllers

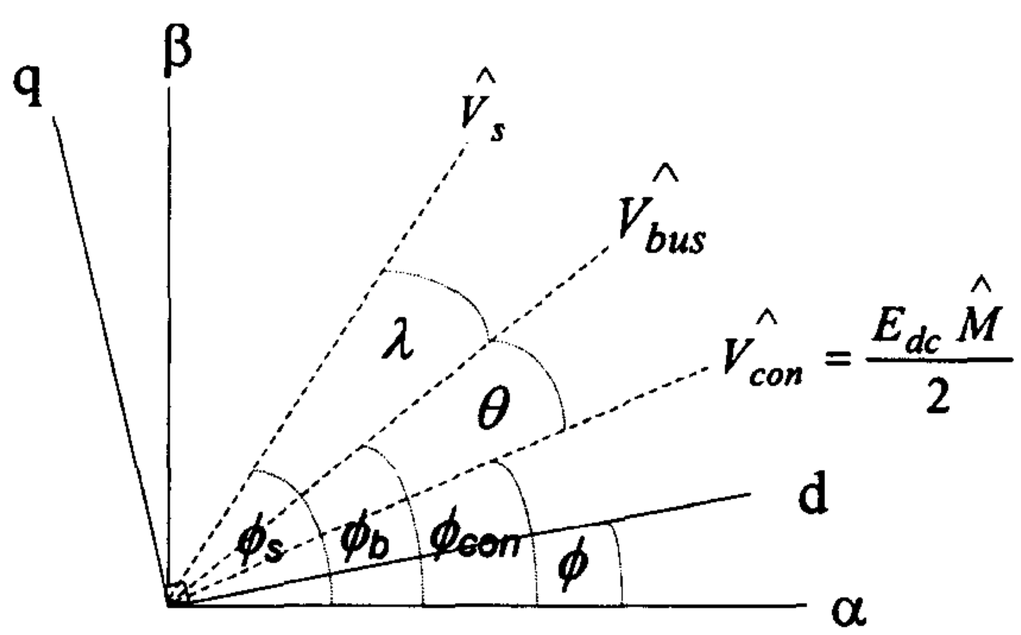

Figure 3.4: The vector diagram for dq-transformation

For the PWM converter, the voltage source equation, the bus voltage equation, the converter terminal voltage equation and the switching signal equation can be written in the dq frame rotating at a frequency ($\omega t+\phi_b$) and fixed to the AC bus voltage vector ($\phi=\phi_b$). These equations are

$$\mathbf{V_{s,dq}} = \hat{V}_s\, e^{j(\phi_s-\phi_b)} = \hat{V}_s\, e^{j\lambda} \tag{3-1}$$

$$\mathbf{V_{bus,dq}} = \hat{V}_{bus}\, e^{j(\phi_b-\phi_b)} = \hat{V}_{bus}\, e^{j0} \tag{3-2}$$

$$\mathbf{V_{con,dq}} = \hat{V}_{con}\, e^{j(\phi_{con}-\phi_b)} = \hat{V}_{con}\, e^{-j\theta} \tag{3-3}$$

$$\mathbf{M_{dq}} = \hat{M}\, e^{j(\phi_{con}-\phi_b)} = \hat{M}\, e^{-j\theta} \tag{3-4}$$

The 3 phase to two phase transformation uses the peak convention defined by:

$$\mathbf{T}[\theta(t)] = \frac{2}{3}\begin{bmatrix} \cos(\theta(t)) & \cos(\theta(t)-\frac{2\pi}{3}) & \cos(\theta(t)+\frac{2\pi}{3}) \\ -\sin(\theta(t)) & -\sin(\theta(t)-\frac{2\pi}{3}) & -\sin(\theta(t)+\frac{2\pi}{3}) \end{bmatrix} \tag{3-5}$$

From (3-3) and (3-4), the relationship between the input and output terminals of the PWM converter on the dq frame is

$$\mathbf{V_{con,dq}} = \frac{E_{dc}\mathbf{M_{dq}}}{2} \tag{3-6}$$

According to (3-1)-(3-6), the equivalent circuit of the system in the dq frame is shown in Figure 3.5, where the PWM converter can be modelled as a transformer. It can be seen in Figure 3.5 that Z^*_{dq} can be derived by using the diagram of the controllers in Figure 3.3. In addition, the P_{CPL} can be considered as a voltage-dependent current source given in (2-9) of Chapter 2.

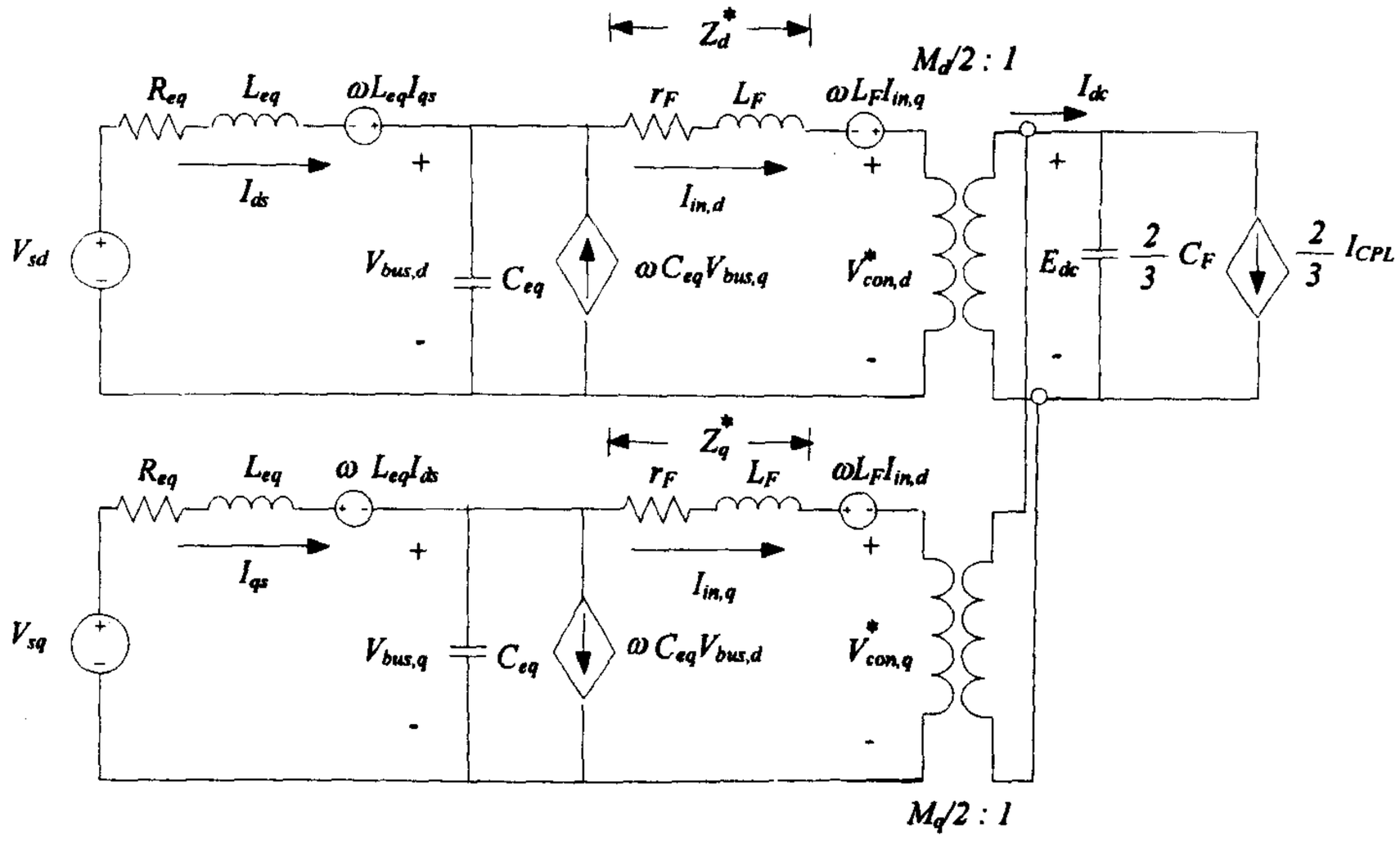

Figure 3.5: The equivalent circuit of the power system in the dq frame

3.3 Deriving the Non-Linear Dynamic Model and Linearized Model

From Figure 3.3, PI controller output Z^*_{dq} can be derived and given by:

$$Z_d^* = -K_{pd} I_{in,d} - K_{pe} K_{pd} E_{dc} + K_{ie} K_{pd} X_e + K_{id} X_d + K_{pe} K_{pd} E_{dc}^* \tag{3-7}$$

$$Z_q^* = -K_{pq} I_{in,q} + K_{iq} X_q + K_{pq} I_{in,q}^* \tag{3-8}$$

Applying KVL and KCL to the circuit in Figure 3.5 with (3-7) and (3-8) determines the set of nonlinear differential equations describing the power system dynamic as:

$$\dot{I}_{ds} = -\frac{R_{eq}}{L_{eq}} I_{ds} + \omega I_{qs} - \frac{1}{L_{eq}} V_{bus,d} + \frac{1}{L_{eq}} V_{sd}$$

$$\dot{I}_{qs} = -\omega I_{ds} - \frac{R_{eq}}{L_{eq}} I_{qs} - \frac{1}{L_{eq}} V_{bus,q} + \frac{1}{L_{eq}} V_{sq}$$

$$\dot{V}_{bus,d} = \frac{1}{C_{eq}} I_{ds} + \omega V_{bus,q} - \frac{1}{C_{eq}} I_{in,d}$$

$$\dot{V}_{bus,q} = \frac{1}{C_{eq}} I_{qs} - \omega V_{bus,d} - \frac{1}{C_{eq}} I_{in,q}$$

$$\dot{I}_{in,d} = -\frac{(r_F + K_{pd})}{L_F} I_{in,d} - \frac{K_{pe} K_{pd}}{L_F} E_{dc} + \frac{K_{ie} K_{pd}}{L_F} X_e + \frac{K_{id}}{L_F} X_d + \frac{K_{pe} K_{pd}}{L_F} E_{dc}^*$$

$$\dot{I}_{in,q} = -\frac{(r_F + K_{pq})}{L_F} I_{in,q} + \frac{K_{iq}}{L_F} X_q + \frac{K_{pq}}{L_F} I_{in,q}^*$$

$$\dot{X}_e = -E_{dc} + E_{dc}^*$$

$$\dot{X}_d = -I_{in,d} - K_{pe} E_{dc} + K_{ie} X_e + K_{pe} E_{dc}^*$$

$$\begin{aligned}
\dot{X}_q &= -I_{in,q} + I^*_{in,q} \\
\dot{E}_{dc} &= \frac{3}{2C_F E_{dc}}(V_{bus,d} I_{in,d} - K_{pe} K_{pd} I_{in,d} E^*_{dc} + K_{pe} K_{pd} I_{in,d} E_{dc} \\
&\quad - K_{ie} K_{pd} I_{in,d} X_e + K_{pd} I^2_{in,d} - K_{id} I_{in,d} X_d + V_{bus,q} I_{in,q} \\
&\quad - K_{pq} I_{in,q} I^*_{in,q} + K_{pq} I^2_{in,q} - K_{iq} I_{in,q} X_q) - \frac{P_{CPL}}{C_F E_{dc}}
\end{aligned} \tag{3-9}$$

This set of equations can not be solved analytically. Therefore the stability analysis is performed using small-signal linearization. The linear model can be derived using the first-order terms of the Taylor expansion of (3-9), so as to achieve a set of linear differential equations around an equilibrium point. Setting the state variables x, input u and output vector y as:

$$\begin{aligned}
x &= < I_{ds}, I_{qs}, V_{bus,d}, V_{bus,q}, I_{in,d}, I_{in,q}, X_e, X_d, X_q, E_{dc} > \\
u &= < \hat{V}_s, E^*_{dc}, I^*_{in,q}, P_{CPL} > \\
y &= < E_{dc} >
\end{aligned} \tag{3-10}$$

The dq linearized model of (3-9) can be written as:

$$\begin{aligned}
\delta \dot{\mathbf{x}} &= \mathbf{A}(\mathbf{x_0}, \mathbf{u_0})\delta\mathbf{x} + \mathbf{B}(\mathbf{x_0}, \mathbf{u_0})\delta\mathbf{u} \\
\delta\mathbf{y} &= \mathbf{C}(\mathbf{x_0}, \mathbf{u_0})\delta\mathbf{x} + \mathbf{D}(\mathbf{x_0}, \mathbf{u_0})\delta\mathbf{u}
\end{aligned} \tag{3-11}$$

where

$$\delta\mathbf{x} = [\delta I_{ds}\ \delta I_{qs}\ \delta V_{bus,d}\ \delta V_{bus,q}\ \delta I_{in,d}\ \delta I_{in,q}\ \delta X_e\ \ \delta X_d\ \ \delta X_q\ \delta E_{dc}]^T$$

$$\delta\mathbf{u} = [\delta V_m\ \ \delta E^*_{dc}\ \ \delta I^*_{in,q}\ \ \delta P_{CPL}]^T, \quad \delta\mathbf{y} = [\delta E_{dc}]$$

The details of $\mathbf{A}(\mathbf{x_0},\mathbf{u_0})$, $\mathbf{B}(\mathbf{x_0},\mathbf{u_0})$, $\mathbf{C}(\mathbf{x_0},\mathbf{u_0})$, and $\mathbf{D}(\mathbf{x_0},\mathbf{u_0})$ are:

$$\mathbf{A}(\mathbf{x_o},\mathbf{u_o}) = \begin{bmatrix}
-\frac{R_{eq}}{L_{eq}} & \omega & -\frac{1}{L_{eq}} & 0 & 0 & 0 & 0 & 0 & 0 & 0 \\
-\omega & -\frac{R_{eq}}{L_{eq}} & 0 & -\frac{1}{L_{eq}} & 0 & 0 & 0 & 0 & 0 & 0 \\
\frac{1}{C_{eq}} & 0 & 0 & \omega & -\frac{1}{C_{eq}} & 0 & 0 & 0 & 0 & 0 \\
0 & \frac{1}{C_{eq}} & -\omega & 0 & 0 & -\frac{1}{C_{eq}} & 0 & 0 & 0 & 0 \\
0 & 0 & 0 & 0 & -\frac{(r_F + K_{pd})}{L_F} & 0 & \frac{K_{ie}K_{pd}}{L_F} & \frac{K_{id}}{L_F} & 0 & -\frac{K_{pe}K_{pd}}{L_F} \\
0 & 0 & 0 & 0 & 0 & -\frac{(r_F + K_{pq})}{L_F} & 0 & 0 & \frac{K_{iq}}{L_F} & 0 \\
0 & 0 & 0 & 0 & 0 & 0 & 0 & 0 & 0 & -1 \\
0 & 0 & 0 & 0 & -1 & 0 & K_{ie} & 0 & 0 & -K_{pe} \\
0 & 0 & 0 & 0 & 0 & -1 & 0 & 0 & 0 & 0 \\
0 & 0 & 0 & 0 & a(10,5) & a(10,6) & a(10,7) & a(10,8) & a(10,9) & a(10,10)
\end{bmatrix}_{10\times 10}$$

where

$$a(10,5) = \frac{3}{2}\left(\frac{V_{bus,do}}{C_F E_{dco}} - \frac{K_{ie}K_{pd}X_{eo}}{C_F E_{dco}} + \frac{2K_{pd}I_{in,do}}{C_F E_{dco}} - \frac{K_{id}X_{do}}{C_F E_{dco}}\right)$$

$$a(10,6) = \frac{3}{2}\left(\frac{V_{bus,qo}}{C_F E_{dco}} + \frac{K_{pq}I_{in,qo}}{C_F E_{dco}} - \frac{K_{iq}X_{qo}}{C_F E_{dco}}\right)$$

$$a(10,7) = -\frac{3}{2}\left(\frac{K_{ie}K_{pd}I_{in,do}}{C_F E_{dco}}\right)$$

$$a(10,8) = -\frac{3}{2}\left(\frac{K_{id}I_{in,do}}{C_F E_{dco}}\right)$$

$$a(10,9) = -\frac{3}{2}\left(\frac{K_{iq}I_{in,qo}}{C_F E_{dco}}\right)$$

$$a(10,10) = \left(\frac{3}{2}\frac{1}{C_F E_{dco}^2}\right)\begin{pmatrix} -V_{bus,do}I_{in,do} + K_{pe}K_{pd}I_{in,do}E_{dco} + K_{ie}K_{pd}I_{in,do}X_{eo} - K_{pd}I_{in,do}^2 \\ + K_{id}I_{in,do}X_{do} - V_{bus,qo}I_{in,qo} + K_{iq}I_{in,qo}X_{qo} \end{pmatrix} + \frac{P_{PCLo}}{C_F E_{dco}^2}$$

and

$$\mathbf{B}(\mathbf{x_o},\mathbf{u_o}) = \begin{bmatrix} \frac{\cos(\lambda_o)}{Leq} & 0 & 0 & 0 \\ \frac{\sin(\lambda_o)}{L_{eq}} & 0 & 0 & 0 \\ 0 & 0 & 0 & 0 \\ 0 & 0 & 0 & 0 \\ 0 & \frac{K_{pe}K_{pd}}{L_F} & 0 & 0 \\ 0 & 0 & \frac{K_{pq}}{L_F} & 0 \\ 0 & 1 & 0 & 0 \\ 0 & K_{pe} & 0 & 0 \\ 0 & 0 & 1 & 0 \\ 0 & -\frac{3}{2}\frac{K_{pe}K_{pd}I_{in,do}}{C_F E_{dco}} & -\frac{3}{2}\frac{K_{pq}I_{in,qo}}{C_F E_{dco}} & -\frac{1}{C_F E_{dco}} \end{bmatrix}_{10\times 4}$$

$$\mathbf{C}(\mathbf{x_o},\mathbf{u_o}) = \begin{bmatrix} 0 & 0 & 0 & 0 & 0 & 0 & 0 & 0 & 0 & 1 \end{bmatrix}_{1\times 10}$$

$$\mathbf{D}(\mathbf{x_o},\mathbf{u_o}) = \begin{bmatrix} 0 & 0 & 0 & 0 \end{bmatrix}_{1\times 4} \qquad (3\text{-}12)$$

3.4 Calculating the Steady-State Equilibrium Value

The dq linearized model from Section 3.3 is derived through the linearization technique around the operating point. According to (3-12), this linearized model has to define $V_{bus,do}$, $V_{bus,qo}$, $I_{in,do}$, $I_{in,qo}$, X_{eo}, X_{do}, X_{qo}, E_{dco}, and λ_o for small-signal simulation and stability analysis. The power flow equation [72] can be applied to determine the steady state values at AC side. The single line diagram of the power system in Figure 3.2 for power flow calculation is depicted in Figure 3.6 in which the line capacitors are ignored assuming C_{eq} is very small.

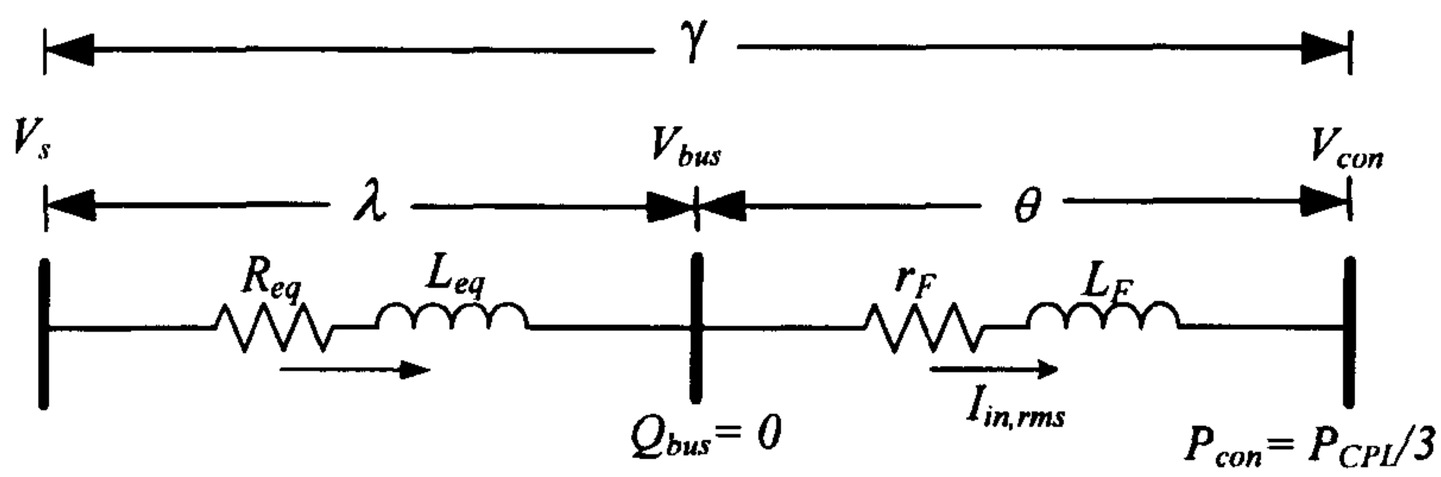

Figure 3.6: The single line diagram for power flow calculations

Figure 3.6 leads to a system of nonlinear equations:

$$
\begin{aligned}
&+\frac{V_{con}V_s}{Z_T+Z_F}\cos(\gamma_{TF}-\gamma)-\frac{V_{con}^2}{Z_T+Z_F}\cos(\gamma_{TF})=P_{CPL}/3\\
&+\frac{V_{con}V_{bus}}{Z_F}\cos(\gamma_F-\theta)-\frac{V_{con}^2}{Z_F}\cos(\gamma_F)=P_{CPL}/3\\
&-\frac{V_{con}V_{bus}}{Z_F}\sin(\gamma_F+\theta)+\frac{V_{bus}^2}{Z_F}\sin(\gamma_F)=Q_{bus}=0\\
&+\frac{V_{bus}V_s}{Z_T}\sin(\theta-\gamma+\gamma_T)-\frac{V_{bus}^2}{Z_T}\sin(\gamma_T)=Q_{bus}=0
\end{aligned}
\tag{3-13}
$$

where the following steady-state value are:

V_{bus} : phase voltage at ac bus (rms)

V_{con} : phase voltage at input terminal of converter (rms)

θ : phase shift between V_{bus} and V_{con} (degree)

γ : phase shift between V_s and V_{con} (degree)

In addition, Z_T, γ_T, Z_F, and γ_F are the magnitude and phase of the transmission line (R_{eq} and L_{eq}) and the AC filter (r_F and L_F), respectively, while γ_{TF} is the combination of angle between the transmission line and the AC filter. P_{CPL} is the constant power load, and Q_{bus} is equal to zero because $I^*_{in,q}$ is set to zero to keep a unity power factor at the AC bus. Equation (3-13) can be solved by using a numerical method so as to achieve the V_{buso}, V_{cono}, θ_o, and γ_o at the steady state conditions. Consequently, $V_{bus,do}$, $V_{bus,qo}$, $I_{in,do}$, $I_{in,qo}$, X_{eo}, X_{do}, X_{qo},

E_{dco}, and λ_o for the linearized model in (3-12) can be calculated by using the steady state value from power flow equations and setting (3-9) equal to zero. The steady state value equations are given as:

$$
\begin{aligned}
V_{bus,do} &= \sqrt{2}V_{buso} \\
V_{bus,qo} &= 0 \\
I_{ino,rms} &= \left| \frac{V_{bus}e^{-j(\gamma-\theta)} - V_{con}e^{-j\gamma}}{Z_F e^{j\gamma_F}} \right| \\
I_{in,do} &= \sqrt{2}I_{ino,rms} \\
I_{in,qo} &= I_{in,q}^{*} = 0 \\
X_{eo} &= \frac{I_{in,do}}{K_{ie}} \\
X_{do} &= \frac{r_F I_{in,do}}{K_{id}} \\
X_{qo} &= \frac{r_F I_{in,qo}}{K_{iq}} = 0 \\
E_{dco} &= E_{dc}^{*} \\
\lambda_o &= \gamma - \theta
\end{aligned}
\tag{3-14}
$$

It can be seen from (3-13) and (3-14) that steady-state values will change when the system operating point, here P_{CPL}, changes. Therefore, we can get the different linearized models of the system in Figure 3.2 for each operating point.

3.5 Small-Signal Simulation and Stability Analysis

The small signal simulation of the power system with the parameters given in Table 3.1 is used to support the accuracy of the mathematical model. The parameters of Table 3.1 correspond to a converter typically supplying 150 kW to standard motor drive systems.

Table 3.1: The set of parameters for the power system in Figure 3.2

parameter	value	description
V_s	230 $V_{rms/phase}$	phase source voltage
ω	$2\pi\times400$ rad/s	source frequency
R_{eq}	0.01 Ω	transmission line resistance
L_{eq}	30 μH	transmission line inductance
C_{eq}	2 nF	transmission line capacitance
r_F	0.1 Ω	ac filter resistance
L_F	100 μH	ac filter inductance
C_F	1000 μF	dc link capacitance
K_{pe}	0.0541 ($\zeta_e = 0.7$, $\omega_e = 2\pi\cdot10$ rad/s)	proportional gain of voltage loop
K_{ie}	2.4279 ($\zeta_e = 0.7$, $\omega_e = 2\pi\cdot10$ rad/s)	integral gain of voltage loop
K_{pd}, K_{pq}	0.403 ($\zeta_i = 0.8$, $\omega_i = 2\pi\cdot500$ rad/s)	proportional gain of current loop
K_{id}, K_{iq}	986.96 ($\zeta_i = 0.8$, $\omega_i = 2\pi\cdot500$ rad/s)	integral gain of current loop
E^*_{dc}	600 V	dc link voltage command input
$I^*_{in,q}$	0 A	current command input

The small signal model derives system in Figure 3.2 is compared with a benchmark SABER model. This is given in Appendix D.3. Note that the power converter in the benchmark SABER model uses the non-switching model. For the DC link voltage control loop having a ω_n (natural frequency) of 10 Hz, Figure 3.7 shows the DC link voltage response to a step change in P_{CPL} from 5kW to 5.5 kW. The small signal model results are practically identical

to those of SABER. Figure 3.8 also shows the same result when the DC link voltage control loop has a natural frequency of 20 Hz.

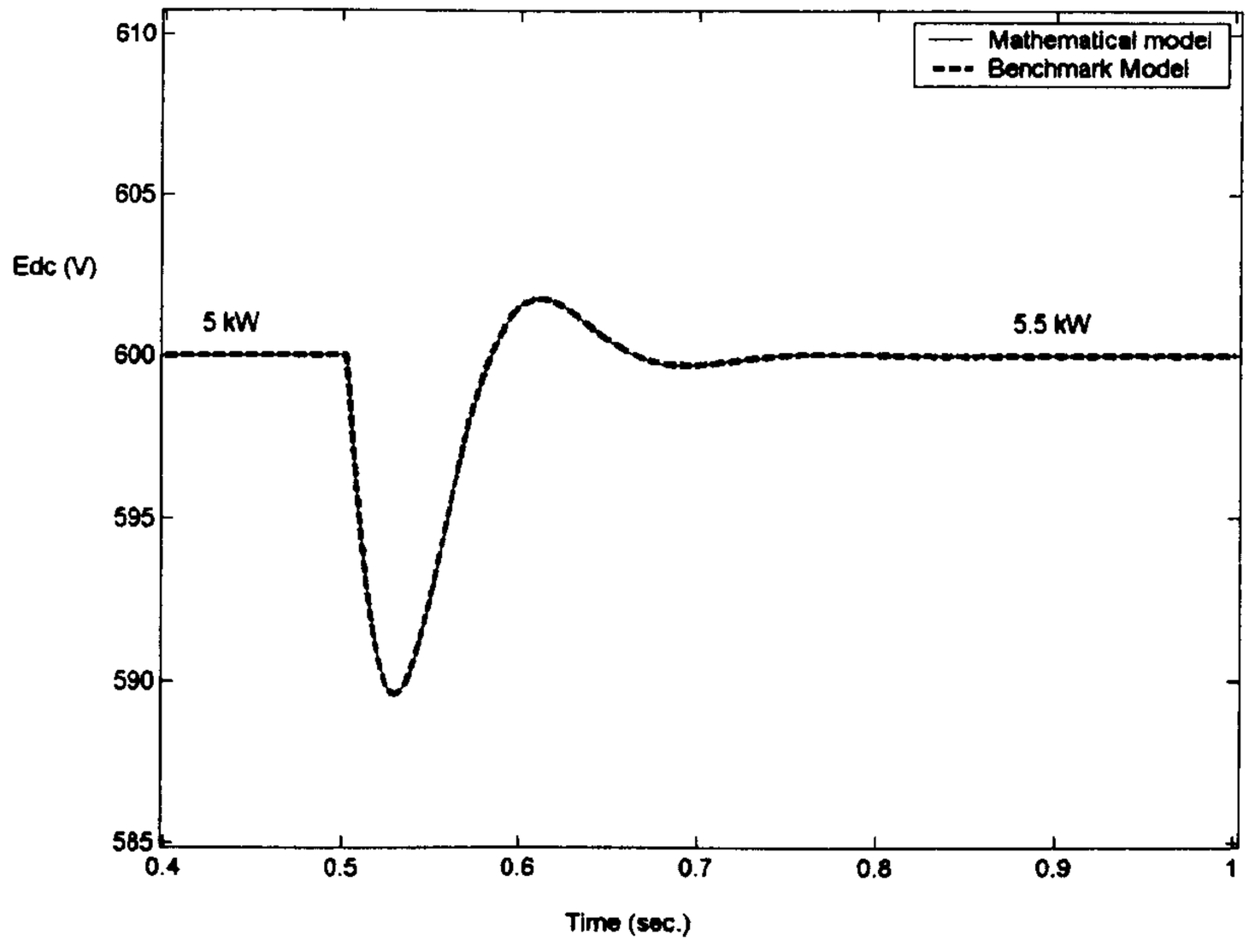

Figure 3.7: Compared step response for $\omega_{n\_e} = 2\pi \cdot 10$ rad/s

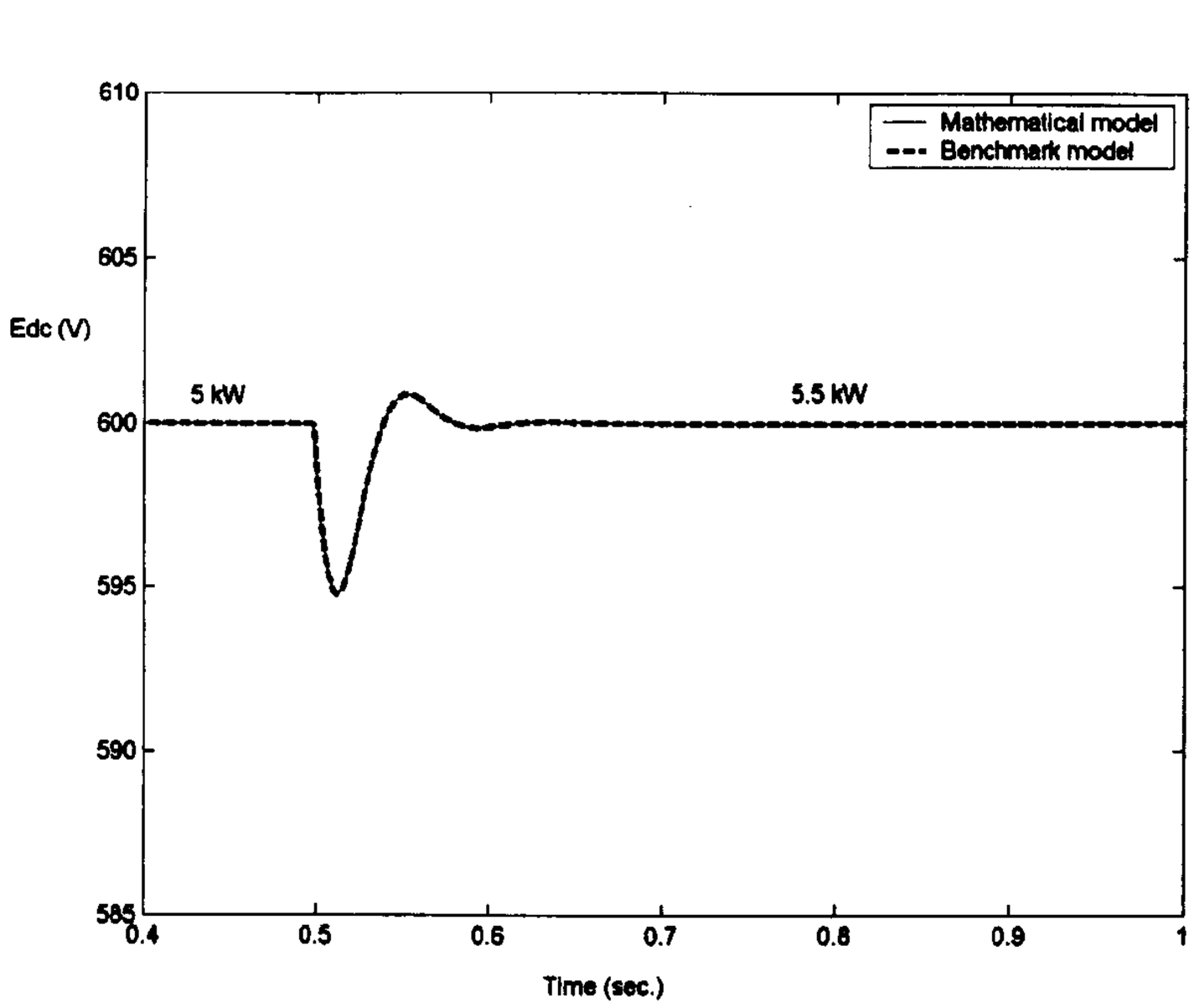

Figure 3.8: Compared step response for $\omega_{n\_e} = 2\pi \cdot 20$ rad/s

For stability analysis, the eigenvalues of the system are calculated from the matrix $\mathbf{A}(\mathbf{x_o},\mathbf{u_o})$ in (3-12). The eigenvalue plot for the power system with the above parameters when P_{CPL} varies from 0 kW to 322 kW is shown in the

Figure 3.9. Note that the maximum power is limited by M_{max} (modulation index limitation), and is equal to 322 kW for M_{max} =1.15. In this case, Figure 3.9 shows that the system is always stable. However, if the natural frequency of voltage control loop is increased to 100Hz, one can get an unstable point at certain a CPL level.

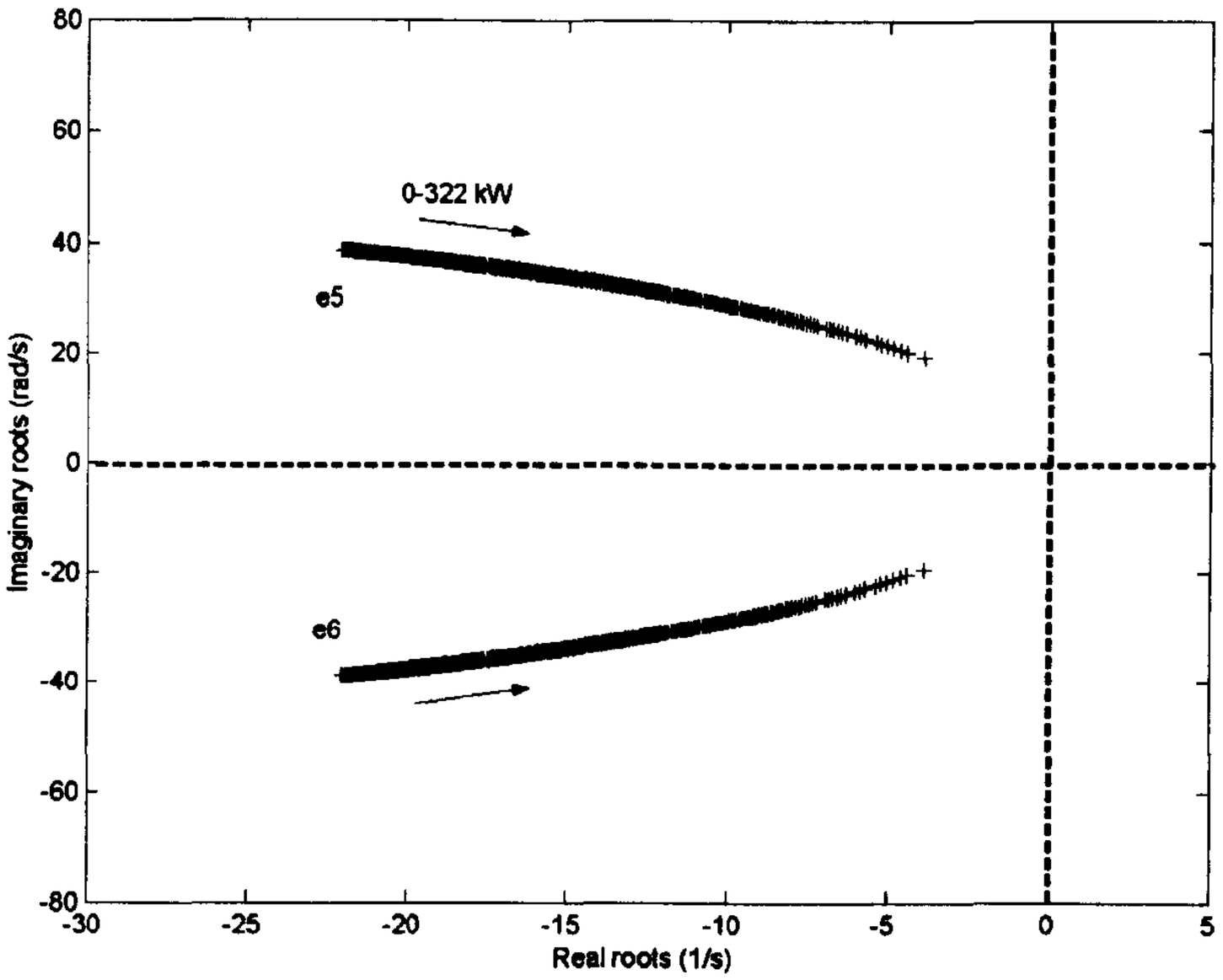

Figure 3.9: Eigenvalue plot for $\omega_{n\_e} = 2\pi \cdot 10$ rad/s

The eigenvalue plot for this case is shown in Figure 3.10. Figure 3.11 shows the zoomed area of interest: as one can see that the system becomes unstable when the P_{CPL} exceeds 320 kW. Figure 3.12 shows the step response of the system to illustrate very good agreement between the analytical results and the SABER simulation results for unstable conditions.

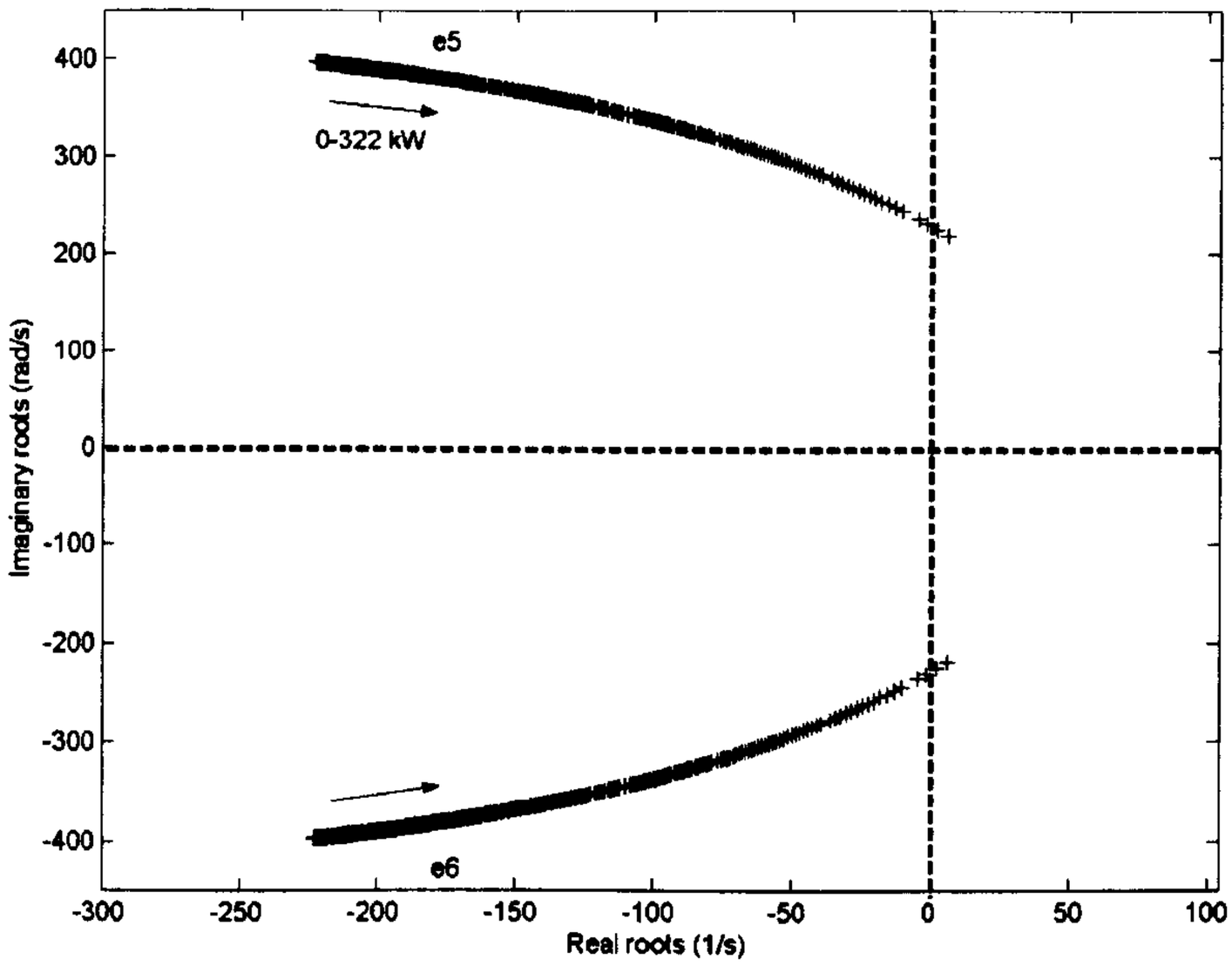

Figure 3.10: Eigenvalue plot for $\omega_{n\_e} = 2\pi \cdot 100$ rad/s

(K_{pe}= 0.541 , K_{ie}=242.79)

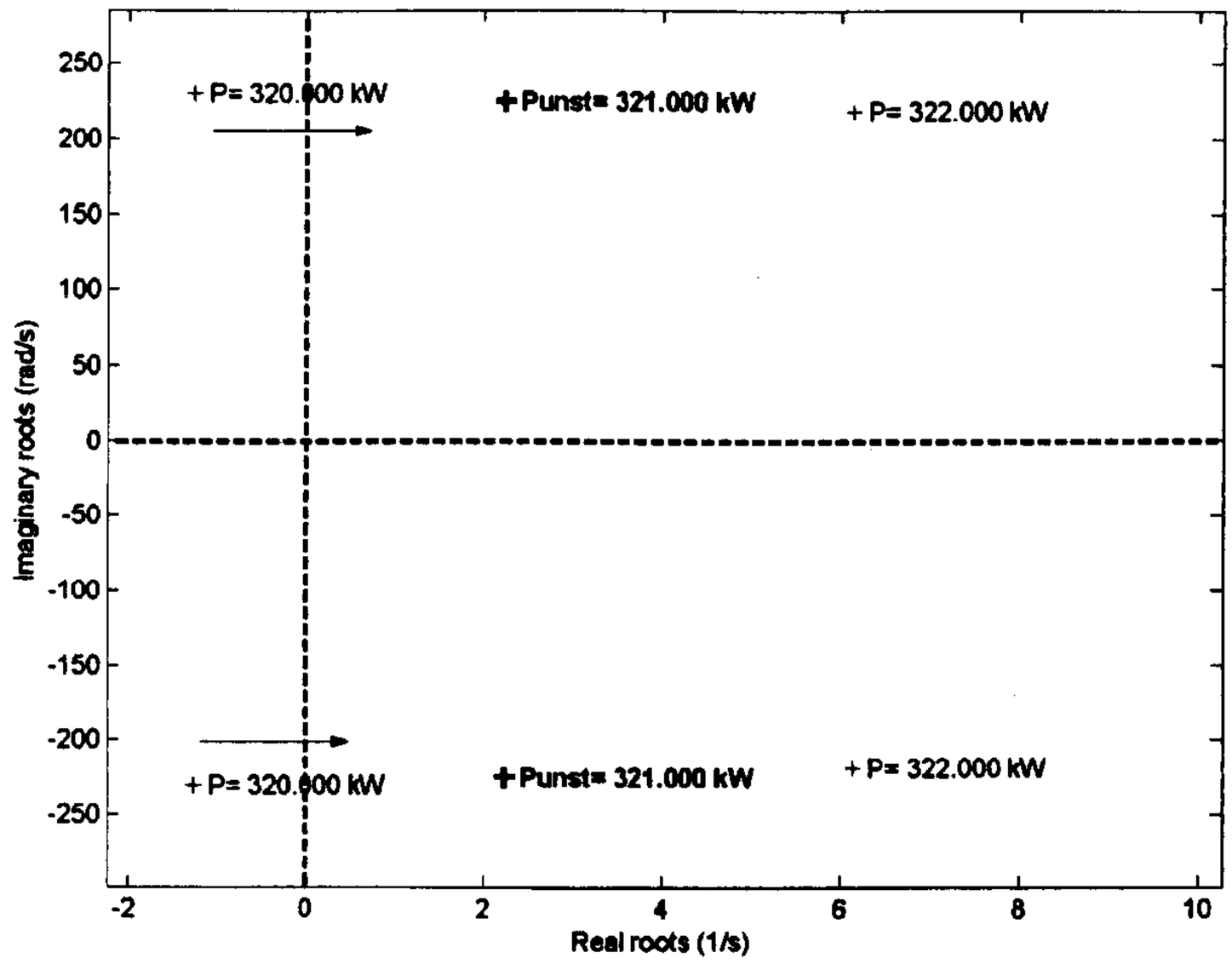

Figure 3.11: Zoomed area of interest from Figure 3.10

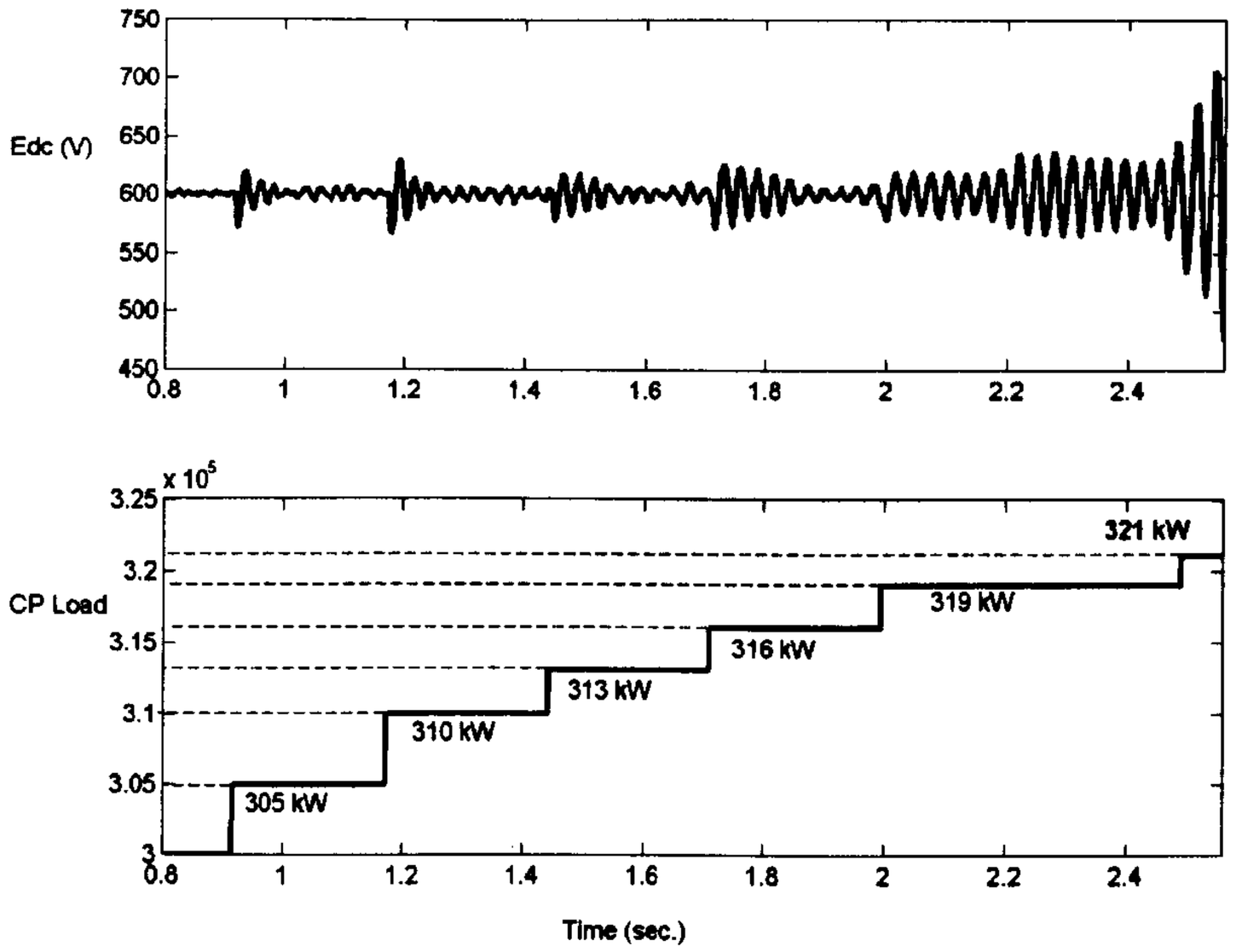

Figure 3.12: Step response for unstable condition ($\omega_{n\_e} = 2\pi \cdot 100$ rad/s)

3.6 Investigating Variations in System Parameters

In this section, the linearized dynamic DQ model is used to predict instability for variations in the system parameters. It can be seen from the results in the previous section that the ω_{n_e} (natural frequency of DC link voltage loop) is very crucial in terms of stability. Therefore, Figure 3.13 shows the eigenvalue plot when the ω_{n_e} varies from 0.5Hz to 100Hz with all other parameters fixed as given in Table 3.1. As can be seen from Figure 3.13 and Figure 3.14, increasing ω_{n_e} can make the system unstable. It is very difficult to explain this conclusion in terms of physical meaning. However, the results show that the PWM rectifier is more robust in terms of stability compare to the six-pulse diode rectifier: the power level at which instability occurs in the PWM rectifier is much higher than those of six-pulse diode rectifier.

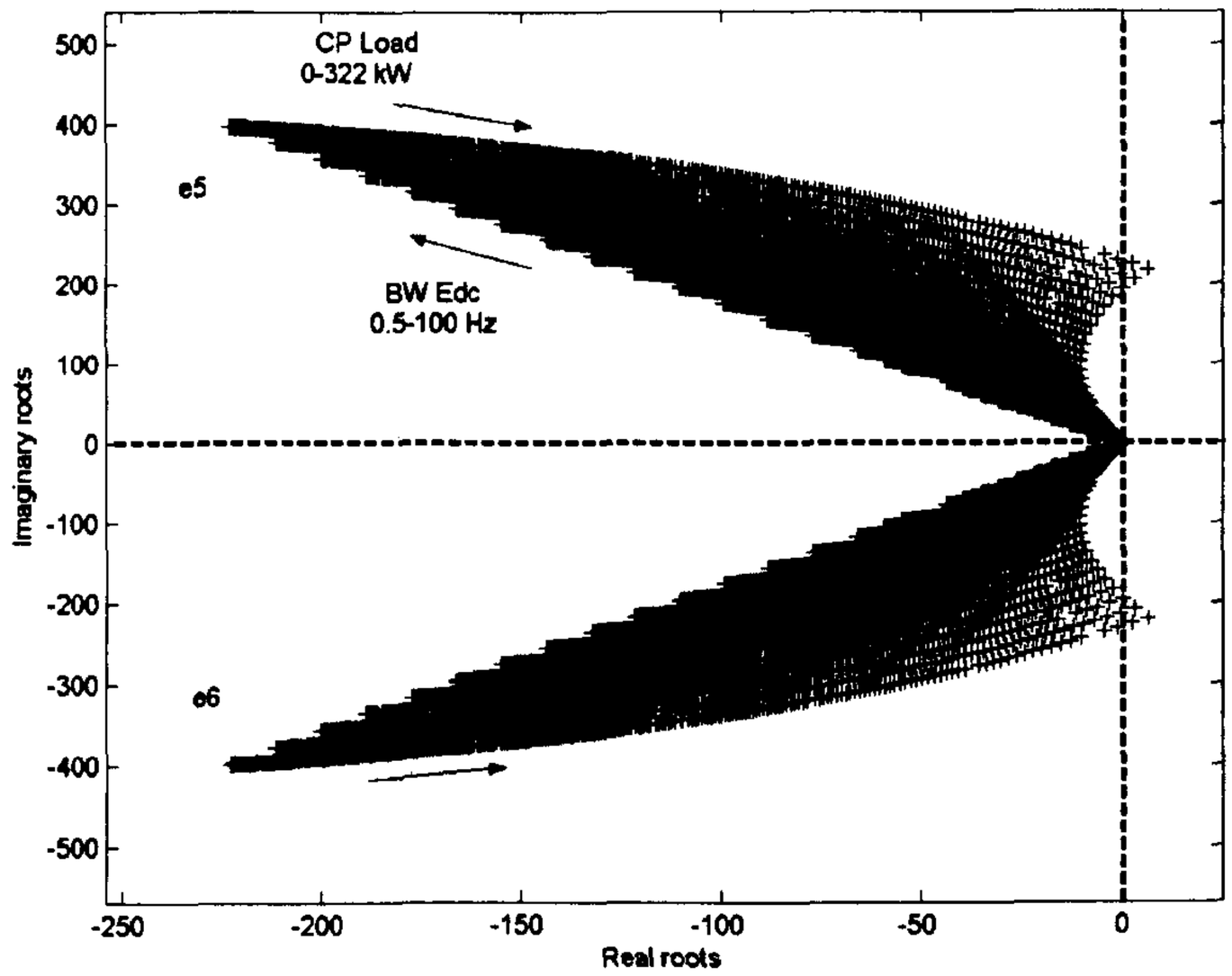

Figure 3.13: Eigenvalue plot for varying ω_{n_e} from 0.5 to 100 Hz

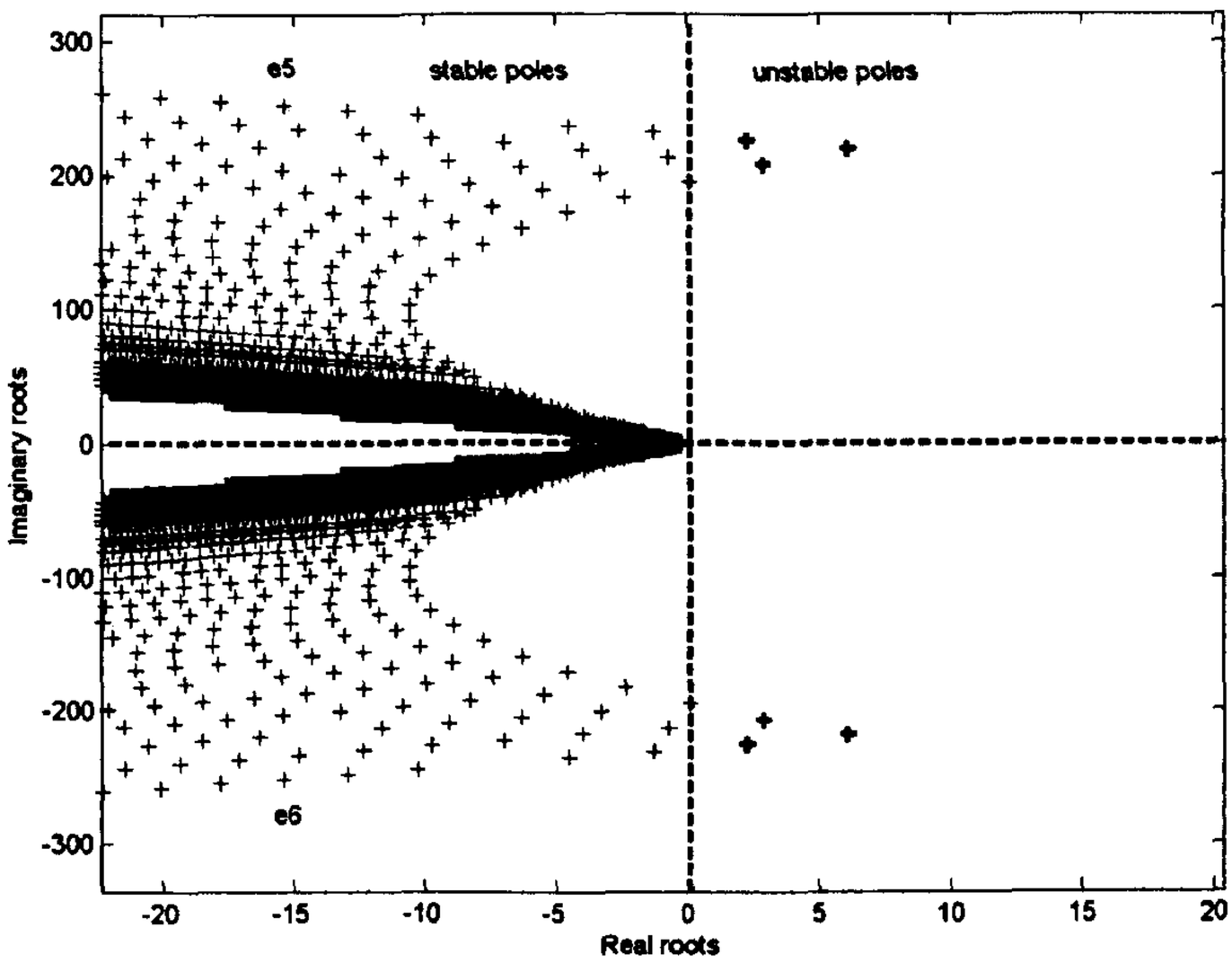

Figure 3.14: Zoomed area of interest from Figure 3.13

3.7 Chapter Summary

In this chapter, the DQ modelling method is applied for modelling and analysis of a three-phase AC distribution power system with an ideal CPL fed through a front-end PWM power converter under conventional vector control. The mathematical model is derived, validated and used to predict the unstable operation of the power system under certain CPL levels and parameters variations. The reported model can be used for thorough investigations of aircraft power system stability for representative architectures and worst-case operational modes. In the next chapter, the power system stability including the effect of actuators dynamic will be considered. Therefore, the dynamic of the CPL is taken into account instead of the ideal CPL that is used in Chapters 2 and 3.

Chapter 4

The Power System Stability including Effects of Actuators Dynamics

4.1 Introduction

The ideal CPL is used for the stability analysis in Chapter 2 and 3. This chapter takes into account the dynamics of controlled electromechanical actuators (EMAs) for an induction machine (IM) [82]. The effects of actuator dynamics have not been reported in previous publications in which the CPL is generally defined as an ideal current source without dynamic behaviour. This chapter also represents how to combine the dynamic of CPL into the power system with a diode rectifier or a PWM rectifier for stability studies using the dq modelling method with the eigenvalue theorem. The stability margins are assessed and compared against those for the power system with the ideal CPLs. The study is supported by intensive time domain simulations. This chapter also considers EMAs using a surface mount permanent magnet (SMPM) machine. As far as the mathematical formulation is concerned, the SMPM machine is considered a special case of the more general equation of the induction machine. The initial formulations were derived neglecting the internal resistance of the DC-link capacitor (r_c). This is a reasonable assumption for normal C_{dc} and r_c values. However, in experimental work it was found useful to put many capacitors in series (to obtain low values) and hence r_c is usually high. The power system with the PM machine and r_c will be described in Section 4.4. This system will be simulated in Chapter 5 and compared with experimental results.

4.2 Electromechanical Actuator Models

The aircraft EMA is represented as a standard motor drive vector-control structure [83] depicted in Figure 4.1, showing an IM drive. The IM drive can be replaced by a PM machine. The same control structure of Figure 4.1 can be used, but with I_{sd} generally set to zero for full flux operation. Detailed consideration can be found in the literature e.g. [84]. This section considers only those details that allow insight into EMA properties as a dynamic CPL.

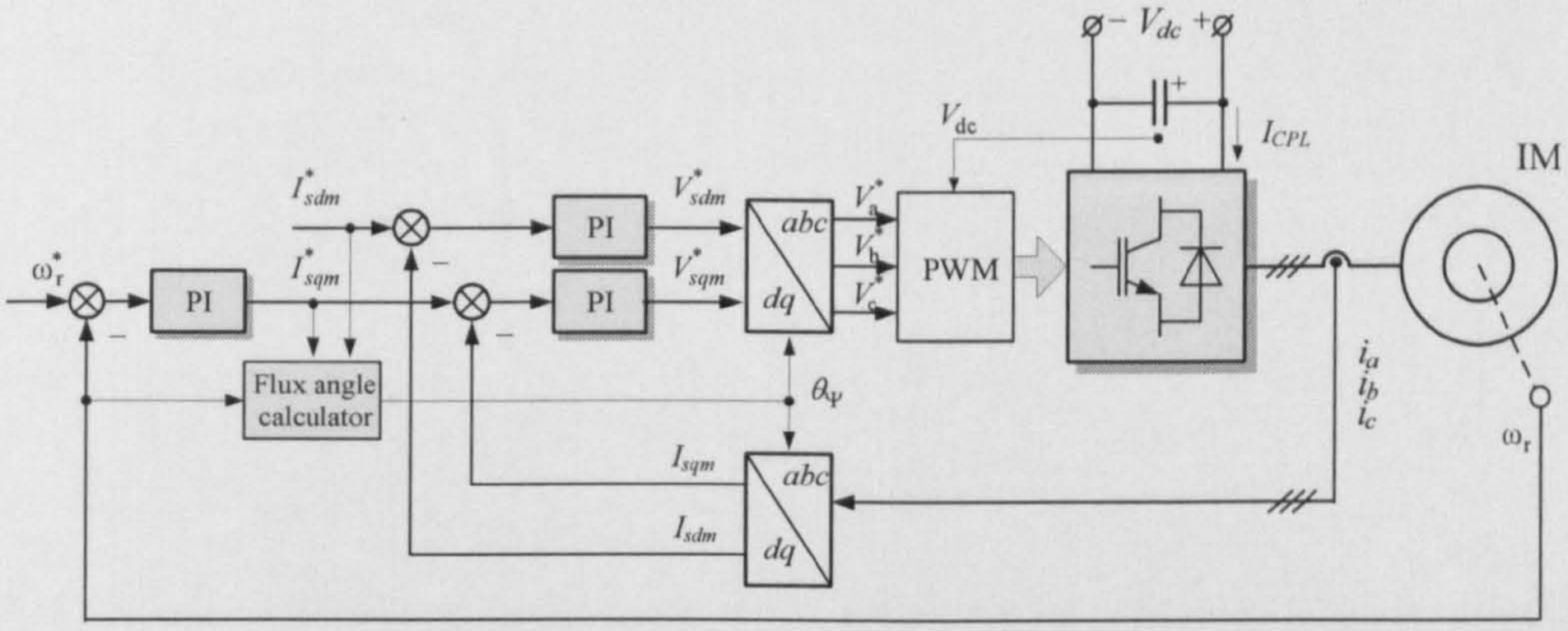

Figure 4.1: The standard motor drive control structure (induction motor)

The corresponding CPL model is developed below. The motor is vector-controlled in a rotating dq reference frame aligned with the rotor flux [83],[84]. The 3 phase to two phase transformation uses the peak convention (see Appendix A) that the vector quantity is equal to the peak of phase quantity [84]. Internal dq-axis current loops and an outer speed control loop are considered by assuming constant flux generation and perfect field orientation during EMA operation. This means that d-axis current dynamic can be neglected and only the q-axis current loop is analysed. The speed and q-current PI-controllers can be written:

$$k_{P\omega}k_{I\omega}^{-1}\dot{\omega}_r + k_{I\omega}^{-1}\dot{I}_{sqm}^* - k_{P\omega}k_{I\omega}^{-1}\dot{\omega}_r^* = -\omega_r + \omega_r^* \qquad (4\text{-}1)$$

$$k_{Pi}k_{Ii}^{-1}\dot{I}_{sqm} + k_{Ii}^{-1}\dot{V}_{sqm}^{*} - k_{Pi}k_{Ii}^{-1}\dot{I}_{sqm}^{*} = -I_{sqm} + I_{sqm}^{*} \tag{4-2}$$

where the symbols have their normal meanings and the q-axis reference voltage V^{*}_{sqm} is the controller output signal from which voltage V_{sqm} is derived from a PWM process. This process should be accurately derived in order to model the dynamic impact of DC-link voltage changes, especially on the DC-link current. The PWM process will measure the instantaneous DC-link voltage value V_{dc}, and the modulation indices for both d- and q-axes can be calculated using the filtered DC-link voltage V_f:

$$m_q = \frac{V_{sqm}^{*}}{V_f},\ m_d = \frac{V_{sdm}^{*}}{V_f} \tag{4-3}$$

$$\tau_f \dot{V}_f = -V_f + (V_{dc}/2) \tag{4-4}$$

where τ_f is a filtering time constant. Usually this filtering is ignored for studies in dynamical performance of actuators resulting in:

$$V_{sqm} = \frac{V_{sqm}^{*}}{V_{dc}/2} \cdot \frac{V_{dc}}{2} = V_{sqm}^{*} \tag{4-5}$$

However, as will be shown later in this chapter, this filtering takes a very important role in representing an actuator as a dynamic CPL for power system stability studies. Therefore, the inverter output voltages in this study are derived using the modulation index calculators as shown in the non-linear block structure of Figure 4.2 for the q-axis channel. The d-axis has the same structure as the q-axis.

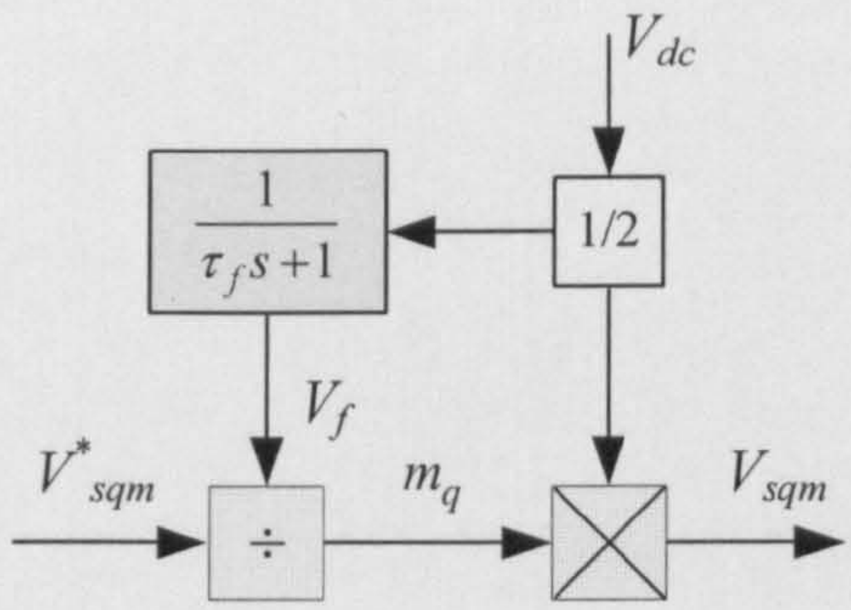

Figure 4.2: Modulation index calculator

The DC current drawn by the inverter (I_{CPL}), neglecting losses, can be found from energy conservation conditions and expressed in terms of the d- and q-axes currents as follows:

$$P_{dc} = \frac{3}{2} P_{dq}$$

$$V_{dc} I_{CPL} = \frac{3}{2}\left[V_{sdm} I_{sdm} + V_{sqm} I_{sqm}\right]$$

$$= \frac{3}{2}\left[\frac{m_d V_{dc}}{2} I_{sdm} + \frac{m_q V_{dc}}{2} I_{sqm}\right]$$

$$I_{CPL} = \frac{3}{2}\left[\frac{m_d I_{sdm}}{2} + \frac{m_q I_{sqm}}{2}\right] \qquad (4\text{-}6)$$

where m_q and m_d are calculated using the proposed modulation index calculator structure.

Equation (4-3) and (4-4) relate V_{dc} and V_{sqm}, while (4-6) relates I_{CPL} to I_{sqm}. To derive the relationship between V_{sqm} and I_{sqm}, it is necessary to consider the general stator voltage equations of the IM machine. In the dq frame travelling at an instantaneous speed ω_e relative to the fixed stator frame, these can be written [66],[83]:

$$V_{sqm} = R_{sm} I_{sqm} + \sigma L_{sm} \dot{I}_{sqm} + \omega_e \sigma L_{sm} I_{sdm} + \frac{L_m}{L_r} \dot{\psi}_{rq} + \omega_e \frac{L_m}{L_r} \psi_{rd} \qquad (4\text{-}7)$$

$$V_{sdm} = R_{sm} I_{sdm} + \sigma L_{sm} \dot{I}_{sdm} - \omega_e \sigma L_{sm} I_{sqm} + \frac{L_m}{L_r} \dot{\psi}_{rd} - \omega_e \frac{L_m}{L_r} \psi_{rq} \qquad (4\text{-}8)$$

where $\sigma = 1 - \dfrac{L_m^2}{L_{sm} L_r}$, and an instantaneous speed ω_e of the dq frame is given by:

$$\omega_e = \frac{P}{2} \omega_r + \omega_{sl} \qquad (4\text{-}9)$$

ω_r is the mechanical speed of the rotor, P is the number of poles, and the slip speed is

$$\omega_{sl} = \frac{I_{sqm}}{\tau_r I_{mrd}} \qquad (4\text{-}10)$$

where $\tau_r = L_r/R_r$, and I_{mrd} is called the equivalent magnetizing current.

The rotor flux is aligned with the d-axis. Hence, the rotor flux in the q-axis (ψ_{rq}) will be zero under field orientation. The field orientation equations can be written by taking (4-7), (4-8) and putting $\psi_{rq} = 0$:

$$V_{sqm} = R_{sm} I_{sqm} + \sigma L_{sm} \dot{I}_{sqm} + \omega_e \sigma L_{sm} I_{sdm} + \omega_e \frac{L_m}{L_r} \psi_{rd} \qquad (4\text{-}11)$$

$$V_{sdm} = R_{sm} I_{sdm} + \sigma L_{sm} \dot{I}_{sdm} - \omega_e \sigma L_{sm} I_{sqm} + \frac{L_m}{L_r} \dot{\psi}_{rd} \qquad (4\text{-}12)$$

Letting $\psi_{rd} = L_m I_{mrd}$ and assuming that the rotor flux is constant, the actual value of the rotor flux is given by:

$$\psi_{rd} = L_m I_{sdm} \tag{4-13}$$

where $I_{mrd} = I_{sdm}$ in steady state for constant flux generation.

Applying (4-13) into (4-11) and (4-12), the stator equations become

$$V_{sqm} = R_{sm} I_{sqm} + \sigma L_{sm} \dot{I}_{sqm} + \omega_e \sigma L_{sm} I_{sdm} + \omega_e \frac{L_m^2}{L_r} I_{sdm} \tag{4-14}$$

$$V_{sdm} = R_{sm} I_{sdm} + \sigma L_{sm} \dot{I}_{sdm} - \omega_e \sigma L_{sm} I_{sqm} + \frac{L_m^2}{L_r} \dot{I}_{sdm} \tag{4-15}$$

For constant flux generation and perfect field orientation, the d-axis current dynamic can be neglected. Therefore, (4-15) becomes:

$$V_{sdm} = R_{sm} I_{sdm} - \omega_e \sigma L_{sm} I_{sqm} \tag{4-16}$$

Substituting (4-9) into (4-14), and noting that $K_f = \sigma L_{sm} I_{sdm} + \frac{L_m^2 I_{sdm}}{L_r}$, $\sigma = 1 - \frac{L_m^2}{L_{sm} L_r}$, and $\tau_s = \frac{\sigma L_{sm}}{R_{sm}}$ yields:

$$\tau_s R_{sm} \dot{I}_{sqm} = \left(-\frac{P}{2} K_f\right) \omega_r - \left(R_{sm} + \frac{K_f}{\tau_r I_{sdm}}\right) I_{sqm} + V_{sqm} \tag{4-17}$$

The V_{sqm} in (4-17), here is the inverter output voltage. This value can be calculated from Figure 4.2.

Substituting (4-9) into (4-16), the d-axis stator equation becomes

$$V_{sdm} = R_{sm} I_{sdm} - \left(\frac{P}{2} \omega_r + \frac{I_{sqm}}{\tau_r I_{sdm}} \right) \sigma L_{sm} I_{sqm} \qquad (4\text{-}18)$$

If the dynamic of the I_{sdm}-control loop is ignored (i.e. $I_{sdm}=I^*_{sdm}$) due to constant flux operation, equation (4-18) may be regarded as the simplified field current loop equation. This is given by:

$$V^*_{sdm} = R_{sm} I^*_{sdm} - \left(\frac{P}{2} \omega_r + \frac{I_{sqm}}{\tau_r I^*_{sdm}} \right) \sigma L_{sm} I_{sqm} \qquad (4\text{-}19)$$

where V^*_{sdm} is the d-axis reference voltage for a PWM process.

Under the field orientation control, I_{sdm} is only responsible for generating the rotor flux. The q-axis current I_{sqm} creates an electrical torque resulting in the motor motion according to the mechanical motion equation:

$$J_m \dot{\omega}_r = K_T I_{sqm} - T_L \qquad (4\text{-}20)$$

where J_m is an inertia, T_L – load torque, and $K_T = \left(\frac{3}{2}\right)\left(\frac{P}{2}\right)\frac{L_m^2}{L_r} I_{sdm}$.

Summarizing (4-1)-(4-20), the non-linear model of the controlled induction motor drive can be depicted in the form of the control block-diagram as shown in Figure 4.3 [82]. Note that the model in Figure 4.3 is capable of representing the DC-link current transients with changes in supply voltage, whilst this dynamic is lost if voltage filtering for PWM production is not included. This can be confirmed by simulation. The step response to a negative change in V_{dc} is simulated using three different motor drive models. The first model is the SABER benchmark model of the system as shown in Figure 4.1 (see

Appendix D.4). The second model is the dq model derived from the EMA model of Figure 4.3 with the DC-link voltage filter. The last one is the dq model without the DC-link voltage filter. The simulation results for the three different models are depicted in Figure 4.4. It can be seen that the dynamic response disappears for the dq model without the DC-link voltage filter. According to this result, the filter takes a very important role in representing an actuator as a non-ideal CPL for power system stability studies.

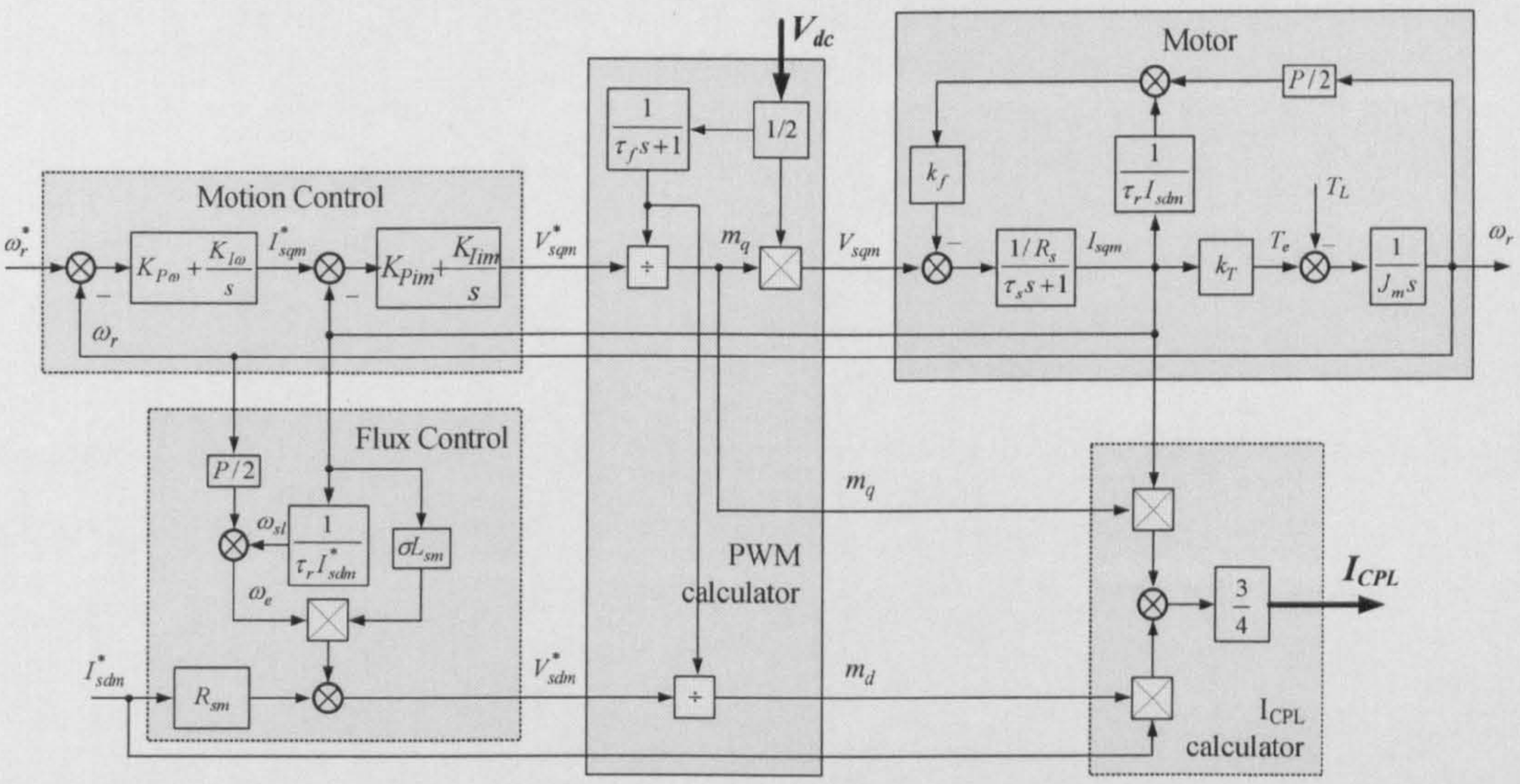

Figure 4.3: Block diagram of the non-linear EMA model

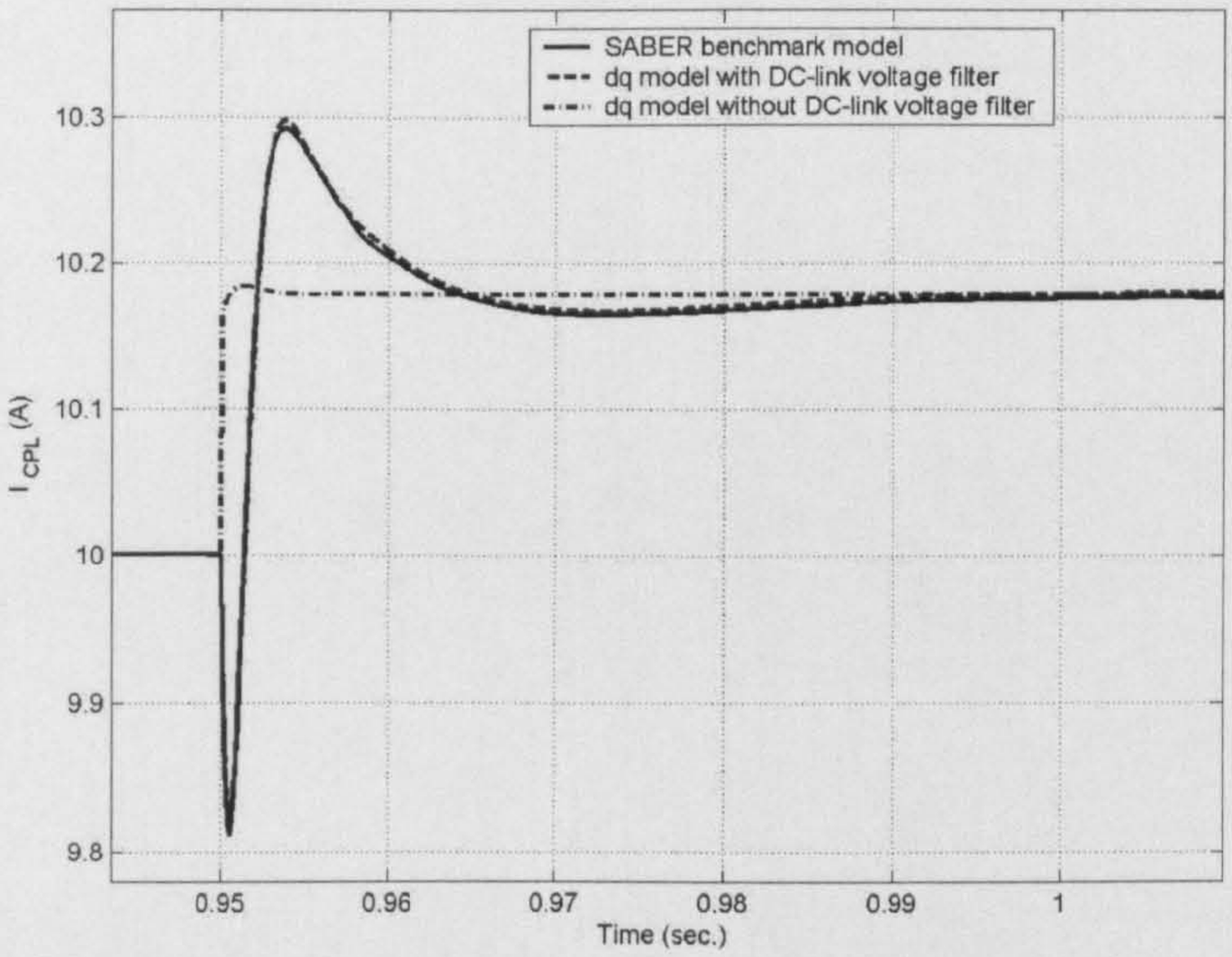

Figure 4.4: The DC-link current (I_{CPL}) when step change of the DC-link voltage occurs

Generally, the load torque T_L of an actuator drive system for an aircraft application depends on the aerodynamic characteristic as shown in Figure 4.5. However, in this research, a step changing in T_L is used for stability studies.

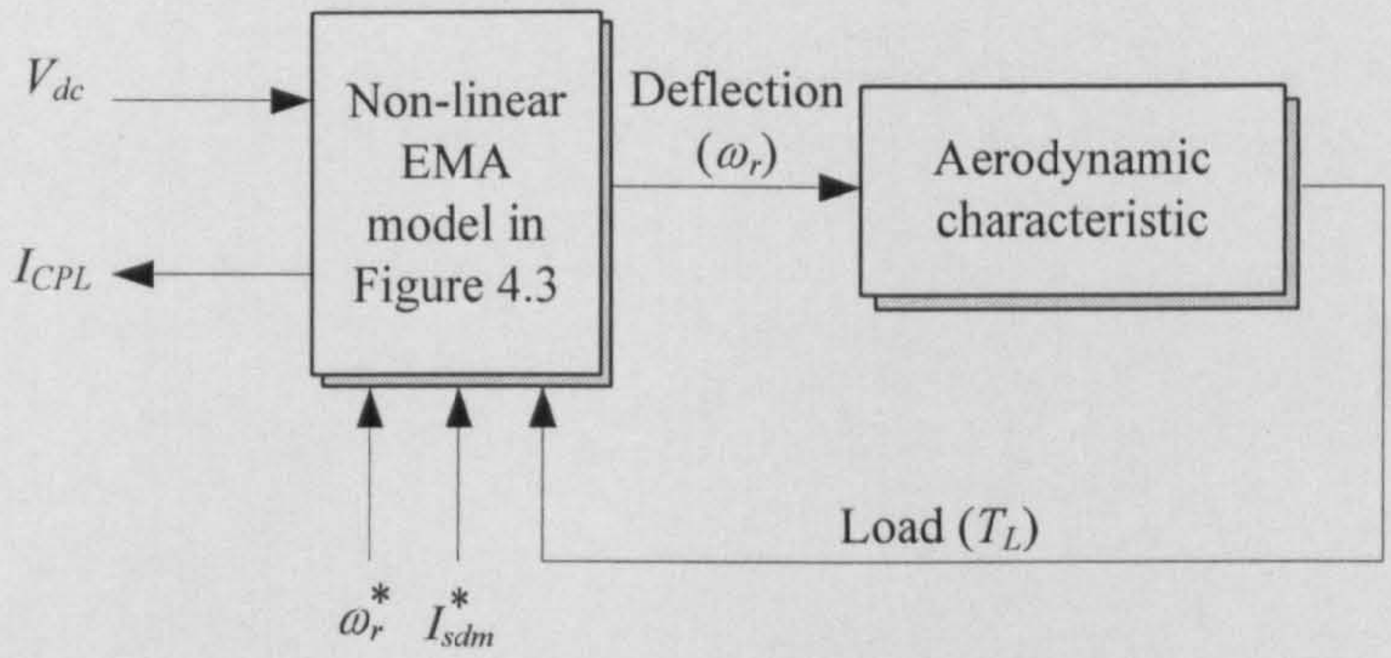

Figure 4.5: The actuator drive model for aircraft power systems

4.3 The Power System with a Diode Rectifier

Generally, the ideal CPL without dynamic behaviour has been used for previous stability analysis of power electronic based systems [13],[18],[20],[37]-[44]. This section describes the model taking into account

the dynamics of the controlled electromechanical actuators (EMAs) with the six-pulse diode rectifier as depicted in Figure 4.6. The dq modelling approach with the eigenvalue theorem is used for stability study. The advantages of this method were mentioned in Chapter 2.

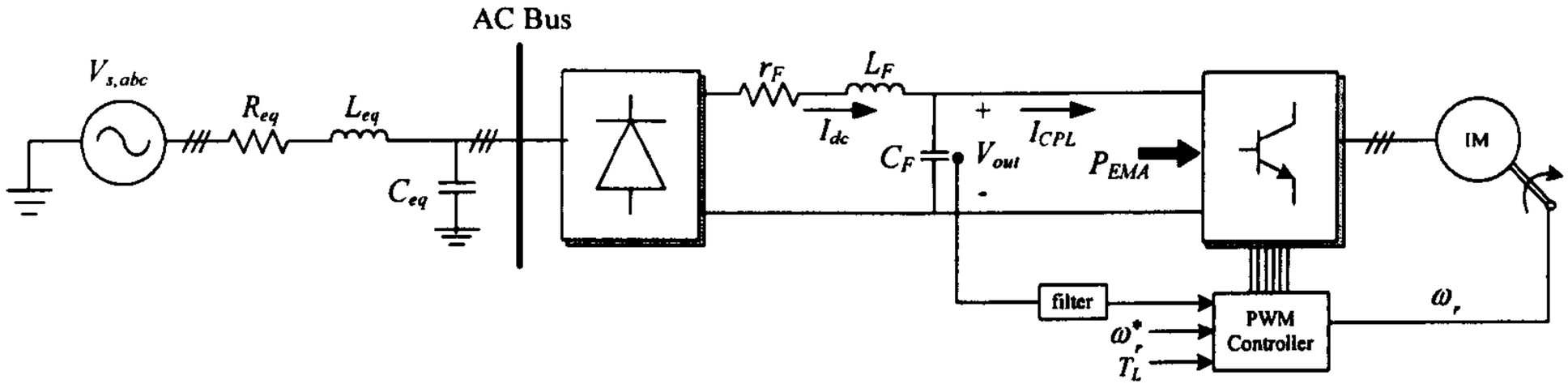

Figure 4.6: Power system with dynamic of CPL

4.3.1 Power System Definition

The power system for this section is depicted in Figure 4.6. It represents the elements of an aircraft AC frequency-wild power system architecture including a three-phase balanced source, transmission line, and uncontrolled rectifier feeding the EMA behaving as a non-ideal CPL through a DC-link filter. Note that P_{EMA} is the power delivered to the non-ideal CPL.

As explained in Chapter 7, other loads can be connected to the AC bus. However, in this chapter only one CPL is considered.

As described in Chapter 2, the cable and diode rectifier can be transformed into the dq-frame by using the dq modelling approach. As a result, the dq frame equivalent circuit of the power system of Figure 4.6 is shown in Figure 4.7 where the diode rectifier is modelled as a transformer and the EMA model of Figure 4.3 represents the dynamic of the CPL. It can be seen that the dynamic of the CPL is used in stead of an ideal CPL.

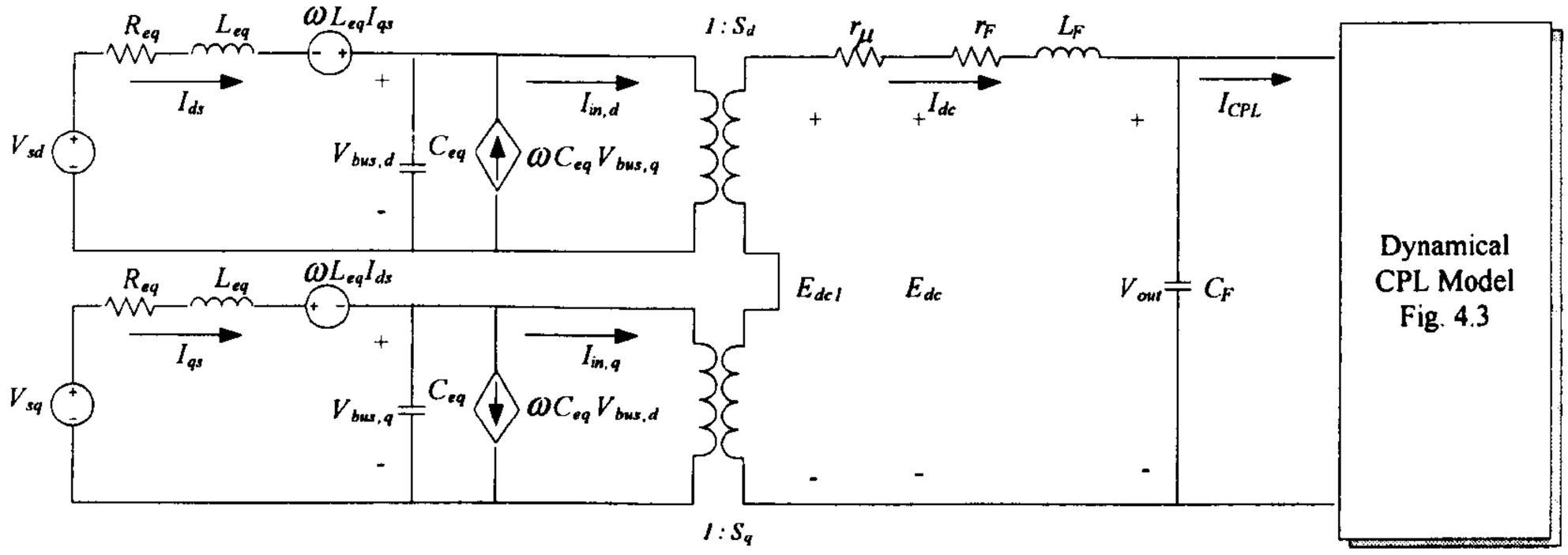

Figure 4.7: The power system of Figure 4.6 in dq-frame

4.3.2 Deriving the Non-Linear Dynamic Model and Linearized Model

Applying KVL and KCL to the equivalent circuit in Figure 4.7 determines the set of nonlinear differential equations. Setting:

$$\text{State variables: } x =< I_{ds}, I_{qs}, V_{bus,d}, V_{bus,q}, I_{dc}, V_{out}, \omega_r, I_{sqm}, V_f, V_{sqm}^*, I_{sqm}^* >$$

$$\text{Input: } u =< V_m, \omega_r^*, T_L > \qquad (4\text{-}21)$$

$$\text{Output: } y =< V_{out} >$$

The nonlinear differential equations representing the dynamic behavior of the cable section with the rectifier and DC-filter is the 6^{th} order nonlinear system:

$$
\begin{aligned}
\dot{I}_{ds} &= -\frac{R_{eq}}{L_{eq}} I_{ds} + \omega I_{qs} - \frac{1}{L_{eq}} V_{bus,d} + \frac{1}{L_{eq}} V_{sd} \\
\dot{I}_{qs} &= -\omega I_{ds} - \frac{R_{eq}}{L_{eq}} I_{qs} - \frac{1}{L_{eq}} V_{bus,q} + \frac{1}{L_{eq}} V_{sq} \\
\dot{V}_{bus,d} &= \frac{1}{C_{eq}} I_{ds} + \omega V_{bus,q} - \sqrt{\frac{3}{2}} \frac{2\sqrt{3}}{\pi C_{eq}} I_{dc} \\
\dot{V}_{bus,q} &= -\omega V_{bus,d} + \frac{1}{C_{eq}} I_{qs} \\
\dot{I}_{dc} &= \sqrt{\frac{3}{2}} \frac{2\sqrt{3}}{\pi L_F} V_{bus,d} - \left(\frac{r_F}{L_F} + \frac{r_\mu}{L_F} \right) I_{dc} - \frac{1}{L_F} V_{out} \\
\dot{V}_{out} &= \frac{1}{C_F} I_{dc} - \frac{1}{C_F} I_{CPL}
\end{aligned}
\tag{4-22}
$$

In (4-22), the rectifier switching functions, S_d and S_q of (2-8) are used. The rotating frame is placed at the rectifier input terminal. The remaining equations describing the dynamics of the CPL of Figure 4.3 are summarized as:

$$
\begin{aligned}
J_m \dot{\omega}_r &= K_T I_{sqm} - T_L \\
\tau_s R_{sm} \dot{I}_{sqm} &= -\frac{P K_f \omega_r}{2} - \left(R_{sm} + \frac{K_f}{\tau_r I_{sdm}} \right) I_{sqm} + \frac{V^*_{sqm} V_{out}}{2 V_f} \\
\tau_f \dot{V}_f &= -V_f + \frac{V_{out}}{2} \\
\frac{K_{Pim}}{K_{Iim}} \dot{I}_{sqm} + \frac{\dot{V}^*_{sqm}}{K_{Iim}} - \frac{K_{Pim} \dot{I}^*_{sqm}}{K_{Iim}} &= -I_{sqm} + I^*_{sqm} \\
\frac{K_{P\omega}}{K_{I\omega}} \dot{\omega}_r + \frac{\dot{I}^*_{sqm}}{K_{I\omega}} - \frac{K_{P\omega} \dot{\omega}^*_r}{K_{I\omega}} &= -\omega_r + \omega^*_r
\end{aligned}
\tag{4-23}
$$

Note that V_{out} in (4-23) has the same meaning as V_{dc} in Figure 4.3.

Equation (4-23) is used with the CPL current equation (4-6) (assuming I_{sdm}^{*} equal to constant) to give:

$$I_{CPL} = \frac{3}{4}\left[\frac{R_{sm}(I_{sdm}^{*})^2}{V_f} - \frac{[(P/2)\omega_r \sigma L_{sm} I_{sdm}^{*} - V_{sqm}^{*}]I_{sqm}}{V_f} - \frac{\sigma L_{sm} I_{sqm}^2}{\tau_r V_f}\right] \quad (4\text{-}24)$$

The set of equations (4-22)-(4-24) describes the nonlinear dynamic of the power system of Figure 4.6 and can be used for fast computation of transient responses for different operation scenarios. For stability analysis, the equations can be linearized for small signal perturbations. The set of equation (4-22)-(4-24) is linearized using a Taylor series expansion with subsequent neglect of high-order components. The linearized model takes the following matrix form:

$$\delta \dot{\mathbf{x}} = \mathbf{A}(\mathbf{x_o}, \mathbf{u_o})\delta\mathbf{x} + \mathbf{B}(\mathbf{x_o}, \mathbf{u_o})\delta\mathbf{u} \quad (4\text{-}25)$$

$$\delta\mathbf{y} = \mathbf{C}(\mathbf{x_o}, \mathbf{u_o})\delta\mathbf{x} + \mathbf{D}(\mathbf{x_o}, \mathbf{u_o})\delta\mathbf{u}$$

where

$$\delta x = [\delta I_{ds}, \delta I_{qs}, \delta V_{bus,d}, \delta V_{bus,q}, \delta I_{dc}, \delta V_{out}, \delta\omega_r, \delta I_{sqm}, \delta V_f, \delta V_{sqm}^{*}, \delta I_{sqm}^{*}]^T$$

$$\delta u = [\delta V_m, \delta\omega_r^{*}, \delta T_L]^T$$

$$\delta y = [\delta V_{out}]$$

The constant matrix $\mathbf{A}(\mathbf{x_o}, \mathbf{u_o})$, $\mathbf{B}(\mathbf{x_o}, \mathbf{u_o})$, $\mathbf{C}(\mathbf{x_o}, \mathbf{u_o})$, and $\mathbf{D}(\mathbf{x_o}, \mathbf{u_o})$ depend on the chosen equilibrium point. The details of these matrixes are given in (4-26). When analysing the dynamic properties of the system in different operational regimes, the linearization is undertaken for each of them. In this research, the power flow equation is employed to determine the steady state value at the AC side for each operating point using a Newton-Raphson numerical method. This will be explained in Section 4.3.3.

$$\mathbf{A}(\mathbf{x_o},\mathbf{u_o}) = \begin{bmatrix} \mathbf{A_D} & \mathbf{A_{Hm}} \\ \mathbf{A_{Vm}} & \mathbf{A_m} \end{bmatrix}_{11\times 11}$$

$$\mathbf{B}(\mathbf{x_o},\mathbf{u_o}) = \begin{bmatrix} \sqrt{\frac{3}{2}}\frac{\cos(\lambda_o)}{L_{eq}} & 0 & 0 \\ \sqrt{\frac{3}{2}}\frac{\sin(\lambda_o)}{L_{eq}} & 0 & 0 \\ 0 & 0 & 0 \\ 0 & 0 & 0 \\ 0 & 0 & 0 \\ 0 & 0 & 0 \\ 0 & 0 & -\frac{1}{J_m} \\ 0 & 0 & 0 \\ 0 & 0 & 0 \\ 0 & K_{Pim}K_{I\omega} & \frac{K_{Pim}K_{P\omega}}{J_m} \\ 0 & K_{I\omega} & \frac{K_{P\omega}}{J_m} \end{bmatrix}_{11\times 3}$$

$$\mathbf{C}(\mathbf{x_o},\mathbf{u_o}) = \begin{bmatrix} 0 & 0 & 0 & 0 & 0 & 1 & 0 & 0 & 0 & 0 & 0 \end{bmatrix}_{1\times 11}$$

$$\mathbf{D}(\mathbf{x_o},\mathbf{u_o}) = \begin{bmatrix} 0 & 0 & 0 \end{bmatrix}_{1\times 3} \qquad (4\text{-}26)$$

where

$$\mathbf{A_D} = \begin{bmatrix} -\frac{R_{eq}}{L_{eq}} & \omega & -\frac{1}{L_{eq}} & 0 & 0 & 0 \\ -\omega & -\frac{R_{eq}}{L_{eq}} & 0 & -\frac{1}{L_{eq}} & 0 & 0 \\ \frac{1}{C_{eq}} & 0 & 0 & \omega & -\sqrt{\frac{3}{2}}\cdot\frac{2\sqrt{3}}{\pi C_{eq}} & 0 \\ 0 & \frac{1}{C_{eq}} & -\omega & 0 & 0 & 0 \\ 0 & 0 & \sqrt{\frac{3}{2}}\cdot\frac{2\sqrt{3}}{\pi L_F} & 0 & -\left(\frac{r_F}{L_F}+\frac{r_\mu}{L_F}\right) & -\frac{1}{L_F} \\ 0 & 0 & 0 & 0 & \frac{1}{C_F} & 0 \end{bmatrix}_{6\times 6}$$

$$\mathbf{A_{Hm}} = \begin{bmatrix} 0 & 0 & 0 & 0 & 0 \\ 0 & 0 & 0 & 0 & 0 \\ 0 & 0 & 0 & 0 & 0 \\ 0 & 0 & 0 & 0 & 0 \\ 0 & 0 & 0 & 0 & 0 \\ \frac{3P\sigma L_{sm} I_{sqmo} I_{sdmo}}{8C_F V_{f,o}} & -\frac{3M_{qo}}{4C_F} + \frac{3\sigma L_{sm} I_{sqmo}}{4\tau_r C_F V_{f,o}} + \frac{3I_{sdmo}\sigma L_{sm}\omega_{eo}}{4C_F V_{f,o}} & \frac{3I_{sdmo}V_{sdmo}}{4C_F V_{f,o}^2} + \frac{3I_{sqmo}V_{sqmo}}{4C_F V_{f,o}^2} & -\frac{3I_{sqmo}}{4C_F V_{f,o}} & 0 \end{bmatrix}_{6\times 5}$$

$$\mathbf{A_{Vm}} = \begin{bmatrix} 0 & 0 & 0 & 0 & 0 & 0 \\ 0 & 0 & 0 & 0 & 0 & \frac{M_{qo}}{2\tau_s R_{sm}} \\ 0 & 0 & 0 & 0 & 0 & \frac{1}{2\tau_F} \\ 0 & 0 & 0 & 0 & 0 & -\frac{K_{Pim} M_{qo}}{2\tau_s R_{sm}} \\ 0 & 0 & 0 & 0 & 0 & 0 \end{bmatrix}_{5\times 6}$$

$$\mathbf{A_m} = \begin{bmatrix} 0 & \frac{K_T}{J_m} & 0 & 0 & 0 \\ -\frac{PK_f}{2\tau_s R_{sm}} & -\frac{1}{\tau_s} - \frac{K_f}{\tau_s R_{sm}\tau_r I_{sdmo}} & -\frac{V_{sqmo}}{\tau_s R_{sm} V_{f,o}} & \frac{1}{\tau_s R_{sm}} & 0 \\ 0 & 0 & -\frac{1}{\tau_F} & 0 & 0 \\ -K_{Pim}K_{I\omega} + \frac{PK_{Pim}K_f}{2\tau_s R_{sm}} & -K_{Iim} - \frac{K_{Pim}K_{P\omega}K_T}{J_m} + \frac{K_{Pim}}{\tau_s} + \frac{K_{Pim}K_f}{\tau_s R_{sm}\tau_r I_{sdmo}} & \frac{K_{Pim}V_{sqmo}}{\tau_s R_{sm} V_{f,o}} & -\frac{K_{Pim}}{\tau_s R_{sm}} & K_{Iim} \\ -K_{I\omega} & -\frac{K_{P\omega}K_T}{J_m} & 0 & 0 & 0 \end{bmatrix}_{5\times 5}$$

4.3.3 Calculating the Steady-State Equilibrium Value

According to (4-26), the linearized model needs to define V_{fo}, λ_o, I_{sqmo}, ω_{eo}, V_{sdmo}, V_{sqmo}, M_{do}, *and* M_{qo} for small-signal simulation and stability analysis.

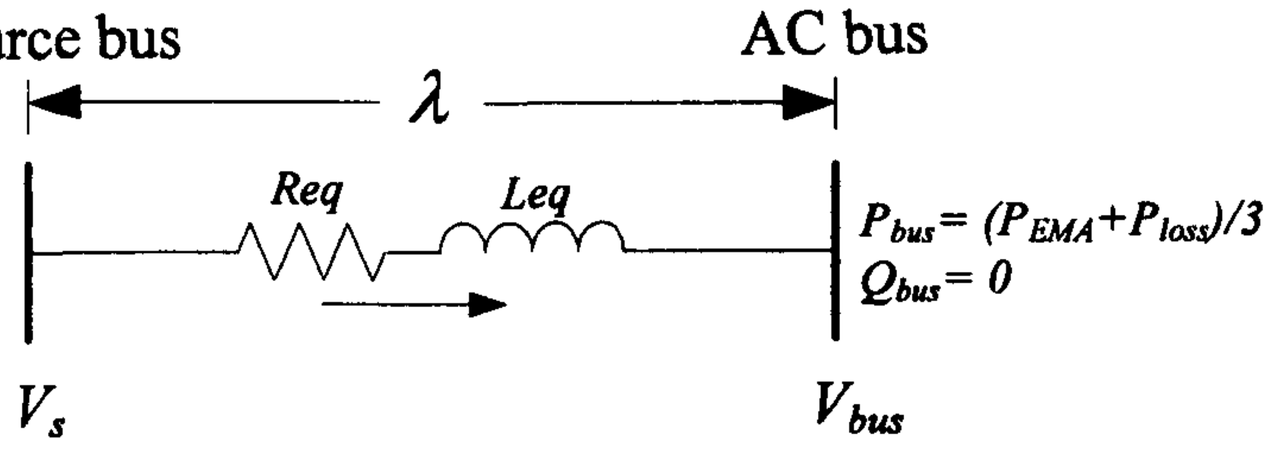

Figure 4.8: The single line diagram for power calculations

The power flow equation [72] can again be applied to determine the steady-state values on the AC side. The single line power flow diagram of the power system of Figure 4.6 is depicted in Figure 4.8 in which the line capacitors are ignored, assuming C_{eq} is very small. Note that Figure 4.8 is the same as that of Figure 2.9. Therefore, $V_{out,o}$ and λ_o can be calculated by solving (2-14), (2-15), and (2-16) using a Newton Raphson routine. However, the dynamic of the CPL is considered instead of the ideal one and P_{CPL} in (2-15) is changed to P_{EMA} as defined by:

$$P_{EMA} = \frac{3}{2}\left(V_{sdmo}I_{sdmo} + V_{sqmo}I_{sqmo}\right) \tag{4-27}$$

I_{sdmo} can be defined from the rated flux of machine, while V_{sqmo}, V_{sdmo}, and I_{sqmo} can be defined by setting (4-17) and (4-20) equal to zero and taking the steady state condition to (4-19). The equations for calculating the steady-state values become:

$$V_{sqmo} = R_{sm}I_{sqmo} + \omega_{eo}\sigma L_{sm}I_{sdmo} + \frac{L_m^2}{L_r}\omega_{eo}I_{sdmo} \tag{4-28}$$

$$V_{sdmo} = R_{sm}I_{sdmo} - \omega_{eo}\sigma L_{sm}I_{sqmo} \tag{4-29}$$

$$I_{sqmo} = \frac{4L_rT_{Lo}}{3PL_m^2I_{sdmo}} \tag{4-30}$$

where $\omega_{eo} = \frac{P}{2}\omega_{ro} + \frac{I_{sqmo}}{\tau_r I_{sdmo}}$

For calculating V_{fo}, one can set (4-4) equal to zero to give:

$$V_{fo} = \frac{V_{out,o}}{2} \tag{4-31}$$

For calculating M_{dqo}, taking the steady state condition to (4-3) yields:

$$M_{do} = \frac{V_{sdmo}}{V_{fo}}, M_{qo} = \frac{V_{sqmo}}{V_{fo}} \tag{4-32}$$

$V_{out,o}$ in (4-31) can be obtained from the power flow equation. It can be seen from (4-27)-(4-32) that the steady-state values depend on the operating point defined from ω_{ro} and T_{Lo}. Therefore, we can get different linearized models of the system in Figure 4.6. For the CPLs, the operating point will include the actuator load speed and load torque.

4.3.4 Small-Signal Simulation and Stability Analysis

The linearized model (4-25) was simulated for small-signal transients against a corresponding 3-phase benchmark circuit model simulated in SABER. The details of SABER model for the system in Figure 4.6 are given in Appendix D.5. The example system parameters are given in Table 4.1. The transmission line and DC-link filter parameters in Table 4.1 are the same value as one in Table 2.1. For example, Figure 4.9 shows the DC-link voltage V_{out} response of the system of Figure 4.6 to a step change of T_L from 80 to 90 Nm at t=0.8 s. with constant speed 975 rpm. Similarly, Figure 4.10 shows the response to a step change of T_L from 200 to 210 Nm at a constant speed 975 rpm. An excellent agreement between both models is achieved under small-signal simulation. The frequency of the ripple DC-link voltage in the Benchmark model is six times the AC system frequency due to the six-pulse diode rectifier.

Table 4.1: The set of parameters for the example system of Figure 4.6

Parameter	Value	Description
V_s	230 $V_{rms/phase}$	phase source voltage
ω	$2\pi \times 400$ rad/s	source frequency
R_{eq}	0.1 Ω	transmission line resistance
L_{eq}	24 μH	transmission line inductance
C_{eq}	2 nF	transmission line capacitance
r_F	0.01 Ω	dc link inductor resistance
L_F	2 mH	dc link inductance
C_F	500 μF	dc link capacitance
Actuator drive 20 kW rated		
ω_r^*	975 rpm	speed reference
$T_{L,rated}$	190 Nm	rated load torque
R_{sm}	0.6 Ω	stator resistance
L_{sm}	30.39 mH	stator leakage inductance
R_r	0.159 Ω	rotor resistance
L_r	30.39 mH	rotor leakage inductance
L_m	29.03 mH	magnetizing inductance
P	6 poles	number of poles in the machine
J_m	0.281 kgm^2	moment of inertia
I_{sdm}	34.115 A	d-axis current for rated flux
τ_F	0.02 sec.	filtering time constant
$\omega_{n,\ speed}$	20 Hz ($K_{P\omega}$=13.27, $K_{I\omega}$=1042.33)	natural frequency of speed loop
$\omega_{n,\ current}$	200 Hz (K_{Pi}=4.75, K_{Ii}=4199.14)	natural frequency of current loop

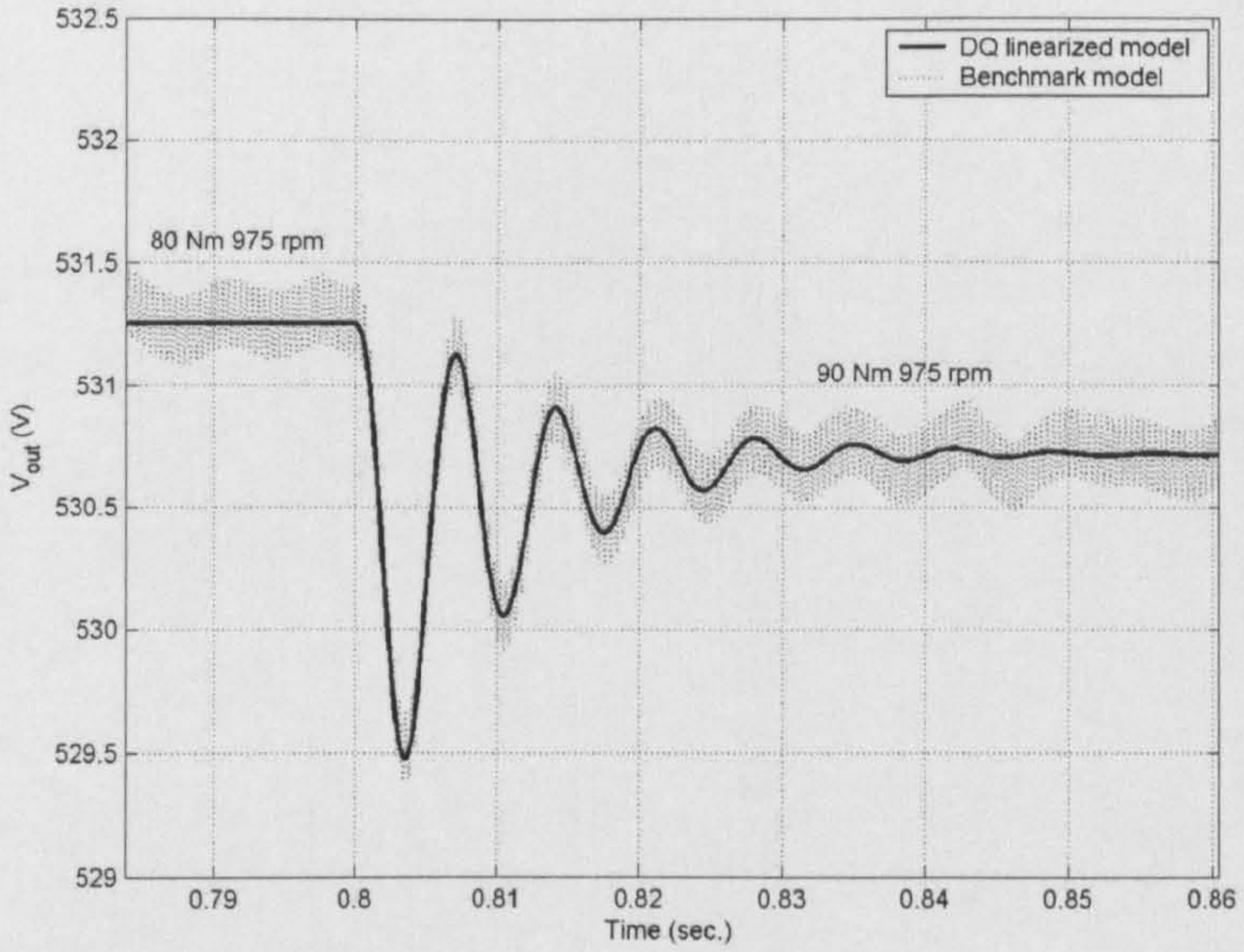

Figure 4.9: Response of V_{out} to a step change of T_L from 80 to 90 Nm in comparison of SABER benchmark model with dq linearized model

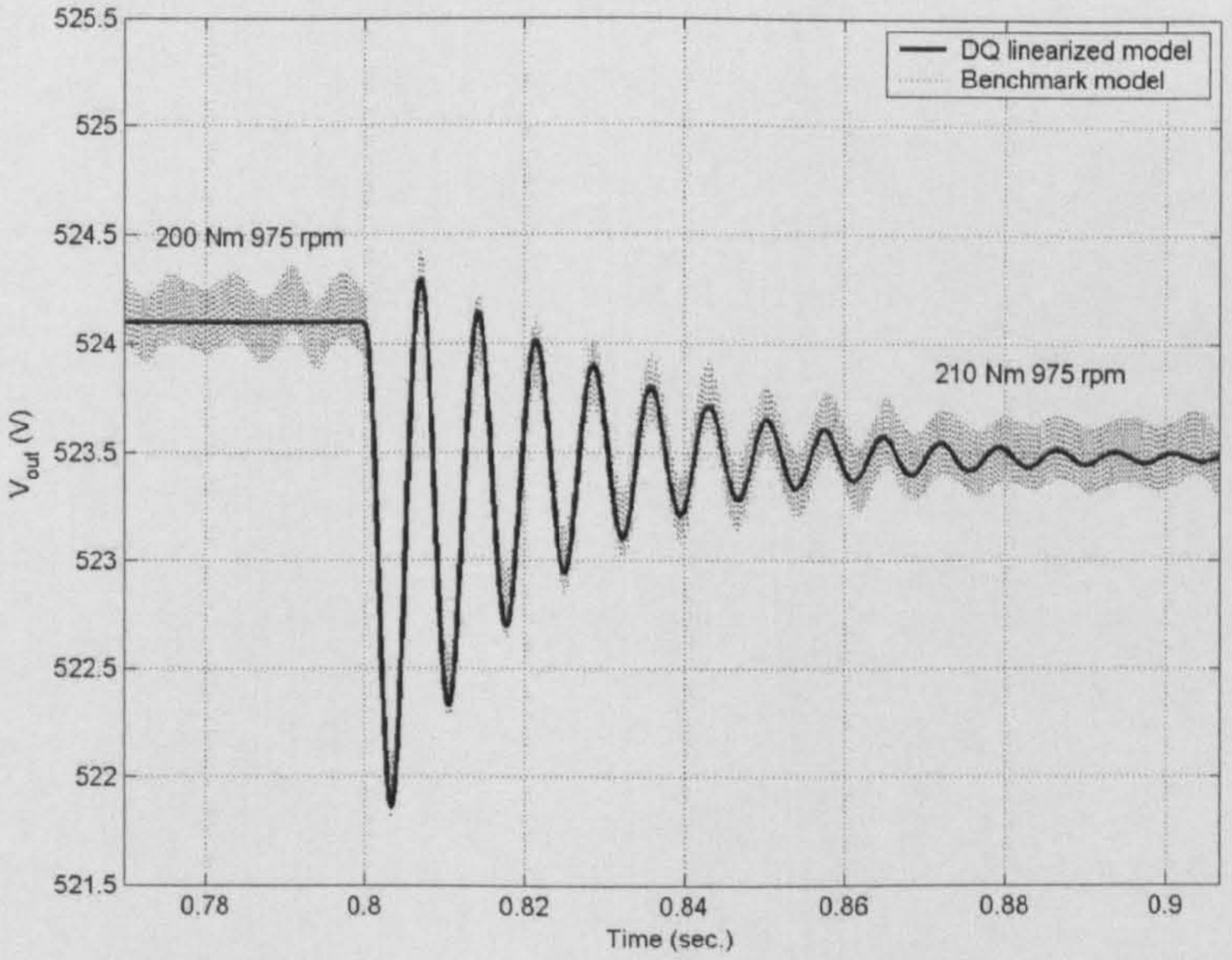

Figure 4.10: Response of V_{out} to a step change of T_L from 200 to 210 Nm in comparison of SABER benchmark model with dq linearized model

For the stability analysis, the linearized model is used with the eigenvalue theorem. The eigenvalues can be calculated from the Jacobian matrix

$\mathbf{A}(\mathbf{x_0}, \mathbf{u_0})$ in (4-26). The eigenvalues for the power system with parameters in Table 4.1 were analyzed for the case when the load torque varies from 0 to 400 Nm at the constant actuator speed reference 975 rpm. This corresponds to the steady-state value of P_{EMA} varying from 1.047 kW to 51.76 kW (~ 2.6 P_{rated}). This root locus is shown in Figure 4.11 and some eigenvalues cross into the right hand plane. Figure 4.12 shows the zoomed area of interest: as one can see, the system becomes unstable when the P_{EMAo} exceeds 36.53 kW for the studied case.

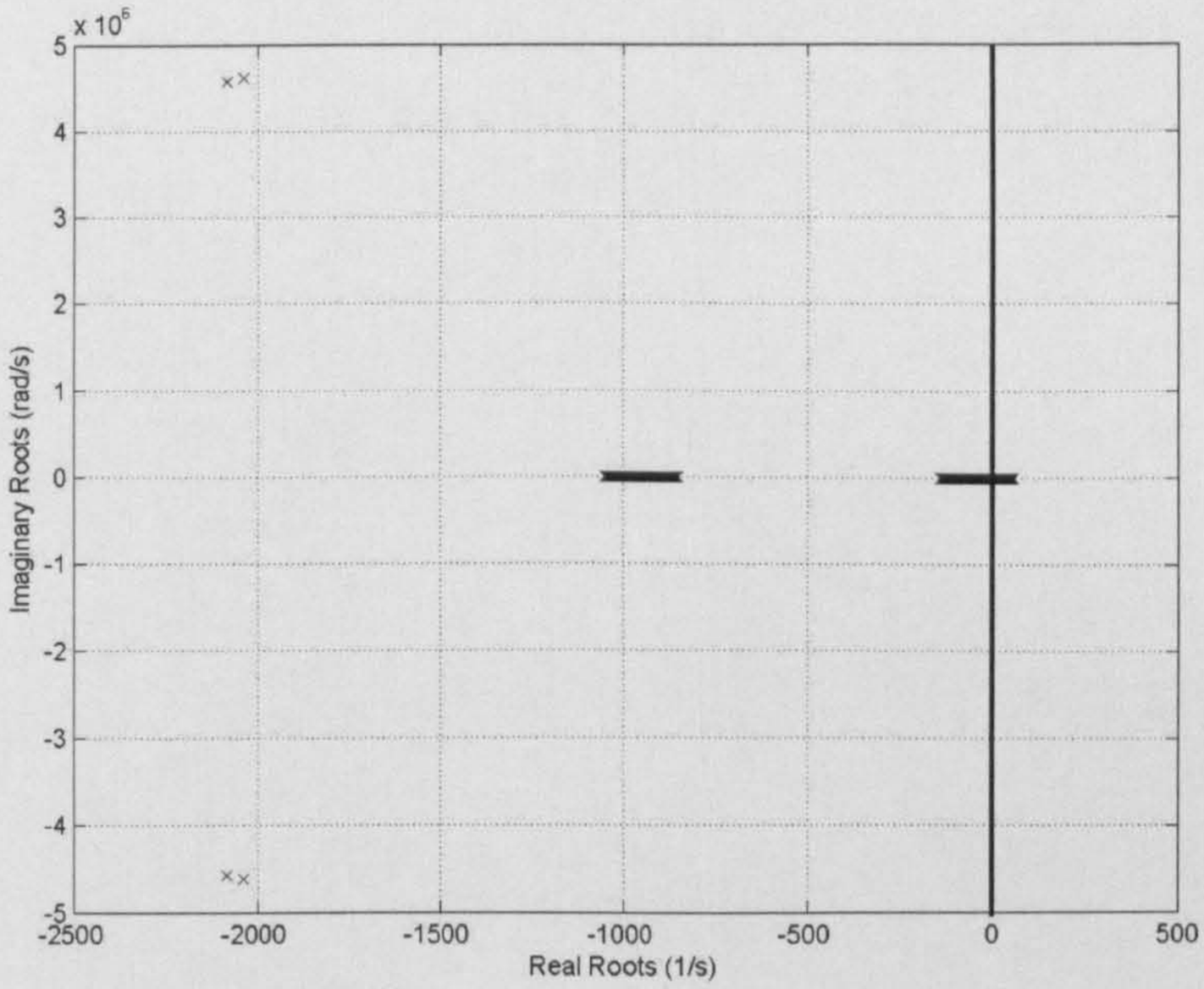

Figure 4.11: Eigenvalue plot for varying P_{EMA}

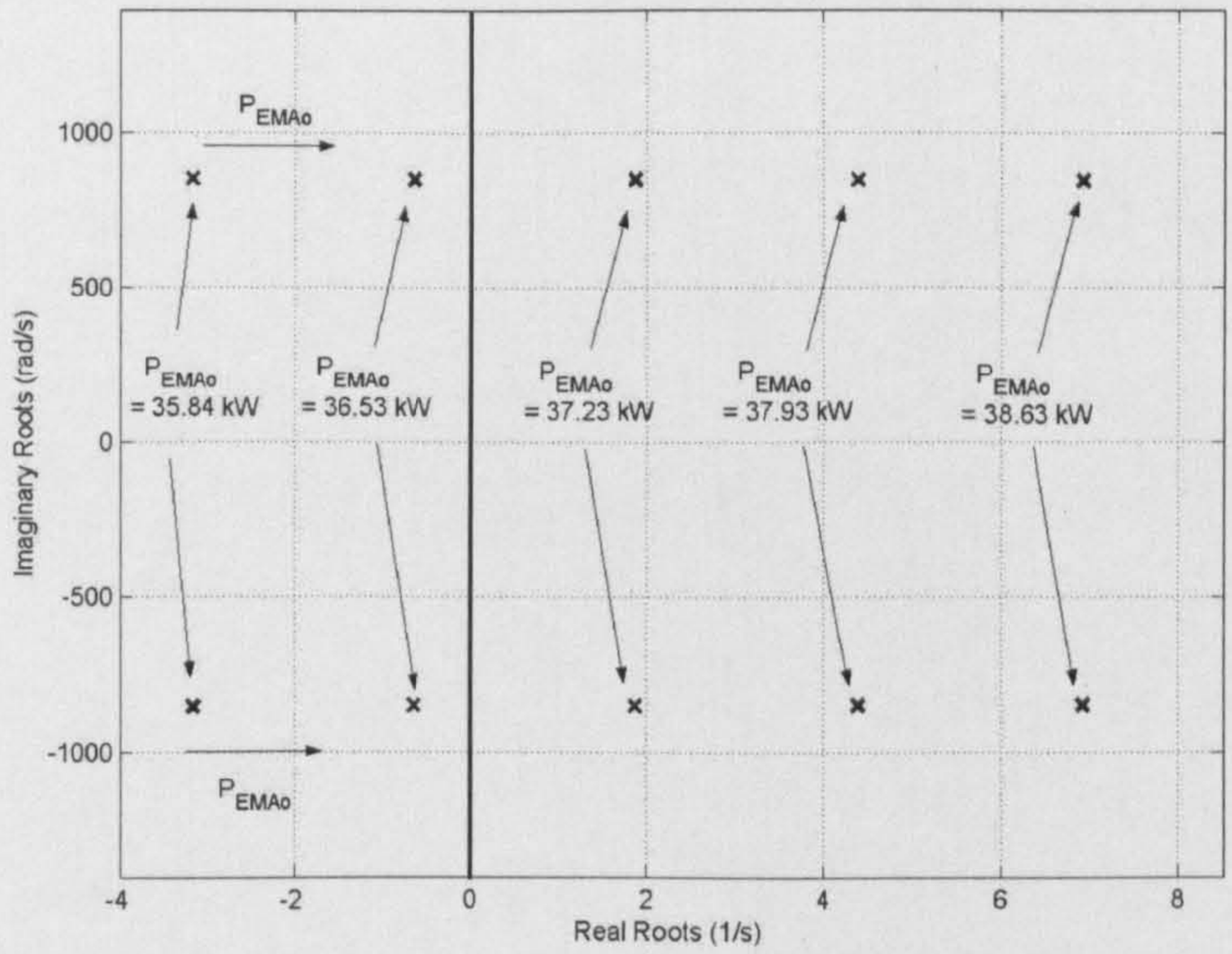

Figure 4.12: Zoomed area of interest from Figure 4.11

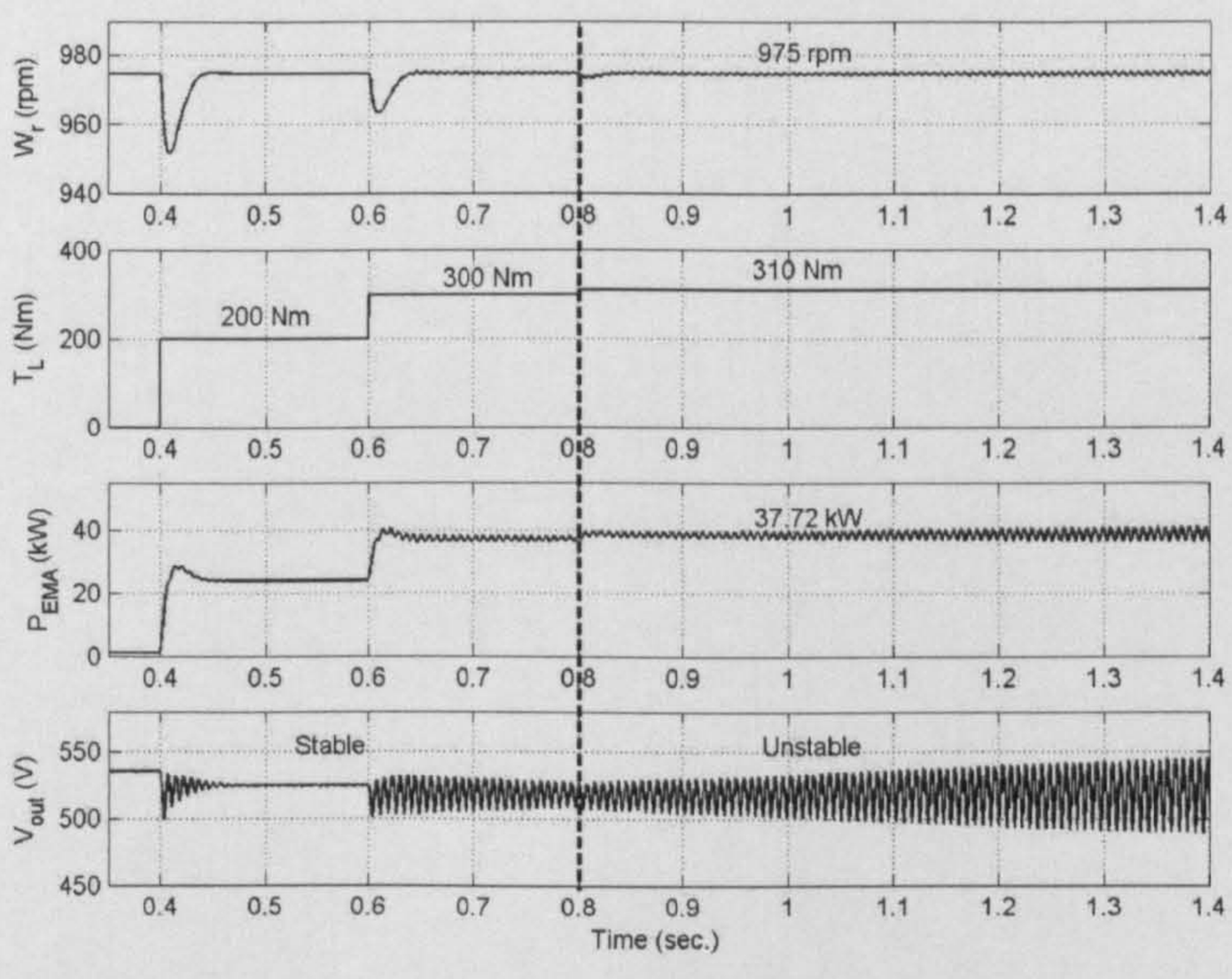

Figure 4.13: Step response for operating point (P_{EMA}) variations

Figure 4.13 shows the SABER time-domain benchmark simulations that confirm the theoretical result with the instability occurring at P_{EMA} of 37.72 kW (~1.89 P_{rated}). This is greater than the 36.53 kW for the unstable condition.

4.3.5 Comparison of Stability Results for Ideal and Non-Ideal CPLs

According to Chapter 2, the power system with parameters in Table 2.1 with an ideal CPL became unstable when P_{CPL} exceeded 17 kW. The root locus for the dominant eigenvalues, comparing the system with ideal and non-ideal CPLs, is shown in Figure 4.14. It can be seen that the impact of the non-ideal CPL is substantial. As a result, the power system becomes unstable when the P_{EMA} exceeds 36.53 kW. This value is much greater than 17 kW for the system with the ideal CPL. Therefore, neglecting CPL dynamics may be beneficial from the viewpoint of power system availability, but may result in very non-optimal design solutions that would impact on overall mass and dimension. These CPL dynamic effects depend on the system parameters such as filtering time constant (τ_F), and the natural frequency of the speed loop ($\omega_{n,speed}$). Hence, the parameter variations in different operational regimes are very interesting. These will be explained in Section 4.3.6.

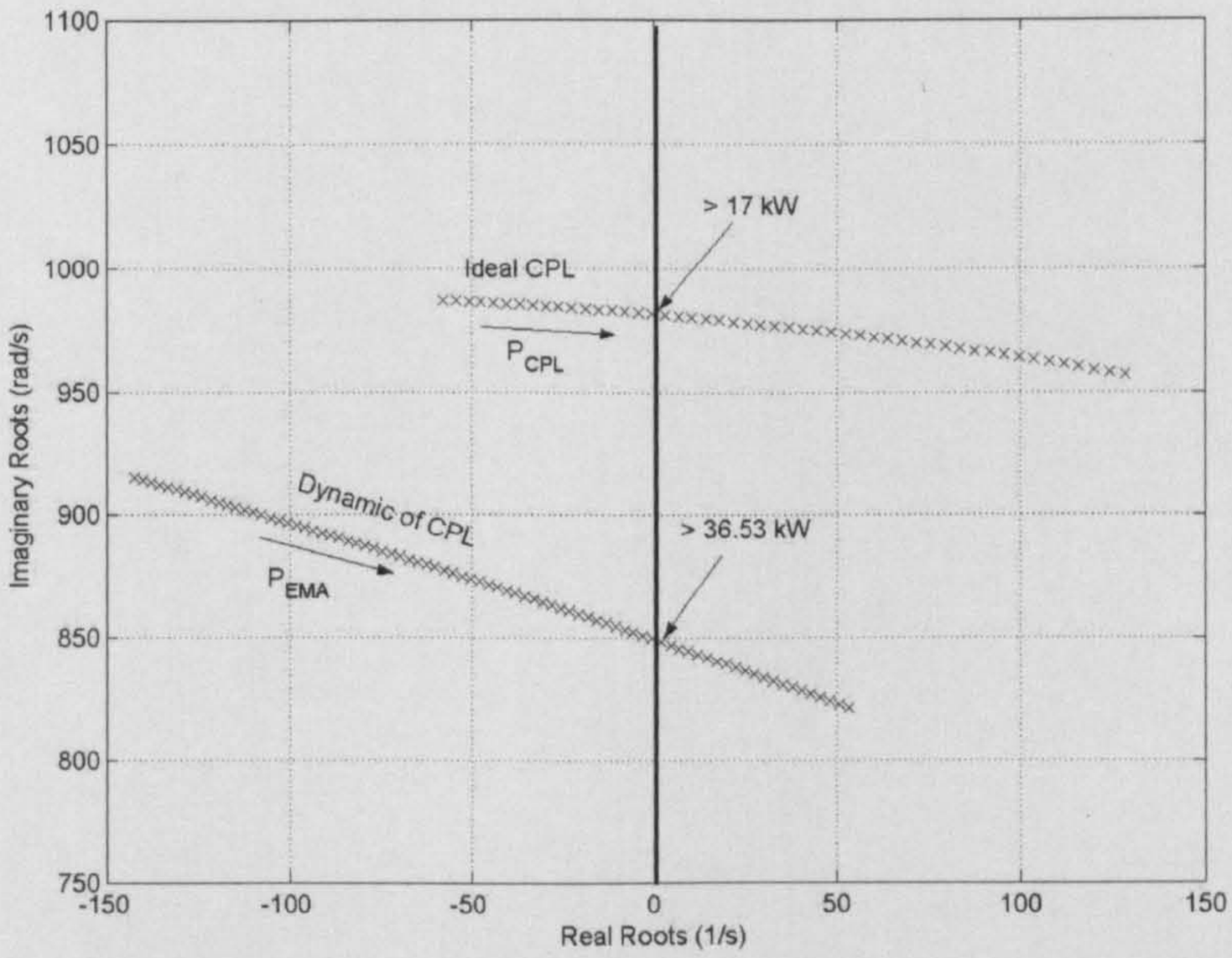

Figure 4.14: Eigenvalues comparison between ideal and non-ideal CPLs

4.3.6 Investigating Stability due to Variations in System Parameters

In this section, the dynamic model is used to predict instability for variations in system parameters. As shown in Figure 4.14, the CPL dynamic can expand the stability margin. However, the dynamic CPL effects depend on the EMA parameters such as filtering time constant (τ_F), and natural frequency of the speed loop ($\omega_{n,speed}$). Therefore, it is very interesting to study the variations in these parameters on stability. For frequency and DC-link filter L_F and C_F variations, the results are the same as that in Chapter 2 in which higher system frequency, smaller L_F, and higher C_F all increase the power level at which instability occurs.

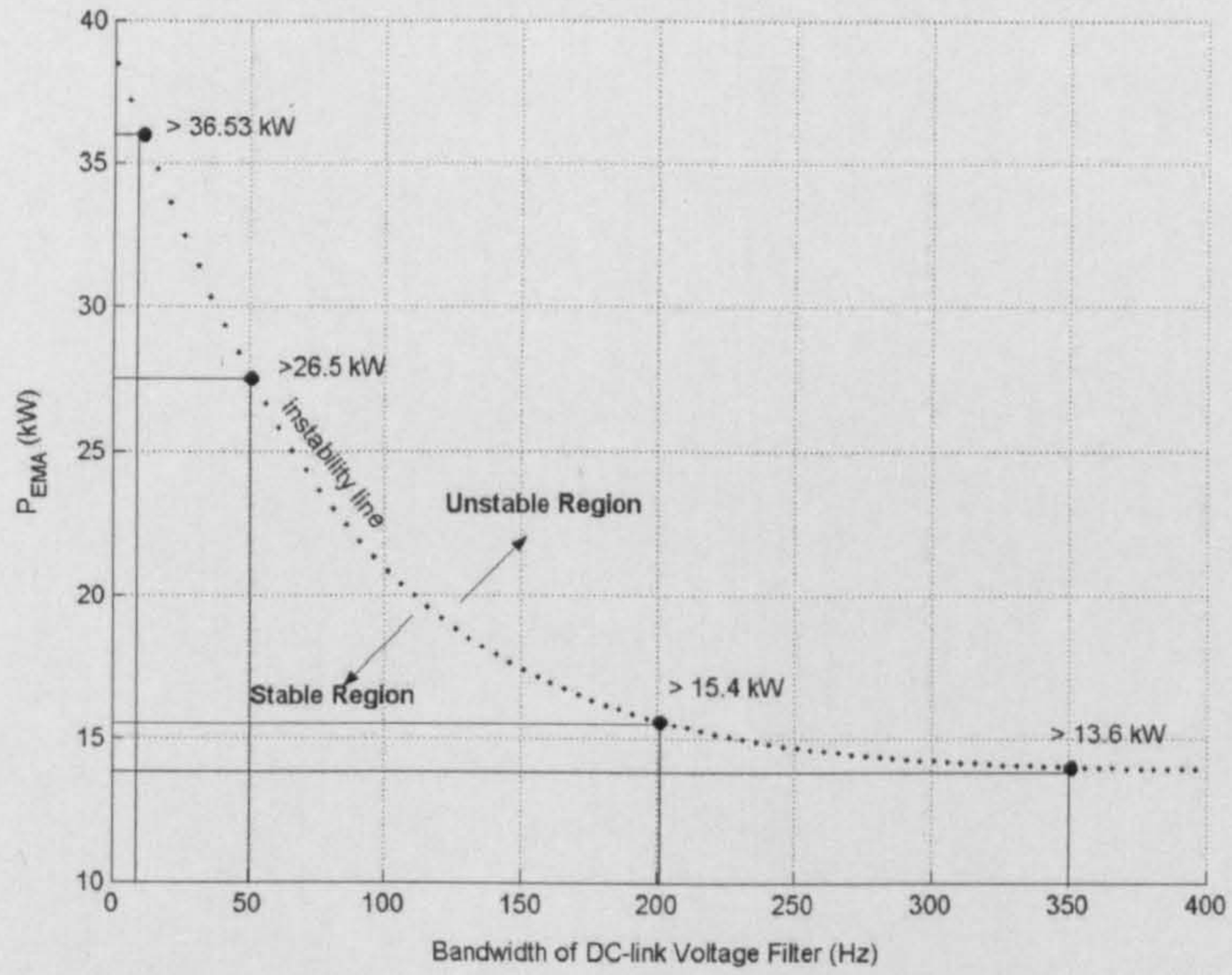

Figure 4.15: Instability power for bandwidth of DC-link voltage filter variations

Figure 4.15 shows the power stability thresholds as the bandwidth of DC-link voltage filter ($f_{cut\text{-}off}$) in (4-4) is varied and others parameters are fixed given in Table 4.1. The relationship between time constant (τ_F) and $f_{cut\text{-}off}$ is given by:

$$\tau_F = \frac{1}{2\pi f_{cut-off}} \tag{4-33}$$

As one can see, reducing the bandwidth of DC-link voltage filter has a significant effect on stability. This would appear to be cheap and effective way of increasing stability margin. In contrast, increasing the bandwidth of DC-link filter can also degrade the system stability. The higher bandwidth can make the system less stable compare to the ideal CPL. This trend is difficult to explain in terms of physical meaning. However, the results in Figure 4.15 show that one can find the way to increase the system stability margin by the appropriate voltage filter bandwidth, depending on the system parameters and on its system operational points. Again, the analytical results of Figure 4.15 are supported by SABER benchmark simulation (see Appendix D.5) shown in Figure 4.16. The top graph shows the changing in P_{EMA}, and the graphs below show the V_{out} responses for different bandwidths of DC-link voltage filter. Good agreement between both models is achieved.

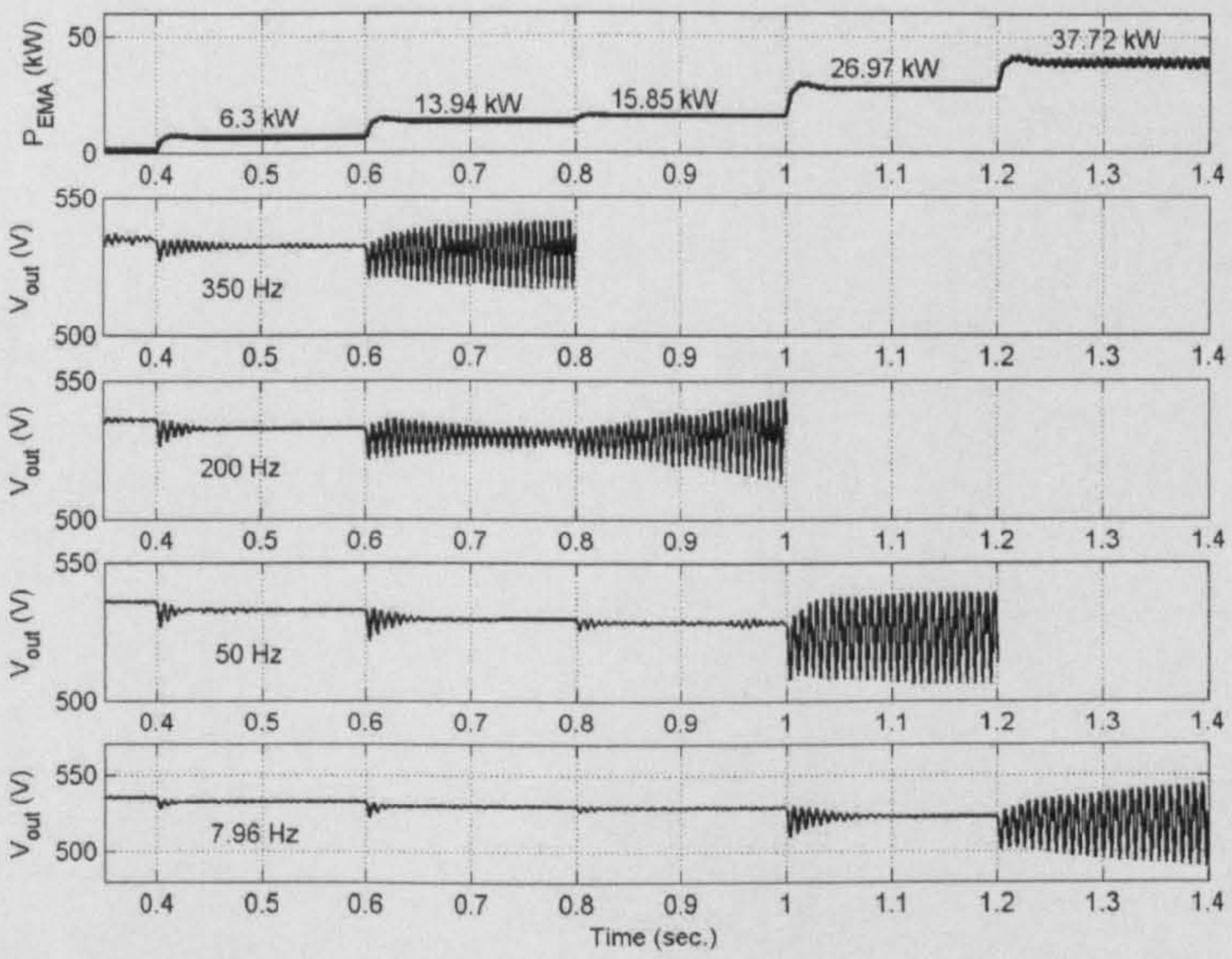

Figure 4.16: Verification of analytical results for DC-link filter variations

Internal CPL dynamics in the form of speed control response is investigated in Figure 4.17. The speed loop PI controller is designed for various natural frequencies with constant damping. Figure 4.17 shows the stable and unstable region for variations in natural frequency of the speed loop with other parameters fixed as given in Table 4.1. In this Figure, the bold points are for the natural frequencies of 10, 20, 30, and 40 Hz. The analytical results of Figure 4.17 are also compared to SABER benchmark simulation as shown in Figure 4.18. The top graph shows the changing P_{EMA}, and the graphs below show the V_{out} responses for different natural frequencies of the speed loop. The proposed model can predict the instability point with high accuracy.

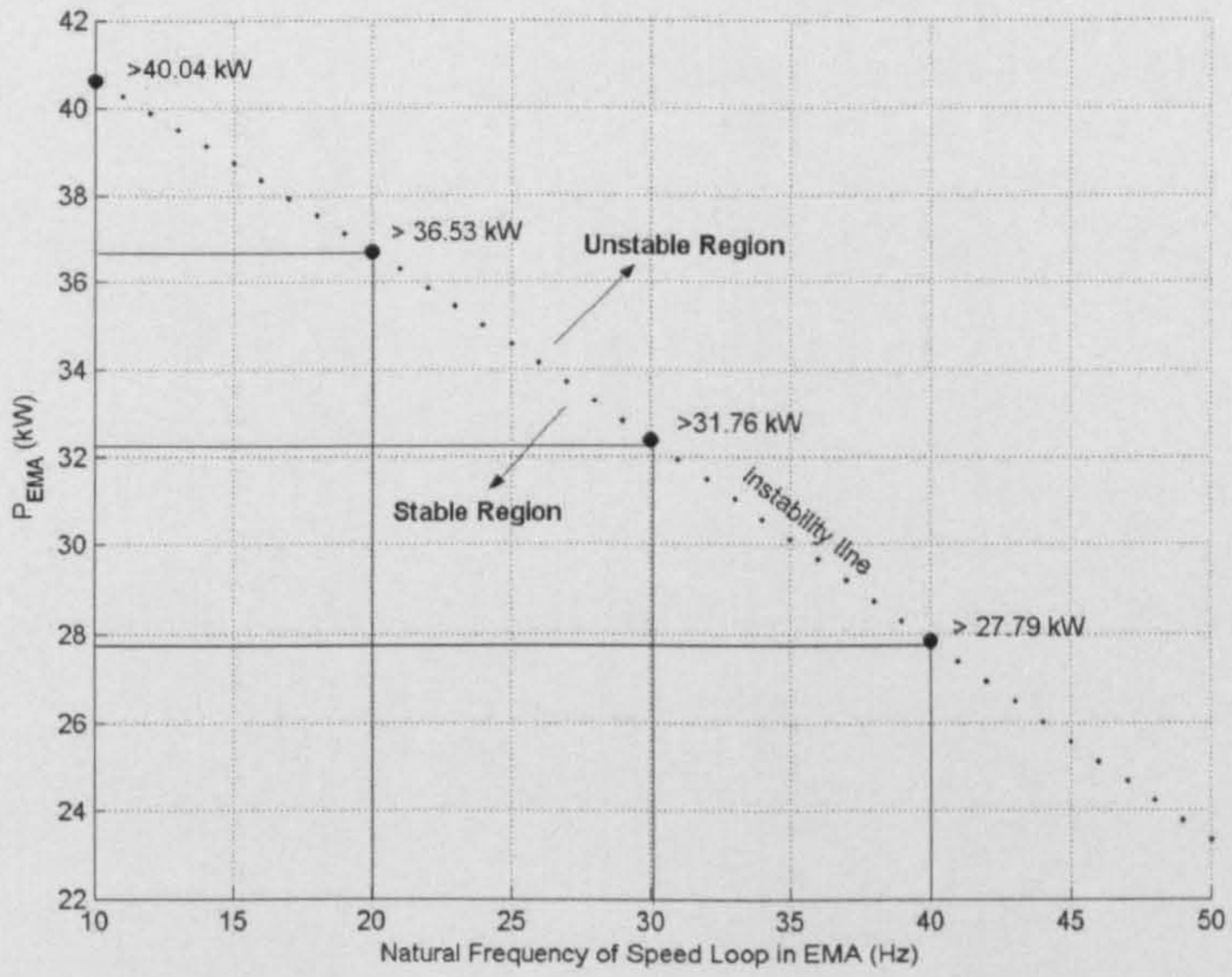

Figure 4.17: Instability power for natural frequency of speed loop variations

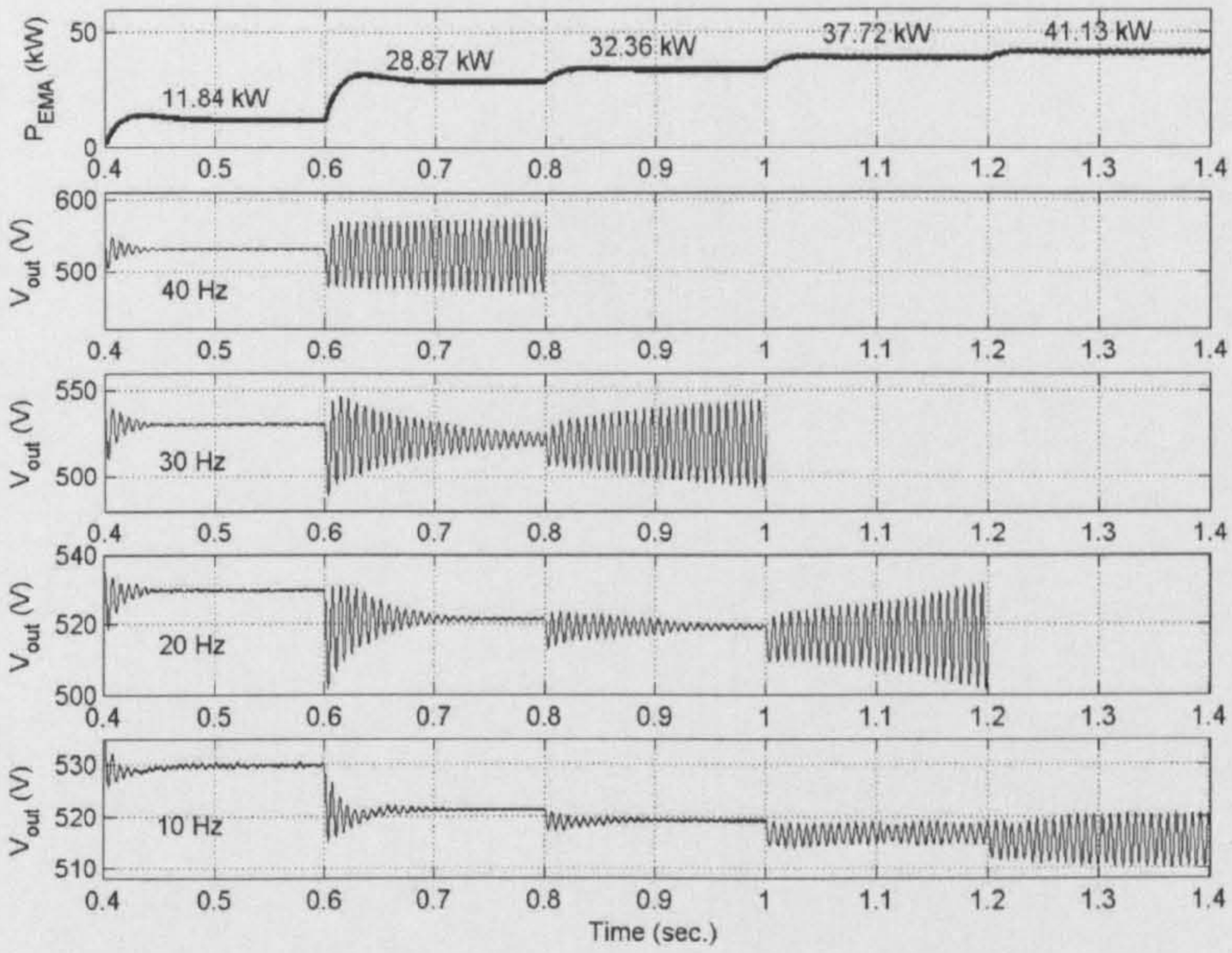

Figure 4.18: Verification of analytical results for speed loop natural frequency variations

It can be seen that the higher the EMA natural frequency of the speed loop control, the lower the power level at which instability occurs. The variation is fairly sensitive to the speed loop response rate.

The effect of dynamic CPL for the power system with a controlled PWM rectifier can be analysed by using (4-23) and (4-24) with (3-9) in Chapter 3. However, from the results of Chapter 3, the power system with a controlled PWM rectifier provides good stability. The system becomes unstable at higher power levels that are much higher than the rated power of the system. Therefore, the details of dynamic CPL with the power system including a controlled PWM rectifier are not shown here, but will be considered in Chapter 7 in which it is shown that it influences the stability results for the whole aircraft power system.

4.4 System with a Permanent Magnet Machine and an internal resistance of DC-Link Capacitor

In this section, the derived non-linear dynamic model and linearized model of the system with the PM machine (Section 4.4.1) including the internal resistance of DC-link capacitor (Section 4.4.2) is illustrated. The dynamic model from this section will be used in Chapter 5 with the experimental results.

4.4.1 Electromechanical Actuator Models for PM Machine

The PM or IM machine can be used to represent the dynamic of a CPL with the same essential structure. For the PM machine, the same control structure as shown in Figure 4.1 can be used, but with I_{sdm} generally set to zero for full flux operation. For this case, (4-6) becomes:

$$I_{CPL} = \frac{3}{2}\left[\frac{m_q I_{sqm}}{2}\right] \tag{4-33}$$

For PM machine, (4-7) and (4-8) are modified. To derive the relationship between V_{sqm} and I_{sqm} for PM machine, it is necessary to consider the general stator voltage equations of the PM machine. In the dq frame travelling at an instantaneous speed ω_e relative to the fixed stator frame, these can be written [83]:

$$V_{sqm} = R_{sm} I_{sqm} + \psi_{sq} + \omega_e \psi_{sd} \tag{4-34}$$

$$V_{sdm} = R_{sm} I_{sdm} + \dot{\psi}_{sd} - \omega_e \psi_{sq} \tag{4-35}$$

where the stator flux linkages on q- and d- axis are:

$$\psi_{sq} = L_q I_{sqm} \tag{4-36}$$

$$\psi_{sd} = L_d I_{sdm} + F_m \tag{4-37}$$

where F_m in (4-37) is the flux of PM machine linking the d-axis stator winding.

For the PM machine, I_{sdm} generally set to zero for full flux operation and substituting (4-36) and (4-37) into (4-34) and (4-35), the stator voltage equations become:

$$V_{sqm} = R_{sm} I_{sqm} + L_q \dot{I}_{sqm} + \omega_e F_m \tag{4-38}$$

$$V_{sdm} = -\omega_e L_q I_{sqm} \tag{4-39}$$

and the instantaneous speed ω_e of the dq frame for PM machine is given by setting ω_{sl} in (4-9) equal to zero:

$$\omega_e = \frac{P}{2}\omega_r \tag{4-40}$$

The mechanical motion equation of PM machine is the same as that of (4-20), but the K_T for PM machine is given by:

$$K_{T,PM} = \frac{3}{2}\frac{P}{2}F_m \tag{4-41}$$

Summarizing (4-33)-(4-41), the non-linear model of the controlled PM motor drive can be depicted in the form of the control block-diagram as shown in Figure 4.19.

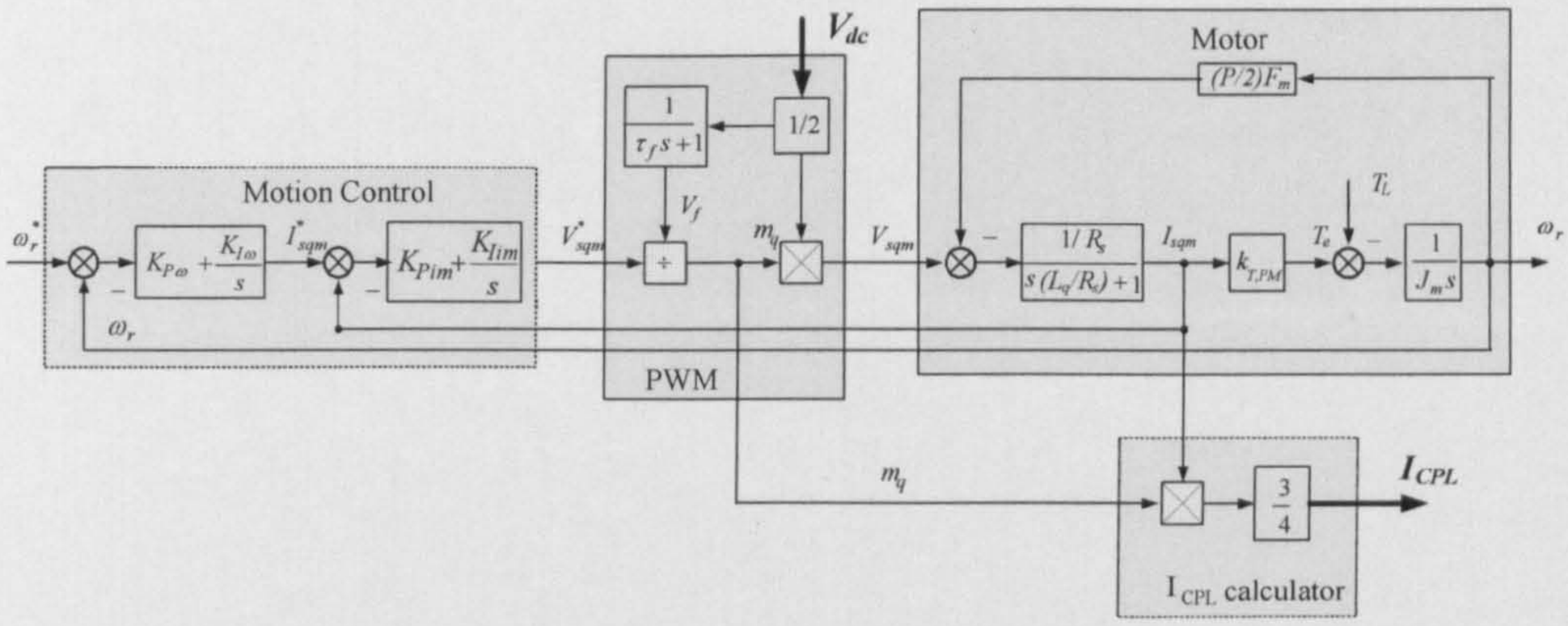

Figure 4.19: Block diagram of the non-linear EMA model for PM machine

The equations describing the dynamics of the CPL of Figure 4.19 are almost the same as those of (4-23), but with the q-axis current dynamic equation changed to:

$$\dot{I}_{sqm} = -\frac{PF_m\omega_r}{2L_q} - \frac{R_{sm}}{L_q} I_{sqm} + \frac{V_{sqm}}{L_q} \tag{4-42}$$

4.4.2 The Dynamic Model Including the Internal Resistance of DC-Link Capacitor

In the experimental rig of Chapter 5, a series connection of low cost high ESR capacitor was used in which r_c is measured at ~0.4 Ω. This is at a level which the increased effect on system stability is noticeable. Hence, the series resistance r_c is included in the mathematical model. As a result, the DC-link current dynamic equation in (4-22) becomes:

$$\dot{I}_{dc} = -\frac{r_c C_F}{L_F}\dot{V}_{out} + \sqrt{\frac{3}{2}}\frac{2\sqrt{3}}{\pi L_F} V_{bus,d} - \frac{(r_\mu + r_L)}{L_F} I_{dc} - \frac{V_{out}}{L_F} \tag{4-43}$$

where $V_{out} \approx V_c$ (V_c is the voltage across DC-link capacitor).

According to (4-42) and (4-43), some small changes are made to the linearized model of the power system in Figure 4.6 in order to be consistent with the experiment in Chapter 5. This linearized model takes the following matrix form:

$$\begin{aligned} \delta\dot{\mathbf{x}} &= \mathbf{A}^*(\mathbf{x_o},\mathbf{u_o})\delta\mathbf{x} + \mathbf{B}^*(\mathbf{x_o},\mathbf{u_o})\delta\mathbf{u} \\ \delta\mathbf{y} &= \mathbf{C}(\mathbf{x_o},\mathbf{u_o})\delta\mathbf{x} + \mathbf{D}(\mathbf{x_o},\mathbf{u_o})\delta\mathbf{u} \end{aligned} \tag{4-44}$$

where the state variable, input, and output vectors are the same as those of (4-25). It can be seen in (4-44) that the constant matrices $\mathbf{A}(\mathbf{x_o},\mathbf{u_o})$ and $\mathbf{B}(\mathbf{x_o},\mathbf{u_o})$ in (4-25) are changed to $\mathbf{A}^*(\mathbf{x_o},\mathbf{u_o})$ and $\mathbf{B}^*(\mathbf{x_o},\mathbf{u_o})$, respectively. These new constant matrices are given by:

$$\begin{aligned} \mathbf{A}^*(\mathbf{x_o},\mathbf{u_o}) &= \mathbf{H}^{-1}\mathbf{A}(\mathbf{x_o},\mathbf{u_o}) \\ \mathbf{B}^*(\mathbf{x_o},\mathbf{u_o}) &= \mathbf{H}^{-1}\mathbf{B}(\mathbf{x_o},\mathbf{u_o}) \end{aligned} \tag{4-45}$$

where

$$\mathbf{H} = \begin{bmatrix} 1 & 0 & 0 & 0 & 0 & 0 & 0 & 0 & 0 & 0 & 0 \\ 0 & 1 & 0 & 0 & 0 & 0 & 0 & 0 & 0 & 0 & 0 \\ 0 & 0 & 1 & 0 & 0 & 0 & 0 & 0 & 0 & 0 & 0 \\ 0 & 0 & 0 & 1 & 0 & 0 & 0 & 0 & 0 & 0 & 0 \\ 0 & 0 & 0 & 0 & 1 & r_c C_F L_F^{-1} & 0 & 0 & 0 & 0 & 0 \\ 0 & 0 & 0 & 0 & 0 & 1 & 0 & 0 & 0 & 0 & 0 \\ 0 & 0 & 0 & 0 & 0 & 0 & 1 & 0 & 0 & 0 & 0 \\ 0 & 0 & 0 & 0 & 0 & 0 & 0 & 1 & 0 & 0 & 0 \\ 0 & 0 & 0 & 0 & 0 & 0 & 0 & 0 & 1 & 0 & 0 \\ 0 & 0 & 0 & 0 & 0 & 0 & 0 & 0 & 0 & 1 & 0 \\ 0 & 0 & 0 & 0 & 0 & 0 & 0 & 0 & 0 & 0 & 1 \end{bmatrix}_{11\times 11}$$

For a PM machine, the matrix elements inside $\mathbf{A}(\mathbf{x_o},\mathbf{u_o})$ are changed as shown below:

$$\mathbf{A_{Hm}} = \begin{bmatrix} 0 & 0 & 0 & 0 & 0 \\ 0 & 0 & 0 & 0 & 0 \\ 0 & 0 & 0 & 0 & 0 \\ 0 & 0 & 0 & 0 & 0 \\ 0 & 0 & 0 & 0 & 0 \\ 0 & -\dfrac{3M_{qo}}{4C_{dc}} & \dfrac{3I_{sdmo}V_{sdmo}}{4C_{dc}V_{f,o}^2} & -\dfrac{3I_{sqmo}}{4C_{dc}V_{f,o}} & 0 \end{bmatrix}_{6\times5}$$

$$\mathbf{A_m} = \begin{bmatrix} 0 & \dfrac{K_T}{J_m} & 0 & 0 & 0 \\ -\dfrac{PF_m}{2L_q} & -\dfrac{R_{sm}}{L_q} & -\dfrac{V_{sqmo}}{L_qV_{f,o}} & \dfrac{1}{L_q} & 0 \\ 0 & 0 & -\dfrac{1}{\tau_F} & 0 & 0 \\ -K_{Pim}K_{I\omega}+\dfrac{PK_{Pim}F_m}{2L_q} & -K_{Iim}-\dfrac{K_{Pim}K_{P\omega}K_T}{J_m}+\dfrac{K_{Pim}R_{sm}}{L_q} & \dfrac{K_{Pim}V_{sqmo}}{L_qV_{f,o}} & -\dfrac{K_{Pim}}{L_q} & K_{Iim} \\ -K_{I\omega} & -\dfrac{K_{P\omega}K_T}{J_m} & 0 & 0 & 0 \end{bmatrix}_{5\times5}$$

Other matrix elements are the same as those of (4-26). The dynamic model in this section will be used in Chapter 5 with experimental validations. This is because a PM machine and four 1000 μF capacitors connected in series are used in the experimental rig.

4.5 Chapter Summary

This chapter deals with the stability analysis of the power system taking into account the dynamics of controlled electromechanical actuators (EMAs). These EMAs have been previously represented as an ideal CPL without dynamic behaviour. The dq modelling approach with the eigenvalue theorem is used to analyse the stability. The results show that the effect of CPL dynamics is significant. The CPL dynamics (in terms of speed bandwidth and DC-link voltage measurement filter) can increase the stable power range compared with the ideal CPL. Although, neglecting the CPL dynamics may be beneficial from the viewpoint of power system availability, it may result in a very non-optimal design solutions that would impact on overall mass and dimension. The CPL dynamic effects depend on the EMA parameters. Therefore, this chapter also describes the stability analysis for parameter variations of different operational regimes. The results show that reducing the

bandwidth of DC-link voltage filter and decreasing the EMA speed control natural frequency can provide higher power levels at which instability occurs. To achieve the accurate model of power system, the dynamic model of the EMA behaving as a non-ideal CPL cannot be ignored. The SABER time-domain simulation was used to support the theoretical stability results. Good agreement between both models was achieved. This chapter also considers the dynamic model for the power system with PM machine (instead of IM) including the internal resistance of a DC-link capacitor. Stability analysis using this model will be described in the next chapter together with experimental results. The next chapter will therefore show the comparison between theoretical and experimental results to confirm that the dq modelling approach can obtain stability results with good accuracy. After this dq models will be applied to more complex power systems.

Chapter 5

Experimental Validations

5.1 Introduction

As mentioned in Chapter 4, the converter and machine drive dynamics departs from that of an ideal constant power load. These dynamics can increase the stable power range compared with the ideal CPL. This chapter will describe experiments undertaken to practically ascertain the effect of the CPL dynamics and hence verify the dq modelling approach described in Chapters 2-4. In particular the experimental results are aimed towards showing the impact on system dynamics of variations in AC supply frequency, actuator speed loop dynamics, and DC link voltage measurement filtering. Some small additions are made to the mathematical model as explained in Section 4.4 in order to be consistent with the experiment. Firstly, a PM machine is used instead of an IM. Secondly, an internal resistance of the DC-link capacitor (r_c) is also included in the dq mathematical model to increase the accuracy. The results from this chapter will be published in [34].

5.2 Experimental Hardware

The power system of the experimental test rig is depicted in Figure 5.1. The rig used in this research is an existing rig in the Power Electronics, Machines, and Control (PEMC) Group at the University of Nottingham. The components in the rig, power converter and controllers, are based on the work of [85]. The description of the hardware and test regime is explained in this section.

5.2.1 Description of Hardware

Figure 5.1 shows the system diagram of the experimental rig. The rig can be divided into three parts. Part I is the programmable AC source. Part II consists of the three-phase inductors, the diode rectifier, the DC-link filters, and the inverters with their controller. Part III is the high speed test rig including the PM machine, power analyser and torque meter.

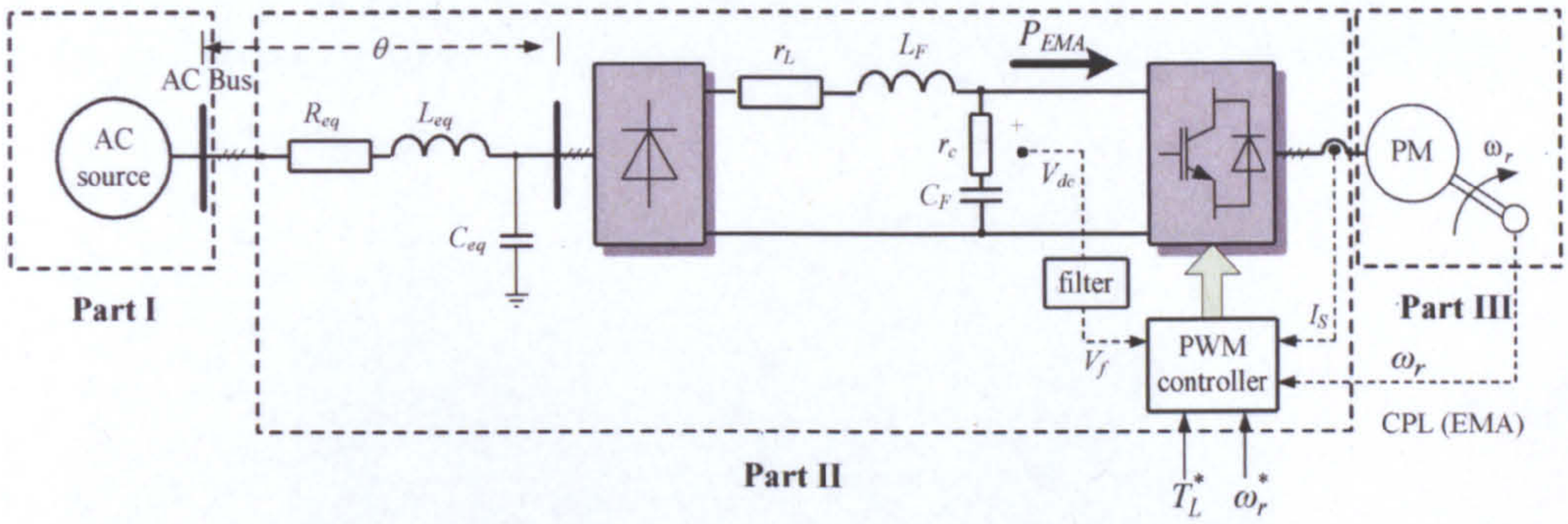

Figure 5.1: The power system of the test setup

Figure 5.2 shows the programmable 12 kVA AC source (model 61705, Chroma) used to represent the ideal voltage AC source. The three-phase output voltages are sinusoidal and can be varied to 300 V and 1.2 kHz.

Figure 5.2: The programmable AC source

The three-phase inductors represent the transmission line elements. The impedance magnitude is made much larger than the internal impedance of the voltage source so that the voltage source may be considered ideal. The three-phase six-pulse diode rectifier, DC link filters, and six-phase two-level voltage source inverter with controllers from [85] were used (see Figure 5.3). The controller was implemented using a Texas instruments C6713 floating point DSP and a high speed Actel, ProAsic3 FPGA. The converter has been constructed using 100A, 1200V inverter leg modules. Low cost electrolytic capacitors were used to implement the DC-link providing the 540 V DC bus.

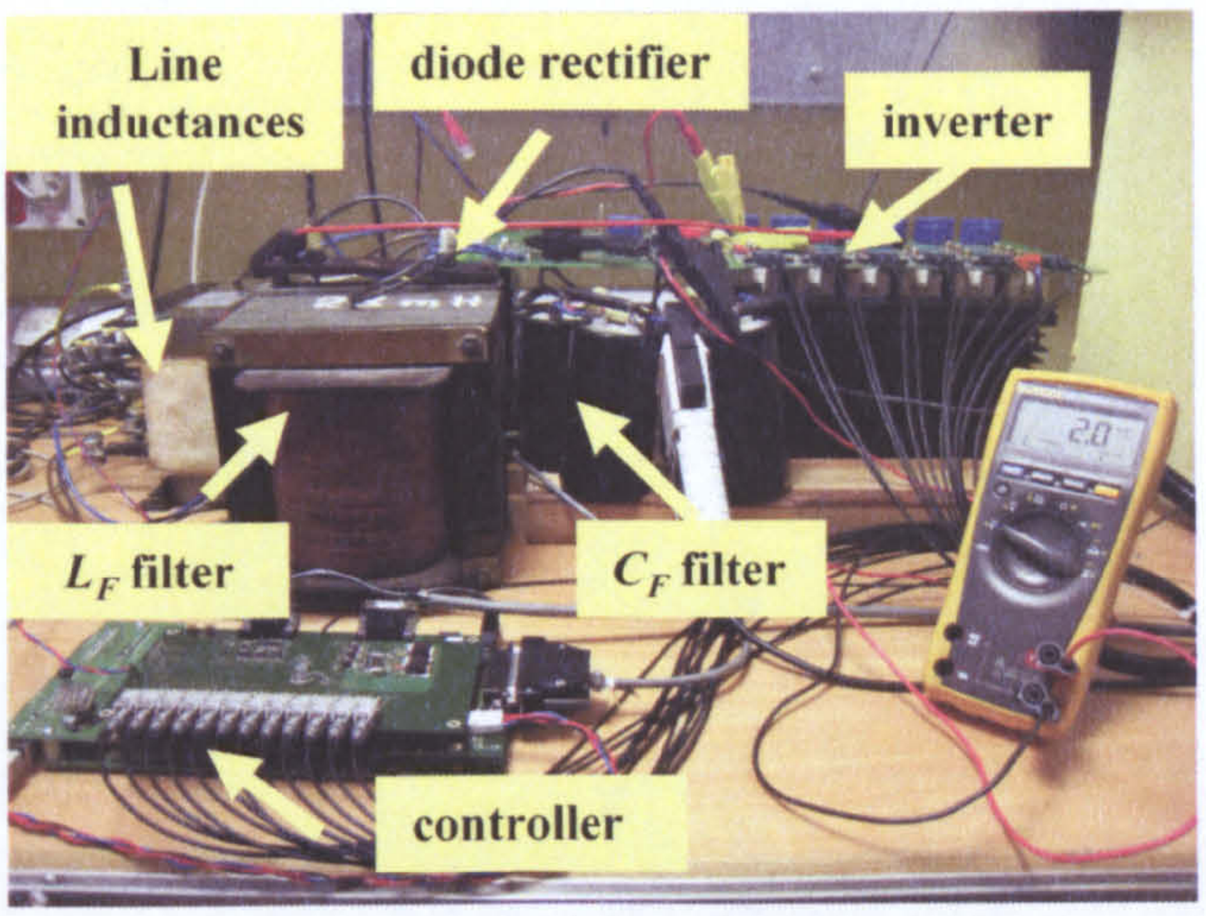

Figure 5.3: Line inductances, DC-link filters, and power converter equipment

The load is a 4kW AC PM motor. The standard motor drive vector control was implemented in the controller board. A power analyser and torque meter measure the input power of the machine and the load torque, respectively. The input power of the machine is equal to P_{EMA} (see Figure 5.1) assuming small power losses in the inverter. The high speed test rig is shown in Figure 5.4 and Figure 5.5. The rig dynamometer applies load torque for the PM motor.

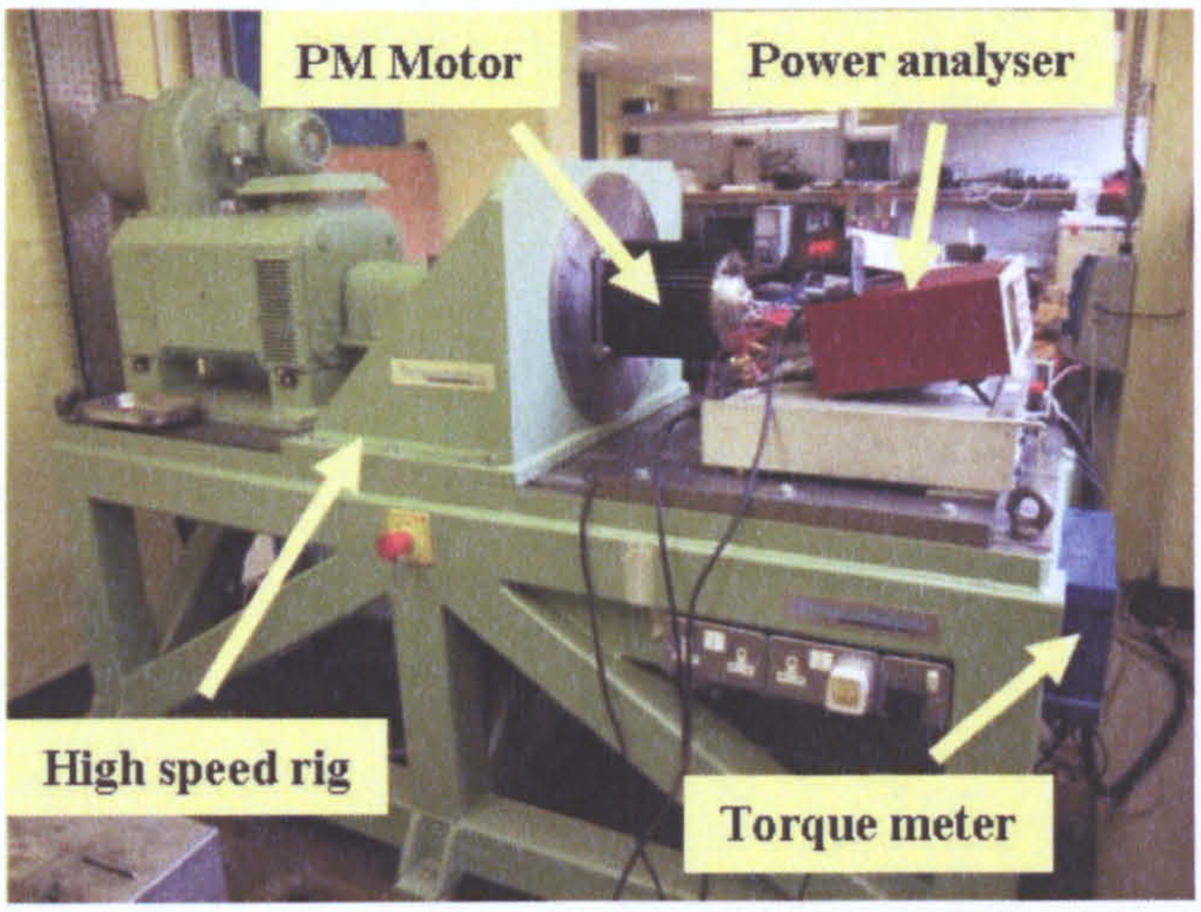

Figure 5.4: The experimental rig of Part III

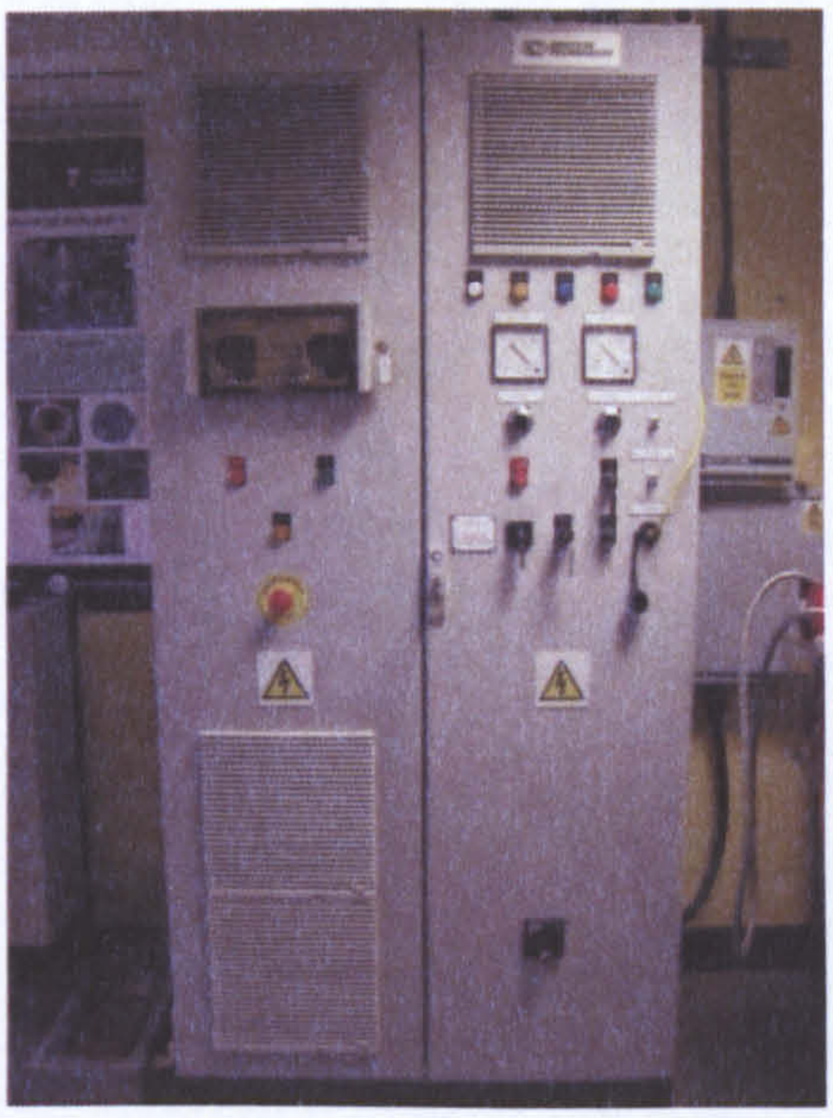

Figure 5.5: The control panel of high speed test rig dynamometer

5.2.2 Test Regime

Before testing, the parameters of the rig need to be determined, especially the inductance and capacitance values of DC-link filters. All inductances were measured from an LCR bridge meter, while resistances were measured by a digital micro-ohmmeter. The three phase line capacitances are very small.

They can be set to 2nF for the mathematical model. This is because the dq mathematical model for the diode rectifier requires a voltage source which can be provided by these capacitances. It will be shown later that the small capacitance value in the model cannot affect to the stability results. Good agreement between the theoretical and experimental results is achieved. For the DC-link capacitance, four capacitors 1000 μF connected in series were used. The variation of the capacitance value for each capacitors is from -10% to +50%, typical of electrolytic capacitors. Therefore, to achieve usable parameter values of capacitance, a step response test was carried out. The diagram for the step response test (damping test) is shown in Figure 5.6 and involves imposing a load resistance change from 214.5 Ω to 135.5 Ω. The DC-link voltage V_{dc} is measured and compared with that from the SABER benchmark simulation. The benchmark model for the damping test is given in Appendix D.6.

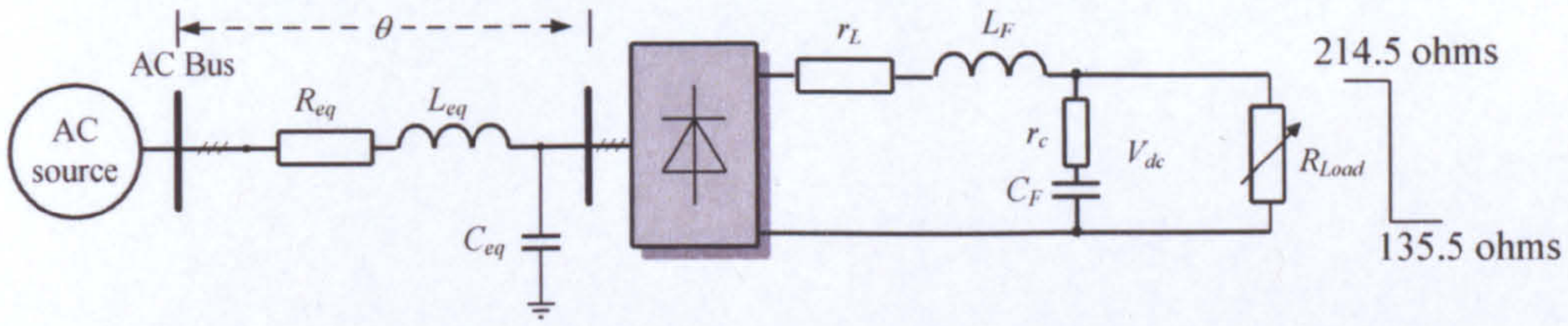

Figure 5.6: Damping test diagram

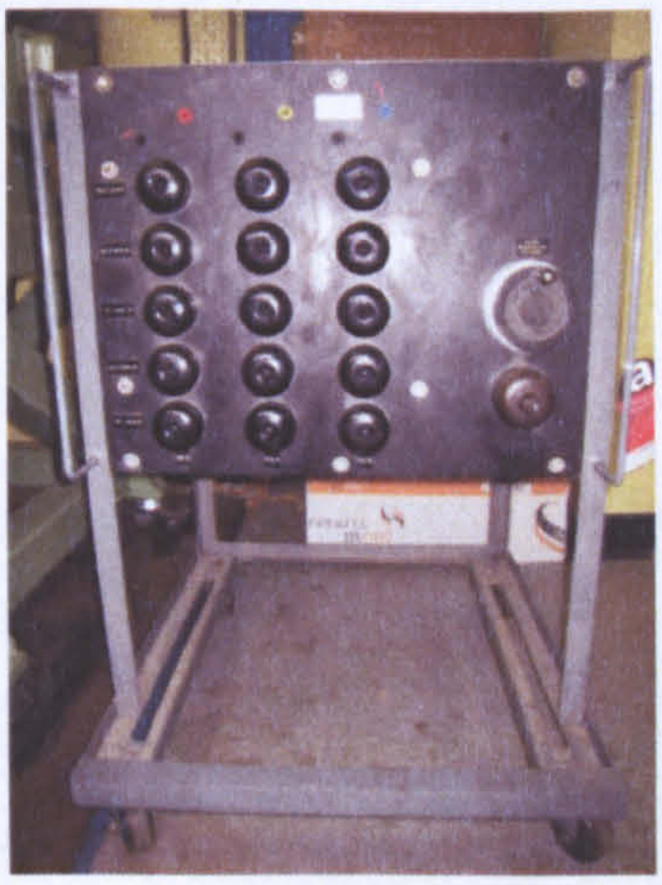

Figure 5.7: The resistive load

In the simulation, the other system parameters are fixed at their measured values (R_{eq}=0.045Ω, L_{eq}=60μH, r_L=0.2Ω, L_{dc}=24.15mH, r_c=0.4Ω) and a voltage of V_s=230V_{rms} 50Hz. These parameters are measured from the LCR bridge meter and digital micro-ohmmeter as previously mentioned. The capacitance value (C_F) in simulation is varied until a matched V_{dc} response is obtained. The results show that C_F=320μF provides good agreement between the simulation and experiment results as shown in Figure 5.8. According to the measurement errors and the large variation in the capacitor value, the system parameters identification is needed to provide the usable parameters for the model.

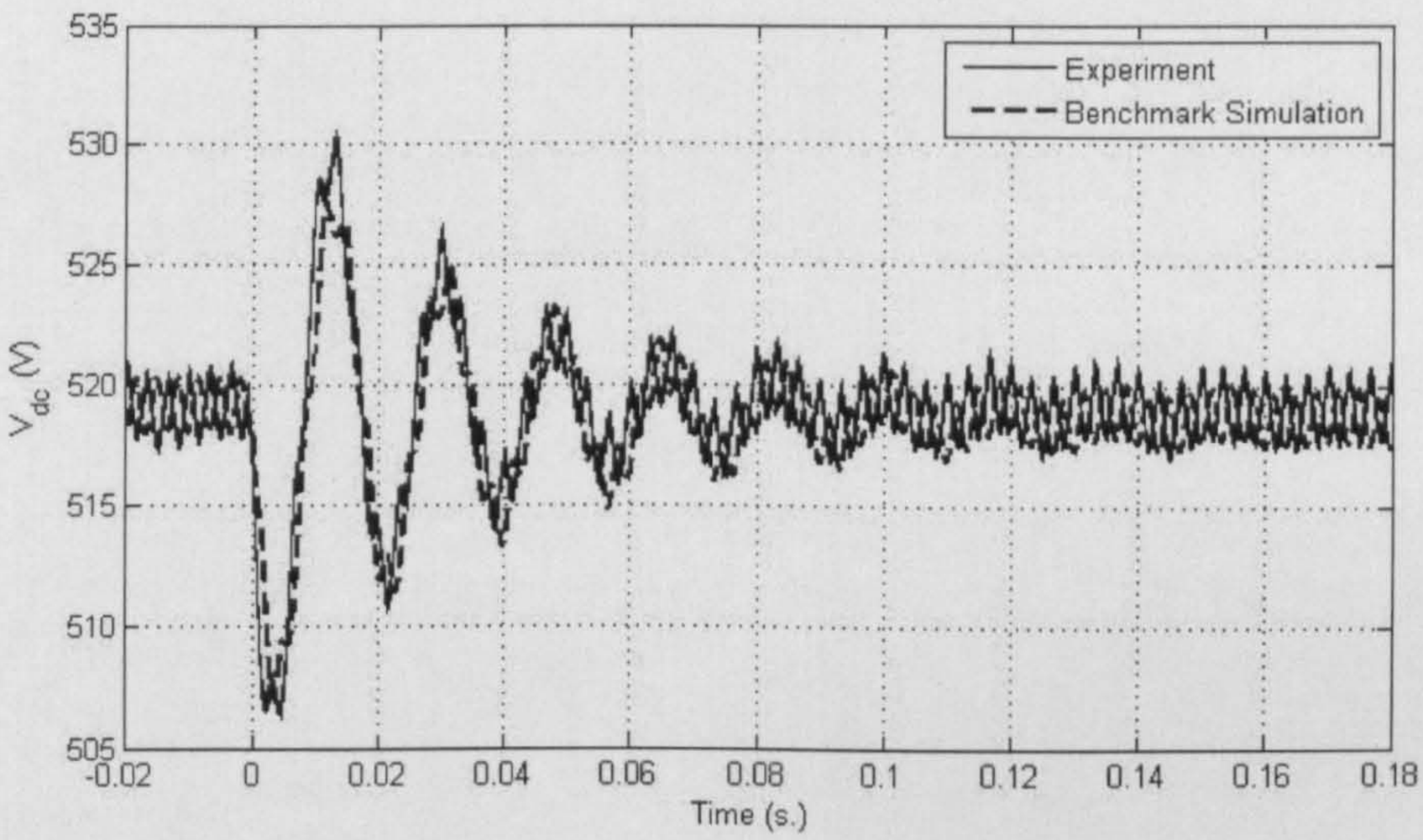

Figure 5.8: DC-link voltage response from the experiment and simulation

According to the results from the damping test, the system parameters of Figure 5.1 including the PM machine and its controllers are shown in Table 5.1. The instability results of the system from the experiment with parameters in Table 5.1 will be shown and compared against the theoretical results in Section 5.3.3.

As stated in Chapter 2, 3, and 4, the dynamic model based on dq modelling approach can be used to predict instability for variations in system parameters. In this chapter, to validate the theoretical results, the rig can be set up for

parameter variations. Firstly, the system frequencies of 50, 100, 200, and 300 Hz were imposed with no DC-link voltage filter, while the other parameters were fixed as shown in Table 5.1. Secondly, the bandwidth values of the DC-link voltage filter were set at 20, 30, 50, 200 and 300 Hz by changing the code in the controller board with other parameters fixed as shown in Table 5.1. Finally, the natural frequency of the speed loop was set to 5, 10, 15, and 20 Hz by changing the code in the controller board with the DC-link voltage filter bandwidth set to 50 Hz. Other parameters were also fixed as shown in Table 5.1. All instability results from the experiment will be shown and compared against the benchmark and theoretical models in Section 5.3.

Table 5.1: The set of parameters for the test rig

Parameter	**Value**	**Description**
V_s	230 $V_{rms/phase}$	phase source voltage
ω	$2\pi \times 50$ rad/s	source frequency
R_{eq}	0.045 Ω	line resistance
L_{eq}	60 μH	line inductance
C_{eq}	2 nF	line capacitance
r_L	0.2 Ω	DC-link inductor resistance
L_F	24.15 mH	DC-link inductance
r_c	0.4 Ω	ESR_c
C_F (from damping test)	320 μF	DC-link capacitance
Actuator drive PM machine 4 kW rated		
ω_{rated}	1140 rpm	rated speed
ω_r^*	800 rpm	speed reference
$T_{L,rated}$	40 Nm	rated load torque
R_s	0.5 Ω	stator resistance
$L_s=L_d=L_q$	2.3 mH	stator leakage inductance
P	20 poles	number of poles
J_m	4e-03 kgm^2	moment of inertia
F_m	0.123 Wb	constant flux of PM machine
$\omega_{n,speed}$	10 Hz ($K_{p\omega}$=0.02, $K_{i\omega}$=0.863)	natural frequency of speed loop
$\omega_{n,current}$	200 Hz (K_{pi}=4.124, K_{ii}=3632)	natural frequency of current loop

5.3 Stability Analysis and Experimental Results

In this section, the experimental results from the rig are compared with the simulation and theoretical results by using the dynamic model from Section 4.4. This is to confirm that the dq modelling approach can obtain stability results with good accuracy before applying this approach to more complex systems in the next chapter.

The linearized model is used with the eigenvalue theorem. The eigenvalues can be calculated from the Jacobian matrix $\mathbf{A}^*(\mathbf{x_o}, \mathbf{u_o})$ in (4-44). The eigenvalues for the experimental power system with parameters in Table 5.1 were analyzed for the case when the load torque varies from 0 to 40 Nm at the constant actuator speed reference 800 rpm. This corresponds to the steady-state value of P_{EMA} varying from 0 to 3.7 kW (~0.93P_{rated}). The dominant root locus is shown in Figure 5.9. It can be seen that the system becomes unstable when the P_{EMAo} exceeds 2.49 kW for the studied case. The results for this case are for the system with no DC-link voltage filter.

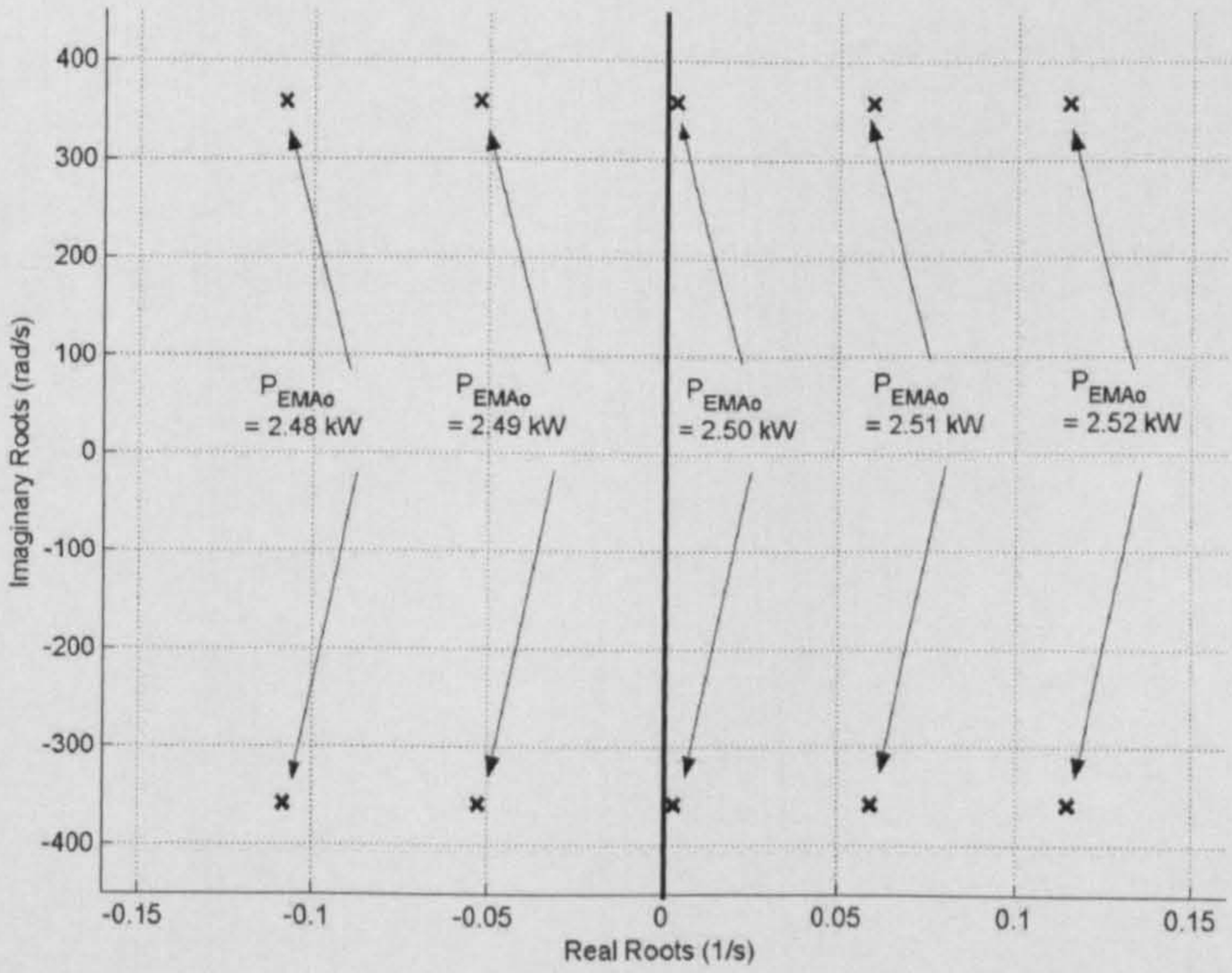

Figure 5.9: The dominant eigenvalue plot of the system in Figure 5.1 with parameters in Table 5.1. (No DC-link voltage filter)

Figure 5.10 shows the SABER time-domain benchmark simulations that confirm the theoretical result with the instability occurring at P_{EMA} of 2.56 kW (~0.64P_{rated}). This is greater than the 2.49 kW for the unstable condition. The SABER benchmark model of the system in Figure 5.1 is given in Appendix D.7. It can be seen from Figure 5.9 and Figure 5.10 that good agreement between theoretical and simulation results are achieved.

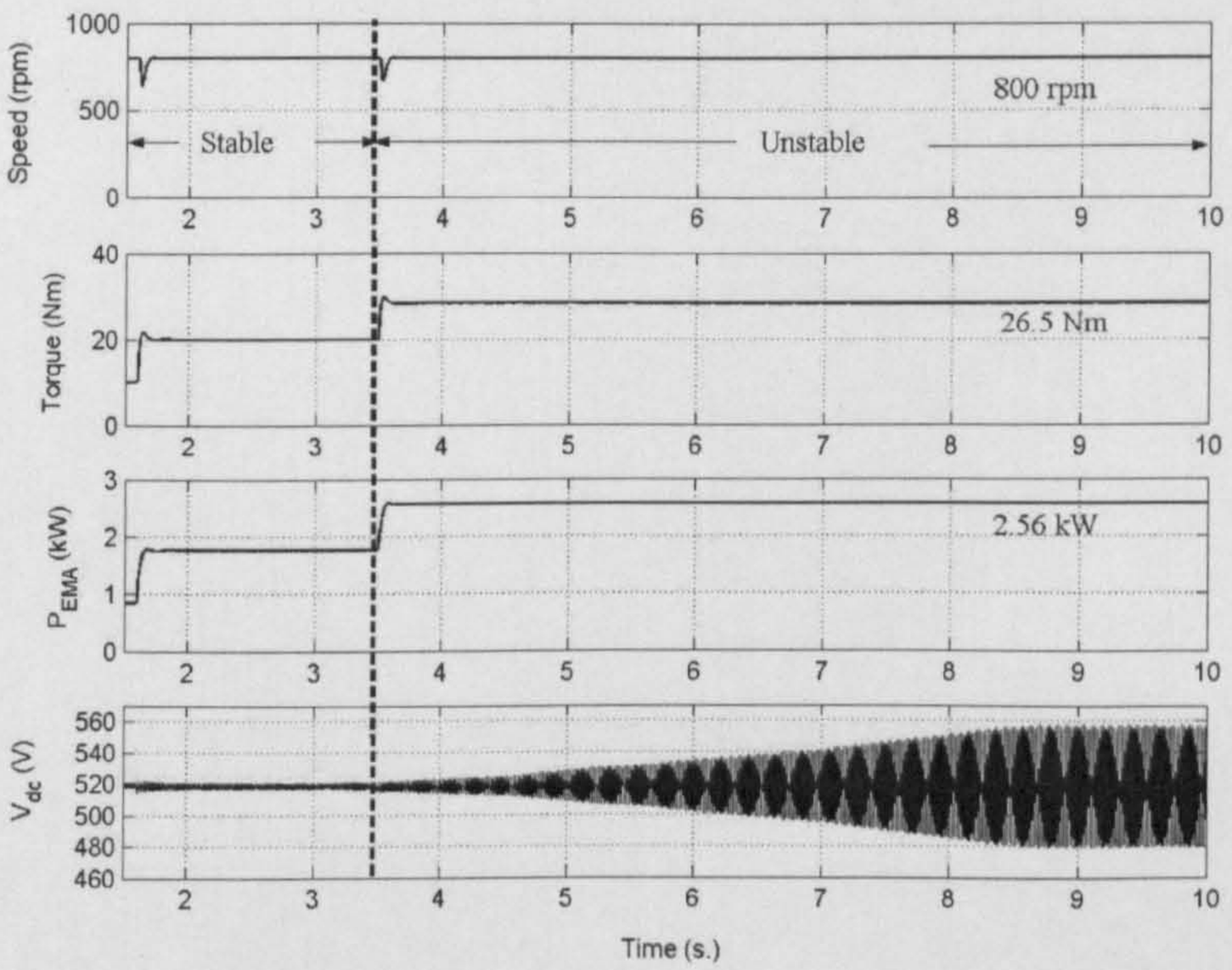

Figure 5.10: The SABER simulation results to support the theoretical result

For experimental validation, the rig was started with V_s=230V_{rms}, 50 Hz, ω_r^* =800 rpm, and T_L=0Nm. The load torque was manually varied by using the control panel of high speed test rig dynamometer as shown in Figure 5.5. In addition, with constant speed here regulated to 800 rpm, the power analyser and torque meter measured P_{EMA} and T_L for each load torque. The load torque was varied until the peak-to-peak of DC-link voltage (V_{pp}) reaches 90V. This situation is considered the unstable condition. Figure 5.11 shows the evolution of the DC-link voltage as P_{EMA} is increased. The 90 V_{pp} of DC-link voltage was therefore set as the set point for unstable condition of the experiment for all cases. The instability shows up as oscillating behaviour, with (for this

instance) a 90V peak-to-peak V_{dc} oscillation. Note that the DC-link voltage waveform (from the non-linear benchmark simulation) also inhibits instability in the form of limit circle oscillations of 90 V peak-to-peak value as shown in Figure 5.10.

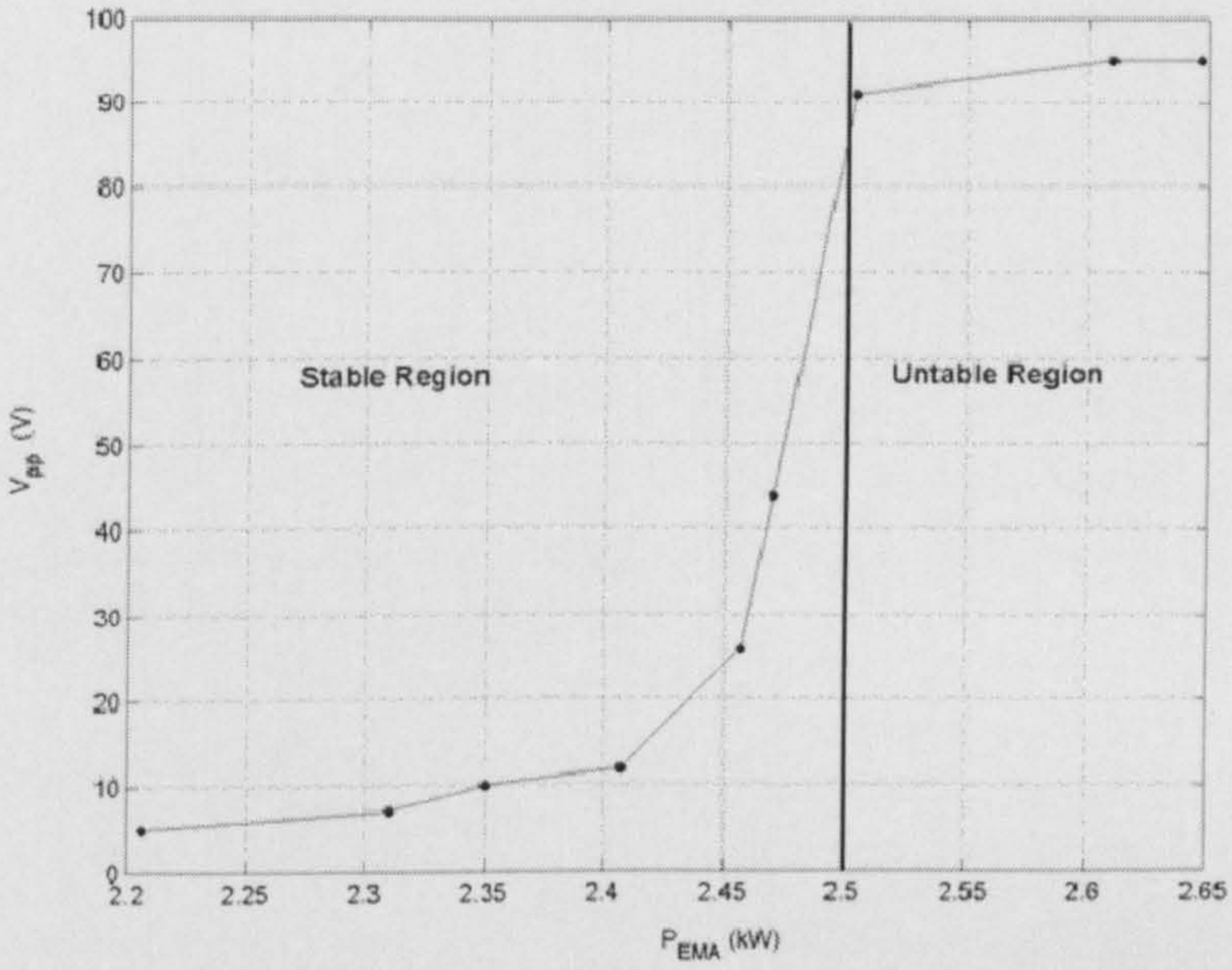

Figure 5.11: Unstable condition for the test rig

Figure 5.12 shows the DC-link voltage from the experiment when taking T_{Lo}=24.63 Nm at 800 rpm (P_{EMA}=2.31 kW). Theory predicts instability at 2.5 kW and the experimental V_{dc} is stable as predicted. Figure 5.13 shows the same DC-link voltage when the system is expected to exhibit unstable operation (T_{Lo}= 26.72 Nm at 800 rpm, P_{EMA}=2.52 kW). Note that the evolution of Vdc in Figure 5.11 corresponds to this condition. According to the results, there is good agreement between theoretical, simulation, and experimental results.

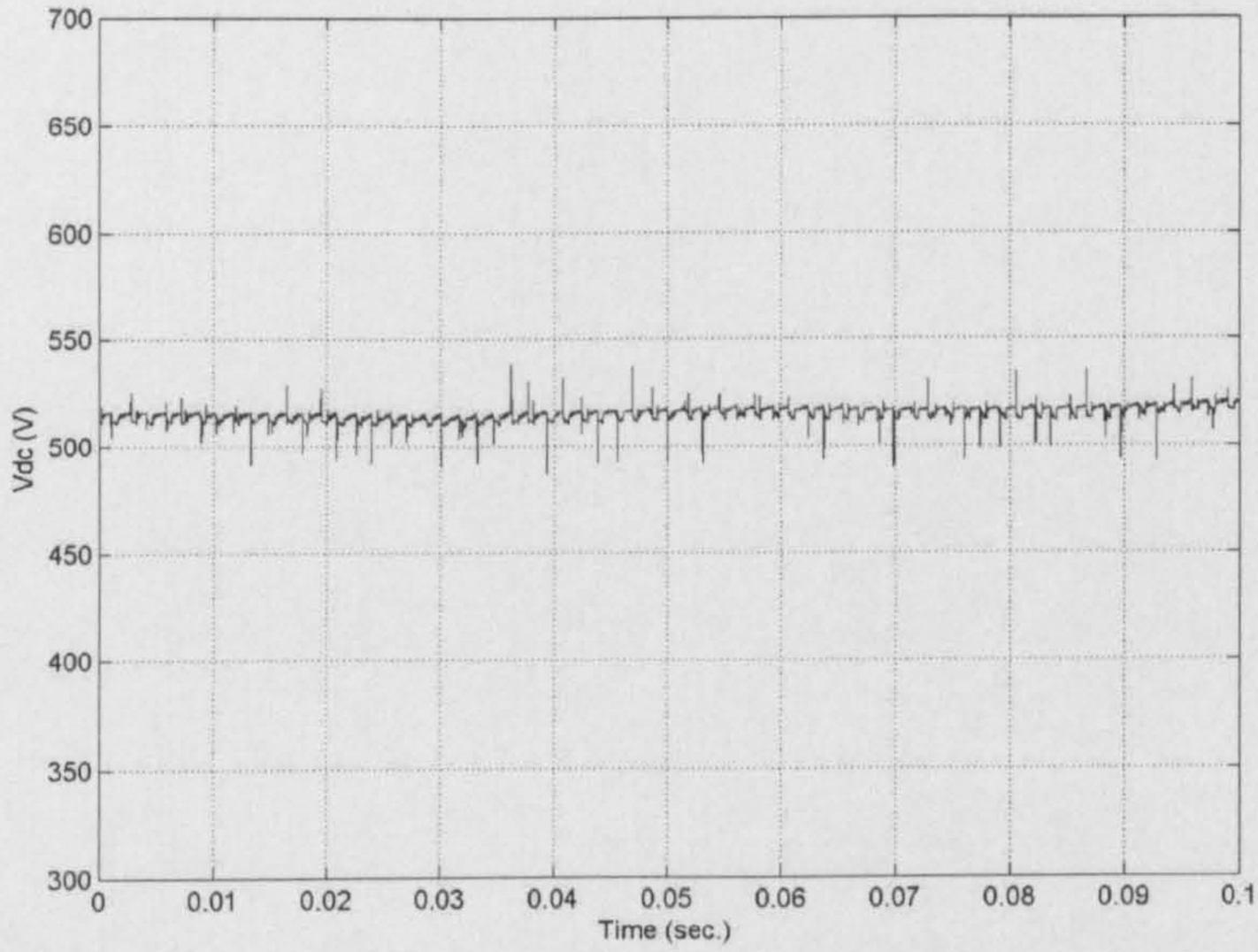

Figure 5.12: Observed DC-link voltage under stable condition (T_{Lo}=24.63 Nm at 800 rpm corresponds to P_{EMA}=2.31 kW)

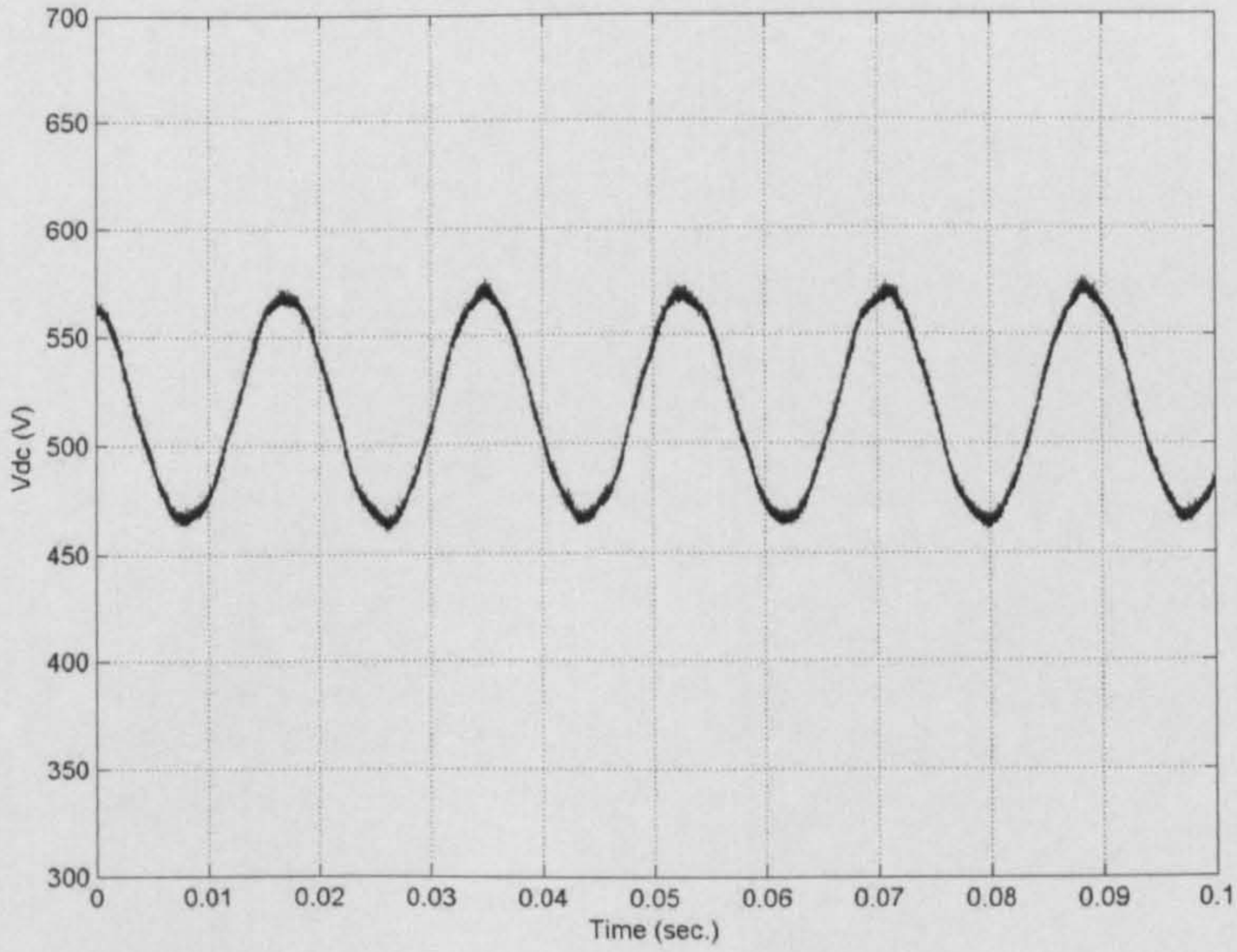

Figure 5.13: Observed DC-link voltage under unstable condition (T_{Lo}=26.72 Nm at 800 rpm corresponds to P_{EMA}=2.52 kW)

The model also allows stability analysis arising from the effects of parameter variations in different operational regimes. Since the considered aircraft power system is frequency-wild, it is very important to study stability variation with

changes in system frequency. Figure 5.14 shows the P_{EMA} values of the rig measured from the power analyser at which instability occurs when the system frequencies of 50, 100, 200, and 300 Hz were imposed with no DC-link voltage filter, while the other parameters are fixed as shown in Table 5.1. However, absence of the voltage filter does not mean that the modulation index is fixed; this just means that modulation index is calculated based-on unfiltered DC-link voltage value. The instability conditions from the mathematical model are also compared with the experimental results in this figure.

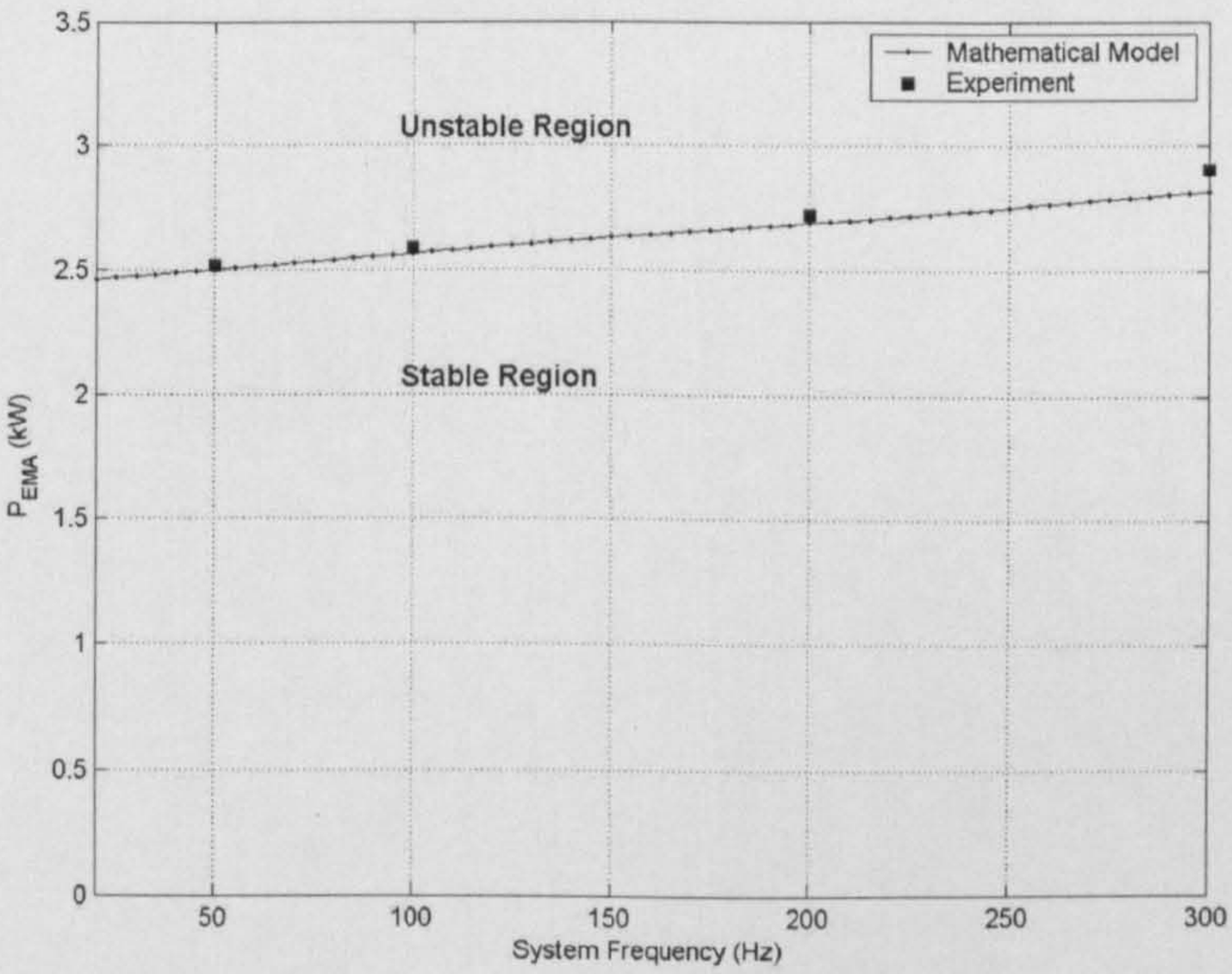

Figure 5.14: The comparison between mathematical model prediction and experiment for the onset of stability when the system frequency is varied with no DC-link voltage filter

The bandwidth of the DC-link voltage filter (ω_F) and the natural frequency of the speed loop ($\omega_{n,speed}$) in an EMA can be imposed by the designer. In the experimental tests, these values are varied by changing the code in the controller board. Therefore, it is very interesting to study the variations in ω_F and $\omega_{n,speed}$ on stability. The comparisons between the mathematical model and experimental result for variations in ω_F, and $\omega_{n,speed}$ are depicted in Figure

5.15 and Figure 5.16, respectively (other parameters fixed as shown in Table 5.1).

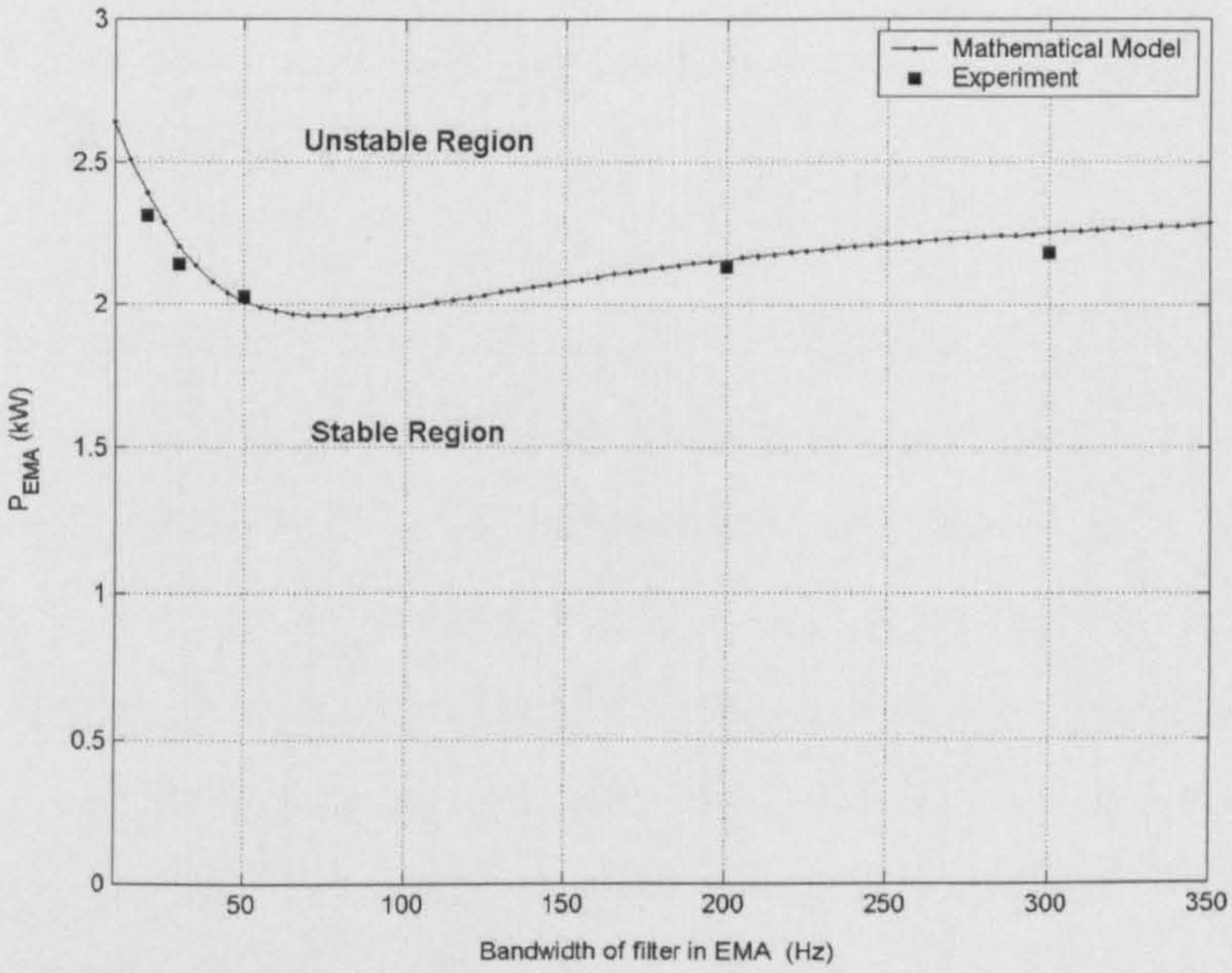

Figure 5.15: The comparison between mathematical model prediction and experiment for the onset of stability when the bandwidth of DC-link voltage filter is varied

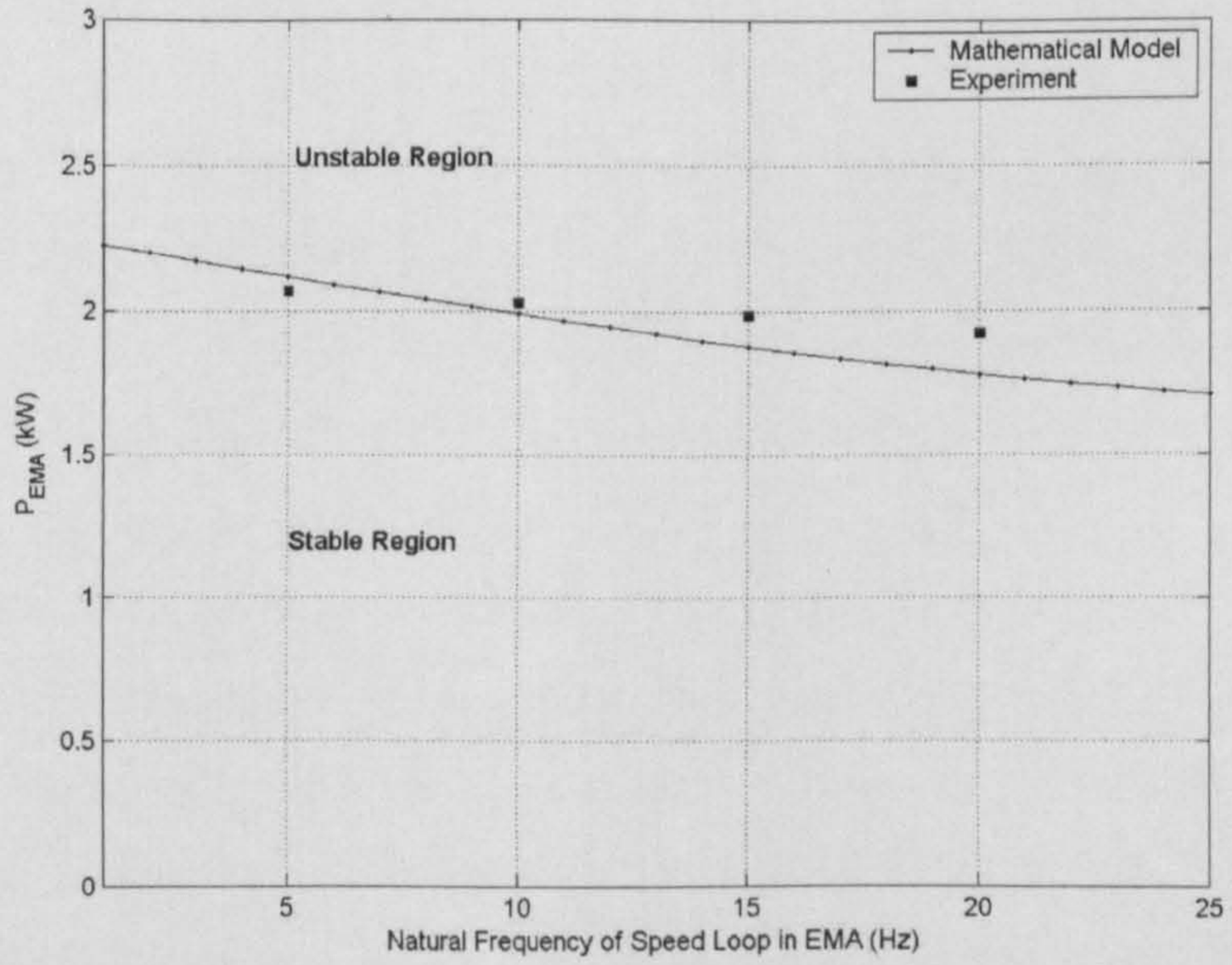

Figure 5.16: The comparison between mathematical model prediction and experiment for the onset of stability when the natural frequency of speed loop is varied with fixed $\omega_F = 2\pi 50$ rad/s

Some discrepancies between the mathematical model prediction and experiment occur in Figure 5.16. This is because the inertia used in the model is only that of SMPM machine, while in practice the inertia of the load is taken into account as well. However, the instability trend (increasing instability as $\omega_{n,speed}$ increases) is the same.

The main outcome of this study is that increasing system frequency and reducing natural frequency of the speed loop can expand the stability range. Interestingly, the effect of ω_F is not monotonic and there is ω_F value at which the power system has the minimal stability. In terms of physical meaning, the results are difficult to explain. For this case, higher bandwidth (>85H_z) of the filter can make the system more stable. The trend is not the same as those of Chapter 4 (reducing bandwidth can make the system more stable). Therefore, it is necessary to keep in mind that adding the DC-link voltage filter can make the system either more or less stable. The trend depends on the system parameters.

5.4 Chapter Summary

In this chapter, the experimental results have been undertaken and compared with theoretical predictions. The power system used for experiment consists of a reasonably ideal voltage source, three-phase transmission lines, a six-pulse diode rectifier, a DC-link filter (including the internal resistance of DC-link capacitor, r_c), and a SMPM machine drive having non-ideal CPL dynamics. The mathematical model was derived by using the dq modelling approach. In addition, the simulation results were also used to support the theoretical results. According to the results, agreement between mathematical model, simulation, and experimental results is achieved that ranges from acceptable to very good. This confirms that the dq modelling approach can obtain stability results with good accuracy. The dq models will be applied to more complex power systems. In the next chapter, the dq modelling method will be applied

to analyse the power system stability including the effect of generator dynamics and the generator control unit (GCU) dynamics. These effects have not been considered in Chapters 2-5. The ideal voltage source has been used to represent an engine generator with GCU by assuming an infinitely fast controller action of the GCU. Therefore, in the next chapter, the effects of generator with GCU dynamics in terms of stability analysis will be illustrated.

Chapter 6

Power System Stability for Systems Containing a Voltage Regulated Synchronous Generator and Actuator Dynamics

6.1 Introduction

According to the results given in Chapter 2 to 5, good agreement between theoretical (dq modelling method) simulation and experimental results is achieved. It confirms that the mathematical model based on a dq modelling approach can predict power system instability with good accuracy. In addition, as mentioned in Chapter 2, the converter models derived from the dq modelling approach can be easily combined with models of other power elements expressed in terms of synchronously rotating frames such as a synchronous generator. Therefore, in this chapter the dq modelling method is used to create a nonlinear dynamic model for a more realistic power system that includes the output voltage dynamics of the synchronous generator (SG) and generator control unit (GCU), as well as the dynamics of electromechanical actuators (non-ideal CPL) as stated in Chapter 4. These effects have been considered in [73],[76],[77] . However, these effects have not been widely discussed in previous publications [13],[18],[20],[37]-[44] in which the constant power load (CPL) is generally defined as an ideal current source without dynamic behaviour (ideal CPL), and the generator with GCU is regarded as an ideal voltage source with an infinitely fast controller action.

The nonlinear model is then linearized using the first order terms of a Taylor's expansion for stability analysis. The details of how to combine the dynamics of a GCU and an electromechanical actuator into a power system with a diode rectifier for stability studies is described in this chapter. The impact of using the dynamic models for the SG-GCU and non-ideal CPL in comparison with the models using an ideal voltage source and ideal CPL is also shown.

6.2 Power System Definition and Assumptions

The power system studied in this chapter is shown in Figure 6.1. It represents the elements of an aircraft AC frequency-wild power system architecture including a 3-phase SG with GCU controlling the generator output voltage, a transmission line represented as a π-equivalent circuit, and a six-pulse diode rectifier feeding the EMA (behaving as a non-ideal CPL as described in Chapter 4) through a DC-link filter. Note that P_{EMA} is the power delivered to the non-ideal CPL.

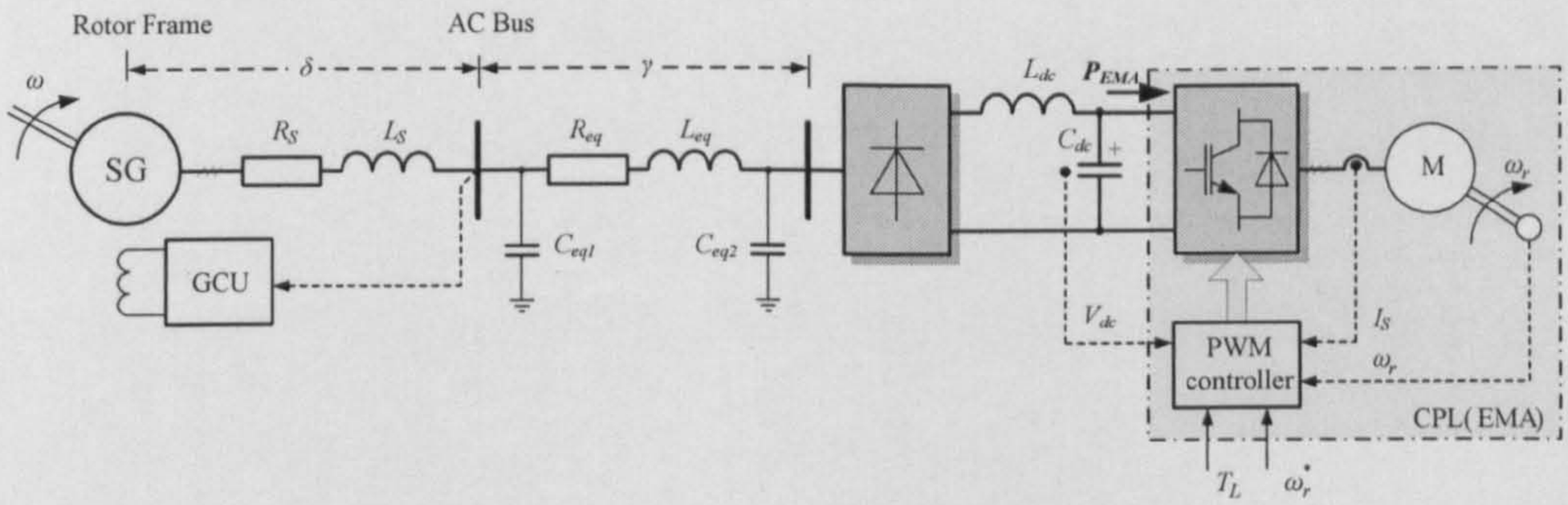

Figure 6.1: The power system studied

The generator shaft is driven from a turbine and is here regarded as a speed source ω since the generator will not normally affect the shaft speed. The AC network is therefore "frequency-wild". In Figure 6.1, the elements R_{eq}, L_{eq}, C_{eq1}, and C_{eq2} represent the AC cable link. If an autotransformer-rectifier unit (ATRU) is used, these elements also represent the resistance and leakage inductance of the autotransformer (see Section 2.6). The DC-link filter is

shown by elements L_{dc} and C_{dc}. The phase between the SG rotor axis and the feed voltage vector is δ, while γ is the phase between the voltage vectors at the SG feeders and at the rectifier input terminals. It is assumed that the 3-phase output voltage of the SG is balanced. The diode rectifier is assumed to operate under continuous conduction mode and the output DC current of the rectifier I_{dc} is constant. In addition, the higher harmonics of the fundamental are neglected. These assumptions are sufficient for stability studies [18].

6.3 Synchronous Generator with GCU

To combine the dynamic of generator and GCU into the power system for stability studies, it is necessary to consider the synchronous generator (SG) model. It is well known that a SG is normally modelled in the dq reference frame fixed on the rotor [66] and is supplemented by a GCU stabilizing the voltage at the generator feeders. The GCU has a cascade control structure with an inner field current control loop. The shaft speed is regarded as an input variable. The equivalent circuit of the SG-GCU in the synchronously rotating dq frame is shown in Figure 6.2. The parameters K_{Pv}, K_{Iv}, K_{Pi}, K_{Ii} are the proportional and integral gains of the voltage and current PI controllers. $V^{*}_{T,rms}$ is the reference for the SG feeder voltage. The SG-GCU model of Figure 6.2 will be used as the dynamic model for stability studies in the next section.

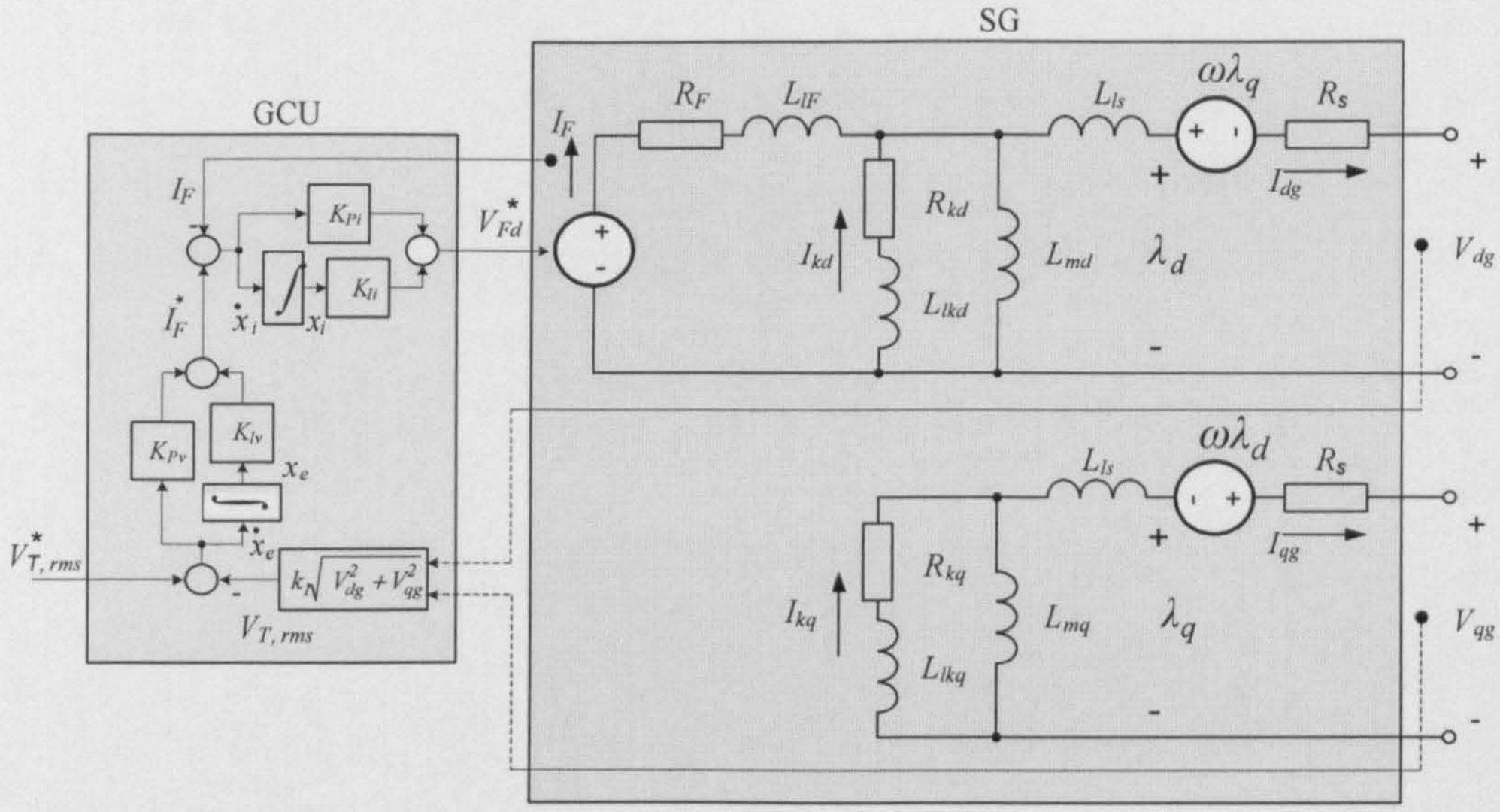

Figure 6.2: The SG-GCU model on dq frame

6.4 Deriving the Non-Linear Model and Linearized Model

As described in Chapter 2, the cable and diode rectifier can be transformed into the dq frame by using the dq modelling approach. From Chapter 4, the dynamical CPL model of Figure 4.3 for IM drive can be combined with the cable, diode rectifier, and SG-GCU model. The equivalent circuit of the power system in Figure 6.1 in dq frame is depicted in Figure 6.3.

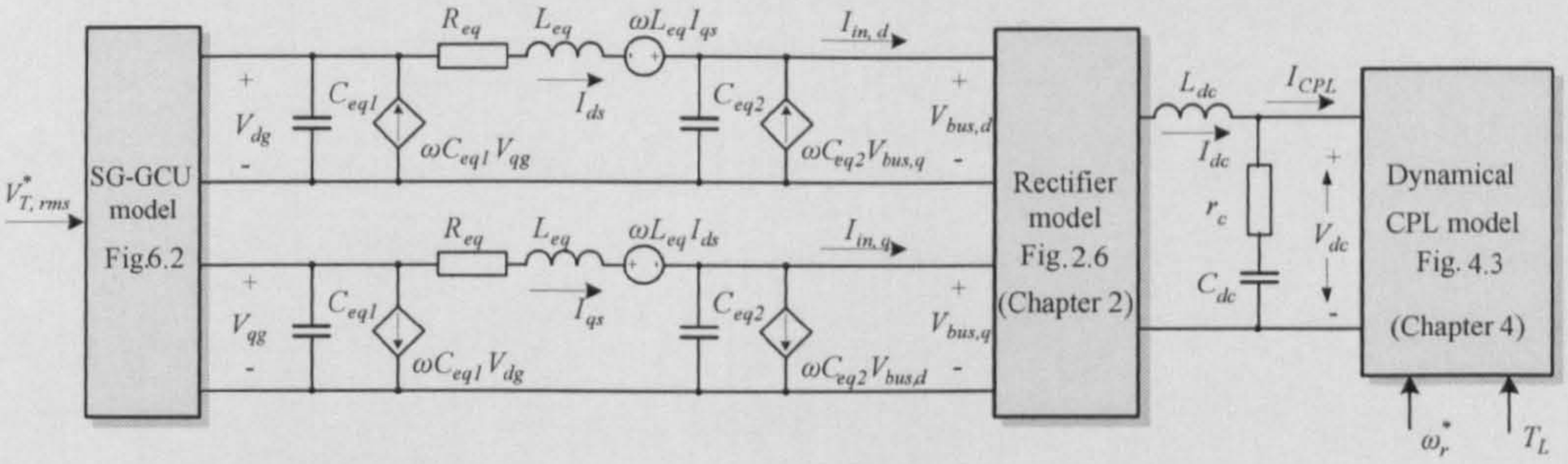

Figure 6.3: The power system model in dq frame

Figure 6.3 shows the input-output relations between different parts of the power system and these can be described in the form of non-linear differential equation for stability analysis. The non-linear set of equations to describe the SG under GCU control can be established according to the model given in Figure 6.2. This is a 7^{th} order system:

$$
\begin{aligned}
&-(L_{ls}+L_{md})\dot{I}_{dg}+L_{md}\dot{I}_{F}+L_{md}\dot{I}_{kd} = R_s I_{dg}-\omega(L_{ls}+L_{mq})I_{qg} \\
&\qquad\qquad + \omega L_{mq} I_{kq} + V_{dg} \\
&-L_{md}\dot{I}_{dg}+(L_{lF}+L_{md})\dot{I}_{F}+L_{md}\dot{I}_{kd}-K_{Pi}\dot{X}_{i} = -R_F I_F + K_{Ii} X_i \\
&-L_{md}\dot{I}_{dg}+L_{md}\dot{I}_{F}+(L_{lkd}+L_{md})\dot{I}_{kd} = -R_{kd} I_{kd} \\
&-(L_{ls}+L_{mq})\dot{I}_{qg}+L_{mq}\dot{I}_{kq} = \omega(L_{ls}+L_{md})I_{dg}-\omega L_{md} I_F - \omega L_{md} I_{kd} \\
&\qquad\qquad + R_s I_{qg} + V_{qg} \\
&-L_{mq}\dot{I}_{qg}+(L_{lkq}+L_{mq})\dot{I}_{kq} = -R_{kq} I_{kq} \\
&\dot{X}_e = V^{*}_{T,rms} - k_1\sqrt{V_{dg}^2+V_{qg}^2} \\
&-K_{Pv}\dot{X}_e+\dot{X}_i = -I_F + K_{Iv} X_e
\end{aligned}
\qquad (6\text{-}1)
$$

where the parameters are given in Table 6.1 and k_1 equal to $1/\sqrt{2}$ for the peak convention (see Appendix A) (the vector quantity is equal to the peak of the phase quantity).

The generator model interfaces to the cable model through the generator feeder voltage components V_{dg} and V_{qg}. Taking into account the derived model of Chapter 2 and the equivalent circuit in Figure 6.3, the dynamic behaviour of the cable section with the diode rectifier (Figure 2.6) and DC-link filters is an 8^{th} order nonlinear system:

$$\dot{V}_{dg} = C_{eq1}^{-1} I_{dg} + \omega V_{qg} - C_{eq1}^{-1} I_{ds}$$

$$\dot{V}_{qg} = C_{eq1}^{-1} I_{qg} - \omega V_{dg} - C_{eq1}^{-1} I_{qs}$$

$$\dot{I}_{ds} = L_{eq}^{-1} V_{dg} - R_{eq} L_{eq}^{-1} I_{ds} + \omega I_{qs} - L_{eq}^{-1} V_{bus,d}$$

$$\dot{I}_{qs} = L_{eq}^{-1} V_{qg} - \omega I_{ds} - R_{eq} L_{eq}^{-1} I_{qs} - L_{eq}^{-1} V_{bus,q}$$

$$\dot{V}_{bus,d} = C_{eq2}^{-1} I_{ds} + \omega V_{bus,q} - 2\sqrt{3}\pi^{-1} C_{eq2}^{-1} I_{dc} \cos(\delta + \gamma) \quad (6\text{-}2)$$

$$\dot{V}_{bus,q} = C_{eq2}^{-1} I_{qs} - \omega V_{bus,d} + 2\sqrt{3}\pi^{-1} C_{eq2}^{-1} I_{dc} \sin(\delta + \gamma)$$

$$\dot{I}_{dc} = -r_c C_{dc} L_{dc}^{-1} \dot{V}_{dc} + 3\sqrt{3}\pi^{-1} L_{dc}^{-1} V_{bus,d} \cos(\delta + \gamma)$$
$$- 3\sqrt{3}\pi^{-1} L_{dc}^{-1} V_{bus,q} \sin(\delta + \gamma) - 3\omega\pi^{-1} L_{eq} L_{dc}^{-1} I_{dc} - L_{dc}^{-1} V_{dc}$$

$$\dot{V}_{dc} = C_{dc}^{-1} I_{dc} - C_{dc}^{-1} I_{CPL}$$

In (6-2), the rectifier switching functions, S_d and S_q of (2-8) are used. Note that the rotating frame is placed at the SG rotor frame. Therefore, the switching function depends on the phase-shift between the rotor frame and the rectifier input terminal voltage frame ($\delta+\gamma$).

The remaining equations to describe the dynamics of the CPL (from Chapter 4) are summarized as:

$$J_m \dot{\omega}_r = K_T I_{sqm} - T_L$$

$$\tau_s R_{sm} \dot{I}_{sqm} = -PK_f \omega_r / 2 - (R_{sm} + \tau_r^{-1} I_{sdm}^{-1} K_f) I_{sqm} + V_{sqm}^* V_F^{-1} V_{dc} / 2$$

$$\tau_f \dot{V}_f = -V_f + V_{dc} / 2 \quad (6\text{-}3)$$

$$k_{Pim} k_{Iim}^{-1} \dot{I}_{sqm} + k_{Iim}^{-1} \dot{V}_{sqm}^* - k_{Pim} k_{Iim}^{-1} \dot{I}_{sqm}^* = -I_{sqm} + I_{sqm}^*$$

$$k_{P\omega} k_{I\omega}^{-1} \dot{\omega}_r + k_{I\omega}^{-1} \dot{I}_{sqm}^* - k_{P\omega} k_{I\omega}^{-1} \dot{\omega}_r^* = -\omega_r + \omega_r^*$$

The CPL current (I_{CPL}) in (6-2) is given in (4-24). This equation can be rewritten:

$$I_{CPL} = \frac{3}{4}\left[\frac{R_{sm}(I_{sdm}^{*})^2}{V_f} - \frac{[(P/2)\omega_r \sigma L_{sm} I_{sdm}^{*} - V_{sqm}^{*}]I_{sqm}}{V_f} - \frac{\sigma L_{sm} I_{sqm}^2}{\tau_r V_f}\right] \quad (6\text{-}4)$$

The set of equations (6-1)-(6-4) describes the non-linear dynamics of the power system in Figure 6.1. These equations can be used for fast computation of transient responses for different operation scenarios. For stability analysis, the equations can be linearized for small-signal perturbations. The 20th order nonlinear model (6-1)-(6-4) is linearized using a Taylor series expansion with subsequent neglect of high-order components. The linearized model takes the following matrix form:

$$\begin{aligned} \delta \dot{\mathbf{x}} &= \mathbf{A}(\mathbf{x}_0, \mathbf{u}_0)\delta\mathbf{x} + \mathbf{B}(\mathbf{x}_0, \mathbf{u}_0)\delta\mathbf{u} \\ \delta\mathbf{y} &= \mathbf{C}(\mathbf{x}_0, \mathbf{u}_0)\delta\mathbf{x} + \mathbf{D}(\mathbf{x}_0, \mathbf{u}_0)\delta\mathbf{u} \end{aligned} \quad (6\text{-}5)$$

where

$$\delta\mathbf{x} = [\delta I_{dg}, \delta I_F, \delta I_{kd}, \delta I_{qg}, \delta I_{kq}, \delta X_e, \delta X_i, \delta V_{dg}, \delta V_{qg}, \delta I_{ds}, \delta I_{qs}, \delta V_{bus,d}, \delta V_{bus,q}, \delta I_{dc}, \delta V_{dc}, \delta\omega_r, \delta I_{sqm}, \delta V_f, \delta V_{sqm}^{*}, \delta I_{sqm}^{*}]^T$$

$$\delta\mathbf{u} = [\delta V_{T,rms}^{*}, \delta\omega_r^{*}, \delta T_L]^T$$

$$\delta\mathbf{y} = [\delta V_{dc}]$$

and

$$\mathbf{A}(\mathbf{x}_0, \mathbf{u}_0) = \mathbf{H}^{-1}\mathbf{A}_1(\mathbf{x}_0, \mathbf{u}_0),\ \mathbf{B}(\mathbf{x}_0, \mathbf{u}_0) = \mathbf{H}^{-1}\mathbf{B}_1(\mathbf{x}_0, \mathbf{u}_0)$$

The constant matrices $\mathbf{A}_1(\mathbf{x}_0, \mathbf{u}_0)$, $\mathbf{B}_1(\mathbf{x}_0, \mathbf{u}_0)$, $\mathbf{C}(\mathbf{x}_0, \mathbf{u}_0)$, and $\mathbf{D}(\mathbf{x}_0, \mathbf{u}_0)$ depend on the chosen equilibrium point. The details of these matrixes and matrix $\mathbf{H}$ are given in (6-6).

$$\mathbf{H} = \begin{bmatrix}
-L_{ls}+L_{md} & L_{md} & L_{md} & 0 & 0 & 0 & 0 & 0&0&0&0&0&0&0 & 0 & 0&0&0&0&0\\
-L_{md} & L_{lF}+L_{md} & L_{md} & 0 & 0 & 0 & -K_{Pi} & 0&0&0&0&0&0&0 & 0 & 0&0&0&0&0\\
-L_{md} & L_{md} & L_{lkd}+L_{md} & 0 & 0 & 0 & 0 & 0&0&0&0&0&0&0 & 0 & 0&0&0&0&0\\
0 & 0 & 0 & -L_{ls}+L_{mq} & L_{mq} & 0 & 0 & 0&0&0&0&0&0&0 & 0 & 0&0&0&0&0\\
0 & 0 & 0 & -L_{mq} & L_{lkq}+L_{mq} & 0 & 0 & 0&0&0&0&0&0&0 & 0 & 0&0&0&0&0\\
0 & 0 & 0 & 0 & 0 & 1 & 0 & 0&0&0&0&0&0&0 & 0 & 0&0&0&0&0\\
0 & 0 & 0 & 0 & 0 & -K_{Pv} & 1 & 0&0&0&0&0&0&0 & 0 & 0&0&0&0&0\\
0 & 0 & 0 & 0 & 0 & 0 & 0 & 1&0&0&0&0&0&0 & 0 & 0&0&0&0&0\\
0 & 0 & 0 & 0 & 0 & 0 & 0 & 0&1&0&0&0&0&0 & 0 & 0&0&0&0&0\\
0 & 0 & 0 & 0 & 0 & 0 & 0 & 0&0&1&0&0&0&0 & 0 & 0&0&0&0&0\\
0 & 0 & 0 & 0 & 0 & 0 & 0 & 0&0&0&1&0&0&0 & 0 & 0&0&0&0&0\\
0 & 0 & 0 & 0 & 0 & 0 & 0 & 0&0&0&0&1&0&0 & 0 & 0&0&0&0&0\\
0 & 0 & 0 & 0 & 0 & 0 & 0 & 0&0&0&0&0&1&0 & 0 & 0&0&0&0&0\\
0 & 0 & 0 & 0 & 0 & 0 & 0 & 0&0&0&0&0&0&1 & r_c C_{dc} L_{dc}^{-1} & 0&0&0&0&0\\
0 & 0 & 0 & 0 & 0 & 0 & 0 & 0&0&0&0&0&0&0 & 1 & 0&0&0&0&0\\
0 & 0 & 0 & 0 & 0 & 0 & 0 & 0&0&0&0&0&0&0 & 0 & 1&0&0&0&0\\
0 & 0 & 0 & 0 & 0 & 0 & 0 & 0&0&0&0&0&0&0 & 0 & 0&1&0&0&0\\
0 & 0 & 0 & 0 & 0 & 0 & 0 & 0&0&0&0&0&0&0 & 0 & 0&0&1&0&0\\
0 & 0 & 0 & 0 & 0 & 0 & 0 & 0&0&0&0&0&0&0 & 0 & 0&0&0&1&0\\
0 & 0 & 0 & 0 & 0 & 0 & 0 & 0&0&0&0&0&0&0 & 0 & 0&0&0&0&1
\end{bmatrix}_{20\times 20}$$

$$\mathbf{A_1(x_o,u_o)} = \begin{bmatrix} \mathbf{A_g} & \mathbf{A_{DU}} & \mathbf{0} \\ \mathbf{A_{DL}} & \mathbf{A_D} & \mathbf{A_{Hm}} \\ \mathbf{0} & \mathbf{A_{Vm}} & \mathbf{A_m} \end{bmatrix}_{20\times 20}$$

$$\mathbf{B_1(x_o,u_o)} = \begin{bmatrix} \mathbf{B_g} \\ \mathbf{B_D} \\ \mathbf{B_m} \end{bmatrix}_{20\times 3}$$

$$\mathbf{C(x_o,u_o)} = \begin{bmatrix} 0 & 0 & 0 & 0 & 0 & 0 & 0 & 0 & 0 & 0 & 0 & 0 & 0 & 0 & 1 & 0 & 0 & 0 & 0 & 0 \end{bmatrix}_{1\times 20}$$

$$\mathbf{D(x_o,u_o)} = \begin{bmatrix} 0 & 0 & 0 \end{bmatrix}_{1\times 3} \qquad (6\text{-}6)$$

where

$$\mathbf{A_g} = \begin{bmatrix}
R_s & 0 & 0 & -\omega(L_{ls}+L_{mq}) & \omega L_{mq} & 0 & 0 \\
0 & -R_F & 0 & 0 & 0 & 0 & K_{Ii} \\
0 & 0 & -R_{kd} & 0 & 0 & 0 & 0 \\
\omega(L_{ls}+L_{md}) & -\omega L_{md} & -\omega L_{md} & R_s & 0 & 0 & 0 \\
0 & 0 & 0 & 0 & -R_{kq} & 0 & 0 \\
0 & 0 & 0 & 0 & 0 & 0 & 0 \\
0 & -1 & 0 & 0 & 0 & K_{Iv} & 0
\end{bmatrix}_{7\times 7}$$

$$\mathbf{A_{DU}} = \begin{bmatrix} 1 & 0 & 0 & 0 & 0 & 0 & 0 & 0 \\ 0 & 0 & 0 & 0 & 0 & 0 & 0 & 0 \\ 0 & 0 & 0 & 0 & 0 & 0 & 0 & 0 \\ 0 & 1 & 0 & 0 & 0 & 0 & 0 & 0 \\ 0 & 0 & 0 & 0 & 0 & 0 & 0 & 0 \\ -\frac{1}{\sqrt{2}}\frac{V_{dgo}}{\sqrt{V_{dgo}^2+V_{qgo}^2}} & -\frac{1}{\sqrt{2}}\frac{V_{qgo}}{\sqrt{V_{dgo}^2+V_{qgo}^2}} & 0 & 0 & 0 & 0 & 0 & 0 \\ 0 & 0 & 0 & 0 & 0 & 0 & 0 & 0 \end{bmatrix}_{7\times 8}$$

$$\mathbf{A_{DL}} = \begin{bmatrix} 1/C_{eq1} & 0 & 0 & 0 & 0 & 0 & 0 \\ 0 & 0 & 0 & 1/C_{eq1} & 0 & 0 & 0 \\ 0 & 0 & 0 & 0 & 0 & 0 & 0 \\ 0 & 0 & 0 & 0 & 0 & 0 & 0 \\ 0 & 0 & 0 & 0 & 0 & 0 & 0 \\ 0 & 0 & 0 & 0 & 0 & 0 & 0 \\ 0 & 0 & 0 & 0 & 0 & 0 & 0 \\ 0 & 0 & 0 & 0 & 0 & 0 & 0 \end{bmatrix}_{8\times 7}$$

$$\mathbf{A_D} = \begin{bmatrix} 0 & \omega & -1/C_{eq1} & 0 & 0 & 0 & 0 & 0 \\ -\omega & 0 & 0 & -1/C_{eq1} & 0 & 0 & 0 & 0 \\ 1/L_{eq} & 0 & -R_{eq}/L_{eq} & \omega & -1/L_{eq} & 0 & 0 & 0 \\ 0 & 1/L_{eq} & -\omega & -R_{eq}/L_{eq} & 0 & -1/L_{eq} & 0 & 0 \\ 0 & 0 & 1/C_{eq2} & 0 & 0 & \omega & -\frac{2\sqrt{3}}{\pi}\frac{\cos(\delta_o+\gamma_o)}{C_{eq2}} & 0 \\ 0 & 0 & 0 & 1/C_{eq2} & -\omega & 0 & \frac{2\sqrt{3}}{\pi}\frac{\sin(\delta_o+\gamma_o)}{C_{eq2}} & 0 \\ 0 & 0 & 0 & 0 & \frac{3\sqrt{3}}{\pi}\frac{\cos(\delta_o+\gamma_o)}{L_{dc}} & -\frac{3\sqrt{3}}{\pi}\frac{\sin(\delta_o+\gamma_o)}{L_{dc}} & -\frac{3\omega L_{eq}}{\pi L_{dc}} & -1/L_{dc} \\ 0 & 0 & 0 & 0 & 0 & 0 & 1/C_{dc} & 0 \end{bmatrix}_{8\times 8}$$

$$\mathbf{A_{Hm}} = \begin{bmatrix} 0 & 0 & 0 & 0 & 0 \\ 0 & 0 & 0 & 0 & 0 \\ 0 & 0 & 0 & 0 & 0 \\ 0 & 0 & 0 & 0 & 0 \\ 0 & 0 & 0 & 0 & 0 \\ 0 & 0 & 0 & 0 & 0 \\ 0 & 0 & 0 & 0 & 0 \\ \frac{3P\sigma L_{sm} I_{sqmo} I_{sdmo}}{8C_F V_{f,o}} & -\frac{3M_{qo}}{4C_F}+\frac{3\sigma L_{sm} I_{sqmo}}{4\tau_r C_F V_{f,o}}+\frac{3I_{sdmo}\sigma L_{sm}\omega_{eo}}{4C_F V_{f,o}} & \frac{3I_{sdmo}V_{sdmo}}{4C_F V_{f,o}^2}+\frac{3I_{sqmo}V_{sqmo}}{4C_F V_{f,o}^2} & -\frac{3I_{sqmo}}{4C_F V_{f,o}} & 0 \end{bmatrix}_{8\times 5}$$

$$\mathbf{A_{Vm}} = \begin{bmatrix} 0 & 0 & 0 & 0 & 0 & 0 & 0 & 0 \\ 0 & 0 & 0 & 0 & 0 & 0 & 0 & \dfrac{M_{qo}}{2\tau_s R_{sm}} \\ 0 & 0 & 0 & 0 & 0 & 0 & 0 & \dfrac{1}{2\tau_F} \\ 0 & 0 & 0 & 0 & 0 & 0 & 0 & -\dfrac{K_{Pim} M_{qo}}{2\tau_s R_{sm}} \\ 0 & 0 & 0 & 0 & 0 & 0 & 0 & 0 \end{bmatrix}_{5\times 8}$$

$$\mathbf{A_m} = \begin{bmatrix} 0 & \dfrac{K_T}{J_m} & 0 & 0 & 0 \\ -\dfrac{PK_f}{2\tau_s R_{sm}} & -\dfrac{1}{\tau_s} - \dfrac{K_f}{\tau_s R_{sm}\tau_r I_{sdmo}} & -\dfrac{V_{sqmo}}{\tau_s R_{sm} V_{f,o}} & \dfrac{1}{\tau_s R_{sm}} & 0 \\ 0 & 0 & -\dfrac{1}{\tau_F} & 0 & 0 \\ -K_{Pim}K_{I\omega} + \dfrac{PK_{Pim}K_f}{2\tau_s R_{sm}} & -K_{lim} - \dfrac{K_{Pim}K_{P\omega}K_T}{J_m} + \dfrac{K_{Pim}}{\tau_s} + \dfrac{K_{Pim}K_f}{\tau_s R_{sm}\tau_r I_{sdmo}} & \dfrac{K_{Pim}V_{sqmo}}{\tau_s R_{sm} V_{f,o}} & -\dfrac{K_{Pim}}{\tau_s R_{sm}} & K_{lim} \\ -K_{I\omega} & -\dfrac{K_{P\omega}K_T}{J_m} & 0 & 0 & 0 \end{bmatrix}_{5\times 5}$$

$$\mathbf{B_g} = \begin{bmatrix} 0 & 0 & 0 \\ 0 & 0 & 0 \\ 0 & 0 & 0 \\ 0 & 0 & 0 \\ 0 & 0 & 0 \\ 1 & 0 & 0 \\ 0 & 0 & 0 \end{bmatrix}_{7\times 3}, \quad \mathbf{B_D} = [\mathbf{0}]_{8\times 3}, \quad \mathbf{B_m} = \begin{bmatrix} 0 & 0 & -1/J_m \\ 0 & 0 & 0 \\ 0 & 0 & 0 \\ 0 & K_{Pim}K_{I\omega} & K_{Pim}K_{P\omega}/J_m \\ 0 & K_{I\omega} & K_{P\omega}/J_m \end{bmatrix}_{5\times 3}$$

6.5 Calculating the Steady-State Equilibrium Value

The dq linearized model from Section 6.4 is derived through the linearization technique around the operating point. According to (6-6), the linearized model needs to define V_{dgo}, V_{qgo}, δ_o, γ_o, I_{sqmo}, M_{qo}, V_{fo}, ω_{eo}, V_{sdmo}, and V_{sqmo} for the small-signal simulation and stability analysis. The power flow equation [72] can be applied to determine the steady-state value at the AC side. The single line power flow diagram of the power system in Figure 6.1 is depicted in Figure 6.4 in which the line capacitors are ignored assuming C_{eq1} and C_{eq2} are very small. L_s in Figure 6.4 equals to L_d (L_d=L_{ls}+L_{md}) [78].

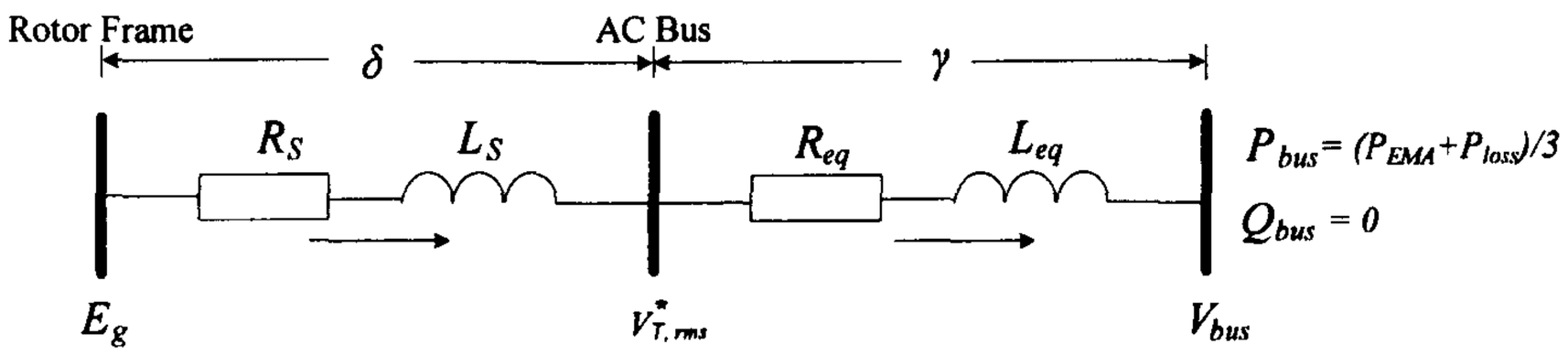

Figure 6.4: The single line diagram for steady state power calculations

Figure 6.4 leads to a system of four nonlinear equations:

$$
\begin{aligned}
&+\frac{V^*_{T,rms}V_{bus}}{Z_T}\cos(\gamma_T-\gamma)-\frac{V^2_{bus}}{Z_T}\cos(\gamma_T)=(P_{EMA}+P_{loss})/3\\
&+\frac{V^*_{T,rms}V_{bus}}{Z_T}\sin(\gamma_T-\gamma)-\frac{V^2_{bus}}{Z_T}\sin(\gamma_T)=0\\
&+\frac{E_gV_{bus}}{Z_{gT}}\cos(\gamma_{gT}-\delta-\gamma)-\frac{V^2_{bus}}{Z_{gT}}\cos(\gamma_{gT})=(P_{EMA}+P_{loss})/3\\
&+\frac{E_gV_{bus}}{Z_{gT}}\sin(\gamma_{gT}-\delta-\gamma)-\frac{V^2_{bus}}{Z_{gT}}\sin(\gamma_{gT})=0
\end{aligned}
\qquad (6\text{-}7)
$$

where V_{bus} is the steady state phase voltage at the input terminal of the diode rectifier (rms), E_g is the steady state phase induced voltage of the SG (rms), δ is the phase shift between the SG rotor axis and the feed voltage vector (AC bus), and γ is the phase shift between the feed voltage vector and the input terminal of the rectifier voltage vector. In addition, $Z_{gT}\angle\gamma_{gT}$ is the combination between SG stator and transmission line impedances and $Z_T\angle\gamma_T$ is the transmission line impedance. Assuming no loss in the diode rectifier, the active and reactive power (per phase) at the input terminal of the rectifier is given by:

$$
\begin{aligned}
P_{bus} &= (P_{EMA}-P_{loss})/3\\
Q_{bus} &= 0
\end{aligned}
\qquad (6\text{-}8)
$$

where P_{EMA} is the power delivered to the non-ideal CPL and P_{loss} is the power loss due to the DC-link inductor resistance. Q_{bus} is set to zero because of the diode rectifier assumption that the fundamental input current is in phase with the input voltage. Equation (6-7) can be solved by iteration using a numerical method such as Newton Raphson so as to get E_{go}, V_{buso}, δ_o, and γ_o at the steady state conditions. Consequently, V_{dco} can then be calculated using:

$$V_{dco}^2 - \frac{3\sqrt{3}}{\pi}(\sqrt{2}V_{buso})V_{dco} + P_{EMA}\frac{3\omega L_{eq}}{\pi} = 0 \qquad (6\text{-}9)$$

It can be seen that (6-9) is a quadratic equation. This equation has two solutions for V_{dco}. These values change when the system operating point, defined from P_{EMA}, changes. The steady state values from the solutions of (6-9) with the set of parameters in Table 6.1 are depicted in Figure 6.5.

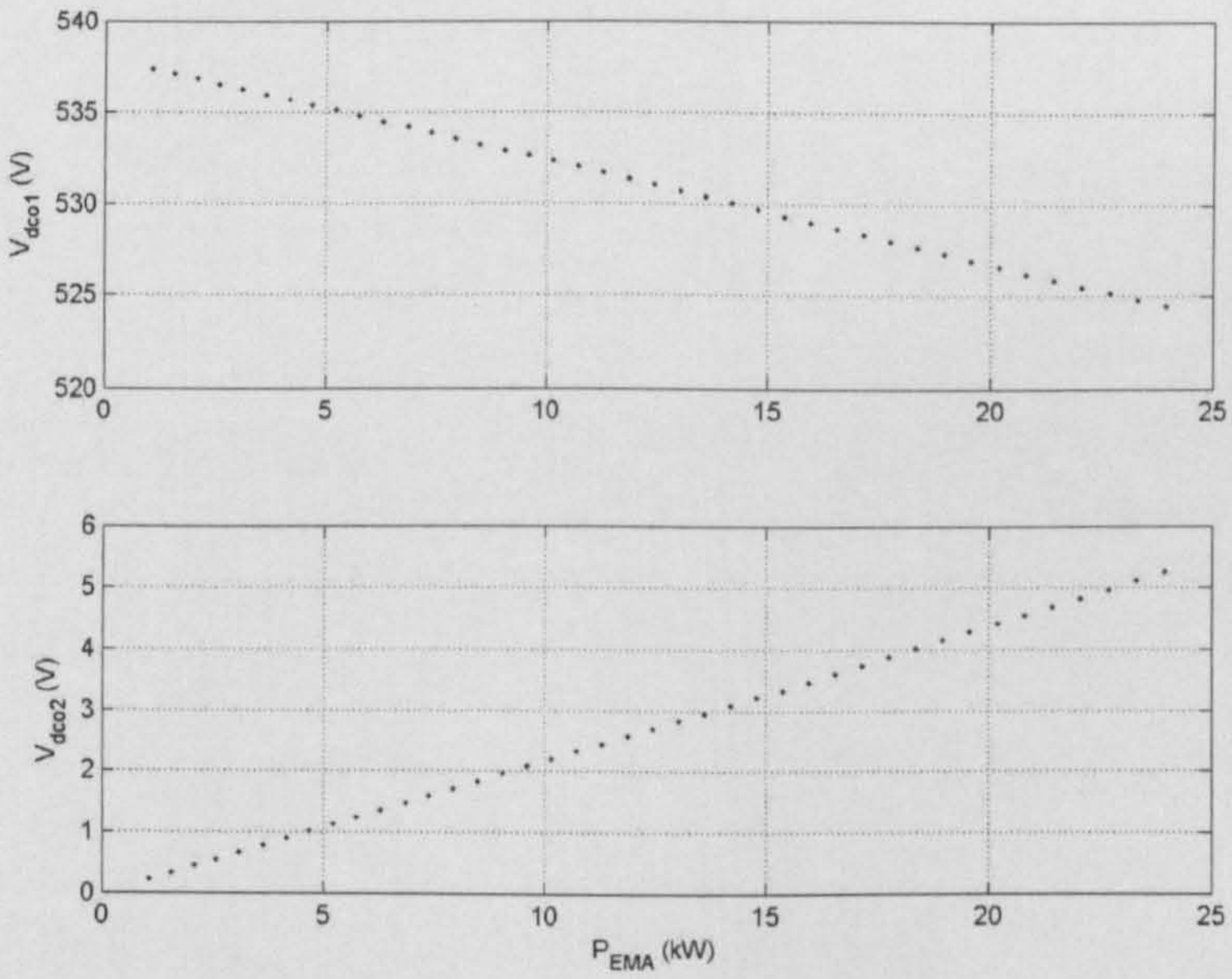

Figure 6.5: The steady state values of V_{dco1} and V_{dco2} as P_{EMA} varies

In Figure 6.5, the V_{dco2} solution is an impractical voltage level and will correspond to an unstable operating point. Therefore it is ignored and V_{dco1} is selected. Note that we can get different linearized models for the system in Figure 6.1 for each operating point.

Table 6.1: The set of parameters for the example system of Figure 6.1

Parameter	Value	Description
Synchronous Generator 111.9 kVA rated with GCU		
R_s	0.0044 Ω	stator resistance
L_{ls}	19.8943 μH	stator leakage inductance
L_{md}	220.164 μH	stator d-axis magnetizing inductance
L_{mq}	161.807 μH	stator q-axis magnetizing inductance
R_F	0.068884 Ω	field resistance
L_{lF}	32.83 μH	field leakage inductance
R_{kd}	0.0142 Ω	d-axis resistance
L_{lkd}	34.079 μH	d-axis leakage inductance
R_{kq}	0.003095 Ω	q-axis resistance
L_{lkq}	144.274 μH	q-axis leakage inductance
P_g	4 poles	number of poles in generator
$V_{T,rms}^*$	230 $V_{rms/phase}$	voltage command for GCU
ω	2π×400 rad/s	source frequency
$\omega_{n,\ voltage}$	15 Hz (K_{Pv}=1.78, K_{Iv}=227.02)	natural frequency of voltage loop in GCU
$\omega_{n,\ current}$	100 Hz (K_{Pi}=0.0487, K_{Ii}=99.88)	natural frequency of current loop in GCU
R_{eq}	0.1 Ω	transmission line resistance
L_{eq}	24 μH	transmission line inductance
C_{eq1} *and* C_{eq2}	2 nF	transmission line capacitance
L_{dc}	2 mH	dc link inductance
r_c	0 Ω	ESR_c
C_{dc}	500 μF	dc link capacitance
Actuator drive 20 kW rated		
ω_r^*	975 rpm	speed reference
$T_{L,rated}$	190 Nm	rated load torque
R_{sm}	0.6 Ω	stator resistance
L_{sm}	30.39 mH	stator leakage inductance
R_r	0.159 Ω	rotor resistance
L_r	30.39 mH	rotor leakage inductance
L_m	29.03 mH	magnetizing inductance
P	6 poles	number of poles in the machine
J_m	0.281 kgm^2	moment of inertia
I_{sdm}	34.115 A	d-axis current for rated flux
τ_F	0.02 sec.	filtering time constant
$\omega_{n,\ speed}$	20 Hz ($K_{P\omega}$=13.27, $K_{I\omega}$=1042.33)	natural frequency of speed loop
$\omega_{n,\ current}$	200 Hz (K_{Pi}=4.75, K_{Ii}=4199.14)	natural frequency of current loop

The steady state dc current I_{dco} can be calculated by using:

$$I_{dco} = \frac{P_{EMA}}{V_{dco}} \tag{6-10}$$

The steady state value of the SG terminal voltage at the feeder bus can be calculating by using:

$$\begin{aligned} V_{dgo} &= R_{eq} I_{dso} - \omega L_{eq} I_{qso} + V_{bus,do} \\ V_{qgo} &= R_{eq} I_{qso} + \omega L_{eq} I_{dso} + V_{bus,qo} \end{aligned} \tag{6-11}$$

where

$$V_{bus,do} = \sqrt{2} V_{buso} \cos(\delta_o + \gamma_o)$$

$$V_{bus,qo} = -\sqrt{2} V_{buso} \sin(\delta_o + \gamma_o)$$

$$I_{in,do} = \frac{2\sqrt{3}}{\pi} \cos(\delta_o + \gamma_o) I_{dco}$$

$$I_{in,qo} = -\frac{2\sqrt{3}}{\pi} \sin(\delta_o + \gamma_o) I_{dco}$$

$$I_{dso} = I_{in,do} - \omega C_{eq2} V_{bus,qo}$$

$$I_{qso} = I_{in,qo} + \omega C_{eq2} V_{bus,do}$$

The remaining equations for calculating V_{fo}, I_{sqmo}, V_{sdmo}, V_{sqmo}, ω_{eo}, and M_{qo} are the same as those in Chapter 4. The steady state values depend on the operating point defined from ω_{ro} and T_{Lo}.

6.6 Small-Signal Simulation and Stability Analysis

The linearized model (6-5) was simulated for small-signal transients against a corresponding 3-phase benchmark circuit model simulated in SABER. The details of SABER model for the system in Figure 6.1 are given in Appendix D.8. The example system parameters are given in Table 6.1. Figure 6.6 shows the V_{dc} response of the system of Figure 6.1 to a step change of load torque from 100 to 110 Nm that occurs at t=0.6 s with a constant speed of 975 rpm.

An excellent agreement between both models is achieved under small-signal simulation.

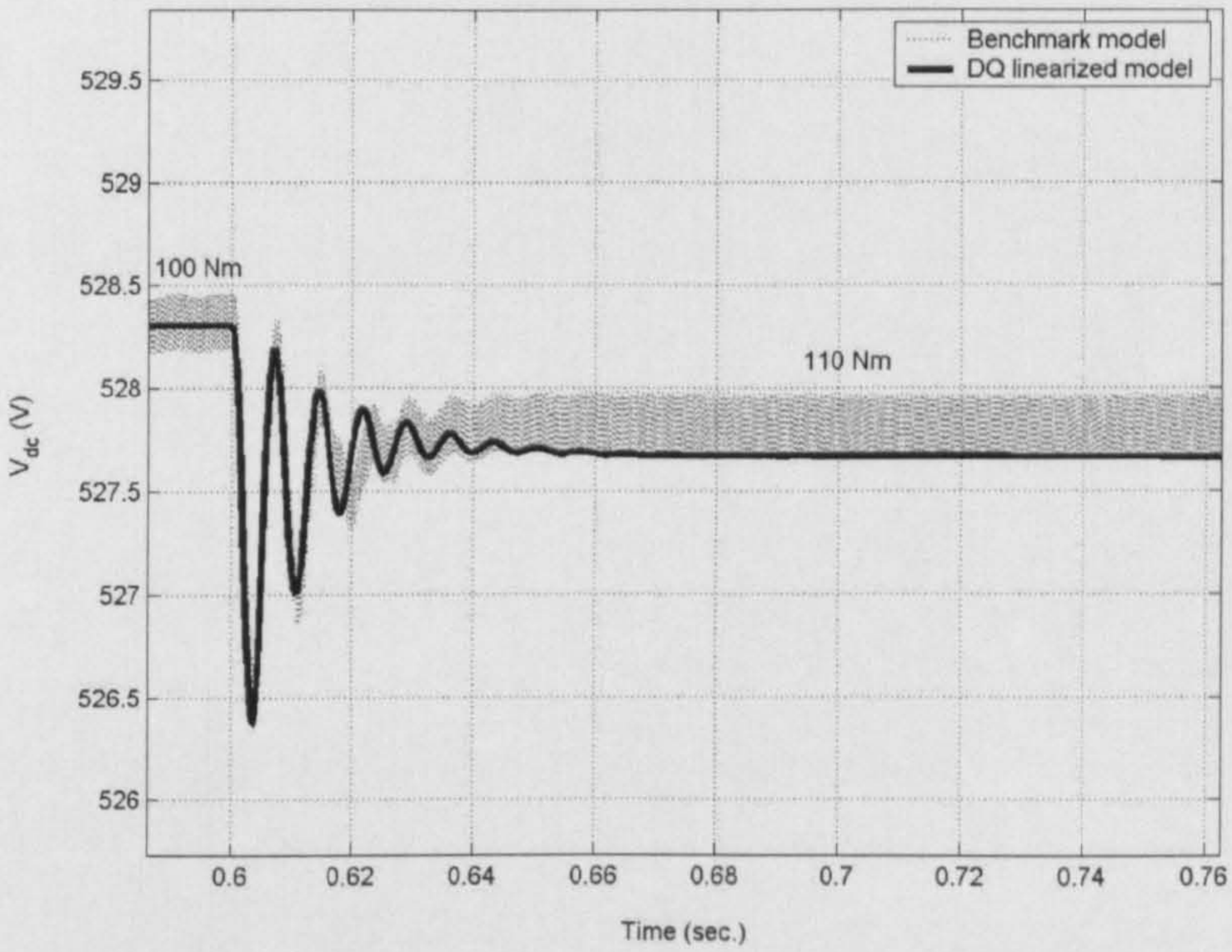

Figure 6.6: Verification for changing T_L from 100 to 110 Nm

In respect of stability analysis, the linearized model from the dq modelling approach is used with the eigenvalue theorem. The eigenvalues can be calculated from the Jacobian matrix $\mathbf{A}(\mathbf{x_0}, \mathbf{u_0})$ in (6-5). The eigenvalues of the linearized $\mathbf{A}(\mathbf{x_0}, \mathbf{u_0})$ matrix for the power system with parameters in Table 6.1 were analyzed for the case when the load torque T_L varies from 0 to 400 Nm at the constant actuator speed reference 975 rpm. This corresponds to the steady-state value of P_{EMA} varying from 1.047 to 51.76 kW. This root locus is shown in Figure 6.7 and some eigenvalues cross into the right hand plane. Figure 6.8 shows the zoomed area of interest: as one can see, the system becomes unstable when the P_{EMA} exceeds 37.925 kW for the studied case.

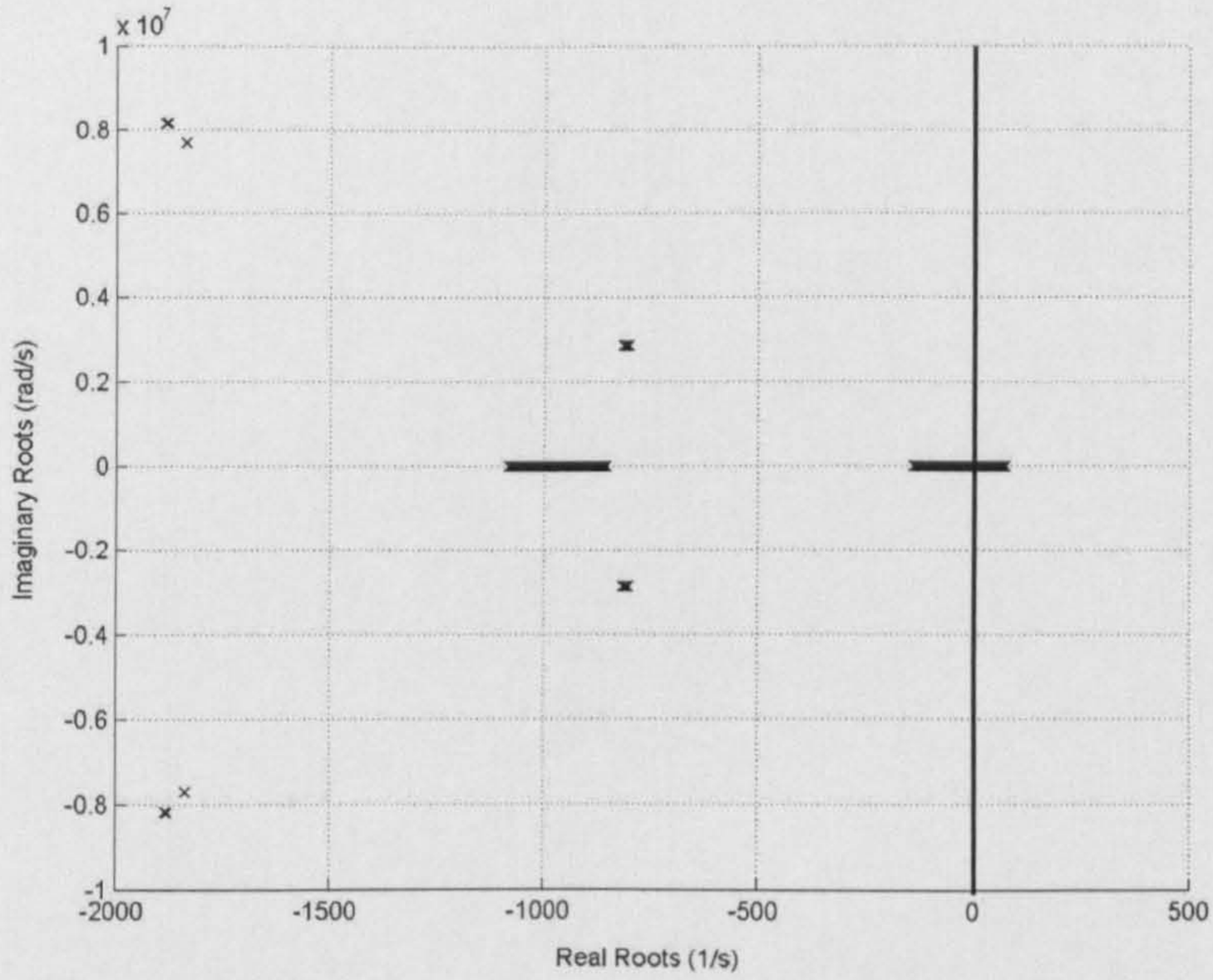

Figure 6.7: Eigenvalue plot from dq linearized model (P_{EMA} varies from 1.047 kW to 51.76 kW)

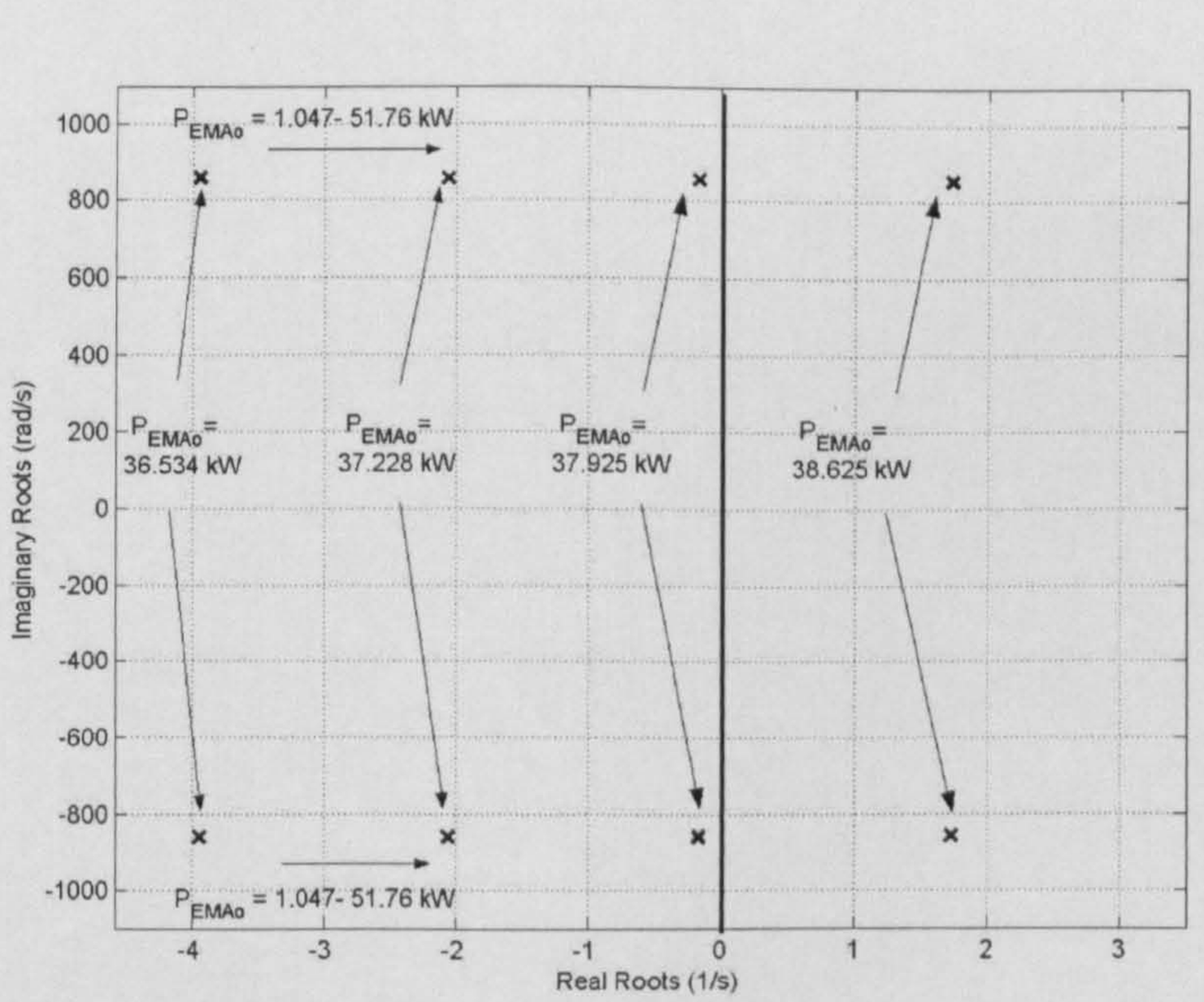

Figure 6.8: Zoomed area of interest from Figure 6.8

Figure 6.9 shows the SABER time-domain benchmark simulations (see Appendix D.8) that confirm the theoretical result with the instability occurring

at P_{EMA} of 38.625 kW. This is greater than the 37.925 kW for the unstable condition.

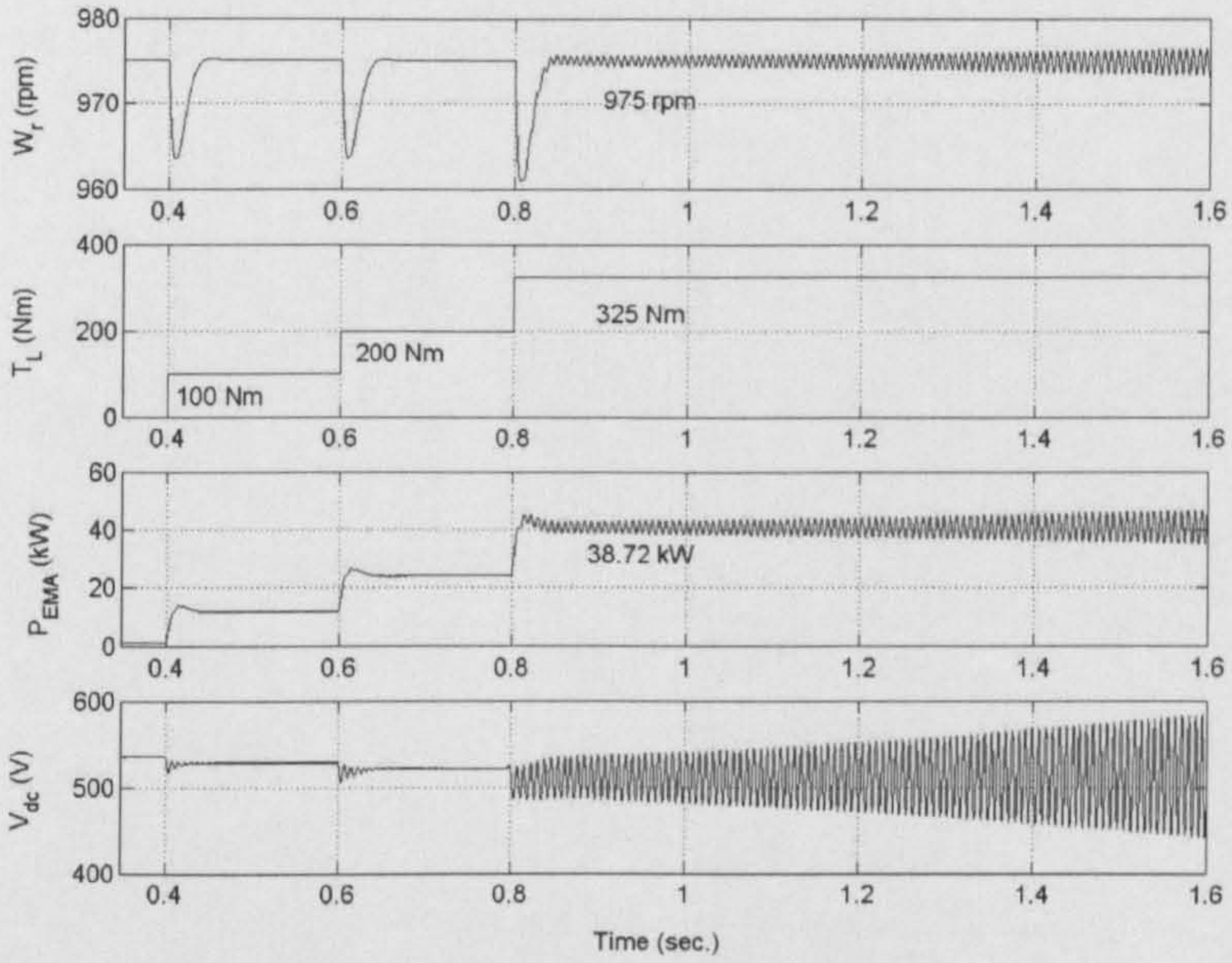

Figure 6.9: Step response for operating point (P_{EMA}) variations

The impact of using the dynamic models for the SG-GCU and non-ideal CPL in comparison with the models using an ideal voltage source and ideal CPL is shown in Table 6.2. The values are taken from mathematical eigenvalue value analysis with parameters given in Table 6.1.

Table 6.2: The effect of SG-GCU and Actuator Dynamics on Stability

Power System with	**Model Dimension**	**Instability Power (kW)**
Ideal voltage source and ideal CPL	8	> 16.00
SG-GCU and ideal CPL	15	> 18.00
Ideal voltage source and dynamic CPL	13	> 35.84
SG-GCU and dynamic CPL	20	> 37.93

The table shows the power level at which instability occurs. It is seen that the incorporation of SG-GCU dynamics has relatively small effect, but the impact of the non-ideal CPL (dynamic CPL) is significant. Neglecting CPL dynamics may be beneficial from the viewpoint of power system availability, but may

result in very non-optimal design solutions that would impact on overall mass and dimension. The model also allows convenient stability analysis including effect of parameter variations in different operational regimes. These will be described in Section 6.7.

6.7 Investigating Stability due to Variations in System Parameters

In this section, the dynamic model is used to predict instability for variations in system parameters. For variations in system frequency, DC-link filter L_{dc} and C_{dc}, filtering time constant τ_F, and natural frequency of speed loop in EMA ($\omega_{n,speed}$), the trend of instability results are the same as those of the previous chapter in which a higher system frequency, smaller L_{dc}, higher C_{dc}, smaller τ_F, and lower $\omega_{n,\,speed}$ all increase the power level at which instability occurs. In this chapter, the dynamic of SG-GCU is considered instead of the ideal voltage source. Therefore, it is very interesting to study the effect of the natural frequency of the voltage loop in GCU. The PI voltage controller is designed for various natural frequencies with constant damping. Figure 6.10 shows the analytical results in the form of eigenvalue loci and the CPL power limit for instability as the natural frequency of the voltage loop is varied and other parameters are fixed as given in Table 6.1. The faster the GCU voltage control the less the power level at which instability occurs. Figure 6.10 also confirms the results of Table 6.2. The variation of threshold CPL level for instability is not large. The analytical results in Figure 6.10 are supported by the SABER benchmark simulation (see Appendix D.8) as shown in Figure 6.11. The top graph shows the changing of P_{EMA}, and the graphs below show the V_{dc} response for different natural frequency of the voltage loop in GCU, here equal to 15 and 45 Hz. Good agreement between both models is achieved.

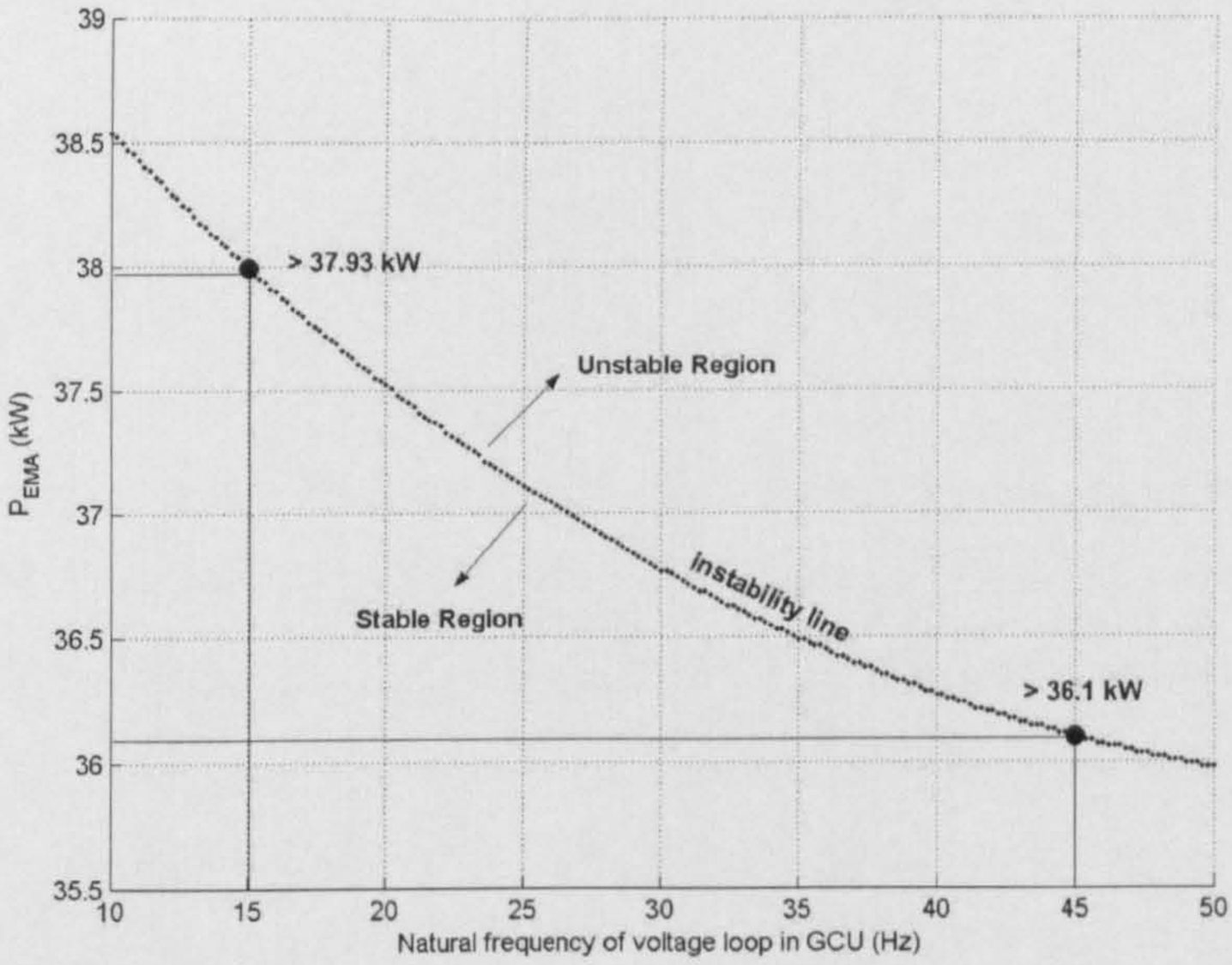

Figure 6.10: Instability power for natural frequency of voltage loop in GCU variations

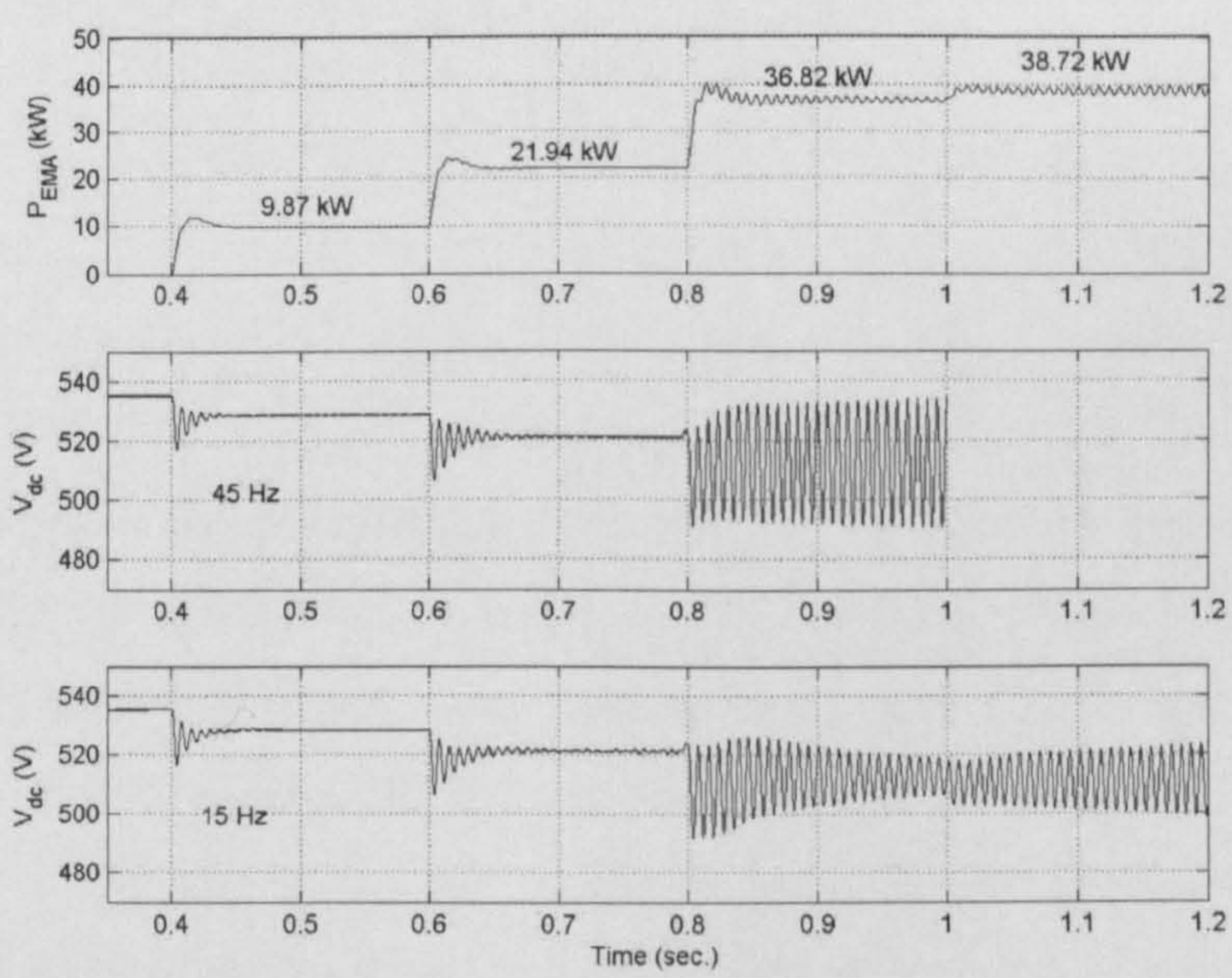

Figure 6.11: Verification of analytical results for natural frequency of voltage loop in GCU variations

6.8 Chapter Summary

This chapter deals with the stability analysis of a power system taking into account the dynamics of the synchronous generator with generator control unit (SG-GCU) and the dynamics of the electromechanical actuators (EMAs). The dynamics of SG-GCU have been previously represented as an ideal voltage source without dynamic behaviour. The dq modelling method with the eigenvalue theorem is used to analyse the stability. The results show that the effect of CPL dynamics is significant, while the effect of SG-GCU dynamics is small. In addition, this chapter also describes the stability analysis for parameter variations of different operational regimes. The results show that the effect of the natural frequency of the voltage loop in the GCU is small in terms of stability. As a result, the dynamics of SG-GCU can be neglected for stability analysis of more complex power system as will be described in Chapter 7, to simplify the mathematical model. Moreover, as described in Chapter 3, if the controlled PWM rectifier is analysed, the vector-control is in terms of the reference frame aligned to the AC bus voltage vector. Due to the dq frame aligned on this AC bus voltage vector, it is very difficult to analyse the power system including both the SG-GCU and the controlled PWM rectifier. This is because the parameters of the generator model become time-varying parameters (depending on the rotor position), when the dq frame of the model is not aligned to the rotor axis. In this chapter it was shown that the dynamics of SG-GCU has negligible effects on stability. Therefore, the dynamics will be neglected for analysing more complex power systems in Chapter 7. The stability analysis of the power system representing real architectures with multiplicity of actuators, aircraft loads and bus geometries will be described with the mathematical model of generalized aircraft power systems in which an ideal voltage source represents the SG-GCU.

Chapter 7

The Mathematical Model of Generalized Aircraft Power Systems for Stability Studies

7.1 Introduction

According to the previous chapters, the results show that the dq modelling approach can predict the instability point of a power system with constant power loads with good accuracy. The simulation and experimental results are used to support and validate the theoretical results. The dq modelling method can be also easily applied for modelling the power system comprising vector-controlled converters such as the controlled PWM rectifier as described in Chapter 3 and the electromechanical actuator drive systems as described in Chapter 4. Moreover, the power converter model derived from the dq modelling approach can be easily combined with models of other power elements expressed in terms of synchronously rotating frames such as a synchronous generator with generator control unit (SG-GCU) as described in Chapter 6. The stability analysis using the dq modelling method for more complex power systems is described in this chapter.

Generally, most research work for stability studies focuses on only an individual converter for its stand-alone operation. The dynamic models of multi-converter systems have been studied for DC distribution system in [59]. Studies for AC distribution system have not been reported. In addition, the interconnection of the converters can affect power quality and system stability [43],[59]. Therefore, this chapter extends the work from the previous chapters

to create the dynamic model of a more generalized aircraft power system representing real architectures with multiplicity of actuators, aircraft loads and bus geometries using the dq modelling approach. As mentioned in Chapter 6, the effect of SG-GCU dynamics is small [76]. Hence, SG-GCU is represented as an ideal voltage source for the generalized aircraft power system. Three example systems including the candidate aircraft power system as described in Chapter 1 are used to illustrate how to apply the more generalized model for a stability study. It is also shown how the theory can be used to predict instability due to possible variations in operating points and system parameters. The simulation results are used to support the theoretical results.

7.2 Generalized Aircraft Power Systems and Dynamic Models

This section introduces the generalized aircraft power system based on the real aircraft power system architecture as detailed in Chapter 1. The generalized aircraft power system for one engine generator is depicted in Figure 7.1 in which a three-phase ideal voltage source is used to represent a SG-GCU. The elements R_{eq1}, L_{eq1}, and C_{eq1} are the equivalent parameters of the transmission line1 between the generator bus (called Gen bus in Figure 7.1) and the HVAC bus; this constitutes the $230V_{rms}$ AC frequency-wild system. R_{TRUj}, L_{TRUj}, and C_{TRUj} represent the AC cable link between the HVAC bus and the input terminal of the diode rectifier bus. If an autotransformer-rectifier unit (ATRU) is used, these elements will be represented by the equivalent transformer impedance including the AC cable. The DC link filters for the diode rectifiers are shown by elements r_{LFj}, L_{Fj}, r_{CFj}, and C_{Fj}. The ideal constant power loads $P_{idealCPL,De}$ may represent other DC loads with regulated DC/DC power converters that can be assumed to have an infinitely fast controller action. The dynamics of constant power loads $P_{dynCPL,Dn}$ as described in Chapter 4 represent the actuator drive systems for DC environmental controls fed through the diode rectifiers. R_{eq2}, L_{eq2}, and C_{eq2} are represented as the transmission line2 parameters between the HVAC bus and the AC essential

bus (AC ESS bus). R_{conk} and L_{conk} are the AC filter parameters for the controlled PWM rectifiers. The PWM converters consist of vector-controllers to keep the voltage across the DC-link constant, here regulated to $V^*_{CF,conl}$ voltage commands, and to keep a unity power factor at the AC ESS bus by setting $I_{qk}{}^*$ equal to zero. The vector-control is in terms of the reference frame aligned to the AC ESS bus voltage vector. Therefore, the generalized aircraft power system in Figure 7.1 can be represented in the dq frame aligned to the AC ESS bus voltage vector. The $P_{idealCPL,Pg}$ and $P_{dynCPL,Pa}$ are the ideal and dynamic CPLs, respectively to represent other aircraft loads for ailerons, rudders, flaps, and elevators. These CPLs are fed through the controlled PWM rectifiers. The resistive and inductive loads R_{Lb} and L_{Lb} represent the electrical wing de-icng connected to the HVAC bus.

In Figure 7.1, we define the following subscripts:

j = the number of diode rectifier units

e= the number of ideal CPLs connected to diode rectifier units

n = the number of dynamic CPLs connected to diode rectifier units

k = the number of controlled PWM rectifier units

g = the number of ideal CPLs connected to controlled PWM rectifier units

a = the number of dynamic CPLs connected to controlled PWM rectifier units

b = the number of resistive and inductive loads

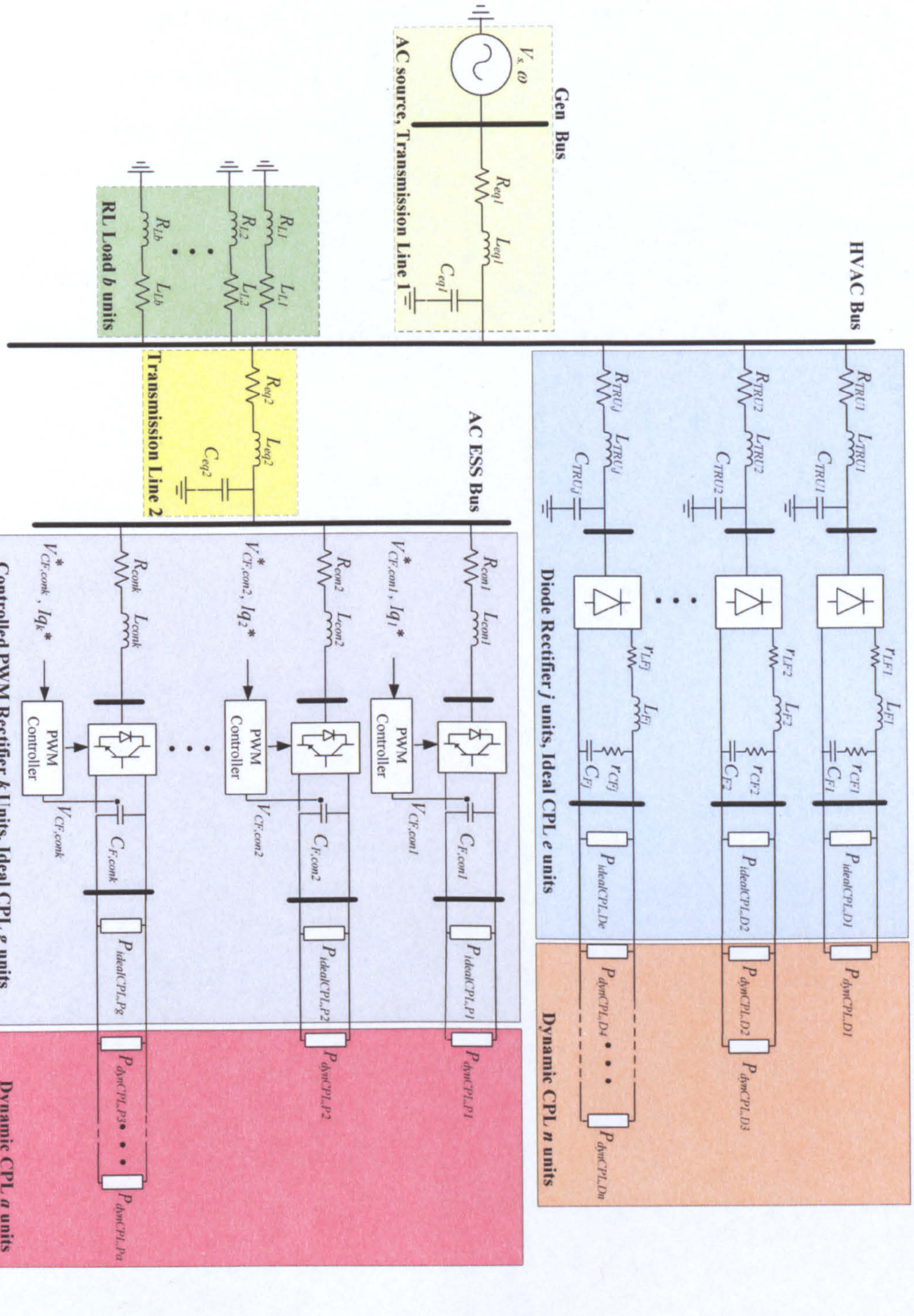

Figure 7.1: The generalized aircraft power system architecture

The dq modelling approach is used to model the power converter such as the diode rectifier (Chapter 2) and controlled PWM rectifier (Chapter 3). According to the previous chapters, this method provides the large-signal

nonlinear model of the AC-DC power system. The large signal model can be linearized for analysing the small-signal stability. The linearized model for the power system including diode rectifiers (Chapter 2), controlled PWM rectifiers (Chapter 3), electromechanical actuator drive systems (Chapter4) is used to obtain the linearized model for the generalized aircraft power system in Figure 7.1 in the dq frame. The dq linearized model of generalized aircraft power systems is of the following form:

$$\begin{aligned} \delta \dot{\mathbf{x}} &= \mathbf{A}(\mathbf{x_o},\mathbf{u_o})\delta\mathbf{x} + \mathbf{B}(\mathbf{x_o},\mathbf{u_o})\delta\mathbf{u} \\ \delta\mathbf{y} &= \mathbf{C}(\mathbf{x_o},\mathbf{u_o})\delta\mathbf{x} + \mathbf{D}(\mathbf{x_o},\mathbf{u_o})\delta\mathbf{u} \end{aligned} \tag{7-1}$$

where the colour blocks are used to represent the elements for each part of the generalized power system in Figure 7.1. The state variable, input, and output vectors in (7-1) can be represented with the different colour blocks as shown below:

$$\begin{aligned}
\delta\mathbf{x} = [&\delta I_{d,eq1}\ \delta I_{q,eq1}\ \delta V_{d,eq1}\ \delta V_{q,eq1}\ |\ \delta I_{d,TRU1}\ \delta I_{q,TRU1}\ \delta V_{d,TRU1}\ \delta V_{q,TRU1}\ \delta I_{LF1}\ \delta V_{CF1}\ |\\
&\delta\omega_{r,D1}\ \delta I_{sqm,D1}\ \delta V_{f,D1}\ \delta V^{*}_{sqm,D1}\ \delta I^{*}_{sqm,D1}\ |\ \delta I_{d,TRU2}\ \delta I_{q,TRU2}\ \delta V_{d,TRU2}\ \delta V_{q,TRU2}\ \delta I_{LF2}\ \delta V_{CF2}\ |\\
&\delta\omega_{r,D2}\ \delta I_{sqm,D2}\ \delta V_{f,D2}\ \delta V^{*}_{sqm,D2}\ \delta I^{*}_{sqm,D2}\ |\ \delta\omega_{r,D3}\ \delta I_{sqm,D3}\ \delta V_{f,D3}\ \delta V^{*}_{sqm,D3}\ \delta I^{*}_{sqm,D3}\ |\\
\cdots&\delta I_{d,TRUj}\ \delta I_{q,TRUj}\ \delta V_{d,TRUj}\ \delta V_{q,TRUj}\ \delta I_{LFj}\ \delta V_{CFj}\ |\ \delta\omega_{r,D4}\ \delta I_{sqm,D4}\ \delta V_{f,D4}\ \delta V^{*}_{sqm,D4}\ \delta I^{*}_{sqm,D4}\ |\\
\cdots&\delta\omega_{r,Dn}\ \delta I_{sqm,Dn}\ \delta V_{f,Dn}\ \delta V^{*}_{sqm,Dn}\ \delta I^{*}_{sqm,Dn}\ |\ \delta I_{d,eq2}\ \delta I_{q,eq2}\ \delta V_{d,eq2}\ \delta V_{q,eq2}\ |\\
&\delta I_{d,con1}\ \delta I_{q,con1}\ \delta X_{e,con1}\ \delta X_{d,con1}\ \delta X_{q,con1}\ \delta V_{CF,con1}\ |\ \delta\omega_{r,P1}\ \delta I_{sqm,P1}\ \delta V_{f,P1}\ \delta V^{*}_{sqm,P1}\ \delta I^{*}_{sqm,P1}\ |\\
&\delta I_{d,con2}\ \delta I_{q,con2}\ \delta X_{e,con2}\ \delta X_{d,con2}\ \delta X_{q,con2}\ \delta V_{CF,con2}\ |\ \delta\omega_{r,P2}\ \delta I_{sqm,P2}\ \delta V_{f,P2}\ \delta V^{*}_{sqm,P2}\ \delta I^{*}_{sqm,P2}\ |\\
\cdots&\delta I_{d,conk}\ \delta I_{q,conk}\ \delta X_{e,conk}\ \delta X_{d,conk}\ \delta X_{q,conk}\ \delta V_{CF,conk}\ |\ \delta\omega_{r,P3}\ \delta I_{sqm,P3}\ \delta V_{f,P3}\ \delta V^{*}_{sqm,P3}\ \delta I^{*}_{sqm,P3}\ |\\
\cdots&\delta\omega_{r,Pa}\ \delta I_{sqm,Pa}\ \delta V_{f,Pa}\ \delta V^{*}_{sqm,Pa}\ \delta I^{*}_{sqm,Pa}\ |\ \delta I_{d,L1}\ \delta I_{q,L1}\ |\ \delta I_{d,L2}\ \delta I_{q,L2}\ \cdots\ \delta I_{d,Lb}\ \delta I_{q,Lb}\ ]^{T}
\end{aligned}$$

$$\begin{aligned}
\delta\mathbf{u} = [&\delta V_{s}\ |\ \delta P_{CPL,D1}\ \delta\omega^{*}_{rD1}\ \delta T_{LD1}\ |\\
&\delta P_{CPL,D2}\ \delta\omega^{*}_{rD2}\ \delta T_{LD2}\ |\ \delta\omega^{*}_{rD3}\ \delta T_{LD3}\ |\\
\cdots&\delta P_{CPL,De}\ |\ \delta\omega^{*}_{rD4}\ \delta T_{LD4}\ \cdots\ \delta\omega^{*}_{rDn}\ \delta T_{LDn}\ |\\
&\delta E^{*}_{1}\ \delta I^{*}_{q1}\ \delta P_{CPL,P1}\ |\ \delta\omega^{*}_{rP1}\ \delta T_{LP1}\ |\\
&\delta E^{*}_{2}\ \delta I^{*}_{q2}\ \delta P_{CPL,P2}\ |\ \delta\omega^{*}_{rP2}\ \delta T_{LP2}\ |\\
\cdots&\delta E^{*}_{k}\ \delta I^{*}_{qk}\ \delta P_{CPL,Pg}\ |\ \delta\omega^{*}_{rP3}\ \delta T_{LP3}\ \cdots\ \delta\omega^{*}_{rPa}\ \delta T_{LPa}\ ]^{T}
\end{aligned}$$

$$\begin{aligned}
\delta\mathbf{y} = [&\delta V_{CF1}\ \delta V_{CF2}\ \cdots\ \delta V_{CFj}\ |\\
&\delta V_{CF,con1}\ \delta V_{CF,con2}\ \cdots\ \delta V_{CF,conk}\ ]^{T}
\end{aligned}$$

(7-2)

and

$$\mathbf{A}(\mathbf{x_o},\mathbf{u_o}) = \mathbf{H}^{-1}\mathbf{A}_1(\mathbf{x_o},\mathbf{u_o}),\ \mathbf{B}(\mathbf{x_o},\mathbf{u_o}) = \mathbf{H}^{-1}\mathbf{B}_1(\mathbf{x_o},\mathbf{u_o}) \tag{7-3}$$

The constant matrices $\mathbf{A_1(x_o,u_o)}$, $\mathbf{B_1(x_o,u_o)}$, $\mathbf{C(x_o,u_o)}$, and $\mathbf{D(x_o,u_o)}$ depend on the chosen equilibrium point. The form of these matrixes and matrix $\mathbf{H}$ are given by:

$$\mathbf{H} = \begin{bmatrix}
\mathbf{I_S} & 0 & 0 & 0 & 0 & 0 & \cdots & 0 & 0 & \cdots & 0 & 0 & 0 & 0 & 0 & 0 & \cdots & 0 & 0 & \cdots & 0 & 0 & 0 & \cdots & 0 \\
0 & \mathbf{H_{D1}} & 0 & 0 & 0 & 0 & \cdots & 0 & 0 & \cdots & 0 & 0 & 0 & 0 & 0 & 0 & \cdots & 0 & 0 & \cdots & 0 & 0 & 0 & \cdots & 0 \\
0 & 0 & \mathbf{I_m} & 0 & 0 & 0 & \cdots & 0 & 0 & \cdots & 0 & 0 & 0 & 0 & 0 & 0 & \cdots & 0 & 0 & \cdots & 0 & 0 & 0 & \cdots & 0 \\
0 & 0 & 0 & \mathbf{H_{D2}} & 0 & 0 & \cdots & 0 & 0 & \cdots & 0 & 0 & 0 & 0 & 0 & 0 & \cdots & 0 & 0 & \cdots & 0 & 0 & 0 & \cdots & 0 \\
0 & 0 & 0 & 0 & \mathbf{I_m} & 0 & \cdots & 0 & 0 & \cdots & 0 & 0 & 0 & 0 & 0 & 0 & \cdots & 0 & 0 & \cdots & 0 & 0 & 0 & \cdots & 0 \\
0 & 0 & 0 & 0 & 0 & \mathbf{I_m} & \cdots & 0 & 0 & \cdots & 0 & 0 & 0 & 0 & 0 & 0 & \cdots & 0 & 0 & \cdots & 0 & 0 & 0 & \cdots & 0 \\
\vdots & \vdots & \vdots & \vdots & \vdots & \vdots & \ddots & \vdots & \vdots & \ddots & \vdots & \vdots & \vdots & \vdots & \vdots & \vdots & \ddots & \vdots & \vdots & \ddots & \vdots & \vdots & \vdots & \ddots & \vdots \\
0 & 0 & 0 & 0 & 0 & 0 & \cdots & \mathbf{H_{Dj}} & 0 & \cdots & 0 & 0 & 0 & 0 & 0 & 0 & \cdots & 0 & 0 & \cdots & 0 & 0 & 0 & \cdots & 0 \\
0 & 0 & 0 & 0 & 0 & 0 & \cdots & 0 & \mathbf{I_m} & \cdots & 0 & 0 & 0 & 0 & 0 & 0 & \cdots & 0 & 0 & \cdots & 0 & 0 & 0 & \cdots & 0 \\
\vdots & \vdots & \vdots & \vdots & \vdots & \vdots & \ddots & \vdots & \vdots & \ddots & \vdots & \vdots & \vdots & \vdots & \vdots & \vdots & \ddots & \vdots & \vdots & \ddots & \vdots & \vdots & \vdots & \ddots & \vdots \\
0 & 0 & 0 & 0 & 0 & 0 & \cdots & 0 & 0 & \cdots & \mathbf{I_m} & 0 & 0 & 0 & 0 & 0 & \cdots & 0 & 0 & \cdots & 0 & 0 & 0 & \cdots & 0 \\
0 & 0 & 0 & 0 & 0 & 0 & \cdots & 0 & 0 & \cdots & 0 & \mathbf{I_T} & 0 & 0 & 0 & 0 & \cdots & 0 & 0 & \cdots & 0 & 0 & 0 & \cdots & 0 \\
0 & 0 & 0 & 0 & 0 & 0 & \cdots & 0 & 0 & \cdots & 0 & 0 & \mathbf{I_P} & 0 & 0 & 0 & \cdots & 0 & 0 & \cdots & 0 & 0 & 0 & \cdots & 0 \\
0 & 0 & 0 & 0 & 0 & 0 & \cdots & 0 & 0 & \cdots & 0 & 0 & 0 & \mathbf{I_m} & 0 & 0 & \cdots & 0 & 0 & \cdots & 0 & 0 & 0 & \cdots & 0 \\
0 & 0 & 0 & 0 & 0 & 0 & \cdots & 0 & 0 & \cdots & 0 & 0 & 0 & 0 & \mathbf{I_P} & 0 & \cdots & 0 & 0 & \cdots & 0 & 0 & 0 & \cdots & 0 \\
0 & 0 & 0 & 0 & 0 & 0 & \cdots & 0 & 0 & \cdots & 0 & 0 & 0 & 0 & 0 & \mathbf{I_m} & \cdots & 0 & 0 & \cdots & 0 & 0 & 0 & \cdots & 0 \\
\vdots & \vdots & \vdots & \vdots & \vdots & \vdots & \ddots & \vdots & \vdots & \ddots & \vdots & \vdots & \vdots & \vdots & \vdots & \vdots & \ddots & \vdots & \vdots & \ddots & \vdots & \vdots & \vdots & \ddots & \vdots \\
0 & 0 & 0 & 0 & 0 & 0 & \cdots & 0 & 0 & \cdots & 0 & 0 & 0 & 0 & 0 & 0 & \cdots & \mathbf{I_P} & 0 & \cdots & 0 & 0 & 0 & \cdots & 0 \\
0 & 0 & 0 & 0 & 0 & 0 & \cdots & 0 & 0 & \cdots & 0 & 0 & 0 & 0 & 0 & 0 & \cdots & 0 & \mathbf{I_m} & \cdots & 0 & 0 & 0 & \cdots & 0 \\
\vdots & \vdots & \vdots & \vdots & \vdots & \vdots & \ddots & \vdots & \vdots & \ddots & \vdots & \vdots & \vdots & \vdots & \vdots & \vdots & \ddots & \vdots & \vdots & \ddots & \vdots & \vdots & \vdots & \ddots & \vdots \\
0 & 0 & 0 & 0 & 0 & 0 & \cdots & 0 & 0 & \cdots & 0 & 0 & 0 & 0 & 0 & 0 & \cdots & 0 & 0 & \cdots & \mathbf{I_m} & 0 & 0 & \cdots & 0 \\
0 & 0 & 0 & 0 & 0 & 0 & \cdots & 0 & 0 & \cdots & 0 & 0 & 0 & 0 & 0 & 0 & \cdots & 0 & 0 & \cdots & 0 & \mathbf{I_L} & 0 & \cdots & 0 \\
0 & 0 & 0 & 0 & 0 & 0 & \cdots & 0 & 0 & \cdots & 0 & 0 & 0 & 0 & 0 & 0 & \cdots & 0 & 0 & \cdots & 0 & 0 & \mathbf{I_L} & \cdots & 0 \\
\vdots & \vdots & \vdots & \vdots & \vdots & \vdots & \ddots & \vdots & \vdots & \ddots & \vdots & \vdots & \vdots & \vdots & \vdots & \vdots & \ddots & \vdots & \vdots & \ddots & \vdots & \vdots & \vdots & \ddots & \vdots \\
0 & 0 & 0 & 0 & 0 & 0 & \cdots & 0 & 0 & \cdots & 0 & 0 & 0 & 0 & 0 & 0 & \cdots & 0 & 0 & \cdots & 0 & 0 & 0 & \cdots & \mathbf{I_L}
\end{bmatrix} \tag{7-4}$$

$$\mathbf{B_1} = \begin{bmatrix}
\mathbf{B_S} & 0 & 0 & 0 & 0 & 0 & \cdots & 0 & 0 & \cdots & 0 & 0 & 0 & 0 & 0 & 0 & 0 & \cdots & 0 & 0 & 0 & \cdots & 0 \\
0 & \mathbf{B_{D1}} & 0 & 0 & 0 & 0 & \cdots & 0 & 0 & \cdots & 0 & 0 & 0 & 0 & 0 & 0 & 0 & \cdots & 0 & 0 & 0 & \cdots & 0 \\
0 & 0 & \mathbf{B_{mD1}} & 0 & 0 & 0 & \cdots & 0 & 0 & \cdots & 0 & 0 & 0 & 0 & 0 & 0 & 0 & \cdots & 0 & 0 & 0 & \cdots & 0 \\
0 & 0 & 0 & \mathbf{B_{D2}} & 0 & 0 & \cdots & 0 & 0 & \cdots & 0 & 0 & 0 & 0 & 0 & 0 & 0 & \cdots & 0 & 0 & 0 & \cdots & 0 \\
0 & 0 & 0 & 0 & \mathbf{B_{mD2}} & 0 & \cdots & 0 & 0 & \cdots & 0 & 0 & 0 & 0 & 0 & 0 & 0 & \cdots & 0 & 0 & 0 & \cdots & 0 \\
0 & 0 & 0 & 0 & 0 & \mathbf{B_{mD3}} & \cdots & 0 & 0 & \cdots & 0 & 0 & 0 & 0 & 0 & 0 & 0 & \cdots & 0 & 0 & 0 & \cdots & 0 \\
\vdots & \vdots & \vdots & \vdots & \vdots & \vdots & \ddots & \vdots & \vdots & \ddots & \vdots & \vdots & \vdots & \vdots & \vdots & \vdots & \vdots & \ddots & \vdots & \vdots & \vdots & \ddots & \vdots \\
0 & 0 & 0 & 0 & 0 & 0 & \cdots & \mathbf{B_{De}} & 0 & \cdots & 0 & 0 & 0 & 0 & 0 & 0 & 0 & \cdots & 0 & 0 & 0 & \cdots & 0 \\
0 & 0 & 0 & 0 & 0 & 0 & \cdots & 0 & \mathbf{B_{mD4}} & \cdots & 0 & 0 & 0 & 0 & 0 & 0 & 0 & \cdots & 0 & 0 & 0 & \cdots & 0 \\
\vdots & \vdots & \vdots & \vdots & \vdots & \vdots & \ddots & \vdots & \vdots & \ddots & \vdots & \vdots & \vdots & \vdots & \vdots & \vdots & \vdots & \ddots & \vdots & \vdots & \vdots & \ddots & \vdots \\
0 & 0 & 0 & 0 & 0 & 0 & \cdots & 0 & 0 & \cdots & \mathbf{B_{mDu}} & 0 & 0 & 0 & 0 & 0 & 0 & \cdots & 0 & 0 & 0 & \cdots & 0 \\
0 & 0 & 0 & 0 & 0 & 0 & \cdots & 0 & 0 & \cdots & 0 & 0 & 0 & 0 & 0 & 0 & 0 & \cdots & 0 & 0 & 0 & \cdots & 0 \\
0 & 0 & 0 & 0 & 0 & 0 & \cdots & 0 & 0 & \cdots & 0 & \mathbf{B_{P1}} & \mathbf{B_{Po1}} & 0 & 0 & 0 & 0 & \cdots & 0 & 0 & 0 & \cdots & 0 \\
0 & 0 & 0 & 0 & 0 & 0 & \cdots & 0 & 0 & \cdots & 0 & 0 & 0 & \mathbf{B_{mP1}} & 0 & 0 & 0 & \cdots & 0 & 0 & 0 & \cdots & 0 \\
0 & 0 & 0 & 0 & 0 & 0 & \cdots & 0 & 0 & \cdots & 0 & 0 & 0 & 0 & \mathbf{B_{P2}} & \mathbf{B_{Po2}} & 0 & \cdots & 0 & 0 & 0 & \cdots & 0 \\
0 & 0 & 0 & 0 & 0 & 0 & \cdots & 0 & 0 & \cdots & 0 & 0 & 0 & 0 & 0 & 0 & \mathbf{B_{mP2}} & \cdots & 0 & 0 & 0 & \cdots & 0 \\
\vdots & \vdots & \vdots & \vdots & \vdots & \vdots & \ddots & \vdots & \vdots & \ddots & \vdots & \vdots & \vdots & \vdots & \vdots & \vdots & \vdots & \ddots & \vdots & \vdots & \vdots & \ddots & \vdots \\
0 & 0 & 0 & 0 & 0 & 0 & \cdots & 0 & 0 & \cdots & 0 & 0 & 0 & 0 & 0 & 0 & 0 & \cdots & \mathbf{B_{Pk}} \; \mathbf{B_{Pog}} & 0 & \cdots & 0 \\
0 & 0 & 0 & 0 & 0 & 0 & \cdots & 0 & 0 & \cdots & 0 & 0 & 0 & 0 & 0 & 0 & 0 & \cdots & 0 & 0 & \mathbf{B_{mP3}} & \cdots & 0 \\
\vdots & \vdots & \vdots & \vdots & \vdots & \vdots & \ddots & \vdots & \vdots & \ddots & \vdots & \vdots & \vdots & \vdots & \vdots & \vdots & \vdots & \ddots & \vdots & \vdots & \vdots & \ddots & \vdots \\
0 & 0 & 0 & 0 & 0 & 0 & \cdots & 0 & 0 & \cdots & 0 & 0 & 0 & 0 & 0 & 0 & 0 & \cdots & 0 & 0 & 0 & \cdots & \mathbf{B_{mPa}} \\
0 & 0 & 0 & 0 & 0 & 0 & \cdots & 0 & 0 & \cdots & 0 & 0 & 0 & 0 & 0 & 0 & 0 & \cdots & 0 & 0 & 0 & \cdots & 0 \\
0 & 0 & 0 & 0 & 0 & 0 & \cdots & 0 & 0 & \cdots & 0 & 0 & 0 & 0 & 0 & 0 & 0 & \cdots & 0 & 0 & 0 & \cdots & 0 \\
\vdots & \vdots & \vdots & \vdots & \vdots & \vdots & \ddots & \vdots & \vdots & \ddots & \vdots & \vdots & \vdots & \vdots & \vdots & \vdots & \vdots & \ddots & \vdots & \vdots & \vdots & \ddots & \vdots \\
0 & 0 & 0 & 0 & 0 & 0 & \cdots & 0 & 0 & \cdots & 0 & 0 & 0 & 0 & 0 & 0 & 0 & \cdots & 0 & 0 & 0 & \cdots & 0
\end{bmatrix} \tag{7-5}$$

$$A_1 = \begin{bmatrix}
A_{LUb} & \cdots & A_{Lb} \\
\vdots & \iddots & \vdots \\
A_{LU2} & & A_{L2} \\
A_{LU1} & & A_{L1} \\
\cdots & A_{HmPa} \cdots A_{mPa} & \cdots \\
\vdots & \iddots & \vdots \\
\cdots & A_{HmP3} \; A_{mP3} & \cdots \\
\cdots & A_{PUk} \cdots A_{Pk} \; A_{VmP3} \cdots A_{VmPa} & \cdots \\
\vdots & \iddots & \vdots \\
\cdots & A_{HmP2} \; A_{mP2} & \cdots \\
\cdots & A_{PU2} \cdots A_{P2} \; A_{VmP2} & \cdots \\
\cdots & A_{HmP1} \; A_{mP1} & \cdots \\
\cdots & A_{PU1} \; A_{P1} \; A_{VmP1} & \cdots \\
A_{TU} & \cdots A_{T} \; A_{TL1} \cdots A_{TLk} & \cdots \\
\cdots & A_{HmDn} \cdots A_{mDn} & \cdots \\
\vdots & \iddots & \vdots \\
\cdots & A_{HmD4} \; A_{mD4} & \cdots \\
A_{DUj} & A_{Dj} \; A_{VmD4} \cdots A_{VmDn} & \cdots \\
\vdots & \iddots & \vdots \\
A_{HmD3} & A_{mD3} & \cdots \\
A_{HmD2} \; A_{mD2} & \cdots & \cdots \\
A_{DU2} & A_{D2} \; A_{VmD2} \; A_{VmD3} & \cdots \\
A_{HmD1} \; A_{mD1} & \cdots & \cdots \\
A_{DU1} \; A_{D1} \; A_{VmD1} & \cdots & \cdots \\
A_s \; A_{DL1} & A_{DL2} \cdots A_{DLj} \cdots A_{TL} \cdots A_{LL1} \; A_{LL2} \cdots A_{LLb}
\end{bmatrix} \tag{7-6}$$

$$\mathbf{C}=\begin{bmatrix}
0 & \mathbf{C_{D1}} & 0 & 0 & 0 & 0 & \cdots & 0 & 0 & \cdots & 0 & 0 & 0 & 0 & 0 & 0 & \cdots & 0 & 0 & \cdots & 0 & 0 & 0 & \cdots & 0 \\
0 & 0 & 0 & \mathbf{C_{D2}} & 0 & 0 & \cdots & 0 & 0 & \cdots & 0 & 0 & 0 & 0 & 0 & 0 & \cdots & 0 & 0 & \cdots & 0 & 0 & 0 & \cdots & 0 \\
\vdots & \vdots & \vdots & \vdots & \vdots & \vdots & \ddots & \vdots & \vdots & \ddots & \vdots & \vdots & \vdots & \vdots & \vdots & \vdots & \ddots & \vdots & \vdots & \ddots & \vdots & \vdots & \vdots & \ddots & \vdots \\
0 & 0 & 0 & 0 & 0 & 0 & \cdots & \mathbf{C_{Dj}} & 0 & \cdots & 0 & 0 & 0 & 0 & 0 & 0 & \cdots & 0 & 0 & \cdots & 0 & 0 & 0 & \cdots & 0 \\
0 & 0 & 0 & 0 & 0 & 0 & \cdots & 0 & 0 & \cdots & 0 & 0 & \mathbf{C_{P1}} & 0 & 0 & 0 & \cdots & 0 & 0 & \cdots & 0 & 0 & 0 & \cdots & 0 \\
0 & 0 & 0 & 0 & 0 & 0 & \cdots & 0 & 0 & \cdots & 0 & 0 & 0 & 0 & \mathbf{C_{P2}} & 0 & \cdots & 0 & 0 & \cdots & 0 & 0 & 0 & \cdots & 0 \\
\vdots & \vdots & \vdots & \vdots & \vdots & \vdots & \ddots & \vdots & \vdots & \ddots & \vdots & \vdots & \vdots & \vdots & \vdots & \vdots & \ddots & \vdots & \vdots & \ddots & \vdots & \vdots & \vdots & \ddots & \vdots \\
0 & 0 & 0 & 0 & 0 & 0 & \cdots & 0 & 0 & \cdots & 0 & 0 & 0 & 0 & 0 & 0 & \cdots & \mathbf{C_{Pk}} & 0 & \cdots & 0 & 0 & 0 & \cdots & 0
\end{bmatrix} \tag{7-7}$$

$$\mathbf{D}=[\mathbf{0}] \tag{7-8}$$

where the subscript of the matrix elements inside the matrices $\mathbf{H}$, $\mathbf{A_1(x_o,u_o)}$, $\mathbf{B_1(x_o,u_o)}$, $\mathbf{C(x_o,u_o)}$, and $\mathbf{D(x_o,u_o)}$ are defined as:

$[\ ]_{\mathbf{s}}$ = the matrices for the AC source and transmission line1

$[\ ]_{\mathbf{DUx,}}[\ ]_{\mathbf{DLx,}}[\ ]_{\mathbf{Dx}}(x=1,2,...,j)$ = the matrices for the j diode rectifier units including the e ideal CPL units

$[\ ]_{\mathbf{HmDx,}}[\ ]_{\mathbf{VmDx,}}[\ ]_{\mathbf{mDx}}(x=1,2,...,n)$ = the matrices for the n dynamic CPL units connected to the diode rectifier

$[\ ]_{\mathbf{T}}$ = the matrices for transmission line2

$[\ ]_{\mathbf{PUx,}}[\ ]_{\mathbf{PLx,}}[\ ]_{\mathbf{Px}}(x=1,2,...,k)$ = the matrices for the k controlled PWM rectifier units including the g ideal CPL units

$[\ ]_{\mathbf{HmPx,}}[\ ]_{\mathbf{VmPx,}}[\ ]_{\mathbf{mPx}}(x=1,2,...,a)$ = the matrices for the a dynamic CPL units connected to the controlled PWM rectifier

$[\ ]_{\mathbf{LUx,}}[\ ]_{\mathbf{LLx,}}[\ ]_{\mathbf{Lx}}(x=1,2,...,b)$ = the matrices for the b RL load units connected to HVAC bus

and the details of these element matrices are given in Appendix E.

The dimension of the matrices in (7-4)-(7-8) is given by:

$$\begin{aligned}
&\mathbf{H} = [\,]_{(4t_1+6j+5n+4t_2+6k+5a+2b)\times(4t_1+6j+5n+4t_2+6k+5a+2b)} \\
&\mathbf{A}_1(\mathbf{x_o},\mathbf{u_o}) = [\,]_{(4t_1+6j+5n+4t_2+6k+5a+2b)\times(4t_1+6j+5n+4t_2+6k+5a+2b)} \\
&\mathbf{B}_1(\mathbf{x_o},\mathbf{u_o}) = [\,]_{(4t_1+6j+5n+4t_2+6k+5a+2b)\times(1+e+2n+2k+g+2a)} \\
&\mathbf{C}(\mathbf{x_o},\mathbf{u_o}) = [\,]_{(j+k)\times(4t_1+6j+5n+4t_2+6k+5a+2b)} \\
&\mathbf{D}(\mathbf{x_o},\mathbf{u_o}) = [\,]_{(j+k)\times(1+e+2n+2k+g+2a)}
\end{aligned} \tag{7-9}$$

where t_1 is set to 1 if there is a transmission line1 between Gen bus and HVAC bus. Otherwise, it is set to 0 if there is no transmission line1 between these buses. Similarly, t_2 is set to 1 if there is a transmission line2 between HVAC bus and AC ESS bus, while it is set to 0 if there is no transmission line2 between these buses. The number of system state variables are equal to $4t_1+6j+5n+4t_2+6k+5a+2b$, and the number of system inputs and outputs are equal to $1+e+2n+2k+g+2a$ and $j+k$, respectively.

The application of the generalized model in (7-1)-(7-9) for power system stability analysis will be illustrated in the three example power systems given in Section 7.3, 7.4, and 7.5, respectively.

7.3 Power System with a Diode Rectifier and Paralleled Actuator Drives on the DC bus

The example power system in this section is shown in Figure 7.2. It consistes of a three-phase voltage source, transmission line, diode rectifier, DC-link filters, and paralleled actuator drives connected to a DC bus. These loads represent CPL dynamics as described in Chapter 4. The electromechanical actuator EMA1 is represented as a 10kW IM drive, while the electromechanical actuator EMA2 is represented as a 20 kW IM drive. The system parameters are given in Table 7.1.

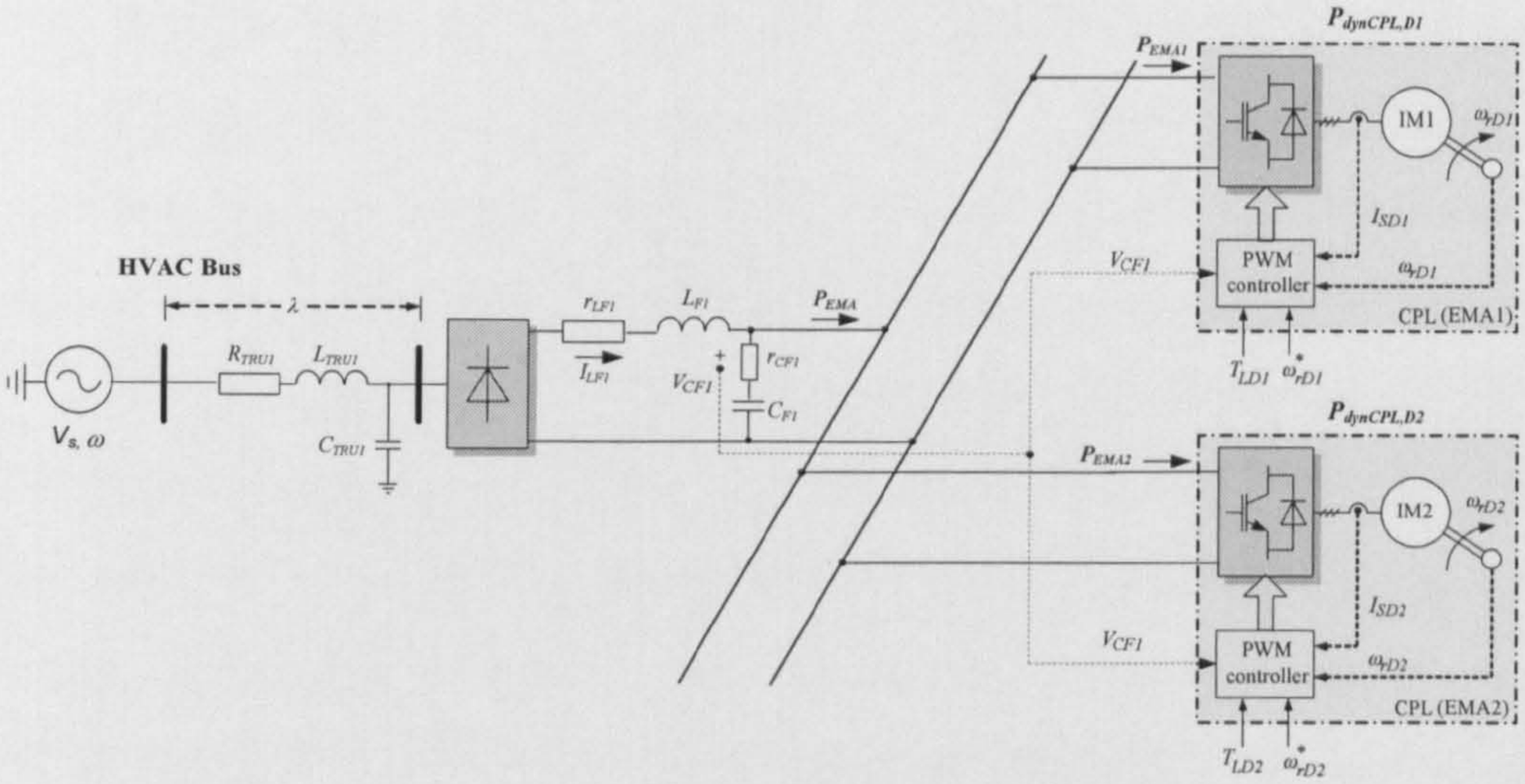

Figure 7.2: The system with diode rectifier and paralleled actuator drives

7.3.1 Forming Linearized Model from the Generalized Model

The linearized model of the system in Figure 7.2 can be determined from the generalized model (7-1)-(7-9) by setting:

- t_1=0 (no transmission line1 between Gen bus and HVAC bus)
- j=1 (single diode rectifier unit)
- e=0 (no ideal CPL connected to the diode rectifier)
- n=2 (two paralleled actuator drives connected to diode rectifier)
- t_2=0 (no transmission line2 between HVAC bus and AC ESS bus)
- k=0 (no controlled PWM rectifier)
- g=0 (no ideal CPL connected to a controlled PWM rectifier)
- a=0 (no actuator drive connected to controlled PWM rectifier)
- b=0 (no RL load)

Note that in this example system there is no transmission line1 between Gen bus and HVAC bus (see Figure 7.1). Therefore, the three-phase voltage source is connected to the HVAC bus without the transmission line1 (no Gen bus). Consequently, the $[\ ]_s$ in matrices $\mathbf{H}$ in (7-4) and $\mathbf{A_1(x_0,u_0)}$ in (7-6) are eliminated because there are no state variables from the transmission line1.

The matrices $\mathbf{A_{DU1}}$ and $\mathbf{A_{DL1}}$ are also eliminated because there are no coupling terms between the transmission line1 and the diode rectifier unit. However, there is a small change in $\mathbf{B_s}$ because, in this case, the voltage source is directly connected to the diode rectifier through its transmission line (R_{TRU1}, L_{TRU1}, and C_{TRU1}). If the voltage source is connected to the transmission line1 (R_{eq1}, L_{eq1}, and C_{eq1}) having 4 state variables, $\mathbf{B_s}$ will be the same as that of (7-5) in Appendix E. The dimension of $\mathbf{B_s}$ is $[\ ]_{4\times1}$ in which the number of rows equals the number of the state variable of transmission line1. Similarly, if the source is connected to the diode rectifier through its transmission line (6 state variables), $\mathbf{B_s}$ will be $[\ ]_{6\times1}$ in which case the number of rows equals the number of the state variable of the diode rectifier units. Therefore, $\mathbf{B_s}$ in (7-5) for the system in Figure 7.2 becomes:

$$\mathbf{B_s} = \begin{bmatrix} \dfrac{\cos(\theta_s)}{L_{TRU1}} \\ \dfrac{\sin(\theta_s)}{L_{TRU1}} \\ 0 \\ 0 \\ 0 \\ 0 \end{bmatrix}_{6\times1} \tag{7-10}$$

It can be seen in (7-10) that L_{eq1} (transmission line1 parameter) in $\mathbf{B_s}$ of (7-5) in Appendix E is changed to L_{TRU1} (transmission line parameter of the diode rectifier unit). The θ_s in (7-10) is λ as shown in Figure 7.2.

According to the above explanation, the linearized model can be then given in the matrix form of 16^{th} order with 5 inputs and 1 output as specified in (7-1)-(7-9):

$$\mathbf{H}=\begin{bmatrix}\mathbf{H_{D1}} & \mathbf{0} & \mathbf{0}\\ \mathbf{0} & \mathbf{I_m} & \mathbf{0}\\ \mathbf{0} & \mathbf{0} & \mathbf{I_m}\end{bmatrix}_{16\times16} \tag{7-11}$$

$$\mathbf{A_1(x_o,u_o)}=\begin{bmatrix}\mathbf{A_{D1}} & \mathbf{A_{HmD1}} & \mathbf{A_{HmD2}}\\ \mathbf{A_{VmD1}} & \mathbf{A_{mD1}} & \mathbf{0}\\ \mathbf{A_{VmD2}} & \mathbf{0} & \mathbf{A_{mD2}}\end{bmatrix}_{16\times16} \tag{7-12}$$

$$\mathbf{B_1(x_o,u_o)}=\begin{bmatrix}\mathbf{B_s} & \mathbf{0} & \mathbf{0}\\ \mathbf{0} & \mathbf{B_{mD1}} & \mathbf{0}\\ \mathbf{0} & \mathbf{0} & \mathbf{B_{mD2}}\end{bmatrix}_{16\times5} \tag{7-13}$$

$$\mathbf{C(x_o,u_o)}=\begin{bmatrix}\mathbf{C_{D1}} & \mathbf{0} & \mathbf{0}\end{bmatrix}_{1\times16} \tag{7-14}$$

$$\mathbf{D(x_o,u_o)}=\begin{bmatrix}\mathbf{0}\end{bmatrix}_{1\times5} \tag{7-15}$$

where

$$\begin{aligned}\delta\mathbf{x}=[&\delta I_{d,TRU1}\ \delta I_{q,TRU1}\ \delta V_{d,TRU1}\ \delta V_{q,TRU1}\ \delta I_{LF1}\ \delta V_{CF1}\\ &\delta\omega_{rD1}\ \delta I_{sqm,D1}\ \delta V_{f,D1}\ \delta V^{*}_{sqm,D1}\ \delta I^{*}_{sqm,D1}\\ &\delta\omega_{rD2}\ \delta I_{sqm,D2}\ \delta V_{f,D2}\ \delta V^{*}_{sqm,D2}\ \delta I^{*}_{sqm,D2}]^{T}\end{aligned} \tag{7-16}$$

$$\delta\mathbf{u}=[\delta V_s\ \delta\omega^{*}_{rD1}\ \delta T_{LD1}\ \delta\omega^{*}_{rD2}\ \delta T_{LD2}]^{T},\ \delta\mathbf{y}=[\delta V_{CF1}]$$

$$\mathbf{A(x_o,u_o)}=\mathbf{H^{-1}A_1(x_o,u_o)},\ \text{and}\ \mathbf{B(x_o,u_o)}=\mathbf{H^{-1}B_1(x_o,u_o)}$$

It can be seen from (7-11)-(7-16) that the linearized model can be easily constructed from the generalized model as given in (7-1)-(7-9). The details of the element matrices can be found in Appendix E. Note that if an internal resistance of the DC-link capacitor is not considered (r_{CF1}=0), the matrix $\mathbf{H}$ in (7-11) becomes the identity matrix $\mathbf{I_{16\times16}}$ because $\mathbf{H_{D1}}$ is set to $\mathbf{I_{6\times6}}$ under this condition.

7.3.2 Calculating the Steady-State Equilibrium Value

The power flow equation can be applied to determine the steady-state values at the AC side as the same manner as those in Chapter 4. Some small additions are made in the nonlinear power flow equations in which

$$P_{EMA} = \sum_{x=1}^{n} P_{EMA,x} = P_{EMA,1} + P_{EMA,2} \qquad (7\text{-}17)$$

where n=2 for this example (n = the number of dynamic CPLs connected to the diode rectifier units).

The steady-state values of an IM can be calculated by using the same equations as those of Chapter 4. These steady-state values depend on the operating point defined from ω_{rD1o}, ω_{rD2o}, T_{LD1o}, and T_{LD2o}. Hence, we can get the different linearized model of the system given in Figure 7.2 when the operating points are varied.

7.3.3 Small-Signal Simulation and Stability Analysis

The linearized model (7-11)-(7-16) was simulated for small-signal transients against a corresponding 3-phase benchmark circuit model simulated in SABER. The details of the SABER model for the system in Figure 7.2 are given in Appendix D.9. The example system parameters are given in Table 7.1. For example, Figure 7.3 shows the response of the DC-link voltage V_{CF1} of the system of Figure 7.2 to a step change in T_{LD2} from 100 to 110 Nm at t=0.6s. with constant speed reference ω^*_{rD2} 975 rpm, while the actuator load speed (ω^*_{rD1}) and load torque (T_{LD1}) of EMA1 are set to 1000 rpm and 50 Nm respectively.

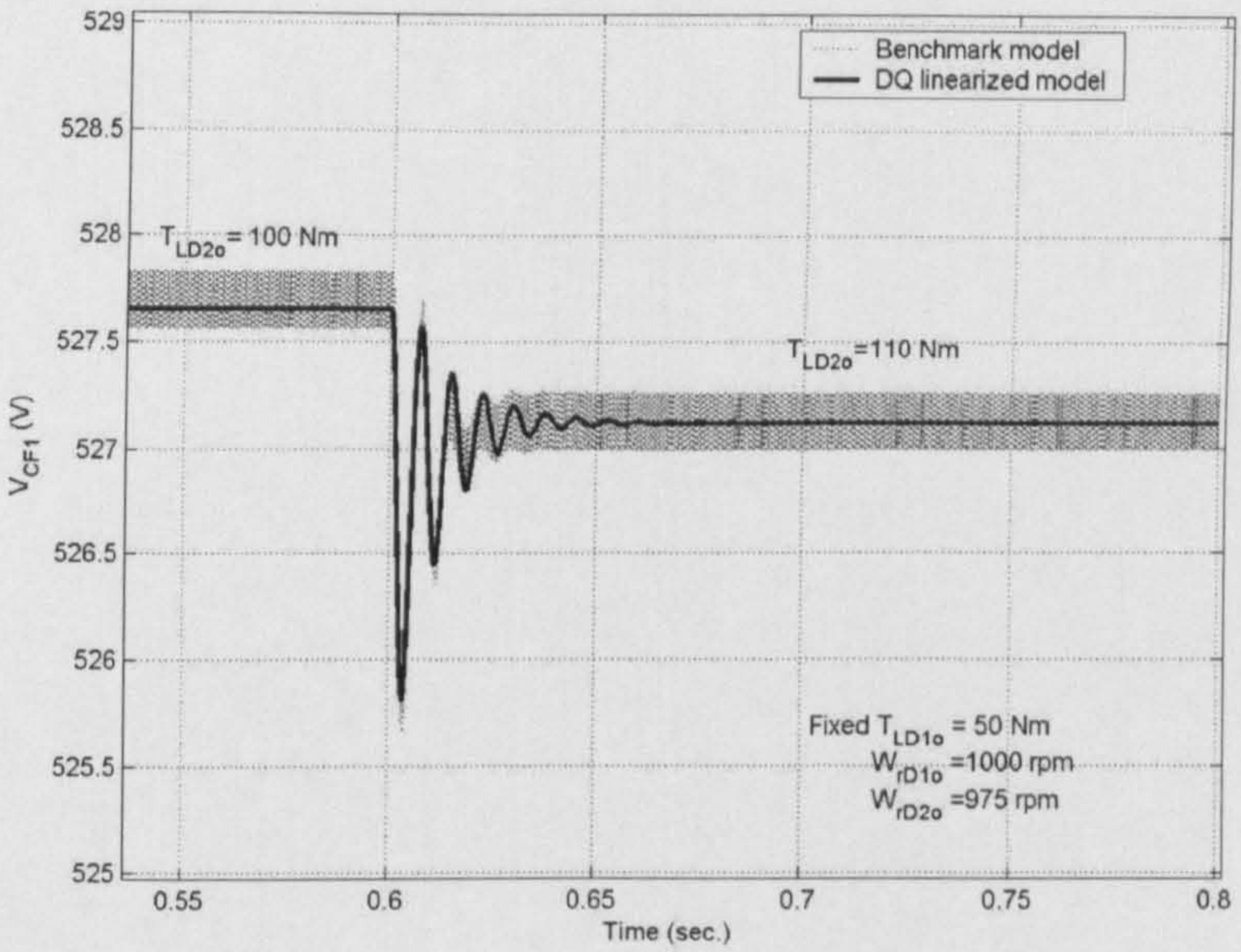

Figure 7.3: Response of V_{CF1} to a step change in T_{LD2} from 100 to 110 Nm. A comparison of SABER benchmark model with the dq linearized model

According to the result given in Figure 7.3, an excellent agreement between both models is achieved under small-signal simulation.

For the stability analysis, the linearized model is used with the eigenvalue theorem. The eigenvalues can be calculated from the Jacobian matrix $\mathbf{A}(\mathbf{x_o}, \mathbf{u_o})$ in (7-12). The eigenvalues for the system with parameters as given in Table 7.1 were analyzed for the case when the load torque of EMA2 (T_{LD2}) varies from 0 to 400 Nm at the constant actuator speed reference ω^*_{rD2} 975 rpm, ω^*_{rD1} 1000 rpm, and constant load torque T_{LD1} 100 Nm. This corresponds to the steady-state value of P_{EMA1} equal to 11.39 kW and P_{EMA2} varying from 1.047 kW to 51.76 kW. The dominant root locus is shown in Figure 7.4. This figure shows that the system becomes unstable when the total power P_{EMAo} exceeds 35.96 kW for the studied case (P_{EMA1}=11.39 kW, P_{EMA2}=24.57 kW).

Table 7.1: The set of parameters for the example system of Figure 7.2

Parameter	Value	Description
V_s	230 $V_{rms/phase}$	phase source voltage
ω	$2\pi \times 400$ rad/s	source frequency
R_{TRU1}	0.1 Ω	transmission line resistance
L_{TRU1}	24 μH	transmission line inductance
C_{TRU1}	2 nF	transmission line capacitance
r_{LF1}	0.05 Ω	dc link inductor resistance
L_{F1}	2 mH	dc link inductance
r_{CF1}	0.05 Ω	ESR_c
C_{F1}	500 μF	dc link capacitance
Actuator drive 10 kW rated (EMA1)		
ω_{rD1}^*	1000 rpm	speed reference
$T_{LD1,rated}$	100 Nm	rated load torque
$R_{sm,D1}$	0.6 Ω	stator resistance
$L_{sm,D1}$	80.3 mH	stator leakage inductance
$R_{r,D1}$	0.258 Ω	rotor resistance
$L_{r,D1}$	83.26 mH	rotor leakage inductance
$L_{m,D1}$	80.3 mH	magnetizing inductance
P_{D1}	4 poles	number of poles in the machine
$J_{m,D1}$	0.8 kgm^2	moment of inertia
$I_{sdm,D1}$	22.41 A	d-axis current for rated flux
$\tau_{F,D1}$	0.003 sec.	filtering time constant
$\omega_{nD1,\ speed}$	20 Hz ($K_{P\omega}$=30.89, $K_{I\omega}$=2426.3)	natural frequency of speed loop
$\omega_{nD1,\ current}$	200 Hz (K_{Pi}=11.09, K_{Ii}=9182.3)	natural frequency of current loop
Actuator drive 20 kW rated (EMA2)		
ω_{rD2}^*	975 rpm	speed reference
$T_{LD2,rated}$	190 Nm	rated load torque
$R_{sm,D2}$	0.6 Ω	stator resistance
$L_{sm,D2}$	30.39 mH	stator leakage inductance
$R_{r,D2}$	0.159 Ω	rotor resistance
$L_{r,D2}$	30.39 mH	rotor leakage inductance
$L_{m,D2}$	29.03 mH	magnetizing inductance
P_{D2}	6 poles	number of poles in the machine
$J_{m,D2}$	0.281 kgm^2	moment of inertia
$I_{sdm,D2}$	34.115 A	d-axis current for rated flux
$\tau_{F,D2}$	0.003 sec.	filtering time constant
$\omega_{nD2,\ speed}$	20 Hz ($K_{P\omega}$=13.27, $K_{I\omega}$=1042.33)	natural frequency of speed loop
$\omega_{nD2,\ current}$	200 Hz (K_{Pi}=4.75, K_{Ii}=4199.14)	natural frequency of current loop

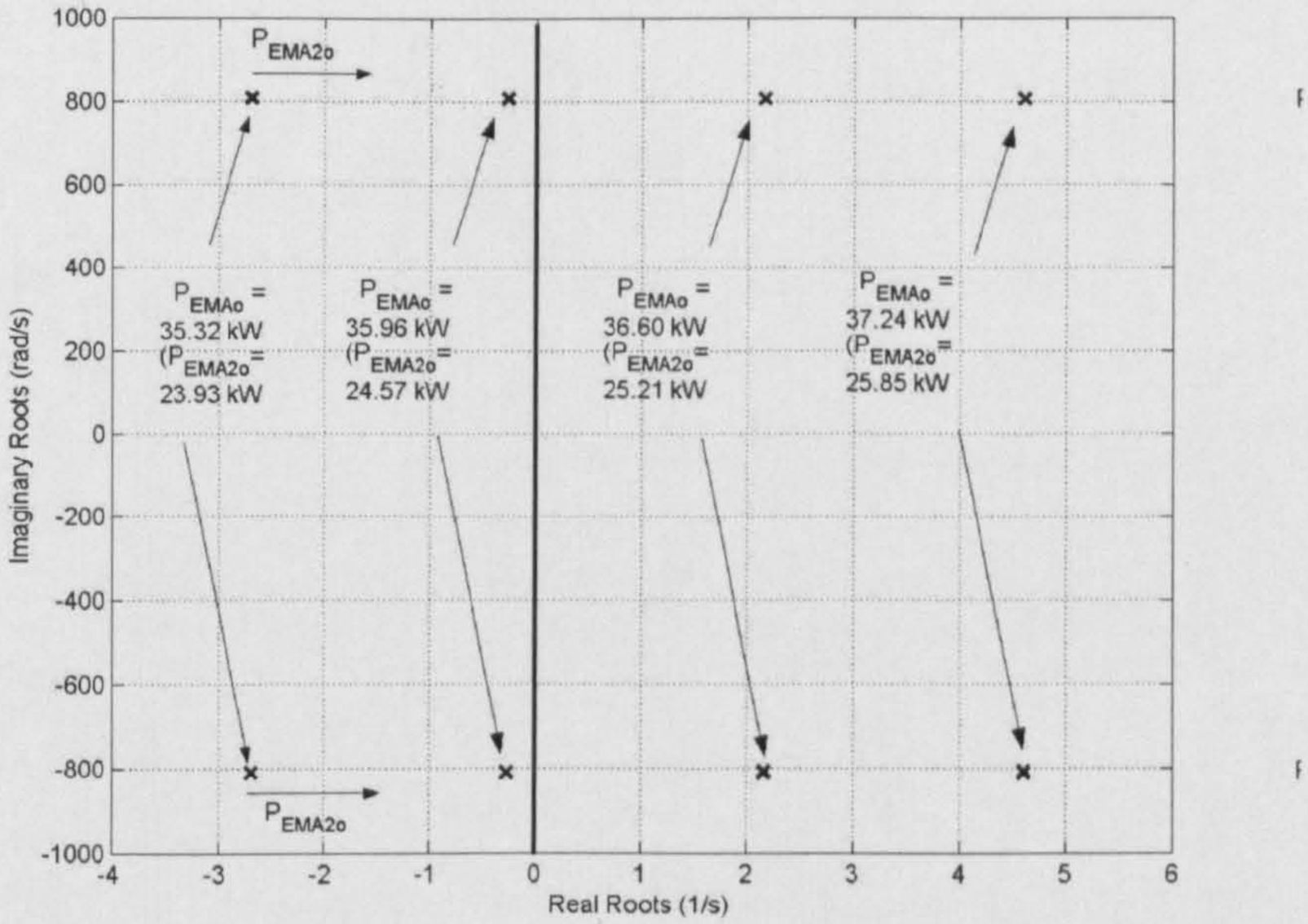

Figure 7.4: Dominant eigenvalue plot for varying P_{EMA2}

Figure 7.5 shows the SABER time-domain benchmark simulations that support the theoretical prediction with the instability occurring at P_{EMA} of 36.63 kW (P_{EMA1}=11.39 kW, P_{EMA2}=25.24 kW). This is greater than the 35.96 kW predicted for an unstable condition.

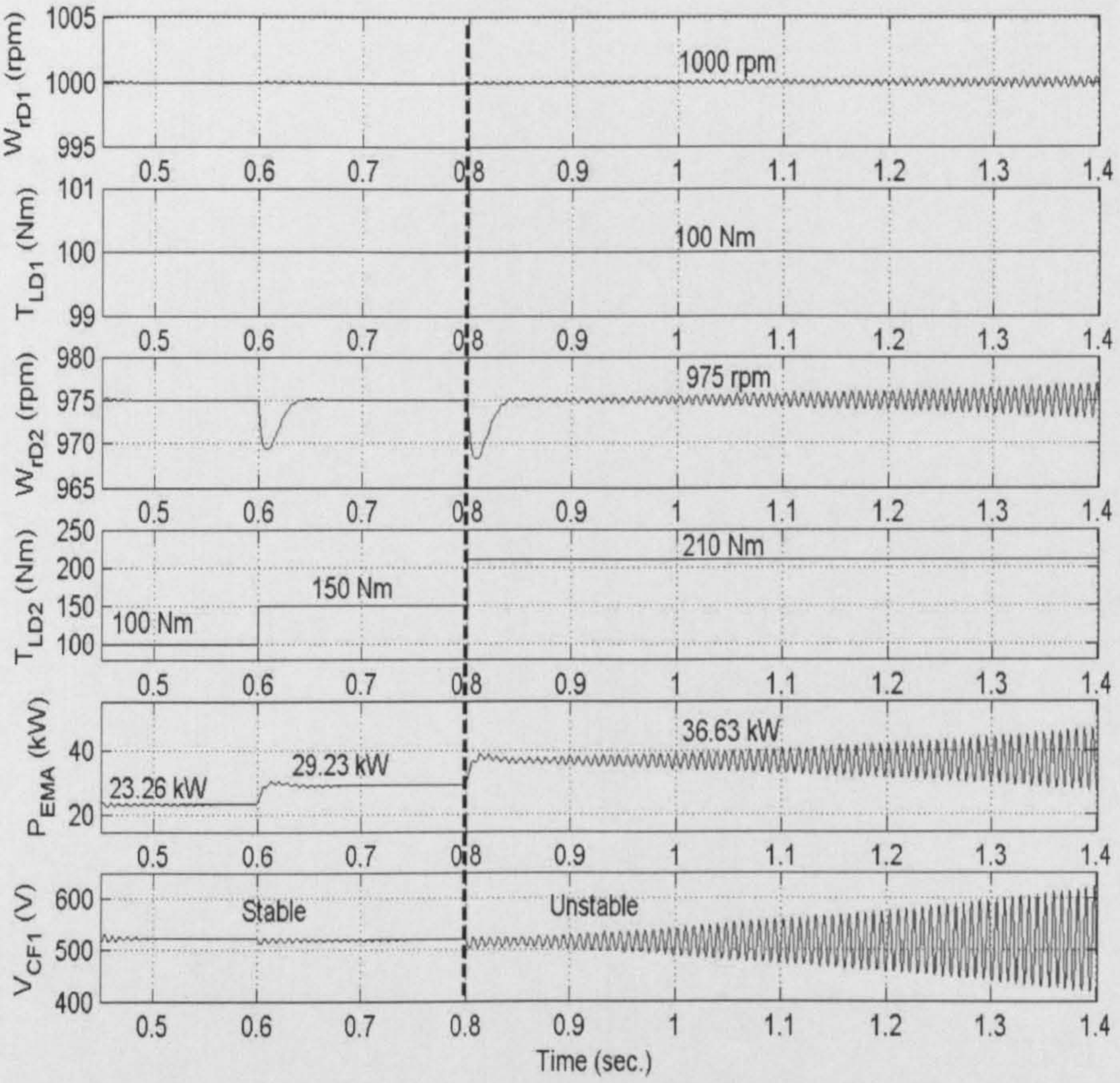

Figure 7.5: Step response for operating point (P_{EMA2}) variations

In this example system, two actuator loads are paralleled and both are connected to the DC bus. Therefore, it is very interesting to study the effect of paralleled loads on the system stability. Figure 7.6 shows the stable and unstable region for variations in P_{EMA1} (10kW IM actuator drive) by varying the load torque T_{LD1} from 0 Nm to 150 Nm with a constant speed reference ω_{rD1} 1000 rpm. Other parameters are fixed as given in Table 7.1. In this figure, the bold points are for the P_{EMA1} of 3.1, 5.8, and 11.39 kW. The analytical results of Figure 7.6 are also compared to the SABER benchmark simulation as shown in Figure 7.7. The top graph shows the changing P_{EMA2} (20 kW IM actuator drive) defined by changing load torque T_{LD2} with a constant speed reference ω_{rD2} 975 rpm. The graphs below show the response of the DC-link voltage V_{CF1} to different P_{EMA1}. The proposed model can predict the instability point with high accuracy.

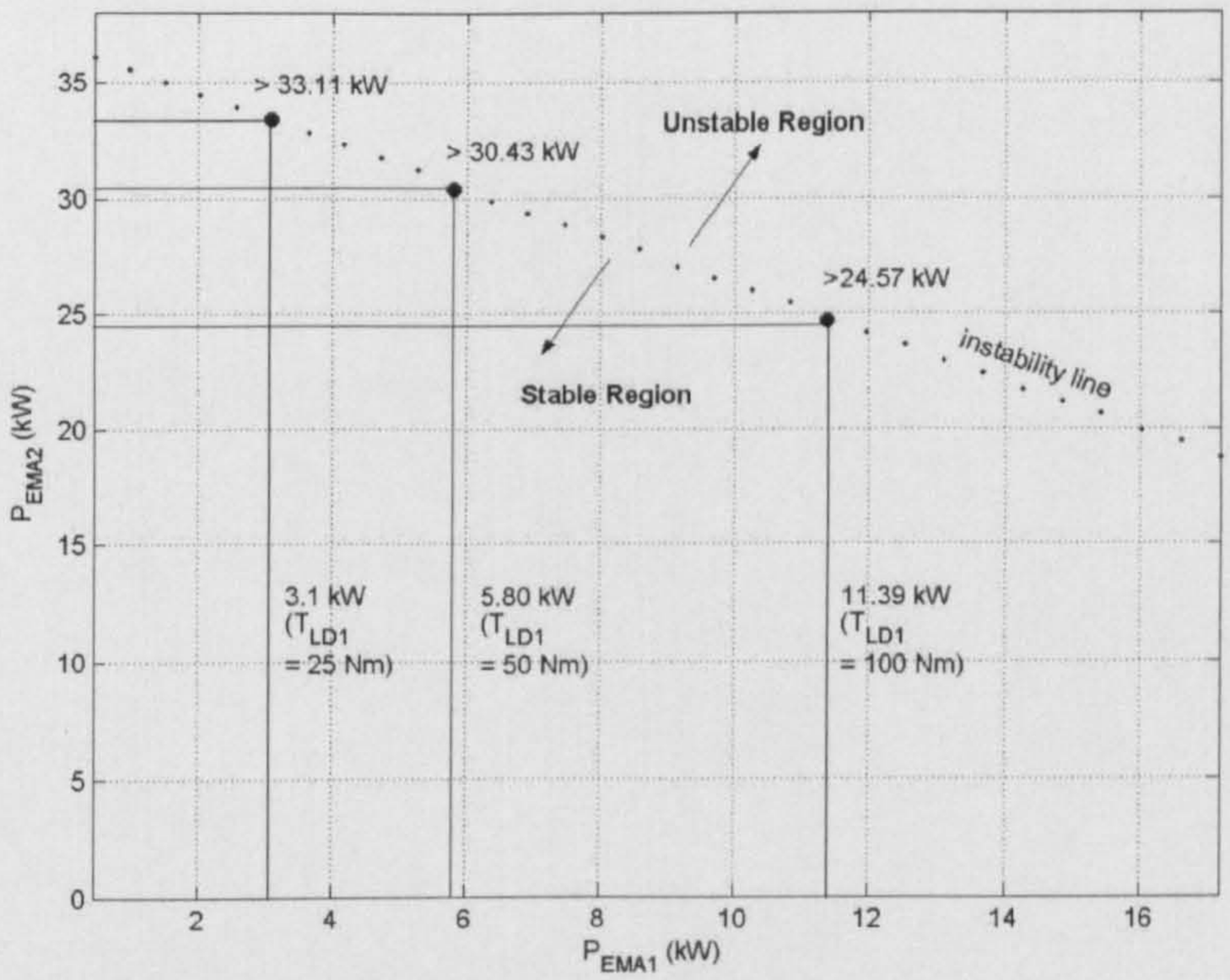

Figure 7.6: Instability power for P_{EMA1} variations

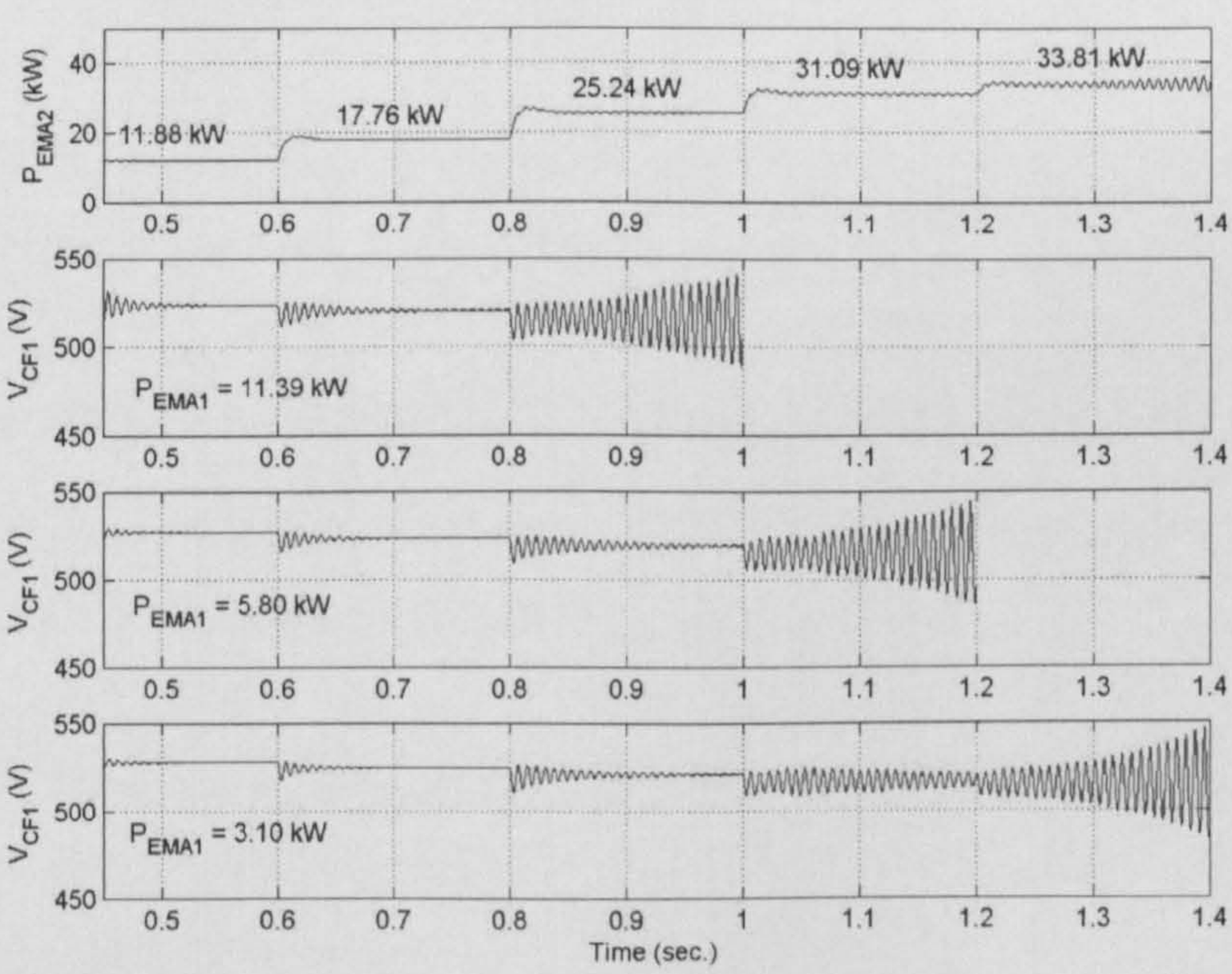

Figure 7.7: Verification of analytical results for P_{EMA1} variations

It can be seen that the 10kW IM actuator drive paralleled with 20kW actuator drive can affect to the instability power level. The higher the value of P_{EMA1}, the lower the value of P_{EMA2} at which instability occurs.

7.4 Power System with Two Paralleled Diode Rectifier Units

The example power system in this section is shown in Figure 7.8. It consists of a three-phase voltage source, transmission line, DC-link filters, and ideal CPLs. Both rectifier units are identical having the same parameters. The example parameters are given in Table 7.2.

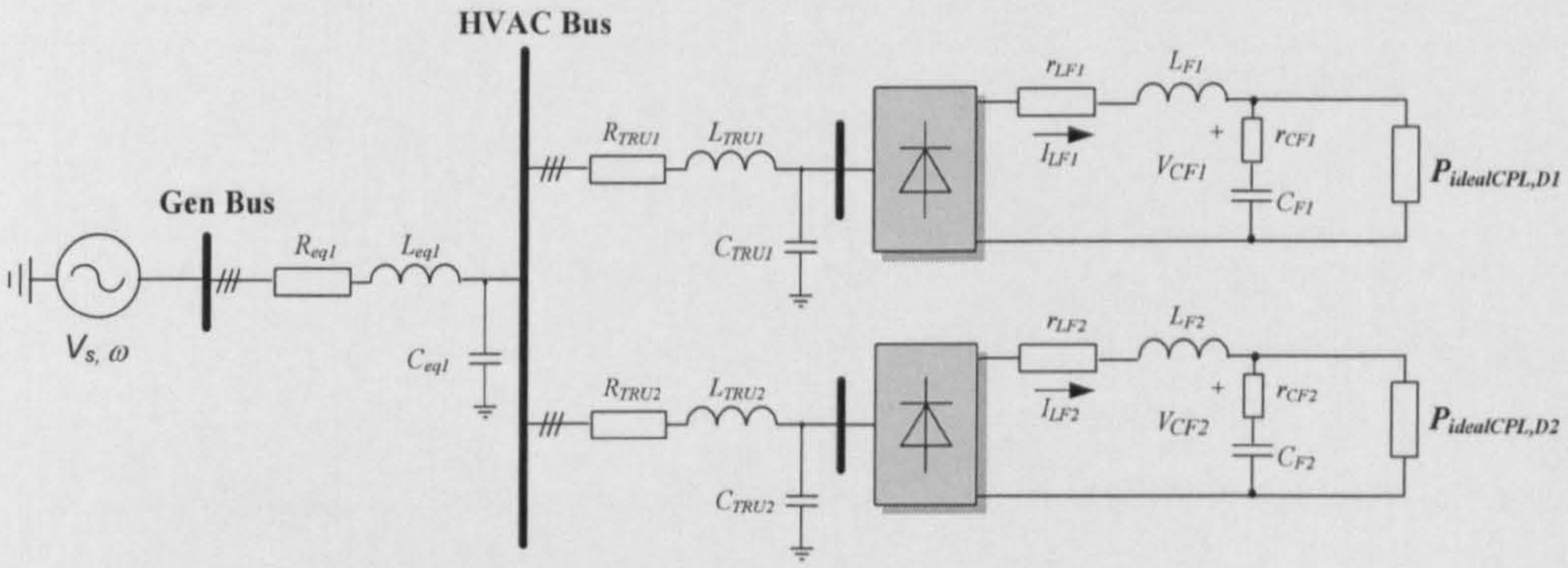

Figure 7.8: The system with paralleled two diode rectifier units

Note that the ideal CPL may represent the DC/DC converter feeding DC loads by assuming an infinitely fast controller action.

7.4.1 Forming Linearized Model from the Generalized Model

The linearized model of the system given in Figure 7.8 can be determined from the generalized model (7-1)-(7-9) by setting:

- t_1=1 (as there is a transmission line1 between Gen bus and HVAC bus)
- j=2 (two diode rectifier units)
- e=2 (two ideal CPLs connected to the diode rectifier)
- n=0 (no actuator drives connected to the diode rectifier)
- t_2=0 (no transmission line2 between the HVAC bus and the AC ESS bus)
- k=0 (no controlled PWM rectifier)
- g=0 (no ideal CPL connected to a controlled PWM rectifier)
- a=0 (no actuator drive connected to a controlled PWM rectifier)
- b=0 (no RL load)

Table 7.2: The set of parameters for the example system of Figure 7.8

Parameter	Value	Description
V_s	230 $V_{rms/phase}$	phase source voltage
ω	$2\pi\times400$ rad/s	source frequency
R_{eq1}	0.1 Ω	transmission line resistance
L_{eq1}	24 μH	transmission line inductance
C_{eq1}	2 nF	transmission line capacitance
$R_{TRU1}= R_{TRU2}$	0.1 Ω	transmission line resistance for rectifier unit
$L_{TRU1}= L_{TRU2}$	50 μH	transmission line inductance for rectifier unit
$C_{TRU1}= C_{TRU2}$	2 nF	transmission line capacitance for rectifier unit
$r_{LF1}= r_{LF2}$	0 Ω	dc link inductor resistance
$L_{F1}= L_{F2}$	2 mH	dc link inductance
$r_{CF1}= r_{CF2}$	0 Ω	ESR_c
$C_{F1}= C_{F2}$	500 μF	dc link capacitance

For this example system, there is a transmission line1 between Gen bus and HVAC bus (t_1=1). According to the above setting, the linearized model can be then given in the matrix form of 16th order with 3 inputs and 2 outputs as specified in equations (7-1)-(7-9):

$$\mathbf{H}=\begin{bmatrix}\mathbf{I_s} & \mathbf{0} & \mathbf{0}\\ \mathbf{0} & \mathbf{H_{D1}} & \mathbf{0}\\ \mathbf{0} & \mathbf{0} & \mathbf{H_{D2}}\end{bmatrix}_{16\times16} \tag{7-18}$$

$$\mathbf{A_1}(\mathbf{x_o},\mathbf{u_o})=\begin{bmatrix}\mathbf{A_s} & \mathbf{A_{DU1}} & \mathbf{A_{DU2}}\\ \mathbf{A_{DL1}} & \mathbf{A_{D1}} & \mathbf{0}\\ \mathbf{A_{DL2}} & \mathbf{0} & \mathbf{A_{D2}}\end{bmatrix}_{16\times16} \tag{7-19}$$

$$\mathbf{B_1}(\mathbf{x_o},\mathbf{u_o})=\begin{bmatrix}\mathbf{B_s} & \mathbf{0} & \mathbf{0}\\ \mathbf{0} & \mathbf{B_{D1}} & \mathbf{0}\\ \mathbf{0} & \mathbf{0} & \mathbf{B_{D2}}\end{bmatrix}_{16\times3} \tag{7-20}$$

$$\mathbf{C}(\mathbf{x_o},\mathbf{u_o})=\begin{bmatrix}\mathbf{0} & \mathbf{C_{D1}} & \mathbf{0}\\ \mathbf{0} & \mathbf{0} & \mathbf{C_{D2}}\end{bmatrix}_{2\times16} \tag{7-21}$$

$$\mathbf{D}(\mathbf{x_o},\mathbf{u_o})=[\mathbf{0}]_{2\times3} \tag{7-22}$$

where

$$\delta\mathbf{x} = [\delta I_{d,eq1}\ \delta I_{q,eq1}\ \delta V_{d,eq1}\ \delta V_{q,eq1}$$
$$\delta I_{d,TRU1}\ \delta I_{q,TRU1}\ \delta V_{d,TRU1}\ \delta V_{q,TRU1}\ \delta I_{LF1}\ \delta V_{CF1}$$
$$\delta I_{d,TRU2}\ \delta I_{q,TRU2}\ \delta V_{d,TRU2}\ \delta V_{q,TRU2}\ \delta I_{LF2}\ \delta V_{CF2}]^T$$

$$\delta\mathbf{u} = [\delta V_s\ \delta P_{CPL,D1}\ \delta P_{CPL,D2}]^T\ \ \delta\mathbf{y} = [\delta V_{CF1}\ \delta V_{CF2}]^T \tag{7-23}$$

and

$$\mathbf{A}(\mathbf{x_0},\mathbf{u_0}) = \mathbf{H}^{-1}\mathbf{A_1}(\mathbf{x_0},\mathbf{u_0}),\ \text{and}\ \mathbf{B}(\mathbf{x_0},\mathbf{u_0}) = \mathbf{H}^{-1}\mathbf{B_1}(\mathbf{x_0},\mathbf{u_0}) \tag{7-24}$$

It can be seen that the matrix $\mathbf{H}$ in (7-18) is the identity matrix $\mathbf{I}_{16\times16}$ because the internal resistance of DC-link capacitors of the system in Figure 7.8 are not concerned (r_{CF1}=r_{CF2}=0). The details of the element matrices for Jacobian matrix of (7-19)-(7-22) are given in Appendix E. $\mathbf{B_s}$ in (7-20) is the same as that of Appendix E. The commutation resistances ($r_{\mu D1}$ and $r_{\mu D2}$) for diode rectifiers are calculated by using only L_{TRU1} and L_{TRU2}, respectively. The line inductance L_{eq1} is not taken into account because C_{eq1} at the HVAC bus acts like a voltage source in the model. Therefore, HVAC bus is equivalent to the voltage source for the diode rectifiers.

7.4.2 Calculating the Steady-State Equilibrium Value

The linearized model in (7-18)-(7-24) needs to define V_{CFo1} in $\mathbf{A_{D1}}$ and $\mathbf{B_{D1}}$, V_{CFo2} in $\mathbf{A_{D2}}$ and $\mathbf{B_{D2}}$, θ_{d1} in $\mathbf{A_{D1}}$, θ_{d2} in $\mathbf{A_{D2}}$, and θ_s in $\mathbf{B_s}$ (see Appendix E). θ_{d1} and θ_{d2} are the phase shift between the dq rotating frame (Bus 2 in Figure 7.9) and the input terminal voltage frame of diode rectifier unit 1 and 2, respectively. θ_s is the phase shift between the dq rotating frame and the source frame. The power flow equation can be used to determine the steady state value at the AC side. The single line diagram of the power system in Figure 7.8 is depicted in Figure 7.9 in which the line capacitors are ignored assuming they are very small.

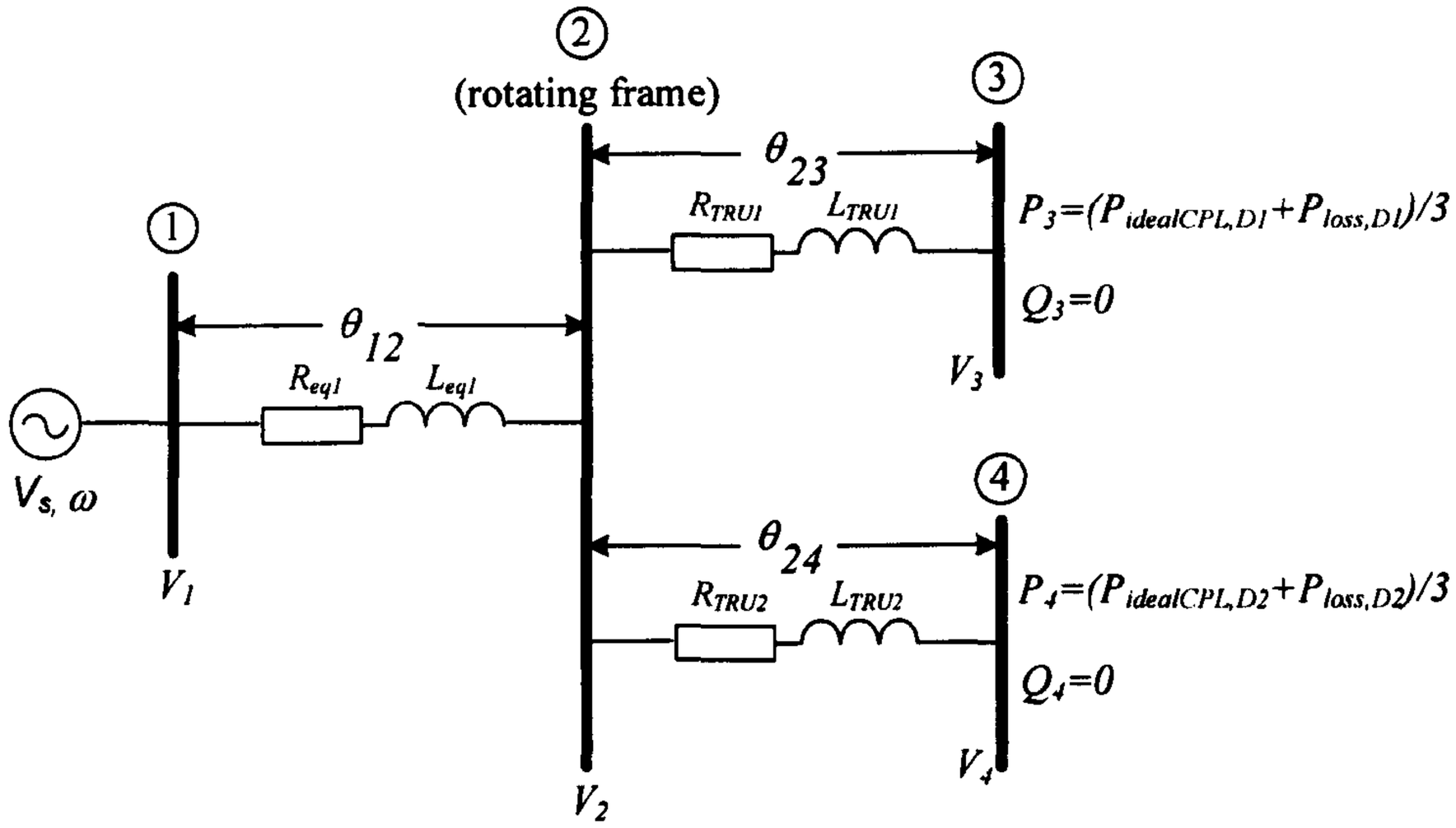

Figure 7.9: The single line diagram for steady state power calculations of Figure 7.8

Figure 7.9 leads to a system of six nonlinear equations:

$$\frac{V_2V_3}{Z_{23}}\cos(\gamma_{23}-\theta_{23})-\frac{V_3^2}{Z_{23}}\cos(\gamma_{23})=P_3=(P_{idealCPL,D1}+P_{loss,D1})/3$$

$$\frac{V_2V_3}{Z_{23}}\sin(\gamma_{23}-\theta_{23})-\frac{V_3^2}{Z_{23}}\sin(\gamma_{23})=Q_3=0$$

$$\frac{V_2V_4}{Z_{24}}\cos(\gamma_{24}-\theta_{24})-\frac{V_4^2}{Z_{24}}\cos(\gamma_{24})=P_4=(P_{idealCPL,D2}+P_{loss,D2})/3$$

$$\frac{V_2V_4}{Z_{24}}\sin(\gamma_{24}-\theta_{24})-\frac{V_4^2}{Z_{24}}\sin(\gamma_{24})=Q_4=0$$

$$\frac{V_1V_2}{Z_{12}}\cos(\gamma_{12}-\theta_{12})+\frac{V_2V_3}{Z_{23}}\cos(\gamma_{23}+\theta_{23})+\frac{V_2V_4}{Z_{24}}\cos(\gamma_{24}+\theta_{24})$$

$$-V_2^2\left[\frac{\cos(\gamma_{12})}{Z_{12}}+\frac{\cos(\gamma_{23})}{Z_{23}}+\frac{\cos(\gamma_{24})}{Z_{24}}\right]=0$$

$$\frac{V_1V_2}{Z_{12}}\sin(\gamma_{12}-\theta_{12})+\frac{V_2V_3}{Z_{23}}\sin(\gamma_{23}+\theta_{23})+\frac{V_2V_4}{Z_{24}}\sin(\gamma_{24}+\theta_{24})$$

$$-V_2^2\left[\frac{\sin(\gamma_{12})}{Z_{12}}+\frac{\sin(\gamma_{23})}{Z_{23}}+\frac{\sin(\gamma_{24})}{Z_{24}}\right]=0 \qquad (7\text{-}25)$$

where

$$Z_{12} = \sqrt{R_{eq1}^2 + (\omega L_{eq1})^2}, \gamma_{12} = \tan^{-1}\left(\frac{\omega L_{eq1}}{R_{eq1}}\right)$$

$$Z_{23} = \sqrt{R_{TRU1}^2 + (\omega L_{TRU1})^2}, \gamma_{23} = \tan^{-1}\left(\frac{\omega L_{TRU1}}{R_{TRU1}}\right)$$

$$Z_{24} = \sqrt{R_{TRU2}^2 + (\omega L_{TRU2})^2}, \gamma_{24} = \tan^{-1}\left(\frac{\omega L_{TRU2}}{R_{TRU2}}\right)$$

In (7-25), V_1, V_2, V_3, and V_4 are the steady state phase voltage (rms) at Bus 1, 2, 3, and 4, respectively. V_1 is set to 230 V_{rms} for this example system. θ_{12}, θ_{23}, and θ_{24} are the phase shift between each bus. The active and reactive power (per phase) at Bus 3 (input terminal of diode rectifier unit1) and Bus 4 (input terminal of diode rectifier unit2) are given by:

$$\begin{aligned} P_3 &= (P_{idealCPL,D1} + P_{loss,D1})/3 \\ Q_3 &= 0 \\ P_4 &= (P_{idealCPL,D2} + P_{loss,D2})/3 \\ Q_4 &= 0 \end{aligned} \tag{7-26}$$

where $P_{idealCPL,D1}$ and $P_{idealCPL,D2}$ are the ideal CPLs and $P_{loss,D1}$ and $P_{loss,D2}$ are the power loss due to r_{LF1} and r_{LF2}, respectively. Q_3 and Q_4 are set to zero because of the diode rectifier assumption as mentioned in Chapter 2. Equation (7-25) can be solved by using a numerical method such as Newton Raphson so as to find V_{2o}, V_{3o}, V_{4o}, θ_{12o}, θ_{23o}, and θ_{24o} at the steady state condition (6 unknowns). Consequently, V_{CFo1} and V_{CFo2} for the linearized model can then be calculated from V_{3o} and V_{4o}, respectively by using (6-9) of Chapter 6. P_{EMA} in (6-9) is changed to $P_{idealCPL,D1}$ (for V_{CFo1}) and $P_{idealCPL,D2}$ (for V_{CFo2}) for this case. In addition, θ_{d1}, θ_{d2}, and θ_s for the linearized model can be determined by:

$$\theta_{d1} = \theta_{23o}, \theta_{d2} = \theta_{24o}, \theta_s = \theta_{12o} \tag{7-27}$$

According to (7-25)-(7-27), the steady-state values changes when the system operating point, defined from $P_{idealCPL,D1}$ and $P_{idealCPL,D2}$, changes. Therefore, we can get different linearized models of (7-18)-(7-24) for the system in Figure 7.8 for each operating point.

7.4.3 Small-Signal Simulation and Stability Analysis

The linearized model (7-18)-(7-24) was simulated for small-signal transients against a nonlinear benchmark model simulated in SABER. The details of the SABER model of the system in Figure 7.8 are given in Appendix D.10. The example system parameters are given in Table 7.2. For example, Figure 7.10 shows the DC-link voltage V_{CF1} and V_{CF2} response of the system of Figure 7.8 to a step change of $P_{idealCPL,D1}$ from 10 to 11 kW at t=0.8s. with fixed $P_{idealCPL,D2}$ equal to 5 kW.

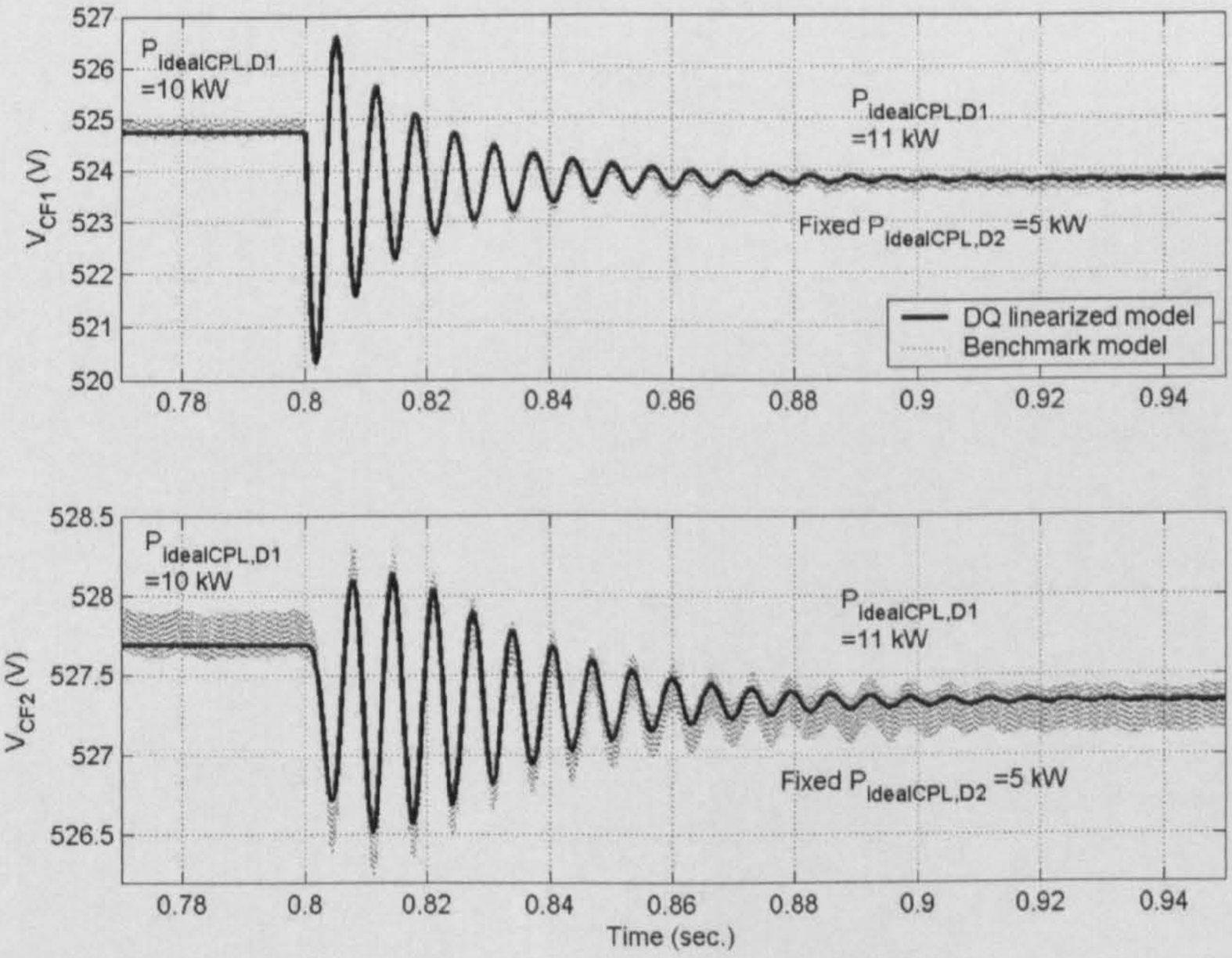

Figure 7.10: Response of V_{CF1} and V_{CF2} to a step change of $P_{idealCPL,D1}$ from 10 to 11 kW (fixed $P_{idealCPL,D2}$=5kW). A comparison of the SABER benchmark model with the dq linearized model

According to the results given in Figure 7.10, a good agreement between both models is achieved under small-signal simulation.

For stability analysis, the linearized model is used with the eigenvalue theorem. The eigenvalue can be calculated from the Jacobian matrix $\mathbf{A}(\mathbf{x_o},\mathbf{u_o})$ in (7-19).

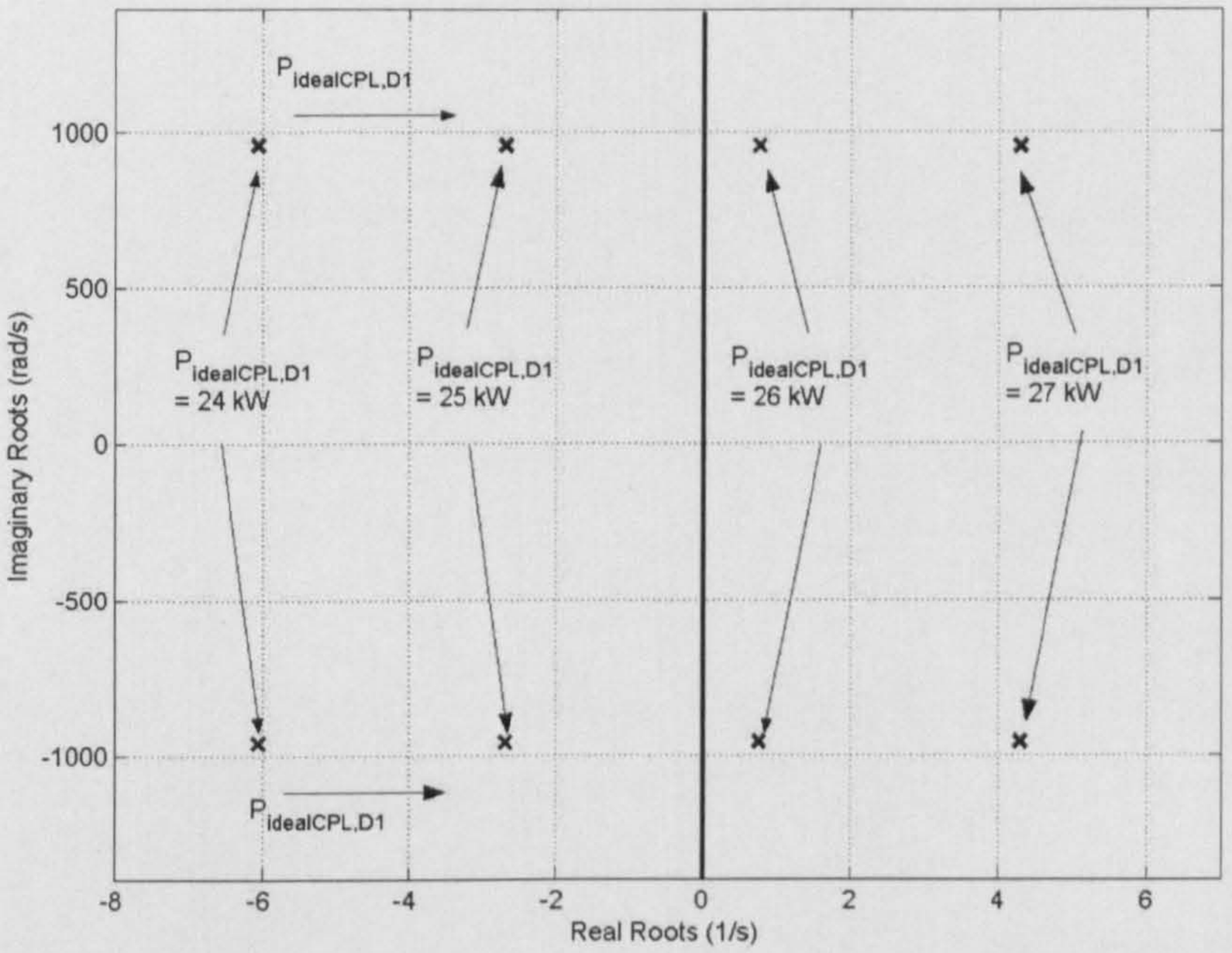

Figure 7.11: Dominant eigenvalue plot for varying $P_{idealCPL,D1}$

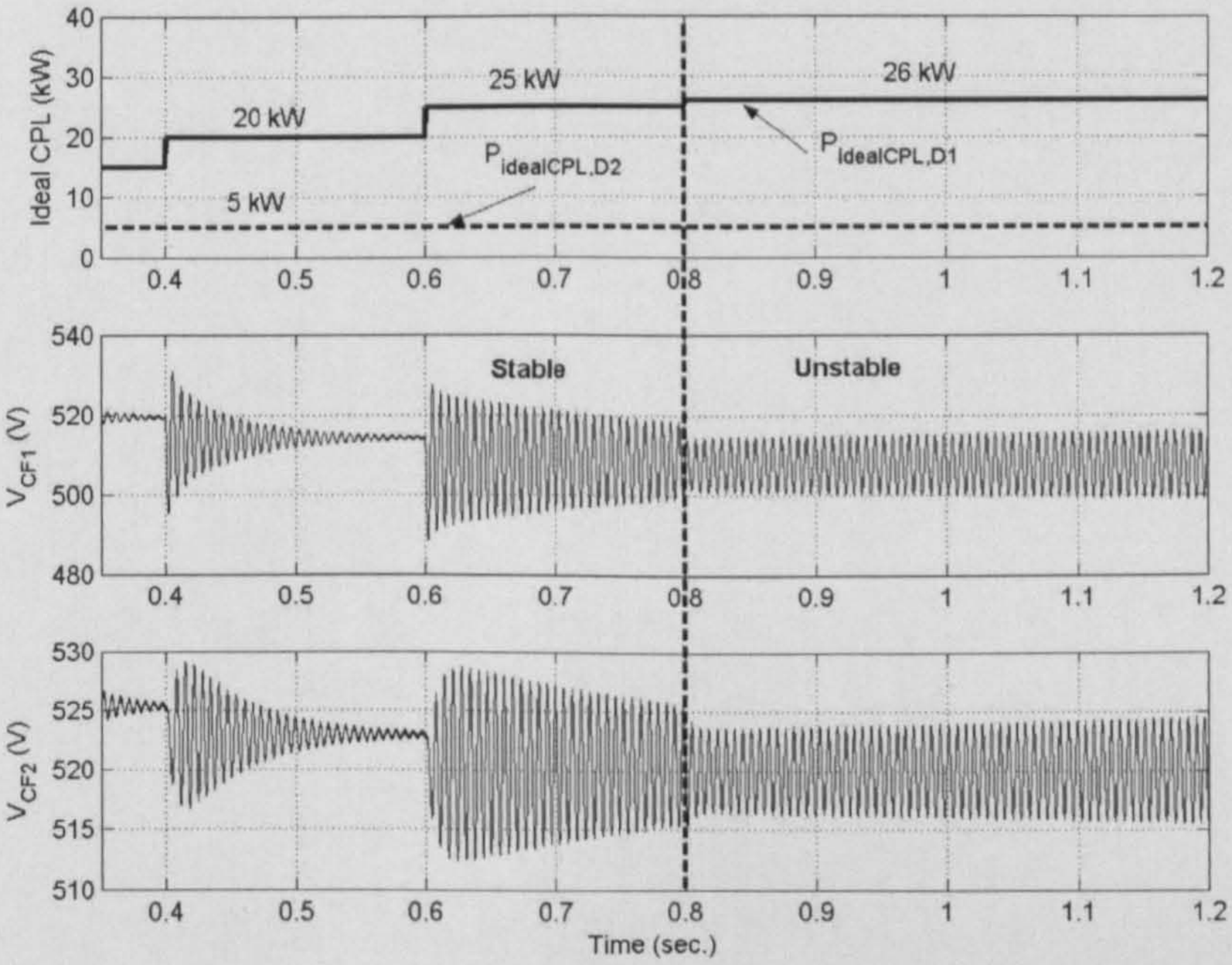

Figure 7.12: Step tresponse for operating point ($P_{idealCPL,D1}$) variations

The eigenvalues for the system with parameters in Table 7.2 were analyzed for the case when the $P_{idealCPL,D1}$ varies from 0-30 kW at the constant $P_{idealCPL,D2}$=5 kW. The dominant root locus is shown in Figure 7.11. This figure shows that the system becomes unstable when the $P_{idealCPL,D1}$ exceeds 25 kW for the studied case. Figure 7.12 shows the SABER time-domain simulations that support the theoretical prediction with the instability occurring at $P_{idealCPL,D1}$ of 26 kW. This is greater than the 25 kW predicted for an unstable condition.

In this section, two diode rectifier units are paralleled and both are connected to the HVAC bus as shown in Figure 7.8. Hence, it is very interesting to study the effect of a paralleled load on the system stability. Figure 7.13 shows the stable and unstable region for variations in $P_{idealCPL,D2}$ with other parameters fixed as given in Table 7.2. The theoretical predictions of Figure 7.13 are also compared with the SABER benchmark model simulation as shown in Figure 7.14.

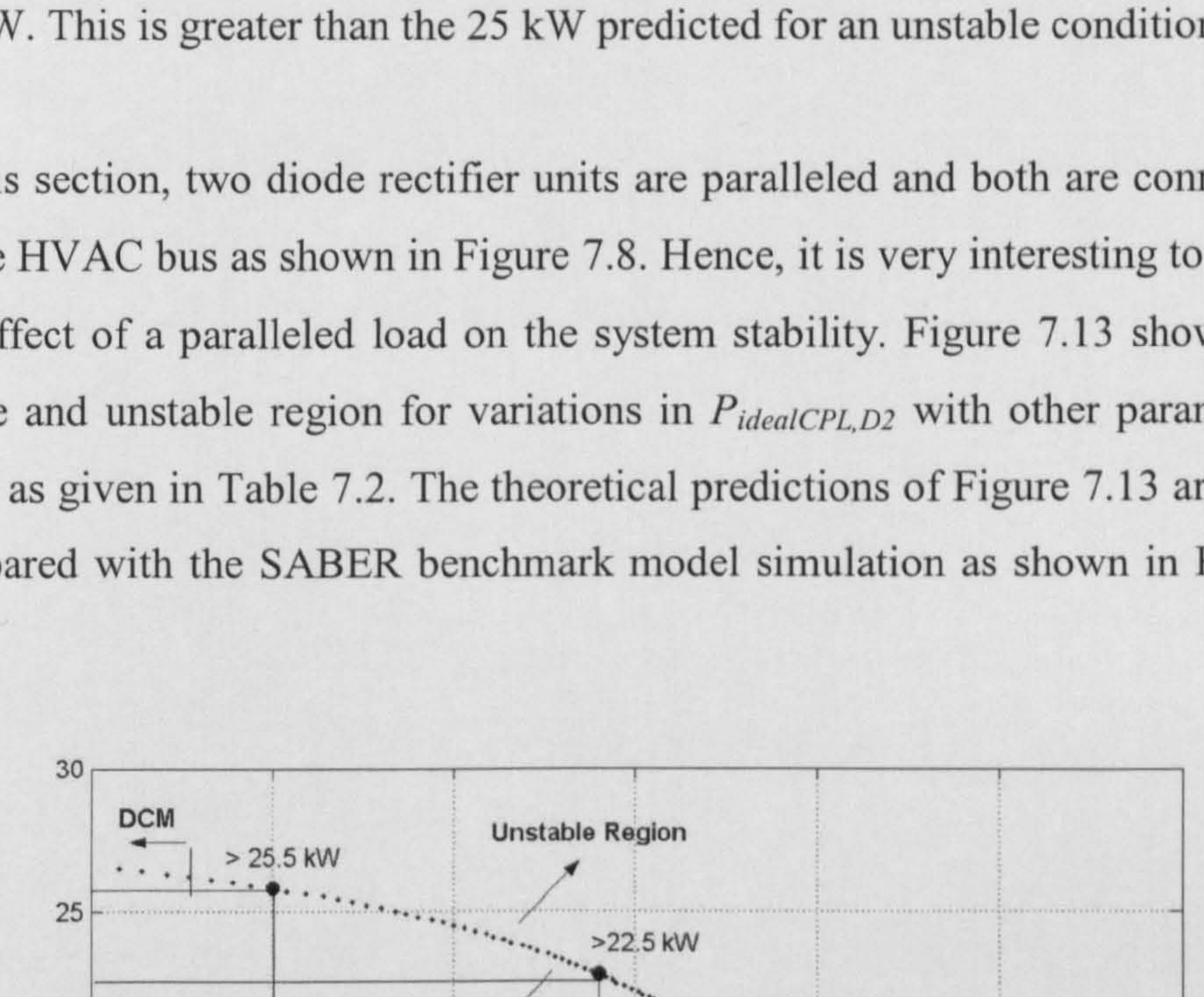

Figure 7.13: Instability power for $P_{idealCPL,D2}$ variations

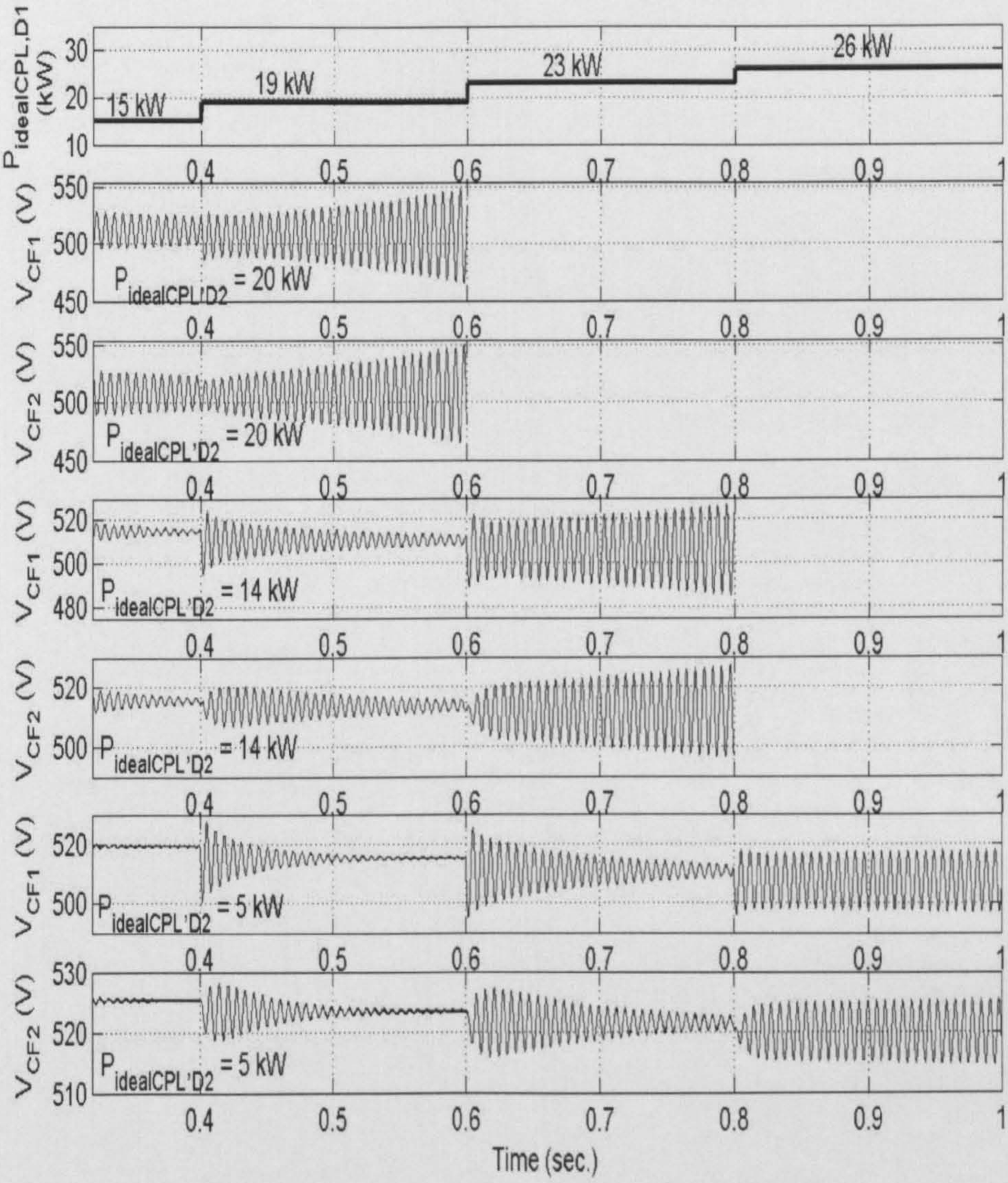

Figure 7.14: Verification of theoretical predictions for $P_{idealCPL,D2}$ variations

The top graph in Figure 7.14 shows the changing $P_{idealCPL,D1}$. The graphs below the top graph in Figure 7.14 show the DC-link voltage V_{CF1} and V_{CF2} responses for different $P_{idealCPL,D2}$. The results show that the proposed model can predict the instability point with high accuracy. Note that the theoretical results cannot predict the instability point under the discontinuous conduction mode (DCM). This is because the dq model is derived under the assumption that the diode rectifier is operated under the continuous conduction mode (CCM).

7.5 A Realistic Aircraft Power System

The example power system in this section is the more realistic aircraft power system as shown in Figure 7.15. The power system is based on an AC distribution power system from the MOET project [9] as mentioned in Chapter 1. The ideal voltage source is used to represent the SG-GCU, the ideal CPL $P_{idealCPL,D1}$ may represent the DC/DC converter feeding other DC loads by assuming the infinitely fast controller action, the dynamic CPL $P_{dynCPL,D1}$ represents the actuator drive system for DC environmental control, and $P_{dynCPL,P1}$ represents the actuator drive system for ailerons, rudders, flaps, spoilers, and elevators. The example parameters are given in Table 7.3 and Table 7.4.

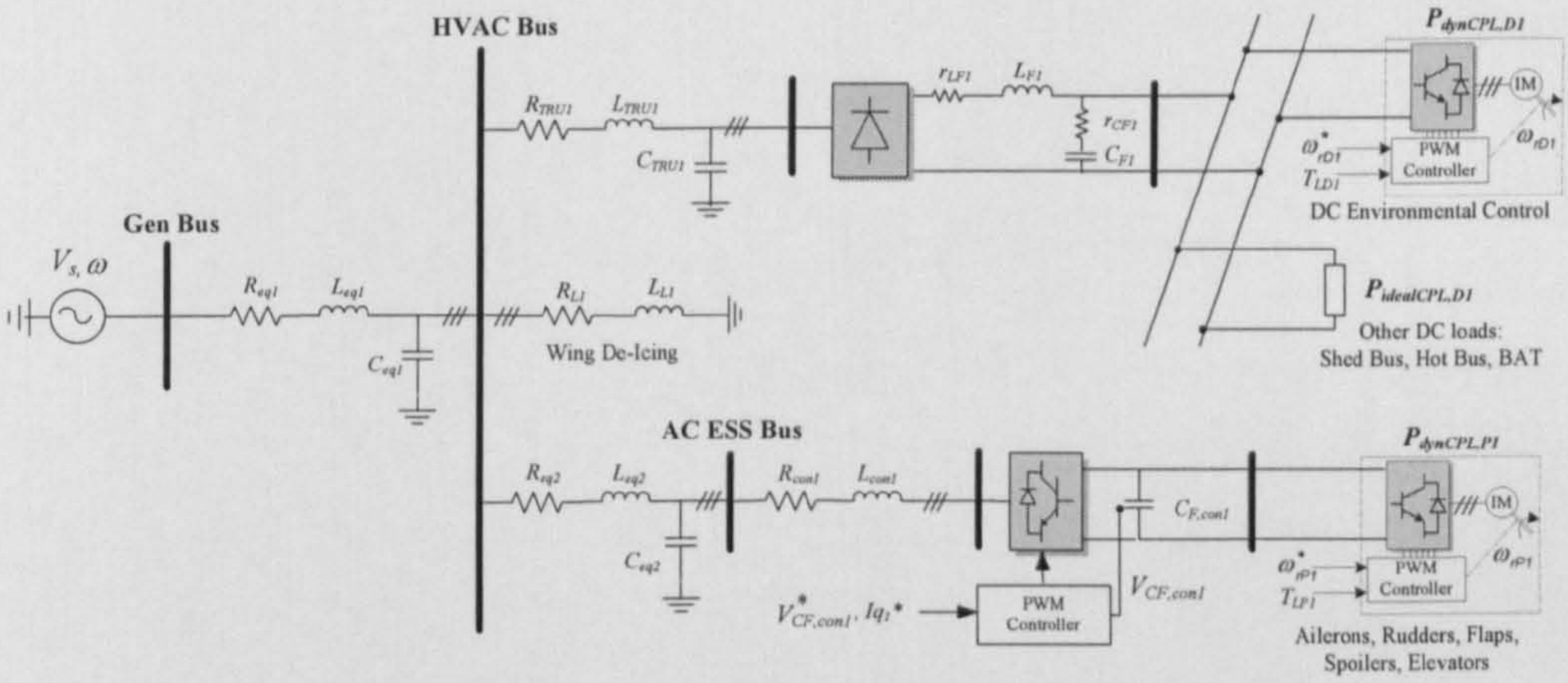

Figure 7.15: The real aircraft power system

7.5.1 Forming the Linearized Model from the Generalized Model

The linearized model of the system in Figure 7.15 can be determined from the generalized model (7-1)-(7-9) by setting:

- t_1=1 (as there is a transmission line1 between Gen bus and HVAC bus)
- j=1 (single diode rectifier units)
- e=1 (single ideal CPLs connected to the diode rectifier)
- n=1 (single actuator drives connected to the diode rectifier)
- t_2=1 (there is a transmission line2 between HVAC bus and AC ESS bus)

- k=1 (single controlled PWM rectifier)
- g=0 (no ideal CPL connected to a controlled PWM rectifier)
- a=1 (single actuator drive connected to a controlled PWM rectifier)
- b=1 (single RL load)

Table 7.3: The parameters for the real aircraft power system of Figure 7.15

Parameter	Value	Description
V_s	230 $V_{rms/phase}$	phase source voltage
ω	2π×400 rad/s	source frequency
R_{eq1}	0.1 Ω	transmission line resistance
L_{eq1}	24 μH	transmission line inductance
C_{eq1}	2 nF	transmission line capacitance
R_{TRU1}	0.1 Ω	transmission line resistance for rectifier unit
L_{TRU1}	50 μH	transmission line inductance for rectifier unit
C_{TRU1}	2 nF	transmission line capacitance for rectifier unit
r_{LF1}	0 Ω	dc link inductor resistance
L_{F1}	2 mH	dc link inductance
r_{CF1}	0 Ω	ESR_c
C_{F1}	500 μF	dc link capacitance
R_{L1}	10 Ω	resistive load for wing de-icing
L_{L1}	0.1 mH	inductive load for wing de-icing
R_{eq2}	0.1 Ω	transmission line resistance
L_{eq2}	24 μH	transmission line inductance
C_{eq2}	2 nF	transmission line capacitance
R_{con1}	0.1 Ω	ac filter inductor resistance for PWM rectifier
L_{con1}	100 μH	ac filter inductance for PWM rectifier
$C_{F,con1}$	500 μF	dc link capacitance for PWM rectifier
$V^*_{CF,con1}$	600 V	dc link voltage command input
I^*_{q1}	0 A	current command input
$P_{idealCPL,D1}$	30 kW	ideal CPL connected to diode rectifier unit
$\omega_{nP1,voltagePWM}$	40 Hz (K_{Pv}=0.11, K_{Iv}=19.42)	natural frequency of voltage loop for PWM rectifier
$\omega_{nP1,currentPWM}$	500 Hz (K_{pd}=K_{pq}=0.4, K_{id}=K_{iq}=986.96)	natural frequency of current loop for PWM rectifier

Table 7.4: The parameters of actuator drive systems of Figure 7.15

Parameter	Value	Description
Actuator drive 10 kW rated ($P_{dynCPL,D1}$)		
ω_{rD1}^*	1000 rpm	speed reference
$T_{LD1,rated}$	100 Nm	rated load torque
$R_{sm,D1}$	0.6 Ω	stator resistance
$L_{sm,D1}$	80.3 mH	stator leakage inductance
$R_{r,D1}$	0.258 Ω	rotor resistance
$L_{r,D1}$	83.26 mH	rotor leakage inductance
$L_{m,D1}$	80.3 mH	magnetizing inductance
P_{D1}	4 poles	number of poles in the machine
$J_{m,D1}$	0.8 kgm^2	moment of inertia
$I_{sdm,D1}$	22.41 A	d-axis current for rated flux
$\tau_{F,D1}$	0.01 sec.	filtering time constant
$\omega_{nD1,\ speed}$	20 Hz ($K_{P\omega}$=30.89, $K_{I\omega}$=2426.3)	natural frequency of speed loop
$\omega_{nD1,\ current}$	200 Hz (K_{Pi}=11.09, K_{Ii}=9182.3)	natural frequency of current loop
Actuator drive 20 kW rated ($P_{dynCPL,P1}$)		
ω_{rP1}^*	975 rpm	speed reference
$T_{LP1,rated}$	190 Nm	rated load torque
$R_{sm,P1}$	0.6 Ω	stator resistance
$L_{sm,P1}$	30.39 mH	stator leakage inductance
$R_{r,P1}$	0.159 Ω	rotor resistance
$L_{r,P1}$	30.39 mH	rotor leakage inductance
$L_{m,P1}$	29.03 mH	magnetizing inductance
P_{P1}	6 poles	number of poles in the machine
$J_{m,P1}$	0.281 kgm^2	moment of inertia
$I_{sdm,P1}$	34.115 A	d-axis current for rated flux
$\tau_{F,P1}$	0.02 sec.	filtering time constant
$\omega_{nP1,\ speed}$	20 Hz ($K_{P\omega}$=13.27, $K_{I\omega}$=1042.33)	natural frequency of speed loop
$\omega_{nP1,\ current}$	200 Hz (K_{Pi}=4.75, K_{Ii}=4199.14)	natural frequency of current loop

According to the above setting, the linearized model can be then given in the matrix form of 32 state-variables, 8 inputs, and 2 outputs as specified in (7-1)-(7-9):

$$\mathbf{H}=\begin{bmatrix} \mathbf{I_s} & \mathbf{0} & \mathbf{0} & \mathbf{0} & \mathbf{0} & \mathbf{0} & \mathbf{0} \\ \mathbf{0} & \mathbf{H_{D1}} & \mathbf{0} & \mathbf{0} & \mathbf{0} & \mathbf{0} & \mathbf{0} \\ \mathbf{0} & \mathbf{0} & \mathbf{I_m} & \mathbf{0} & \mathbf{0} & \mathbf{0} & \mathbf{0} \\ \mathbf{0} & \mathbf{0} & \mathbf{0} & \mathbf{I_T} & \mathbf{0} & \mathbf{0} & \mathbf{0} \\ \mathbf{0} & \mathbf{0} & \mathbf{0} & \mathbf{0} & \mathbf{I_P} & \mathbf{0} & \mathbf{0} \\ \mathbf{0} & \mathbf{0} & \mathbf{0} & \mathbf{0} & \mathbf{0} & \mathbf{I_m} & \mathbf{0} \\ \mathbf{0} & \mathbf{0} & \mathbf{0} & \mathbf{0} & \mathbf{0} & \mathbf{0} & \mathbf{I_L} \end{bmatrix}_{32\times 32} \tag{7-28}$$

$$\mathbf{A_1}(\mathbf{x_o},\mathbf{u_o})=\begin{bmatrix} \mathbf{A_s} & \mathbf{A_{DU1}} & \mathbf{0} & \mathbf{A_{TU}} & \mathbf{0} & \mathbf{0} & \mathbf{A_{LU1}} \\ \mathbf{A_{DL1}} & \mathbf{A_{D1}} & \mathbf{A_{HmD1}} & \mathbf{0} & \mathbf{0} & \mathbf{0} & \mathbf{0} \\ \mathbf{0} & \mathbf{A_{VmD1}} & \mathbf{A_{mD1}} & \mathbf{0} & \mathbf{0} & \mathbf{0} & \mathbf{0} \\ \mathbf{A_{TL}} & \mathbf{0} & \mathbf{0} & \mathbf{A_T} & \mathbf{A_{PU1}} & \mathbf{0} & \mathbf{0} \\ \mathbf{0} & \mathbf{0} & \mathbf{0} & \mathbf{A_{PL1}} & \mathbf{A_{P1}} & \mathbf{A_{HmP1}} & \mathbf{0} \\ \mathbf{0} & \mathbf{0} & \mathbf{0} & \mathbf{0} & \mathbf{A_{VmP1}} & \mathbf{A_{mP1}} & \mathbf{0} \\ \mathbf{A_{LL1}} & \mathbf{0} & \mathbf{0} & \mathbf{0} & \mathbf{0} & \mathbf{0} & \mathbf{A_{L1}} \end{bmatrix}_{32\times 32} \tag{7-29}$$

$$\mathbf{B_1}(\mathbf{x_o},\mathbf{u_o})=\begin{bmatrix} \mathbf{B_s} & \mathbf{0} & \mathbf{0} & \mathbf{0} & \mathbf{0} \\ \mathbf{0} & \mathbf{B_{D1}} & \mathbf{0} & \mathbf{0} & \mathbf{0} \\ \mathbf{0} & \mathbf{0} & \mathbf{B_{mD1}} & \mathbf{0} & \mathbf{0} \\ \mathbf{0} & \mathbf{0} & \mathbf{0} & \mathbf{0} & \mathbf{0} \\ \mathbf{0} & \mathbf{0} & \mathbf{0} & \mathbf{B_{P1}} & \mathbf{0} \\ \mathbf{0} & \mathbf{0} & \mathbf{0} & \mathbf{0} & \mathbf{B_{mP1}} \\ \mathbf{0} & \mathbf{0} & \mathbf{0} & \mathbf{0} & \mathbf{0} \end{bmatrix}_{32\times 8} \tag{7-30}$$

$$\mathbf{C}(\mathbf{x_o},\mathbf{u_o})=\begin{bmatrix} \mathbf{0} & \mathbf{C_{D1}} & \mathbf{0} & \mathbf{0} & \mathbf{0} & \mathbf{0} & \mathbf{0} \\ \mathbf{0} & \mathbf{0} & \mathbf{0} & \mathbf{0} & \mathbf{C_{P1}} & \mathbf{0} & \mathbf{0} \end{bmatrix}_{2\times 32} \tag{7-31}$$

$$\mathbf{D}(\mathbf{x_o},\mathbf{u_o})=[\mathbf{0}]_{2\times 8} \tag{7-32}$$

where

$$\delta\mathbf{x} = [\delta I_{d,eq1}\ \delta I_{q,eq1}\ \delta V_{d,eq1}\ \delta V_{q,eq1}$$
$$\delta I_{d,TRU1}\ \delta I_{q,TRU1}\ \delta V_{d,TRU1}\ \delta V_{q,TRU1}\ \delta I_{LF1}\ \delta V_{CF1}$$
$$\delta\omega_{r,D1}\ \delta I_{sqm,D1}\ \delta V_{f,D1}\ \delta V^{*}_{sqm,D1}\ \delta I^{*}_{sqm,D1}$$
$$\delta I_{d,eq2}\ \delta I_{q,eq2}\ \delta V_{d,eq2}\ \delta V_{q,eq2}$$
$$\delta I_{d,con1}\ \delta I_{q,con1}\ \delta X_{e,con1}\ \delta X_{d,con1}\ \delta X_{q,con1}\ \delta V_{CF,con1}$$
$$\delta\omega_{r,P1}\ \delta I_{sqm,P1}\ \delta V_{f,P1}\ \delta V^{*}_{sqm,P1}\ \delta I^{*}_{sqm,P1}$$
$$\delta I_{d,L1}\ \delta I_{q,L1}\ ]^{T}$$

$$\delta\mathbf{u} = [\delta V_s\ \delta P_{CPL,D1}\ \delta\omega^{*}_{rD1}\ \delta T_{LD1}\ \delta E^{*}_{1}\ \delta I^{*}_{q1}\ \delta\omega^{*}_{rP1}\ \delta T_{LP1}]^{T}$$

$$\delta\mathbf{y} = [\delta V_{CF1}\ \delta V_{CF,con1}]^{T} \tag{7-33}$$

and

$$\mathbf{A}(\mathbf{x_o},\mathbf{u_o}) = \mathbf{H}^{-1}\mathbf{A_1}(\mathbf{x_o},\mathbf{u_o}),\ \mathbf{B}(\mathbf{x_o},\mathbf{u_o}) = \mathbf{H}^{-1}\mathbf{B_1}(\mathbf{x_o},\mathbf{u_o}) \tag{7-34}$$

Note that $\mathbf{B_s}$ in (7-30) is the same as that of Appendix E because there is the transmission line1 between Gen bus and HVAC bus (t_1=1). In this section, the dq frame is aligned on the AC ESS bus voltage vector.

7.5.2 Calculating the Steady-State Equilibrium Value

The linearized model in (7-28)-(7-34) needs to define V_{CFo1} in $\mathbf{A_{D1}}$, $\mathbf{A_{mD1}}$, $\mathbf{A_{HmD1}}$, $\mathbf{B_{D1}}$, the set of steady-state values for 10kW IM drive ($V_{sqmo,D1}$, $V_{sdmo,D1}$, $I_{sdmo,D1}$, $I_{sqmo,D1}$, $\omega_{eo,D1}$) and $M_{qo,D1}$ in $\mathbf{A_{mD1}}$, $\mathbf{A_{VmD1}}$, $\mathbf{A_{HmD1}}$, the set of steady-state values of controlled PWM rectifier (X_{eo1}, X_{do1}, X_{qo1}, $V_{CFo,con1}$, I_{indo1}, I_{inqo1}, V_{busdo1}, V_{busqo1}) in $\mathbf{A_{P1}}$, $\mathbf{B_{P1}}$, the set of steady-state values for 20kW IM drive ($V_{sqmo,P1}$, $V_{sdmo,P1}$, $I_{sdmo,P1}$, $I_{sqmo,P1}$, $\omega_{eo,P1}$) and $M_{qo,P1}$ in $\mathbf{A_{mP1}}$, $\mathbf{A_{VmP1}}$, $\mathbf{A_{HmP1}}$, θ_{d1} in $\mathbf{A_{D1}}$, and θ_s in $\mathbf{B_s}$.

The sets of steady-state values for 10kW and 20kW IM drives can be calculated from the operating point defined from the actuator load speed and load torque (ω_{rD1o}, T_{LD1o}, ω_{rP1o}, T_{LP1o}) by using (4-28)-(4-30) of Chapter 4. These steady-state values are then used to determine $P_{dynPCL,D1}$ and $P_{dynCPL,P1}$

by (4-27) of Chapter 4. Note that $P_{dynPCL,D1}$ and $P_{dynCPL,P1}$ are the power delivered to the dynamic CPL connected to diode rectifier unit and controlled PWM rectifier, respectively. The steady-state power values $P_{dynPCL,D1}$ and $P_{dynCPL,P1}$ are then used for power flow calculation with $P_{idealCPL,D1}$ to achieve the rest steady-state values such as V_{CFo1}, θ_{d1}, θ_s, V_{busdo1}, V_{busqo1}, I_{indo1}, and I_{inqo1}.

The power flow equation can be used to determine the steady-state value at the AC side. The single line power diagram of the power system in Figure 7.15 is depicted in Figure 7.16 in which the line capacitors are ignored assuming they are very small.

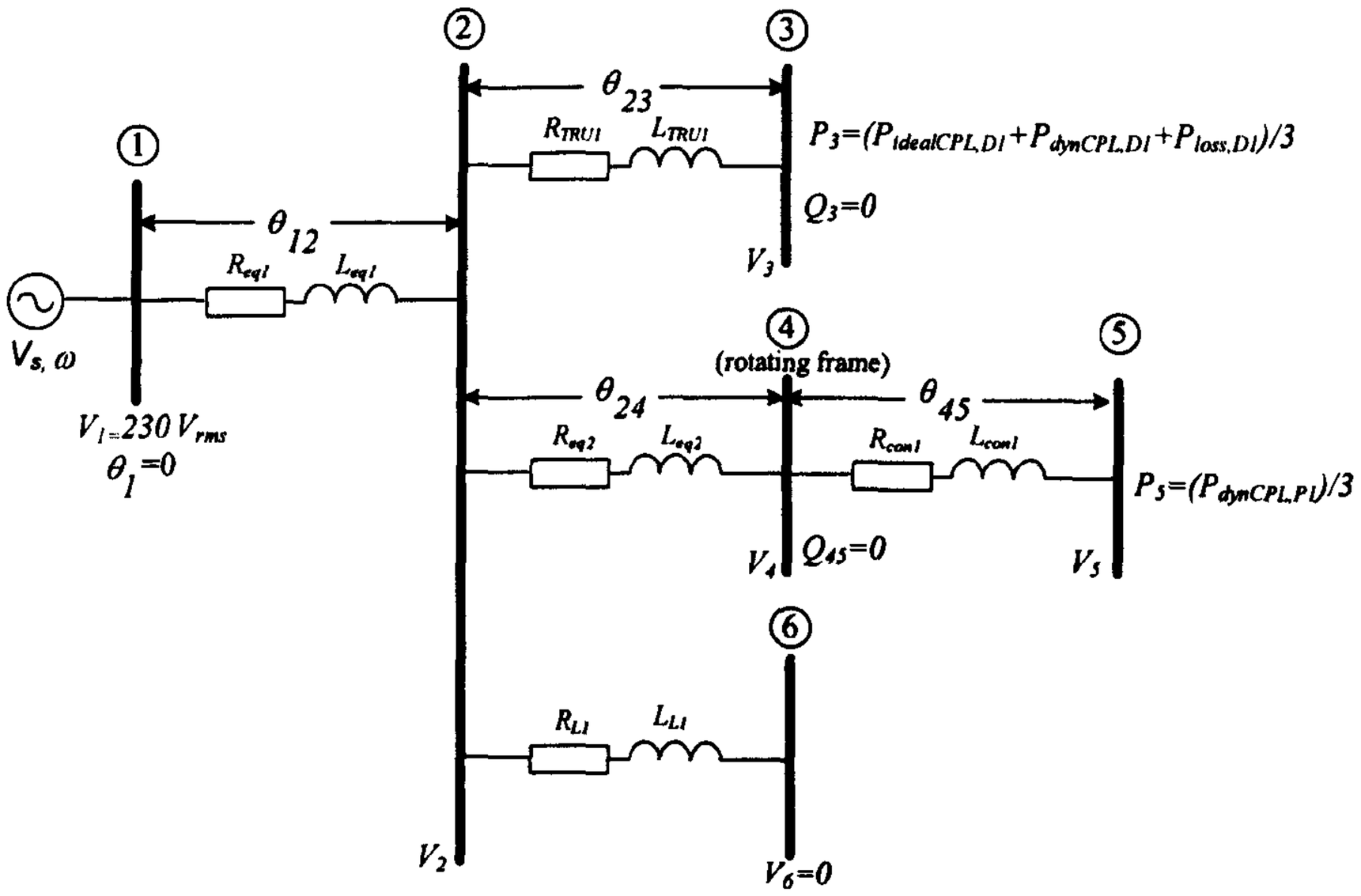

Figure 7.16: The single line diagram for steady-state power calculations of Figure 7.15 (θ_1 is the reference frame set to zero)

Figure 7.16 leads to a system of eight nonlinear equations:

$$
\begin{aligned}
&\frac{V_2V_3}{Z_{23}}\cos(\gamma_{23}-\theta_{23})-\frac{V_3^2}{Z_{23}}\cos(\gamma_{23})=P_3\\
&\quad=(P_{idealCPL,D1}+P_{dynCPL,D1}+P_{loss,D1})/3\\
&\frac{V_2V_3}{Z_{23}}\sin(\gamma_{23}-\theta_{23})-\frac{V_3^2}{Z_{23}}\sin(\gamma_{23})=Q_3=0\\
&\frac{V_4V_5}{Z_{45}}\cos(\gamma_{45}-\theta_{45})-\frac{V_5^2}{Z_{45}}\cos(\gamma_{45})=P_5=(P_{dynCPL,P1})/3\\
&\frac{V_1V_2}{Z_{12}}\cos(\gamma_{12}-\theta_{12})+\frac{V_2V_3}{Z_{23}}\cos(\gamma_{23}+\theta_{23})+\frac{V_2V_4}{Z_{24}}\cos(\gamma_{24}+\theta_{24})\\
&-V_2^2\left[\frac{\cos(\gamma_{12})}{Z_{12}}+\frac{\cos(\gamma_{23})}{Z_{23}}+\frac{\cos(\gamma_{24})}{Z_{24}}+\frac{\cos(\gamma_{26})}{Z_{26}}\right]=0\\
&\frac{V_1V_2}{Z_{12}}\sin(\gamma_{12}-\theta_{12})+\frac{V_2V_3}{Z_{23}}\sin(\gamma_{23}+\theta_{23})+\frac{V_2V_4}{Z_{24}}\sin(\gamma_{24}+\theta_{24})\\
&-V_2^2\left[\frac{\sin(\gamma_{12})}{Z_{12}}+\frac{\sin(\gamma_{23})}{Z_{23}}+\frac{\sin(\gamma_{24})}{Z_{24}}+\frac{\sin(\gamma_{26})}{Z_{26}}\right]=0\\
&\frac{V_1V_2}{Z_{12}}\cos(\gamma_{12}-\theta_{12})+\frac{V_2V_3}{Z_{23}}\cos(\gamma_{23}+\theta_{23})+\frac{V_2V_5}{Z_{25}}\cos(\gamma_{25}+\theta_{24}+\theta_{45})\\
&-V_2^2\left[\frac{\cos(\gamma_{12})}{Z_{12}}+\frac{\cos(\gamma_{23})}{Z_{23}}+\frac{\cos(\gamma_{25})}{Z_{25}}+\frac{\cos(\gamma_{26})}{Z_{26}}\right]=0\\
&\frac{V_1V_2}{Z_{12}}\sin(\gamma_{12}-\theta_{12})+\frac{V_2V_3}{Z_{23}}\sin(\gamma_{23}+\theta_{23})+\frac{V_2V_5}{Z_{25}}\sin(\gamma_{25}+\theta_{24}+\theta_{45})\\
&-V_2^2\left[\frac{\sin(\gamma_{12})}{Z_{12}}+\frac{\sin(\gamma_{23})}{Z_{23}}+\frac{\sin(\gamma_{25})}{Z_{25}}+\frac{\sin(\gamma_{26})}{Z_{26}}\right]=0\\
&-\frac{V_4V_5}{Z_{45}}\sin(\gamma_{45}-\theta_{45})+\frac{V_4^2}{Z_{45}}\sin(\gamma_{45})=Q_{45}=0
\end{aligned}
\tag{7-35}
$$

where

$$Z_{12}=\sqrt{R_{eq1}^2+(\omega L_{eq1})^2},\gamma_{12}=\tan^{-1}\left(\frac{\omega L_{eq1}}{R_{eq1}}\right)$$

$$Z_{23}=\sqrt{R_{TRU1}^2+(\omega L_{TRU1})^2},\gamma_{23}=\tan^{-1}\left(\frac{\omega L_{TRU1}}{R_{TRU1}}\right)$$

$$Z_{24}=\sqrt{R_{eq2}^2+(\omega L_{eq2})^2},\gamma_{24}=\tan^{-1}\left(\frac{\omega L_{eq2}}{R_{eq2}}\right)$$

$$Z_{45} = \sqrt{R_{con1}^2 + (\omega L_{con1})^2}, \gamma_{45} = \tan^{-1}\left(\frac{\omega L_{con1}}{R_{con1}}\right)$$

$$Z_{25} = \sqrt{(R_{eq2} + R_{con1})^2 + \omega^2 (L_{eq2} + L_{con1})^2}, \gamma_{25} = \tan^{-1}\left(\frac{\omega(L_{eq2} + L_{con1})}{(R_{eq2} + R_{con1})}\right)$$

$$Z_{26} = \sqrt{R_{L1}^2 + (\omega L_{L1})^2}, \gamma_{26} = \tan^{-1}\left(\frac{\omega L_{L1}}{R_{L1}}\right)$$

In (7-35), V_1, V_2, V_3, V_4, V_5 and V_6 are the steady state phase voltage (rms) at Bus 1, 2, 3, 4, 5, and 6, respectively. V_1 is set to 230 V_{rms} and V_6 is set to 0 for this example system. θ_{12}, θ_{23}, θ_{24} and θ_{45} are the phase shift between each bus. The active and reactive power (per phase) at Bus 3 (input terminal of diode rectifier unit), the active power (per phase) at Bus 5 (input terminal of controlled PWM rectifier unit), and the reactive power flow from Bus 4 to Bus 5, all are given by:

$$\begin{aligned} P_3 &= (P_{idealCPL,D1} + P_{dynCPL,D1} + P_{loss,D1})/3 \\ Q_3 &= 0 \\ P_5 &= (P_{dynCPL,P1})/3 \\ Q_{45} &= 0 \end{aligned} \tag{7-36}$$

where $P_{dynCPL,D1}$ and $P_{dynCPL,P1}$ can be calculated from the actuator operating points as mentioned before. $P_{idealCPL,D1}$ is the ideal CPL connected to diode rectifier unit. $P_{loss,D1}$ is the power loss due to r_{LF1} and Q_3 is set to zero because of the diode rectifier assumption as mentioned in Chapter 2. Q_{45} is set to zero because I_{q1}^* of controlled PWM rectifier is set to zero to keep a unity power factor at Bus 4. Equation (7-35) can be solved by using a numerical method such as Newton Raphson so as to find V_{2o}, V_{3o}, V_{4o}, V_{5o}, θ_{12o}, θ_{23o}, θ_{24o} and θ_{45o} at the steady state condition (8 unknowns).

Consequently, V_{CFo1} for linearized model can then be calculated from V_{3o} by using (6-9) of Chapter 6. P_{EMA} in (6-9) is changed to $P_{idealCPL,D1}+P_{dynCPL,D1}$ for this case. $M_{qo,D1}$ can be calculated from V_{CFo1} by using (4-32) of Chapter 4.

The set of steady-state values of controlled PWM rectifier (X_{eo1}, X_{do1}, X_{qo1}, $V_{CFo,con1}$, I_{indo1}, I_{inqo1}, V_{busdo1}, V_{busqo1}) can be calculated from V_{4o}, V_{5o} and θ_{45o} by using (3-14) of Chapter 3. In addition, θ_{d1}, and θ_s for linearized model in (7-28)-(7-34) can be determined by:

$$\theta_{d1} = \theta_{43o}, \theta_s = \theta_{14o} \tag{7-37}$$

where

$$\theta_{2o} = \theta_{1o} - \theta_{12o} = -\theta_{12o}$$
$$\theta_{3o} = \theta_{2o} - \theta_{23o}$$
$$\theta_{4o} = \theta_{2o} - \theta_{24o}$$
$$\theta_{5o} = \theta_{4o} - \theta_{45o}$$
$$\theta_{43o} = \theta_{4o} - \theta_{3o}$$
$$\theta_{14o} = \theta_{1o} - \theta_{4o} = -\theta_{4o}$$

According to (7-35)-(7-37), the steady-state values changes when the system operating point, defined from $P_{idealCPL,D1}$, $P_{dynCPL,D1}$, and $P_{dynCPL,P1}$, changes. Therefore, we can get different linearized model of (7-28)-(7-34) for the system in Figure 7.15 for each operating point.

7.5.3 Small-Signal Simulation and Stability Analysis

The linearized model (7-28)-(7-34) was simulated for small-signal transients against corresponding 3-phase benchmark circuit model simulated in SABER. The details of the SABER model for the system in Figure 7.15 are given in Appendix D.11. The example system parameters are given in Table 7.3 and Table 7.4. For example, Figure 7.17 shows the DC-link voltage responses of V_{CF1} and $V_{CF,con1}$ in the system of Figure 7.15 to a step change in T_{LD1} from 30 to 50 Nm at t=1.6s. and other parameters are fixed as shown in Table 7.3 and Table 7.4. Similarly, the DC-link voltage responses to a step change of $P_{ideal,D1}$ from 25 to 30 kW and T_{LP1} from 30 to 50 Nm are also depicted in Figure 7.18 and Figure 7.19, respectively. It can be seen that there is good agreement

between SABER benchmark model and 32nd order dq linearized model is achieved under small-signal simulation.

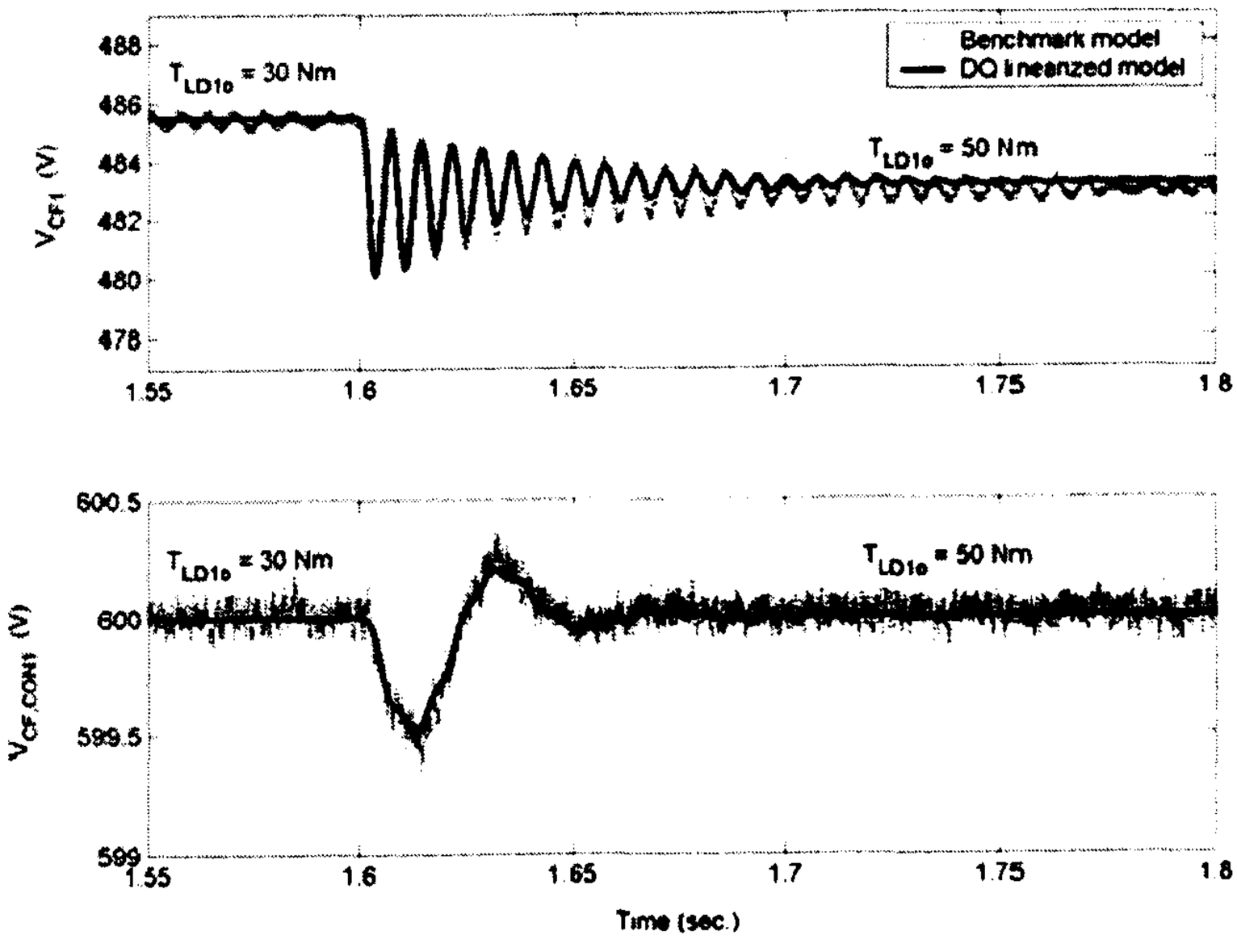

Figure 7.17: Responses of V_{CF1} and $V_{CF,con1}$ to a step change of T_{LD1} from 30 to 50 Nm. A comparison of the SABER benchmark model with the dq linearized model

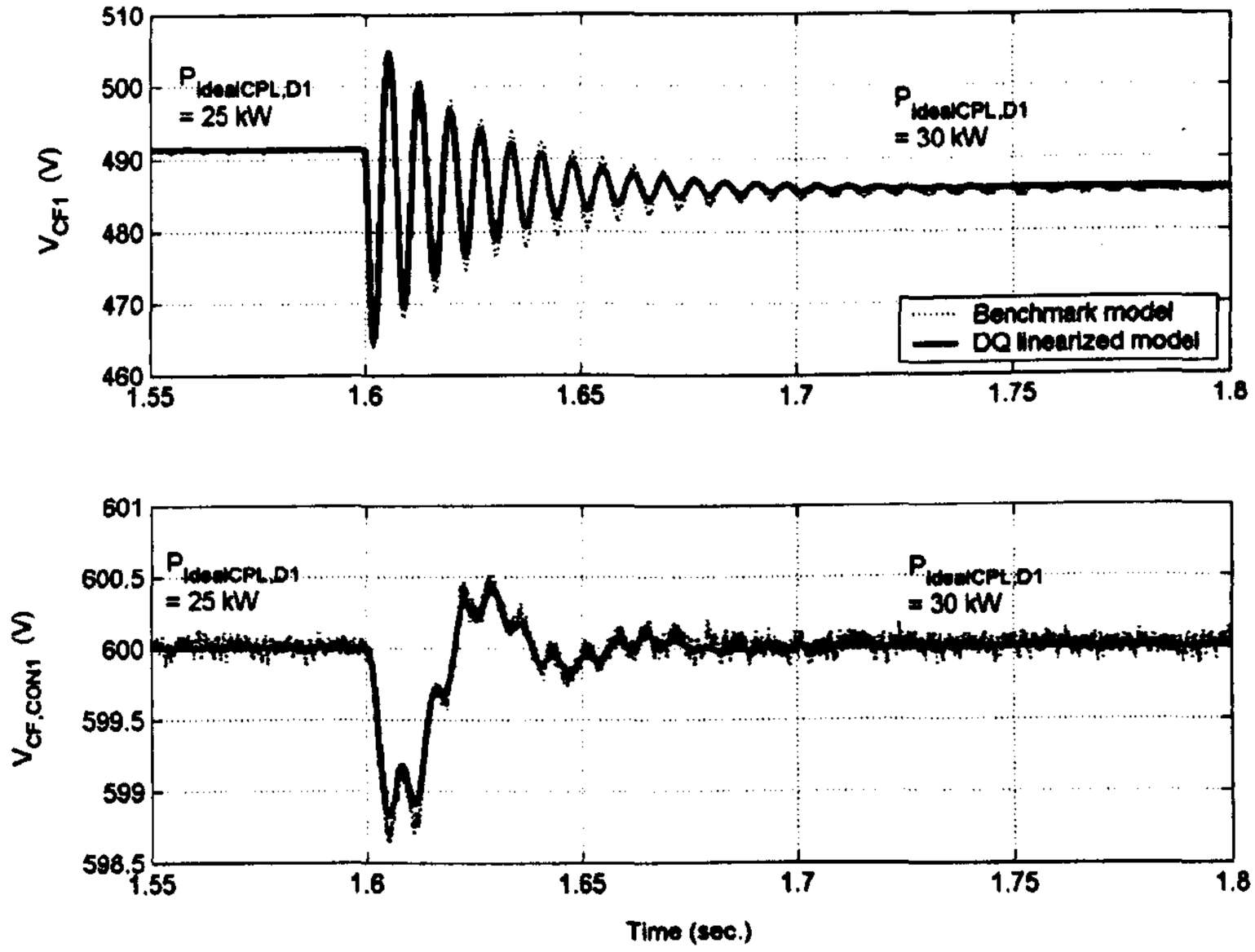

Figure 7.18: Responses of V_{CF1} and $V_{CF,con1}$ to a step change of $P_{ideal,D1}$ (ideal CPL fed through diode rectifier unit) from 25 to 30 kW. A comparison of the SABER benchmark model with the dq linearized model

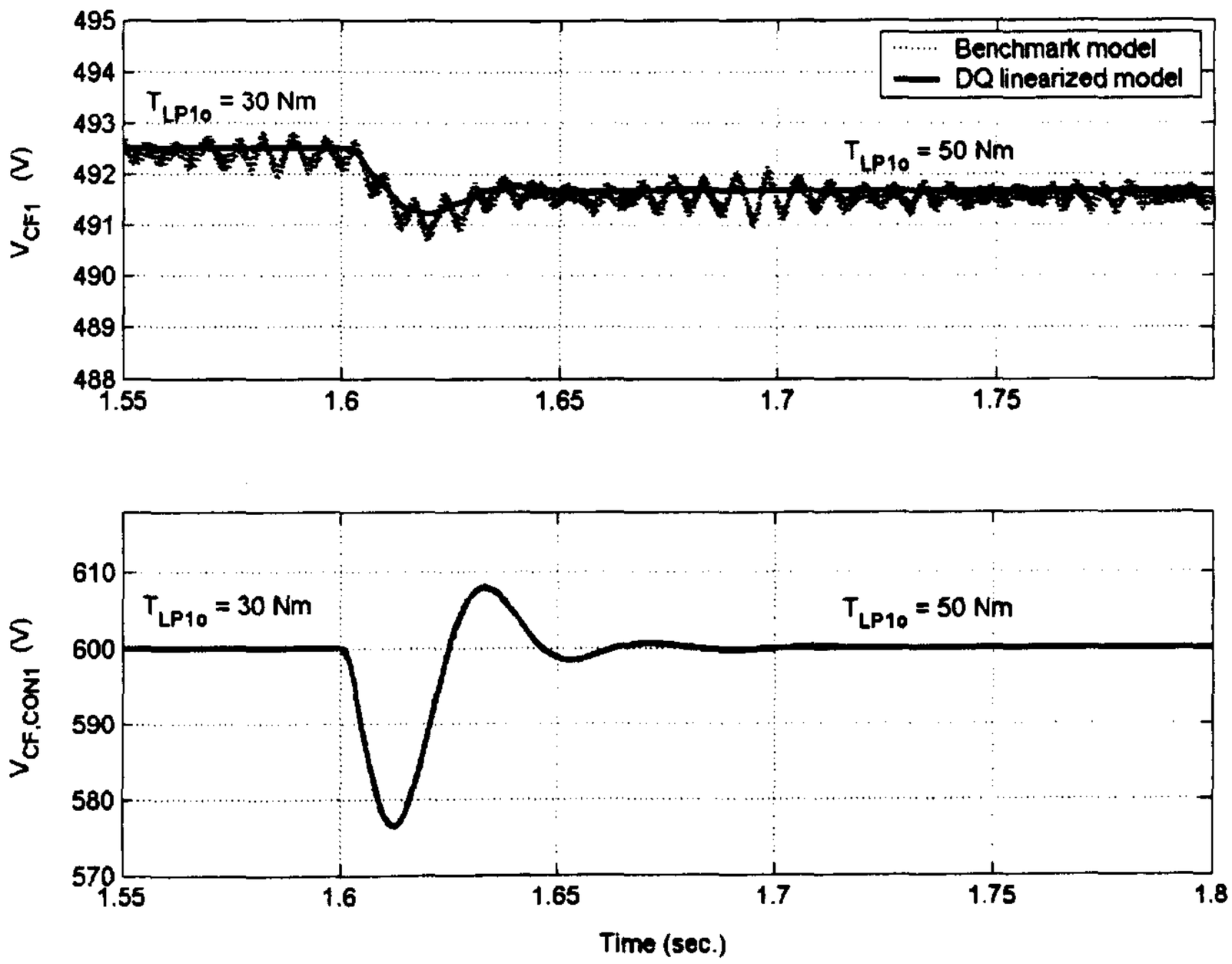

Figure 7.19: Responses of V_{CF1} and $V_{CF,con1}$ to a step change of T_{LP1} from 30 to 50 Nm. A comparison of the SABER benchmark model with the dq linearized model

For the stability analysis, the linearized model is used with the eigenvalue theorem. The eigenvalues can be calculated from the Jacobian matrix $\mathbf{A}(\mathbf{x_o},\mathbf{u_o})$ in (7-29). The eigenvalues for the system with parameters in Table 7.3 and Table 7.4 were analyzed for the case when the load torque of T_{LD1} (10 kW IM drive) varies from 0 to 150 Nm with the other constant system inputs as shown in Table 7.3 and Table 7.4 (ω^*_{rD1}=1000 rpm, $P_{ideal,D1}$=30 kW, T_{LP1}=190 Nm, ω^*_{rP1}=975 rpm, $V^*_{CF,con1}$=600V, and I^*_{q1}=0A). This variation corresponds to the steady-state value of $P_{dynCPL,D1}$ varying from 0.45 to 17.20 kW. The dominant root locus is shown in Figure 7.20. This figure shows that the system becomes unstable when the power $P_{dynCPL,D1}$ exceeds 10.7 kW (T_{LD1}=94 Nm, ω^*_{rD1}=1000 rpm) for the studied case. Figure 7.21 shows the SABER time-domain benchmark simulations that support the theoretical prediction with the instability occurring at $P_{dynCPL,D1}$ of 10.8 kW. This is greater than the 10.7 kW predicted for an unstable condition.

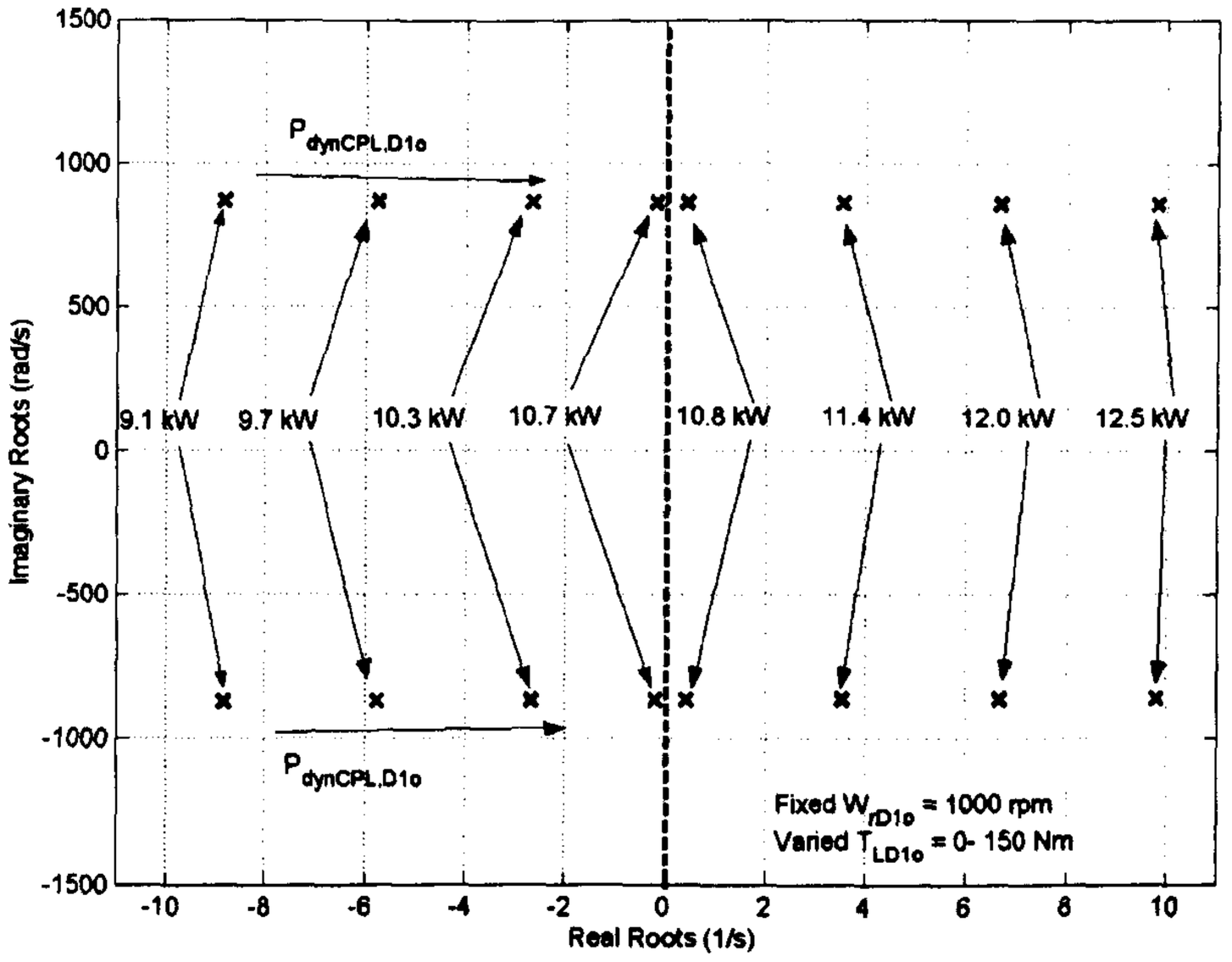

Figure 7.20: Dominant eigenvalue plot for varying $P_{dynCPL,D1}$

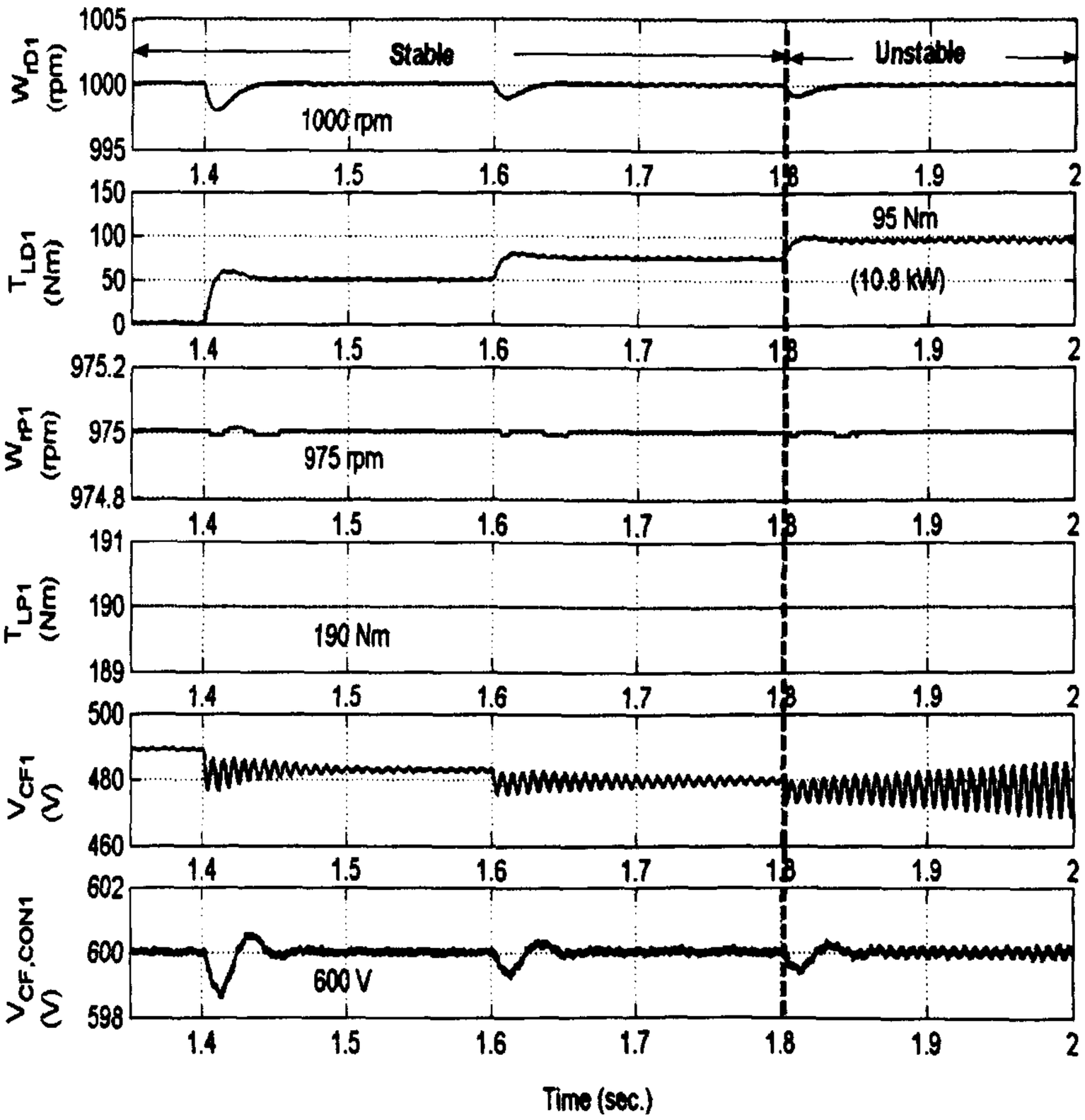

Figure 7.21: Step response for operating point ($P_{dynCPL,D1}$) variations

For the real aircraft power system as shown in Figure 7.15, $P_{idealCPL,D1}$ is paralleled with $P_{dynCPL,D1}$ and both are connected to a DC bus fed through a diode rectifier unit. It is interesting to analyse the stability when the operating point of both loads varies. This is to understand the effect of load variations on the stability margin.

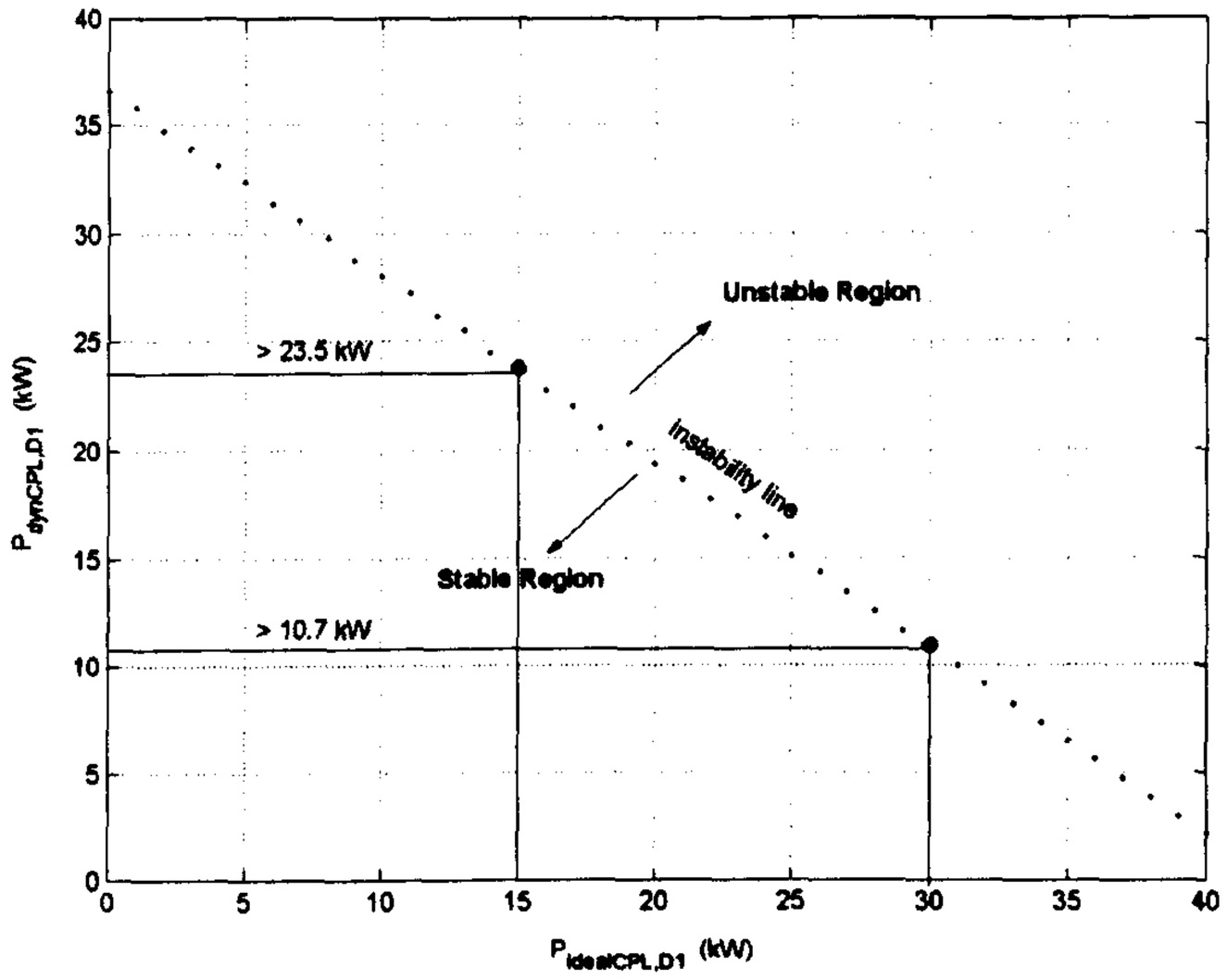

Figure 7.22: Instability power for $P_{idealCPL,D1}$ variations

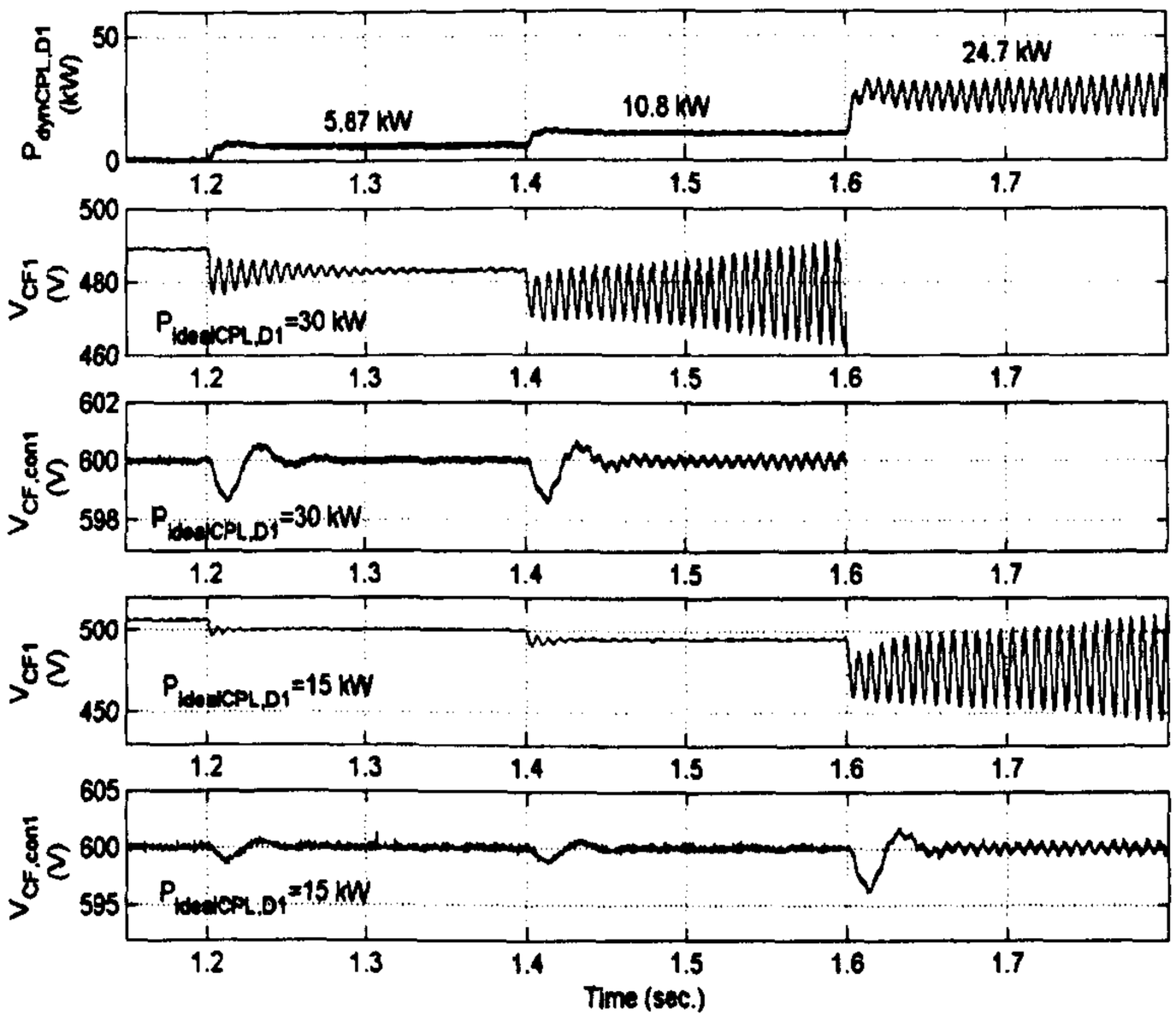

Figure 7.23: Verification of analytical results for $P_{idealCPL,D1}$ variations

Figure 7.22 shows that when the $P_{idealCPL,DI}$ (ideal CPL fed through diode rectifier) increases, the system becomes less stable. For example, the $P_{dynCPL,DI}$ (dynamic CPL fed by the diode rectifier) should not exceed 10.7 kW at $P_{idealCPL,DI}$=30 kW, but is stable if $P_{idealCPL,DI}$ is less than 30 kW. The theoretical predictions are supported by the SABER benchmark simulation shown in Figure 7.23.

Figure 7.24 shows that varying $P_{dynCPL,PI}$ affects the value of the parallel power feed $P_{dynCPL,DI}$ at which system instability occurs. For example, Figure 7.24 shows that, at $P_{dynCPL,PI}$ = 21.42kW, the value of $P_{dynCPL,DI}$ at which instability occurs is seen to be 10.7kW. However when $P_{dynCPL,PI}$ is increased to 59.48kW, the value of $P_{dynCPL,DI}$ at which instability occurs reduced to 8.9kW. The explanation can be given as follows: when $P_{dynCPL,PI}$ is increased, the voltage drop in transmission line between Gen and HVAC buses is increased. This results in the reduction of diode rectifier DC-link voltage. Increase in the voltage drop reduces $P_{dynCPL,DI}$ at which instability occurs. For this reason, we cannot analyse the individual converter systems independently. An analysis of the total system must be undertaken.

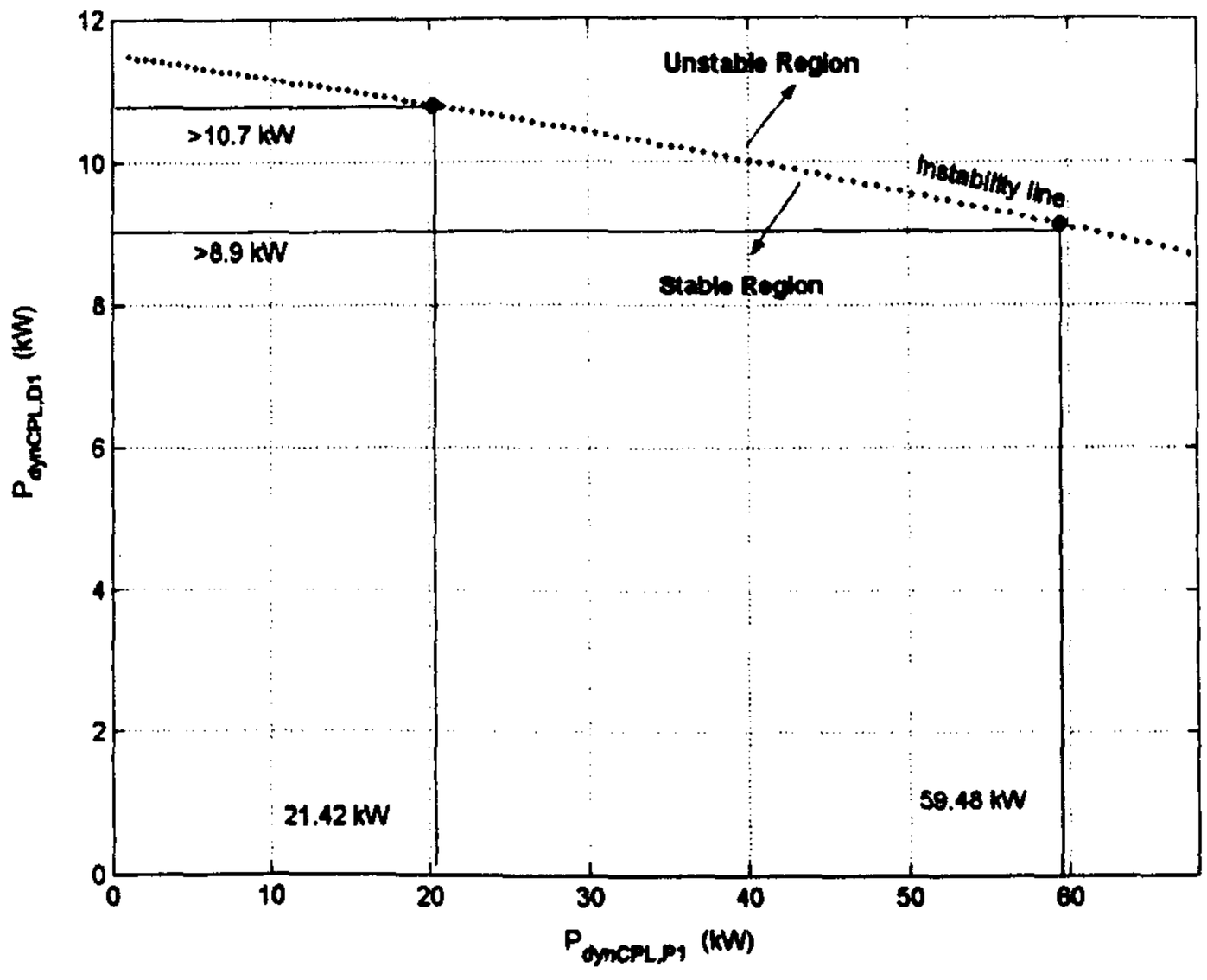

Figure 7.24: Instability power for $P_{dynCPL,PI}$ variations

The theoretical predictions of Figure 7.24 are supported by the SABER benchmark simulation shown in Figure 7.25.

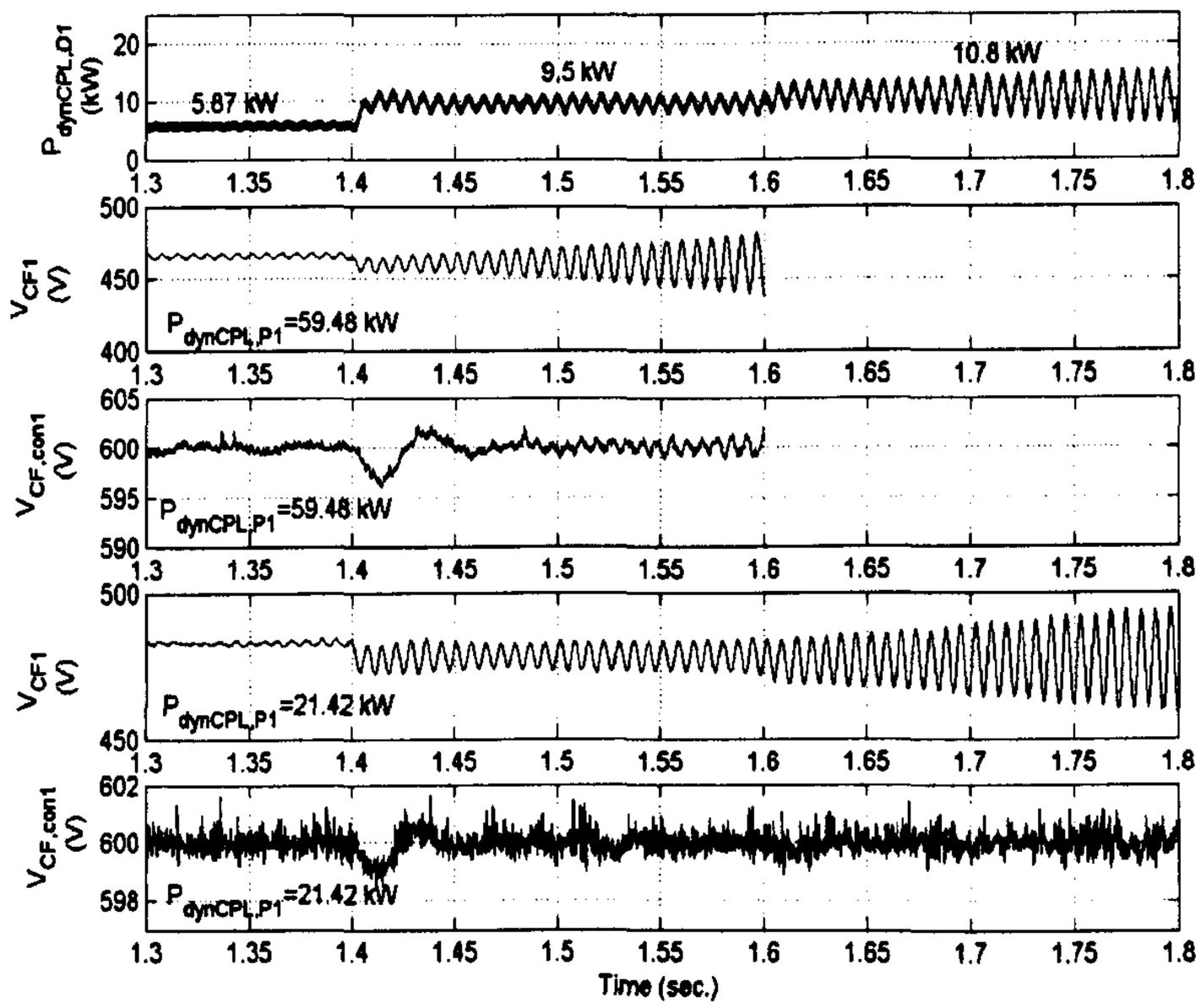

Figure 7.25: Verification of analytical results for $P_{dynCPL,P1}$ variations

7.6 Chapter Summary

This chapter deals with the modelling and stability of a more generalized aircraft power system based on a AC distribution power system. The model is derived from the dq modelling method. The generalized model allows for representation in an algorithmic way of realistic architectures with a multiplicity of actuators, aircraft loads, bus geometries and wild frequency in the system. A previously reported method, the state space averaging (SSA) modelling method and the average value modelling approach, are not easily applicable. The generalized model based on dq modelling approach is illustrated by three example power systems including a realistic aircraft power system. The results show that the linearized model of the system can be easily constructed from the generalized model. The SABER time-domain simulations are used to support the results from the theoretical stability

predictions. The proposed model can predict instability due to possible variations in the operating points and system parameters. Therefore, the generalized model in this chapter is very powerful and flexible for the analysis of the multi-converter systems. It is shown that analysing individual power converter systems independently will yield incorrect results.

Chapter 8

Conclusion and Discussion

8.1 Conclusion and Discussion

The thesis presents the development of effective models capable of representing the electrical power system dynamic behaviour for stability studies. The dq modelling method is applied to derive individual power system component models. The proposed model can be used to predict the instability point for variations in operating points and/or system parameters. Agreement between the theoretical estimation, simulation, and experimental results for a simple system are achieved that ranges from acceptable to very good. Finally, the subsystem models described in the thesis can be used to constitute the corresponding generalized power system model as a powerful and flexible stability analysis tool. The element models can be interconnected in an algorithmic way according to the architecture selected. The generalized model is also applied to a more complex and realistic aircraft power system with simulation validations for thorough investigations of aircraft power system stability. The conclusions and further discussions as well as proposals for future work are given in this chapter.

Chapter 2 investigated the modelling and stability analysis of AC-DC power system with a six-pulse diode rectifier and also shows how the model of six-pulse diode rectifier can be used to represent the twelve-pulse autotransformer rectifier unit. The results from Chapter 2 show that dq, SSA, and average-value modelling approaches can provide equivalent circuits of a power system to create a mathematical model for stability study. However, the average-value model is not easily applicable for the complex power systems with the

multiplicity of actuators, aircraft loads, and bus geometries. Hence, the dq modelling approach was selected for modelling the aircraft power systems in this research. The application of the dq modelling method for stability analysis of the system consisting of CPLs has not been reported in previous publications. For stability studies, the eigenvalue theorem was used in this research. This is because when the impedance method is used, it is difficult to derive the source and load impedances for complex AC systems having parallel power converter connections. In addition, the dq modelling approach with the eigenvalue theorem was used to analyse the stability for variations in system parameters. The results show that increasing system frequency, reducing value of DC link inductance, and increasing the value of DC link capacitor can extend the power level at which instability occurs. The SABER time-domain simulation was used to validate the theoretical instability predictions.

Chapter 3 exploits the advantages of dq modelling approach. This method was used to model the power system with an ideal CPL fed through a controlled PWM rectifier. Since the controlled PWM rectifier uses dq structures, the dq modelling method was straightforward and appropriate. Stability analysis used the eigenvalue approach. The dq model of a controlled PWM rectifier for stability studies has not been reported in previous publications. The mathematical model is derived, validated and used to predict the unstable operation of the power system under certain CPL levels and parameters variations. The results show that increasing the bandwidth of voltage loop control reduces system stability, while the other parameters are not significant in terms of their impact on stability.

Chapter 4 investigated the stability analysis of the power system taking into account the dynamics of controlled electromechanical actuators (EMAs). These EMAs have been previously represented as an ideal CPL in Chapter 2 and 3 without dynamic behaviour. The dq modelling approach with the eigenvalue theorem was used to analyse the stability. The results show that the

effect of CPL dynamics was significant. The CPL dynamics (in terms of speed bandwidth and DC-link voltage measurement filter) can increase the stable power range compared with the ideal CPL. Although neglecting the CPL dynamics may be beneficial from the viewpoint of power system availability, it may result in a very non-optimal design solutions that would impact on overall mass and dimension. The CPL dynamic effects depend on the EMA parameters. The results show that reducing the bandwidth of the DC-link voltage filter (for some cases) and decreasing the EMA speed control natural frequency can extend the power levels for stable operation. To achieve an accurate model of a power system, the dynamic model of the EMA behaving as a non-ideal CPL cannot be ignored. The SABER time-domain simulation was used to support the theoretical stability results. Good agreement between both models was achieved. The dynamic model for the power system with PM machine (instead of IM) including the internal resistance of a DC-link capacitor was also considered. Stability analysis using this model was described in Chapter 5 with experimental results.

In Chapter 5, the experimental results have been undertaken and compared with theoretical predictions. The power system used for experiment consists of a reasonably ideal voltage source, three-phase transmission lines, a six-pulse diode rectifier, a DC-link filter (including the internal resistance of DC-link capacitor, r_c), and a SMPM machine drive having non-ideal CPL dynamics. The mathematical model was derived by using the dq modelling approach. In addition, the simulation results were also used to support the theoretical results. According to the results, agreement between the mathematical model, simulation, and experimental results were achieved that ranges from acceptable to very good. This confirms that the dq modelling approach can obtain stability results with good accuracy. After this the dq models were applied to more complex power systems in Chapter 6 and 7. The predicted results from the model for the complex system were supported by the SABER time-domain simulation.

Chapter 6 investigated the stability analysis of a power system taking into account the dynamics of the synchronous generator with a generator control unit (SG-GCU) and the dynamics of the electromechanical actuators (EMAs). The dynamics of SG-GCU have been previously represented as an ideal voltage source without dynamic behaviour in Chapter 2-5. The dq modelling method with the eigenvalue theorem was used to analyse the stability. The results show that the effect of CPL dynamics was significant, while the effect of SG-GCU dynamics was small. In addition, this chapter also describes the stability analysis for parameter variations of different operational regimes. The results show that the effect of the natural frequency of the voltage loop in the GCU was small in terms of stability. As a result, the dynamics of SG-GCU can be neglected for stability analysis of a more complex power system as described in Chapter 7, to simplify the mathematical model. Moreover, as described in Chapter 3, if the controlled PWM rectifier is analysed, the vector-control is in terms of the reference frame aligned to the AC bus voltage vector. Due to the dq frame being aligned on this AC bus voltage vector, it is very difficult to analyse the power system including both the SG-GCU and the controlled PWM rectifier. This is because the parameters of the generator model become time-varying parameters (depending on the rotor position), when the dq frame of the model is not aligned to the rotor axis. In this chapter it was shown that the dynamics of SG-GCU has negligible effects on stability. Therefore, these dynamics were neglected for analysing more complex power systems in Chapter 7 in which an ideal voltage source represents the SG-GCU.

Chapter 7 introduced the modelling and stability of the generalized aircraft power system based on a AC distribution power system from the MOET project. The model was derived from the dq modelling method. The generalized model allows for representation in an algorithmic way of real architectures with a multiplicity of actuators, aircraft loads, bus geometries and wild frequency in the system. A previously reported method, the state space averaging (SSA) modelling method and the average value modelling approach, are not easily applicable. The generalized model based on dq

modelling approach was illustrated by three example power systems including a more realistic aircraft power system. The results show that the linearized model of the system can be easily constructed from the generalized model. The SABER time-domain simulations are used to support the results from the theoretical stability predictions. The proposed model can predict instability due to possible variations in the operating points and system parameters. Therefore, the generalized model in this chapter is very powerful and flexible for the analysis of the multi-converter system. It can provide more accurate results than that of analysing only individual power converter systems. The results show that we cannot analyse the individual converter system separately for these aircraft power systems that include a multiplicity of actuators, aircraft loads and bus geometries.

8.2 Future Works

The possible future works that can be developed from the work of the thesis are listed below:

- The dq modelling method can be applied to model the power system consisting of a matrix converter (AC/AC converter). The dq model can then be used to analyse the system stability. This is because the matrix converters with their controls behave as a constant power load causing the negative impedance instability into the power system.

- The generalized aircraft power system presented in the thesis is very powerful and flexible for stability studies. It is very interesting if the stability results of more complex power systems of Chapter 7 can be validated experimentally. Moreover, the generalized model based on dq modelling method can be used to implement a stability analysis tool via a graphical user interface to make the system usable to a general engineer.

• The small-signal stability analysis is used in the thesis through the linearized model using the first order terms of Taylor expansion. The main assumption for small-signal stability study is that the operating point of aircraft power system is not changed rapidly for normal operating modes. However, it is very interesting to apply the large-signal stability analysis using nonlinear approaches instead of the eigenvalue theorem. The large-signal models are already provided from the dq modelling method. These models can be used with a large-signal stability analysis for the aircraft power system.

• Development of the dq modelling method to model the other power system architecture. This system consists of a synchronous generator (SG) and generator control unit (GCU) to control the voltage at the DC bus instead of the generator feeder bus.

8.3 Publications

The research given in the thesis has resulted in 3 conference papers [32],[33],[34], two papers submitted to IEEE transaction on Aerospace and Electronic System, and we are currently drafting more journal and conference papers from the work of the thesis.

Appendix A

Transformation Conventions

A.1 Transformation Conventions

A three phase quantities can be transformed into a two axis frame (dq frame) rotating at an instantaneous speed (ω). This is called dq transformation. The dq transformation equation is given by [84]:

$$\lfloor f_{dq} \rfloor = \mathbf{T}[\omega t][f_{abc}] \tag{A-1}$$

where f may be a voltage, current, or flux of a machine and the dq transformation matrix is defined as:

$$\mathbf{T}[\omega t] = K\begin{bmatrix} \cos(\omega t) & \cos(\omega t - \frac{2\pi}{3}) & \cos(\omega t + \frac{2\pi}{3}) \\ -\sin(\omega t) & -\sin(\omega t - \frac{2\pi}{3}) & -\sin(\omega t + \frac{2\pi}{3}) \end{bmatrix} \tag{A-2}$$

K is a constant coefficient depending on the type of transformation conventions. K is equal to 2/3 for peak conventions [84]. The vector diagram of dq transformation is shown in Figure A.1.

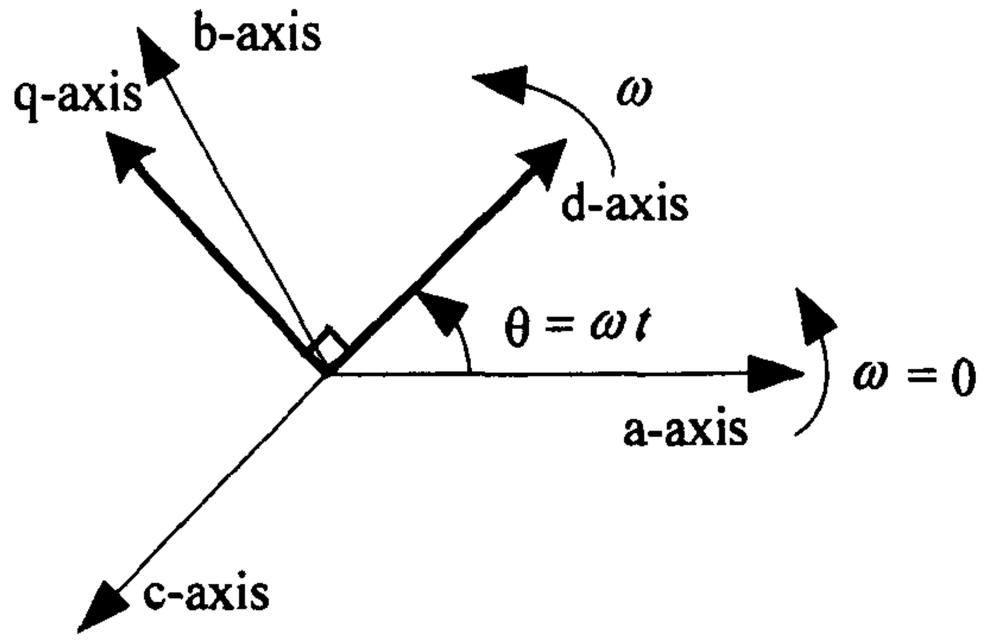

Figure A.1: The vector diagram of dq transformation

Similarly, a two axis frame (dq frame) can be transformed into a three phase frame called an inverse dq transformation. An inverse dq transformation is given by:

$$[f_{abc}] = \mathbf{T}^{-1}[\omega t][f_{dq}] \tag{A-3}$$

where the inverse dq transformation matrix is defined as:

$$\mathbf{T}^{-1}[\omega t] = \begin{bmatrix} \cos(\omega t) & -\sin(\omega t) \\ \cos(\omega t - \frac{2\pi}{3}) & -\sin(\omega t - \frac{2\pi}{3}) \\ \cos(\omega t - \frac{2\pi}{3}) & -\sin(\omega t + \frac{2\pi}{3}) \end{bmatrix} \tag{A-4}$$

Appendix B

DQ Transformations of Line Elements

B.1 Series *RL* Circuit

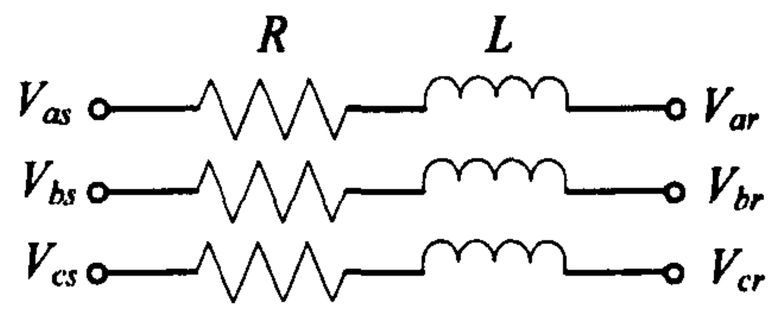

Figure B.1: The three-phase RL lines

Considering the three-phase *RL* lines as shown in Figure B.1, the three-phase voltage drop equations are given by:

$$\Delta \mathbf{V} = \mathbf{V_s} - \mathbf{V_r} = R\mathbf{i} + L\frac{d}{dt}\mathbf{i} \tag{B-1}$$

where

$$\Delta \mathbf{V} = \begin{bmatrix} \Delta V_a \\ \Delta V_b \\ \Delta V_c \end{bmatrix}, \mathbf{V_s} = \begin{bmatrix} V_{as} \\ V_{bs} \\ V_{cs} \end{bmatrix}, \mathbf{V_r} = \begin{bmatrix} V_{ar} \\ V_{br} \\ V_{cr} \end{bmatrix}, \text{and } \mathbf{i} = \begin{bmatrix} i_a \\ i_b \\ i_c \end{bmatrix}$$

Taking the dq transformation of (A-3) and (A-4) into (B-1), the voltage drop of phase *a* in dq frame is given by:

$$\Delta V_a = \Delta V_d \cos(\omega t) - \Delta V_q \sin(\omega t) \tag{B-2}$$

Similarly, the i_a in terms of the dq currents is given by:

$$i_a = i_d \cos(\omega t) - i_q \sin(\omega t) \tag{B-3}$$

Considering only phase a and taking (B-3) into (B-1), the voltage drop equation of phase a in terms of dq currents is given by:

$$\Delta V_a = \left(Ri_d - \omega L i_q + \frac{d}{dt} i_d \right) \cos(\omega t) - \left(Ri_q + \omega L i_d + \frac{d}{dt} i_q \right) \sin(\omega t) \tag{B-4}$$

Equating the coefficients of $\cos(\omega t)$ and $\sin(\omega t)$ between (B-2) and (B-4) to yield the voltage drop in dq frame:

$$\begin{aligned} \Delta V_d &= \left(Ri_d - \omega L i_q + \frac{d}{dt} i_d \right) \\ \Delta V_q &= \left(Ri_q + \omega L i_d + \frac{d}{dt} i_q \right) \end{aligned} \tag{B-5}$$

According to (B-5), the dq equivalent circuit of the three-phase lines as shown in Figure B.1 is depicted in Figure B.2.

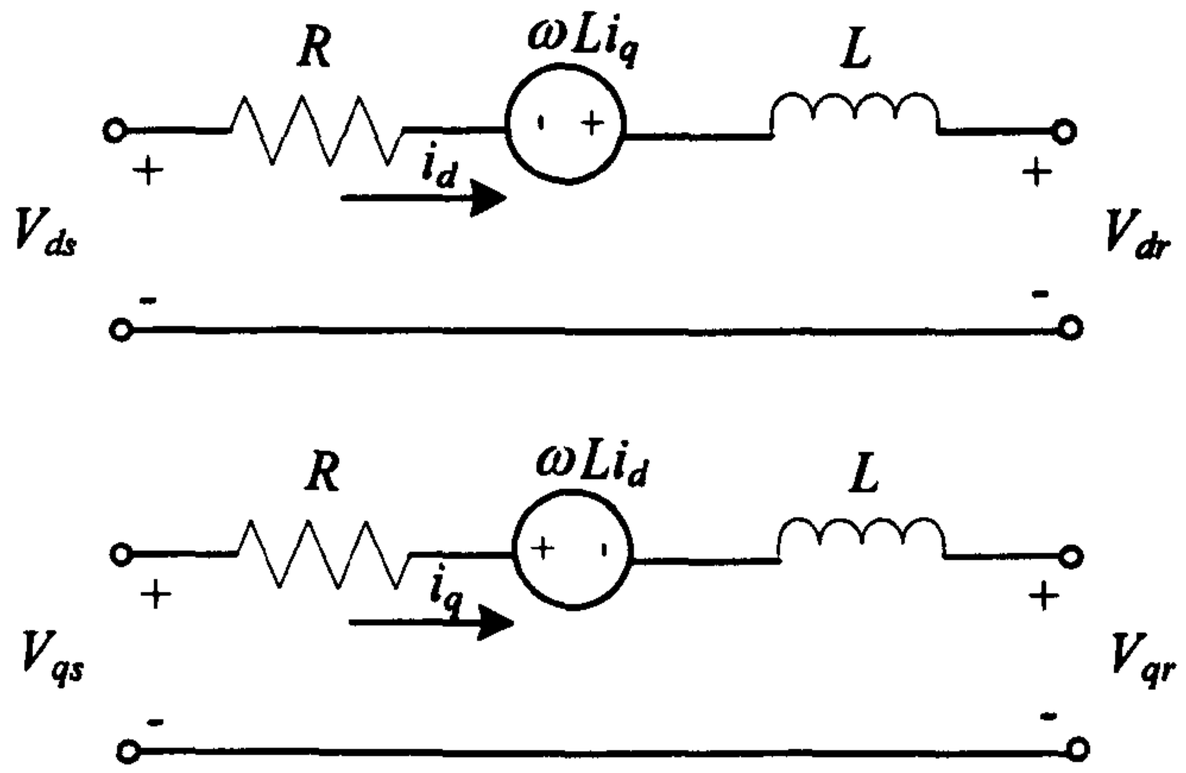

Figure B.2: The equivalent circuit of line series *RL* in dq frame

B.2 Shunt Capacitances

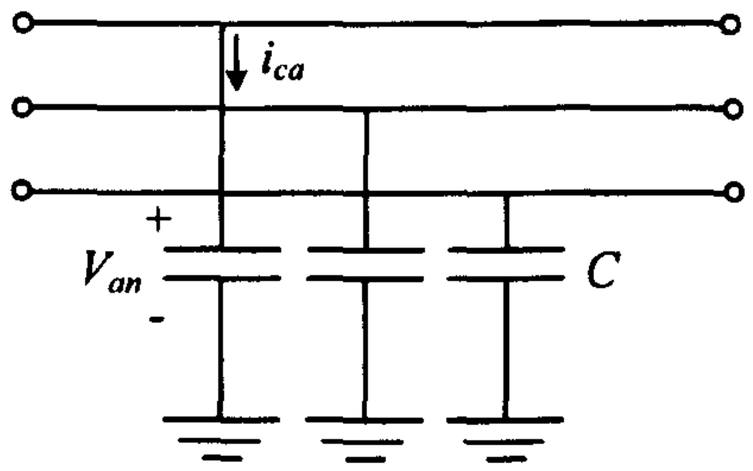

Figure B.3: Three-phase shunt capacitances

Considering the three-phase shunt capacitances as shown in Figure B.3, the three-phase capacitor currents are given by:

$$\mathbf{i_c} = C\frac{d}{dt}\mathbf{V} \tag{B-6}$$

where

$$\mathbf{i_c} = \begin{bmatrix} i_{ca} \\ i_{cb} \\ i_{cc} \end{bmatrix}, \text{ and } \mathbf{V} = \begin{bmatrix} V_{an} \\ V_{bn} \\ V_{cn} \end{bmatrix}$$

Taking the dq transformation of (A-3) and (A-4) into (B-6), the capacitor current of phase a in terms of dq voltage is given by:

$$\begin{aligned} i_{ca} = C\frac{d}{dt}V_{an} = &\left(-\omega C V_q + C\frac{d}{dt}V_d\right)\cos(\omega t) - \\ &\left(+\omega C V_d + C\frac{d}{dt}V_q\right)\sin(\omega t) \end{aligned} \tag{B-7}$$

and we know that the i_{ca} in terms of dq currents is:

$$i_{ca} = i_{cd}\cos(\omega t) - i_{cq}\sin(\omega t) \tag{B-8}$$

Equating the coefficients of cos(ωt) and sin(ωt) between (B-7) and (B-8) to yield the capacitor current in dq frame:

$$\begin{aligned} i_{cd} &= \left(-\omega C V_q + C \frac{d}{dt} V_d \right) \\ i_{cq} &= \left(+\omega C V_d + C \frac{d}{dt} V_q \right) \end{aligned} \tag{B-9}$$

According to (B-5), the dq equivalent circuit of the three-phase shunt capacitances as shown in Figure B.3 is depicted in Figure B.4.

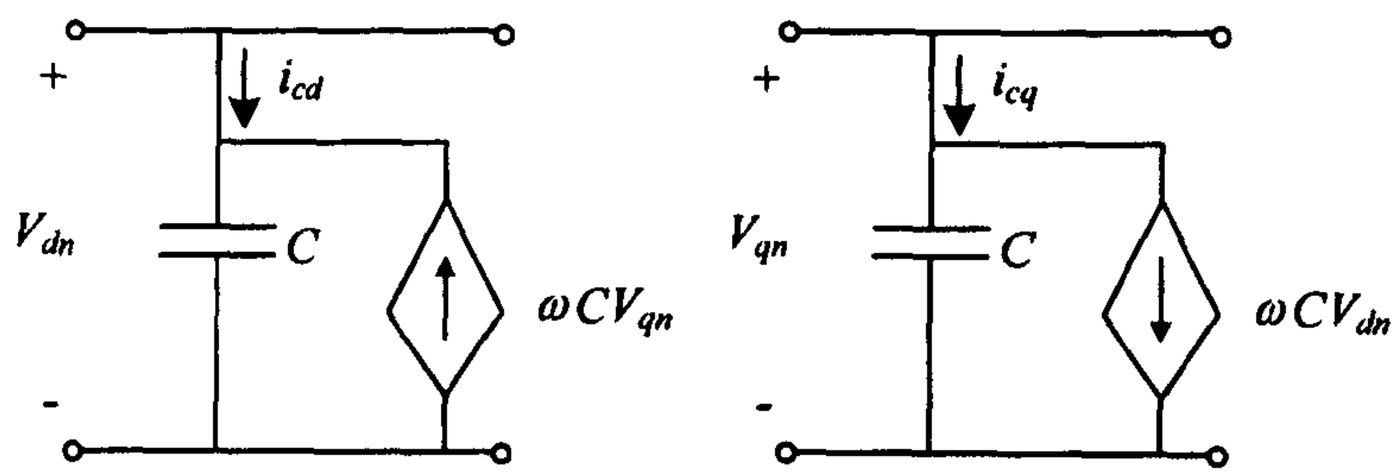

Figure B.4: The equivalent circuit of shunt capacitances in dq frame

Appendix C

Linearization Approach

C.1 Linearization Approach

Deriving control laws for non-linear systems are difficult. Therefore, a linearization method is used to linearize non-linear systems under the assumption that the system is going to be controlled about a steady state operating point such that any travel away from the operating point will be small [70]. Hence, only small changes about the steady state or equilibrium state point may be considered. Normally, the Taylor Series expansion [70],[71] is used to linearize the non-linear system. The Taylor Series expansion of $f(x)$ around the point x_o is given by:

$$f(x) = f(x_o) + \left.\frac{df}{dx}\right|_{x=x_o} (x - x_o) + \frac{1}{2}\left.\frac{d^2 f}{dx^2}\right|_{x=x_o} (x - x_o)^2 + \ldots \qquad \text{(C-1)}$$

This can be written as:

$$f(x) = f(x_o) + \left.\frac{df}{dx}\right|_{x=x_o} (x - x_o) + \text{high order terms} \qquad \text{(C-2)}$$

According to (C-2), the first order terms of the Taylor expansions is used to linearize the non-linear systems around the operating point x_o.

Consider the i^{th} equation of state x_i for some general function f_i:

$$\dot{x}_i = f_i(x_1, x_2, \ldots, x_n, u_1, u_2, \ldots, u_m) \tag{C-3}$$

If we consider only small changes about the equilibrium point, we can define the delta states and delta inputs as:

$$\begin{aligned} \delta x_j &= x_j - x_{oj} \quad (\text{for } 1 \le j \le n) \\ \delta u_j &= u_j - u_{oj} \quad (\text{for } 1 \le j \le m) \end{aligned} \tag{C-4}$$

Taking the first order terms of Taylor expansions with (C-4) into (C-3), the linearized equation of f_i around the equilibrium point x_o is given by:

$$\begin{aligned} \left(\dot{x}_o + \delta\dot{x}\right)_i &= f_i(\mathbf{x_o} + \delta\mathbf{x}, \mathbf{u_o} + \delta\mathbf{u}) \\ &= f_i(\mathbf{x_o}, \mathbf{u_o}) + \delta x_1 \left.\frac{\partial f_i}{\partial x_1}\right|_{\mathbf{x_o},\mathbf{u_o}} + \delta x_2 \left.\frac{\partial f_i}{\partial x_2}\right|_{\mathbf{x_o},\mathbf{u_o}} + \ldots \\ &\quad + \delta u_1 \left.\frac{\partial f_i}{\partial u_1}\right|_{\mathbf{x_o},\mathbf{u_o}} + \ldots \end{aligned} \tag{C-5}$$

Setting that the equilibrium points are given by $x_{1o}, x_{2o}, \ldots, x_{no}, u_{1o}, u_{2o}, \ldots, u_{mo}$, therefore

$$\dot{x}_{io} = f_i(x_{1o}, x_{2o}, \ldots, x_{no}, u_{1o}, u_{2o}, \ldots, u_{mo}) = 0 \quad \forall i \in \{1,2,\ldots,n\} \tag{C-6}$$

According to (C-6), the linearization of f_i about the equilibrium point in (C-5) becomes:

$$\delta\dot{\mathbf{x}} = \begin{bmatrix} \frac{\partial f_1}{\partial x_1} & \frac{\partial f_1}{\partial x_2} & \cdots & \frac{\partial f_1}{\partial x_n} \\ \vdots & \vdots & \ddots & \vdots \\ \frac{\partial f_n}{\partial x_1} & \frac{\partial f_n}{\partial x_2} & \cdots & \frac{\partial f_n}{\partial x_n} \end{bmatrix} \delta\mathbf{x} + \begin{bmatrix} \frac{\partial f_1}{\partial u_1} & \frac{\partial f_1}{\partial u_2} & \cdots & \frac{\partial f_1}{\partial u_m} \\ \vdots & \vdots & \ddots & \vdots \\ \frac{\partial f_n}{\partial u_1} & \frac{\partial f_n}{\partial u_2} & \cdots & \frac{\partial f_n}{\partial u_m} \end{bmatrix} \delta\mathbf{u} \tag{C-7}$$

or

$$\delta \dot{\mathbf{x}} = \mathbf{A}(\mathbf{x}_0, \mathbf{u}_0)\delta\mathbf{x} + \mathbf{B}(\mathbf{x}_0, \mathbf{u}_0)\delta\mathbf{u} \qquad \text{(C-8)}$$

where $\mathbf{x}_o$ and $\mathbf{u}_o$ are the equilibrium points satisfying (C-6). Knowing $\mathbf{x}_o$ and $\mathbf{u}_o$, matrixes $\mathbf{A}(\mathbf{x}_o,\mathbf{u}_o)$ and $\mathbf{B}(\mathbf{x}_o,\mathbf{u}_o)$ called Jacobian matrix are then derived to form (C-8) which represents a linear set of differential equations for small motions about the equilibrium point. Similarly, the output equation can be linearized using the first order term of Taylor Series expansions. This can be written as:

$$\delta\mathbf{y} = \mathbf{C}(\mathbf{x}_0, \mathbf{u}_0)\delta\mathbf{x} + \mathbf{D}(\mathbf{x}_0, \mathbf{u}_0)\delta\mathbf{u} \qquad \text{(C-9)}$$

In this research, the (C-8) and (C-9) are used for the small signal simulation and stability analysis.

Appendix D

The SABER Benchmark Models

D.1 The Benchmark Model for the System of Figure 2.2

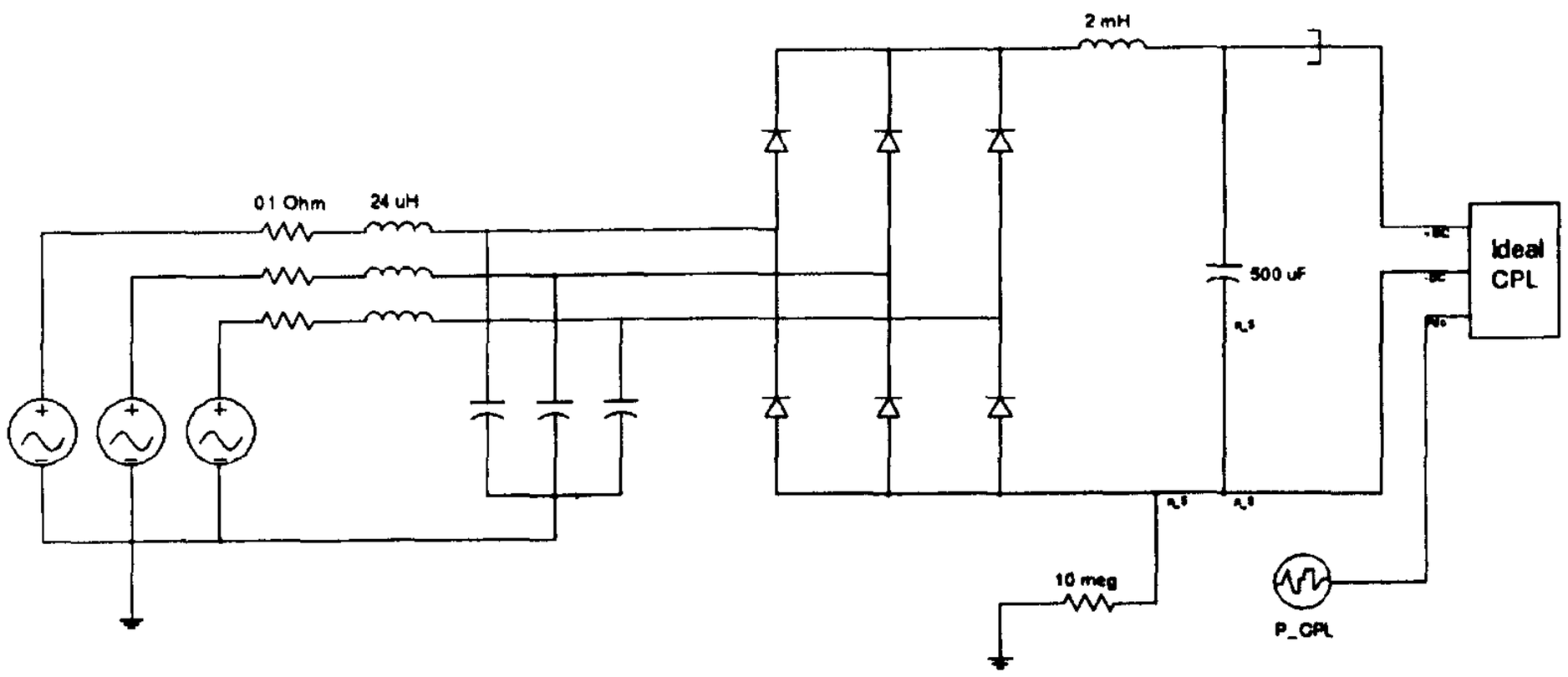

Figure D.1: The Benchmark Model for the System of Figure 2.2

The ideal CPL block of Figure D.1 refers to (2-9). The elements inside ideal CPL block are shown in Figure D.2.

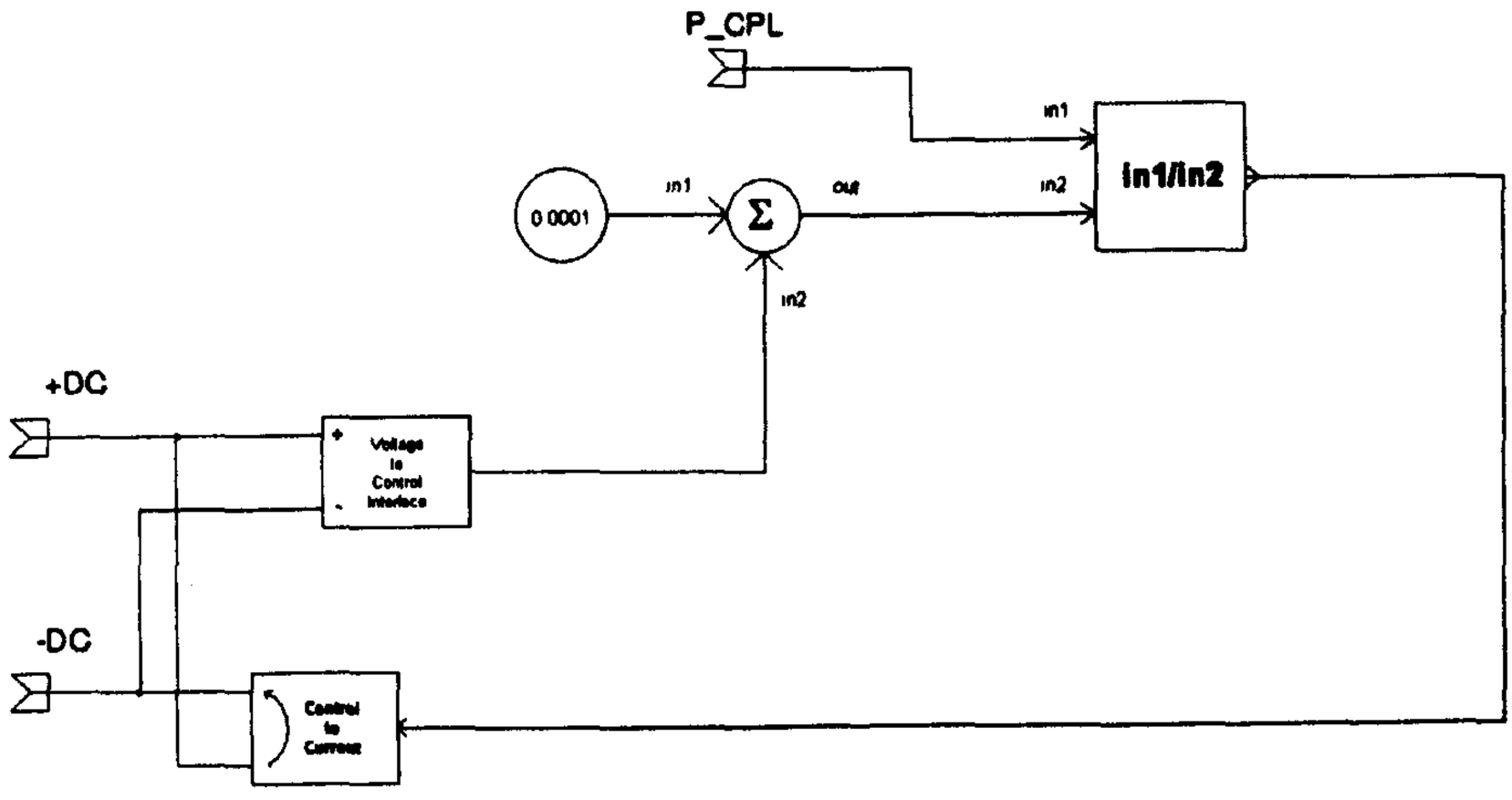

Figure D.2: The details of the ideal CPL block

D.2 The Benchmark Model for the System of Figure 2.32

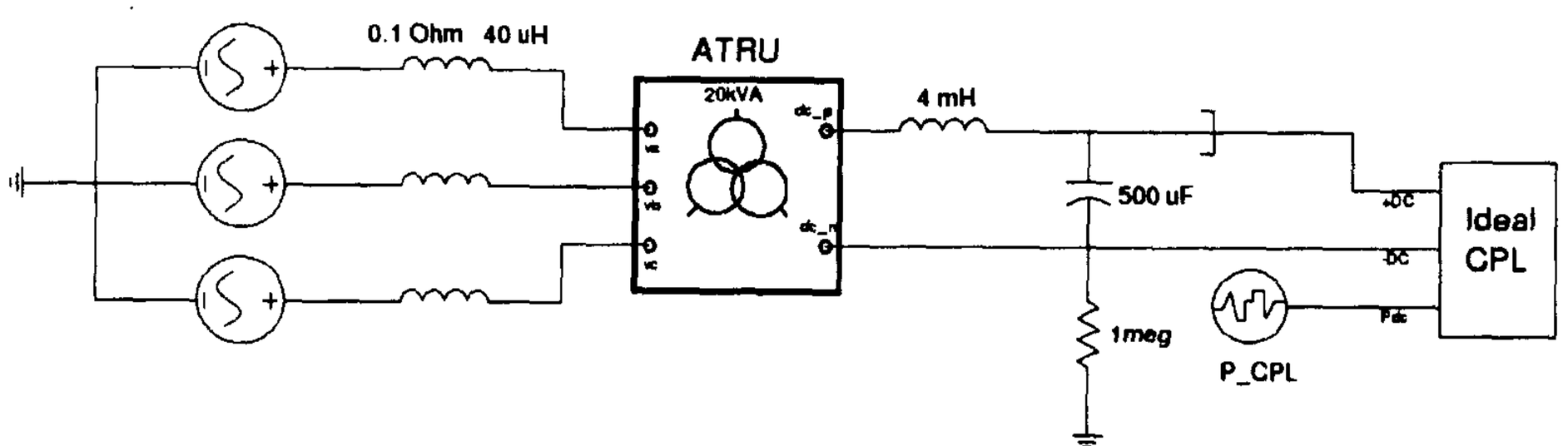

Figure D.3: The Benchmark Model for the System of Figure 2.32

The details inside ATRU block of Figure D.3 are shown in Figure D.4.

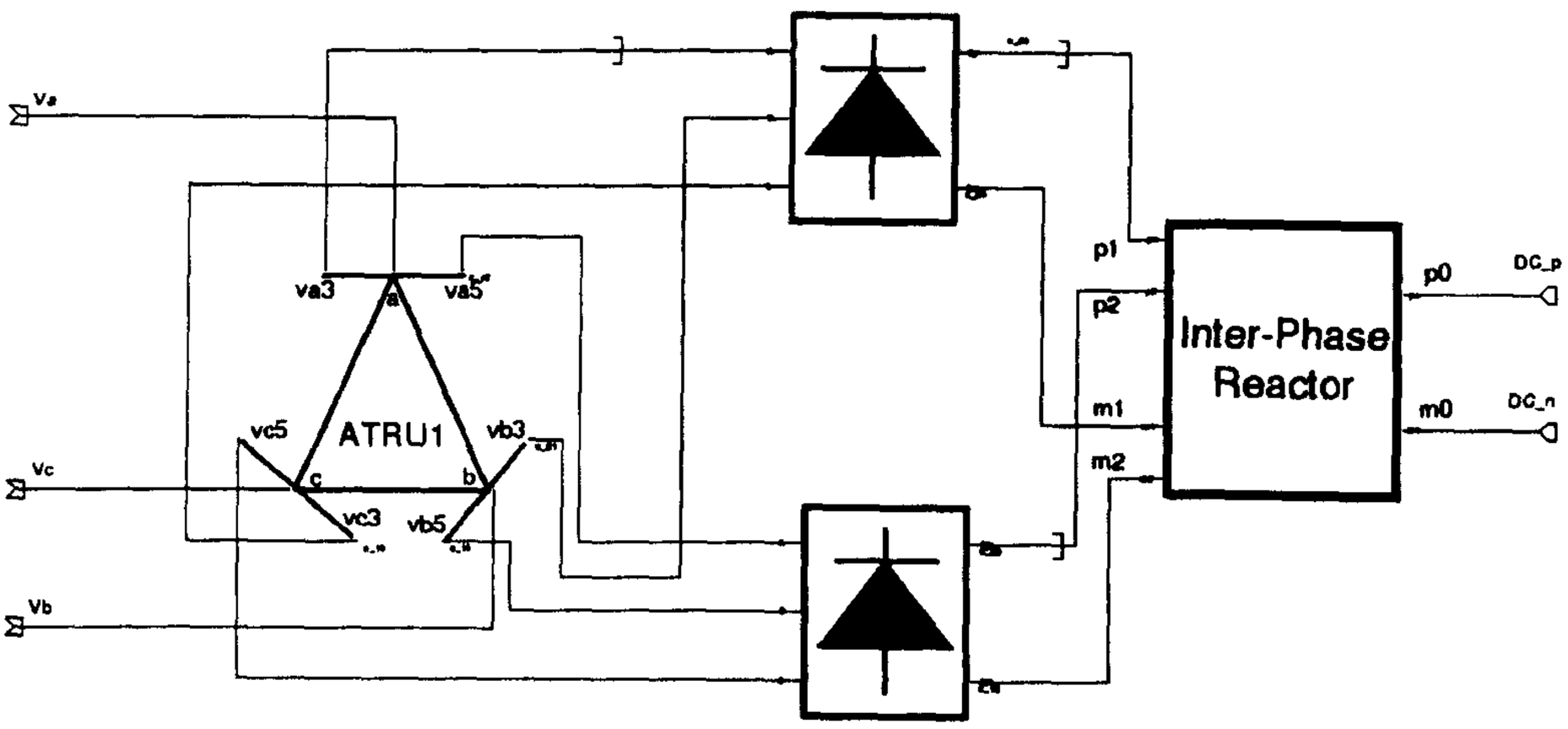

Figure D.4: The details inside ATRU block

The details inside the blocks of Inter-Phase Reactor and ATRU1 of Figure D.4 are shown in Figure D.5 and Figure D.6, respectively.

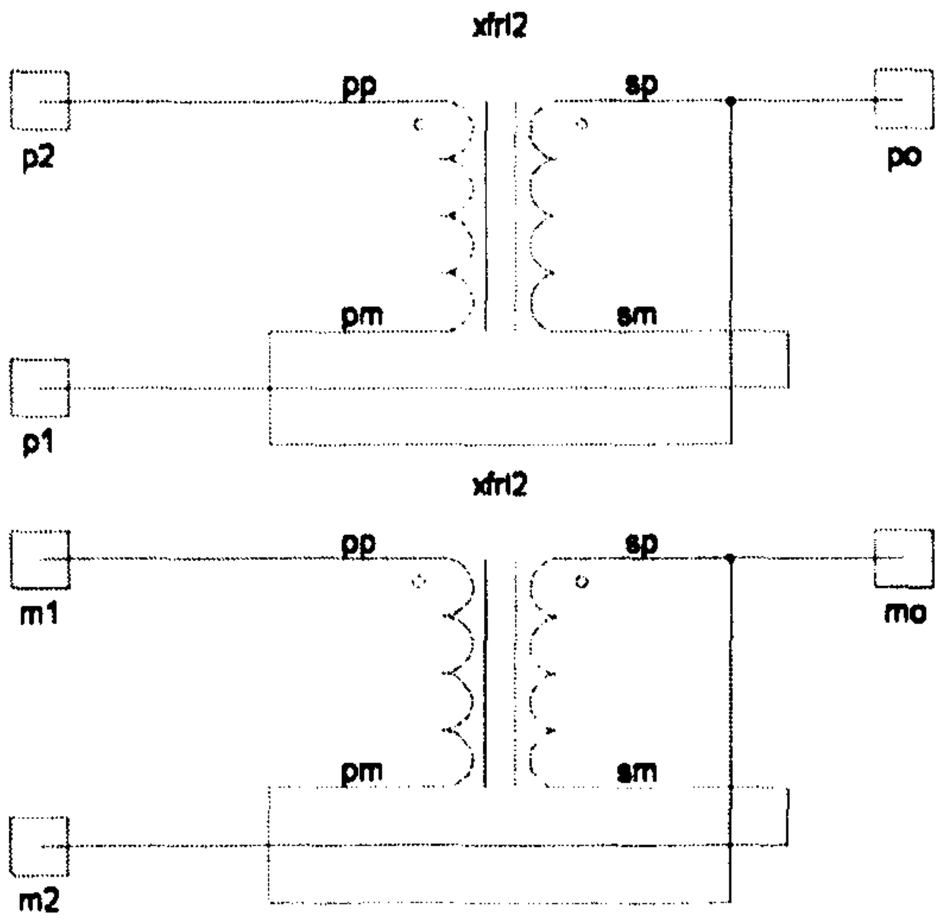

Figure D.5: Inter-Phase Reactor block

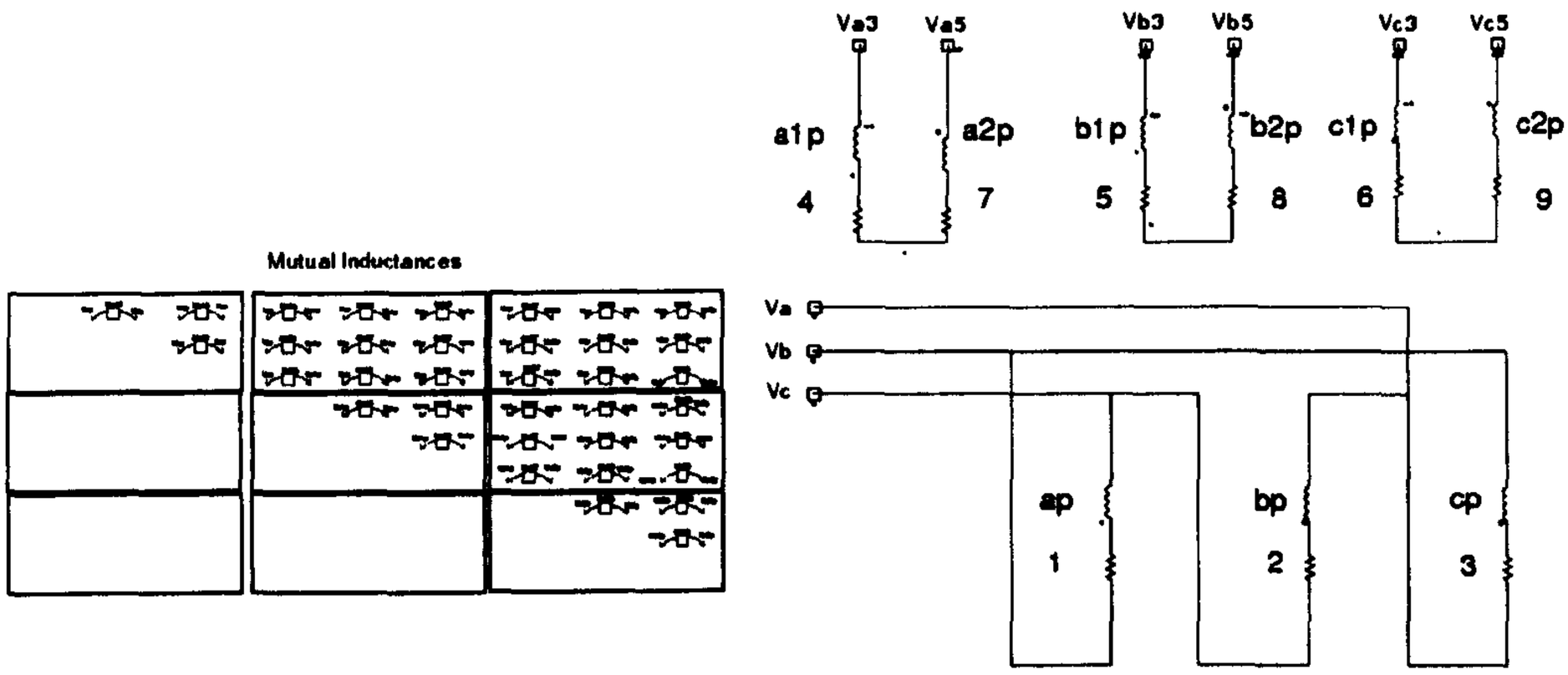

Figure D.6: ATRU1 block

D.3 The Benchmark Model for the System of Figure 3.2

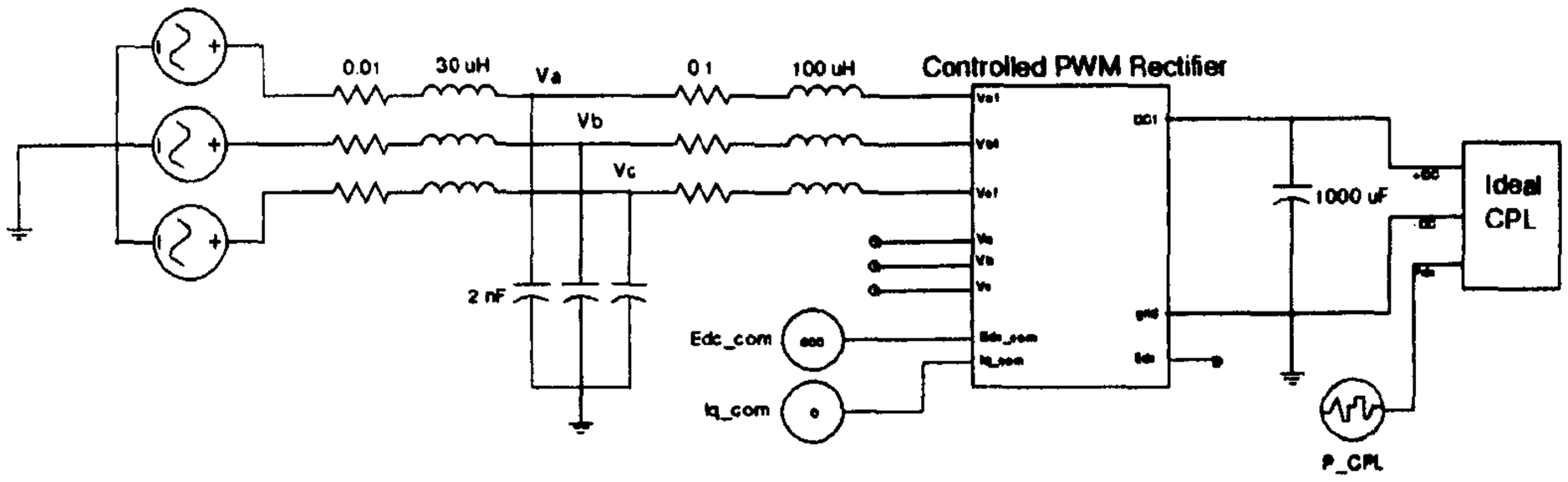

Figure D.7: The Benchmark Model for the System of Figure 3.2

The details inside the controlled PWM rectifier block of Figure D.7 consist of the power converter and controllers as depicted in Figure D.8.

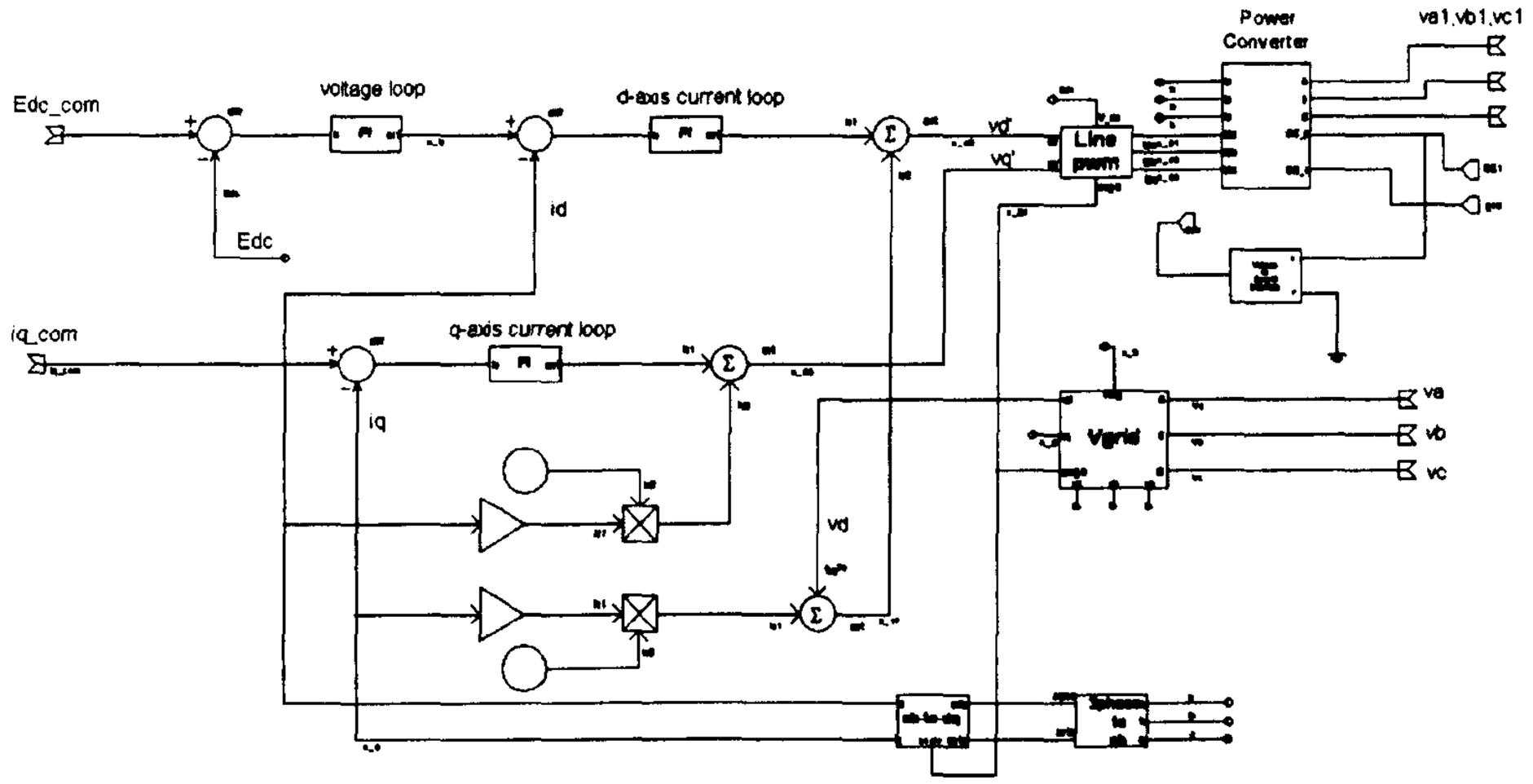

Figure D.8: The details inside the Controlled PWM Rectifier

The power converter block of Figure D.8 uses the non-switching model to represent the six switches as IGBTs. This model is constructed from the voltage and current port equations as a function of the control signals M_a etc which may be switched signals or PWM modulating waves. These equations are:

$$[V_a \quad V_b \quad V_c] = \frac{E_{dc}}{2}[M_a \quad M_b \quad M_c] \tag{D-1}$$

$$I_{dc} = I_a \frac{M_a + 1}{2} + I_b \frac{M_b + 1}{2} + I_c \frac{M_c + 1}{2} \tag{D-2}$$

The details of the power converter block of Figure D.8 are depicted in Figure D.9.

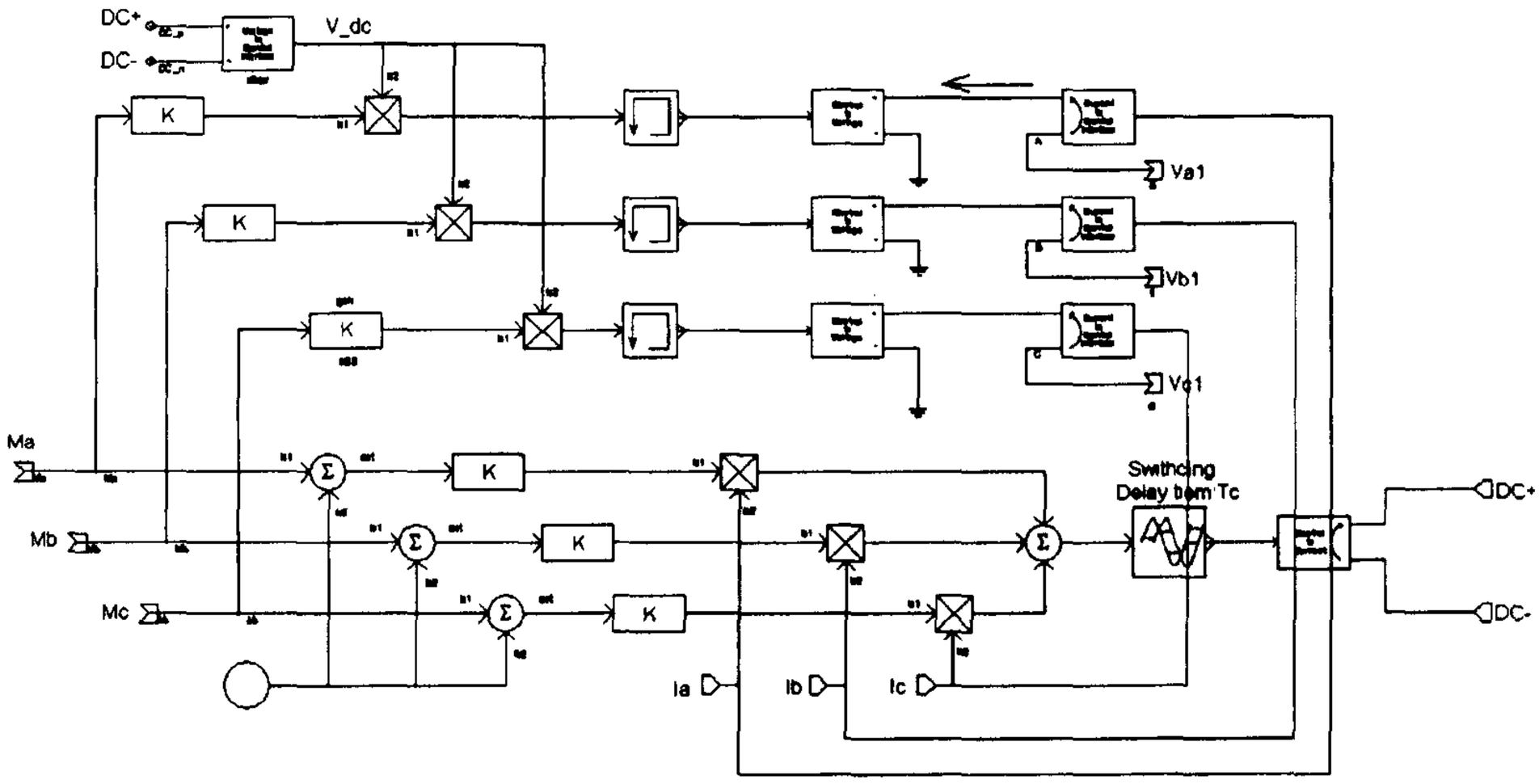

Figure D.9: The details of the power converter block

Note that the power converter non-switching model provides the fundamental signals the same as those simulated from the switching model.

D.4 The Benchmark Model for the System of Figure 4.1

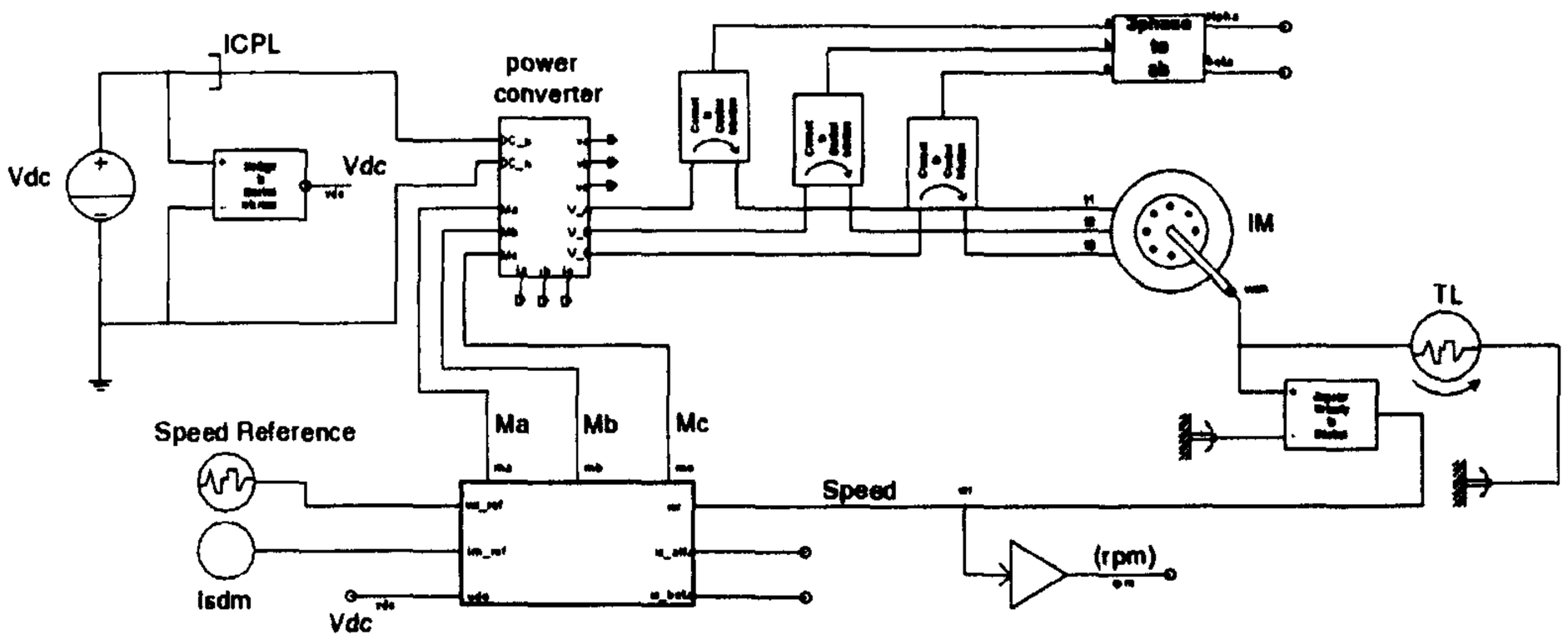

Figure D.10: The Benchmark Model for the System of Figure 4.1

The power converter of Figure D.10 is the same as one of Figure D.9.

D.5 The Benchmark Model for the System of Figure 4.6

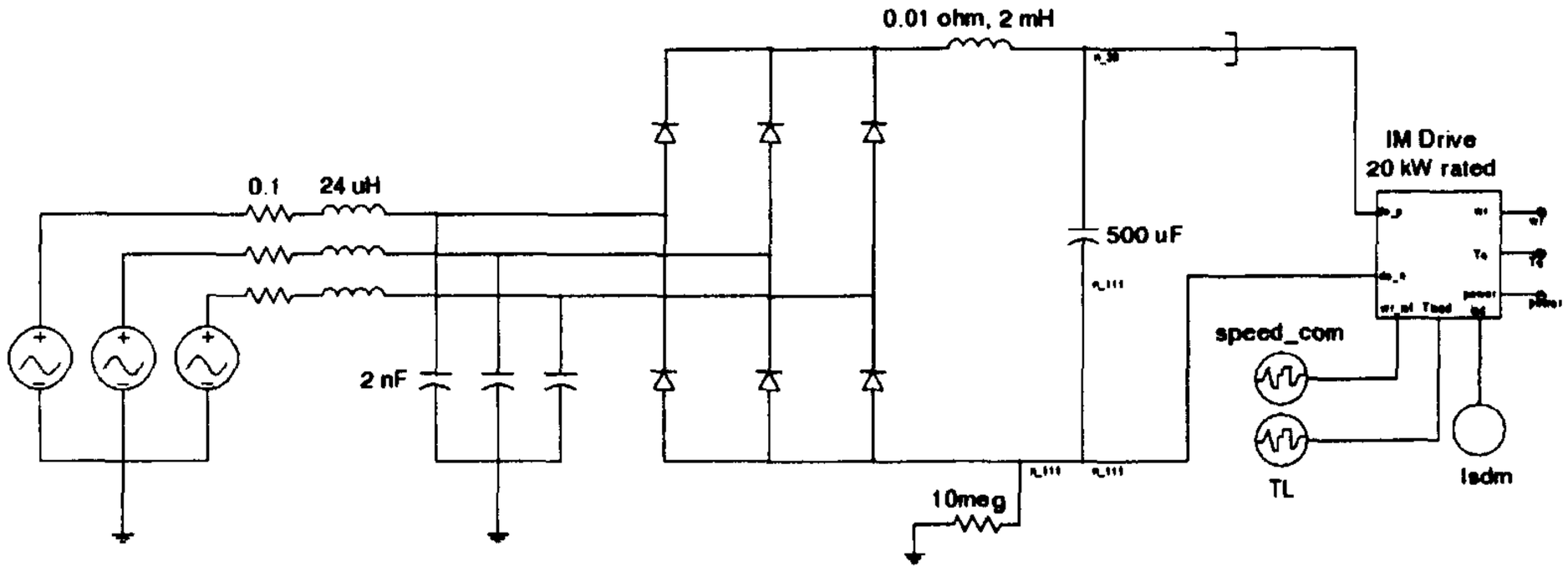

Figure D.11: The Benchmark Model for the System of Figure 4.6

The details inside the IM drive block of Figure D.11 are the elements in Figure D.10.

D.6 The Benchmark Model for the Damping Test of Figure 5.6

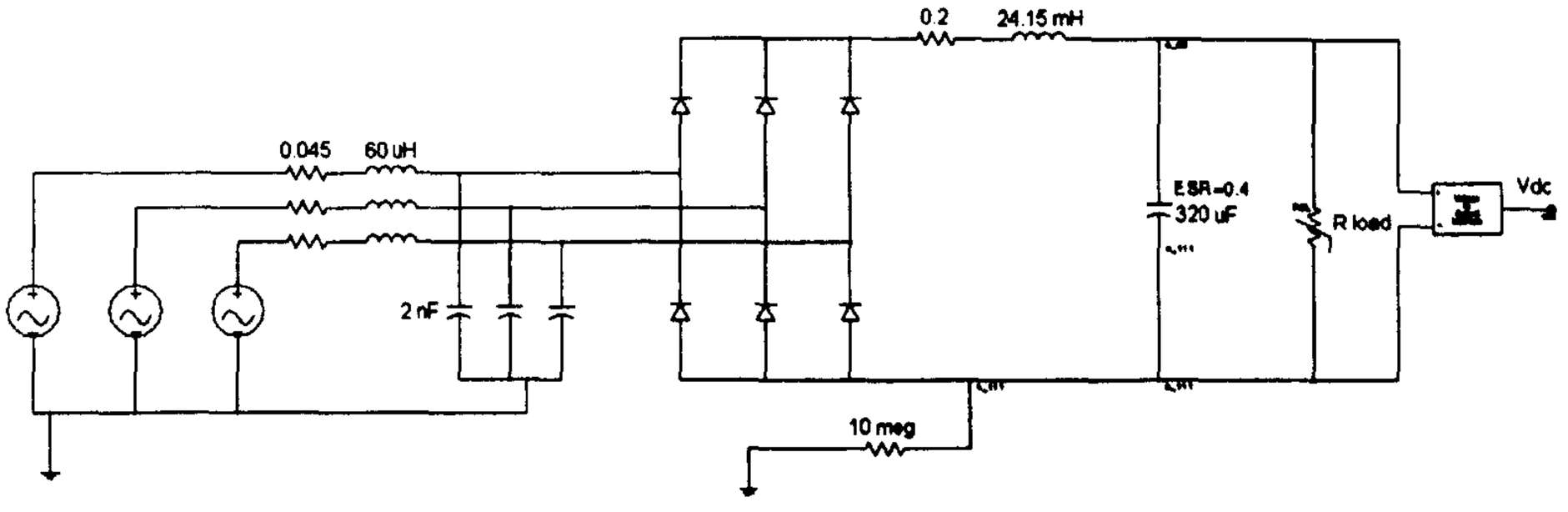

Figure D.12: The Benchmark Model for the Damping Test of Figure 5.6

D.7 The Benchmark Model for the System of Figure 5.1

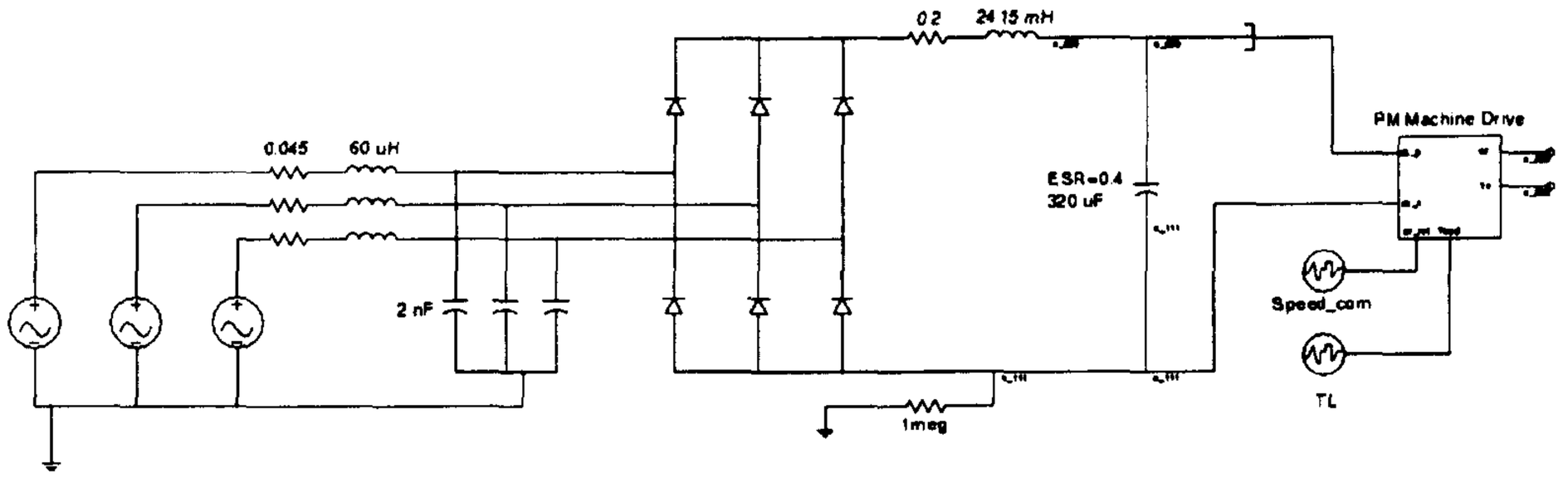

Figure D.13: The Benchmark Model for the System of Figure 5.1

The details inside the PM machine drive block of Figure D.13 are the same structure as that of Figure D.10 (PM is used instead of IM). As mentioned in Chapter 5, for PM machine drive, the I_{sdm} d-axis command current is set to zero for full flux operation.

D.8 The Benchmark Model for the System of Figure 6.1

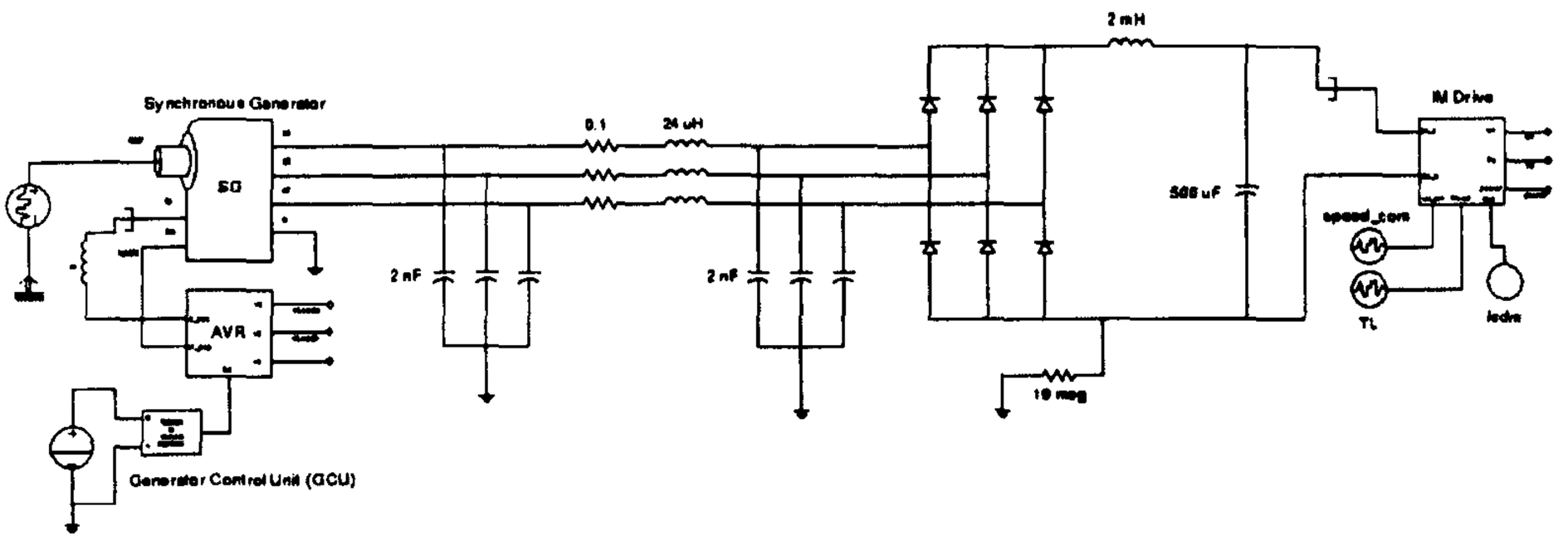

Figure D.14: The Benchmark Model for the System of Figure 6.1

The details inside the IM drive block of Figure D.14 are the elements in Figure D.10. The details inside AVR block of Figure D.14 are shown in Figure D.15.

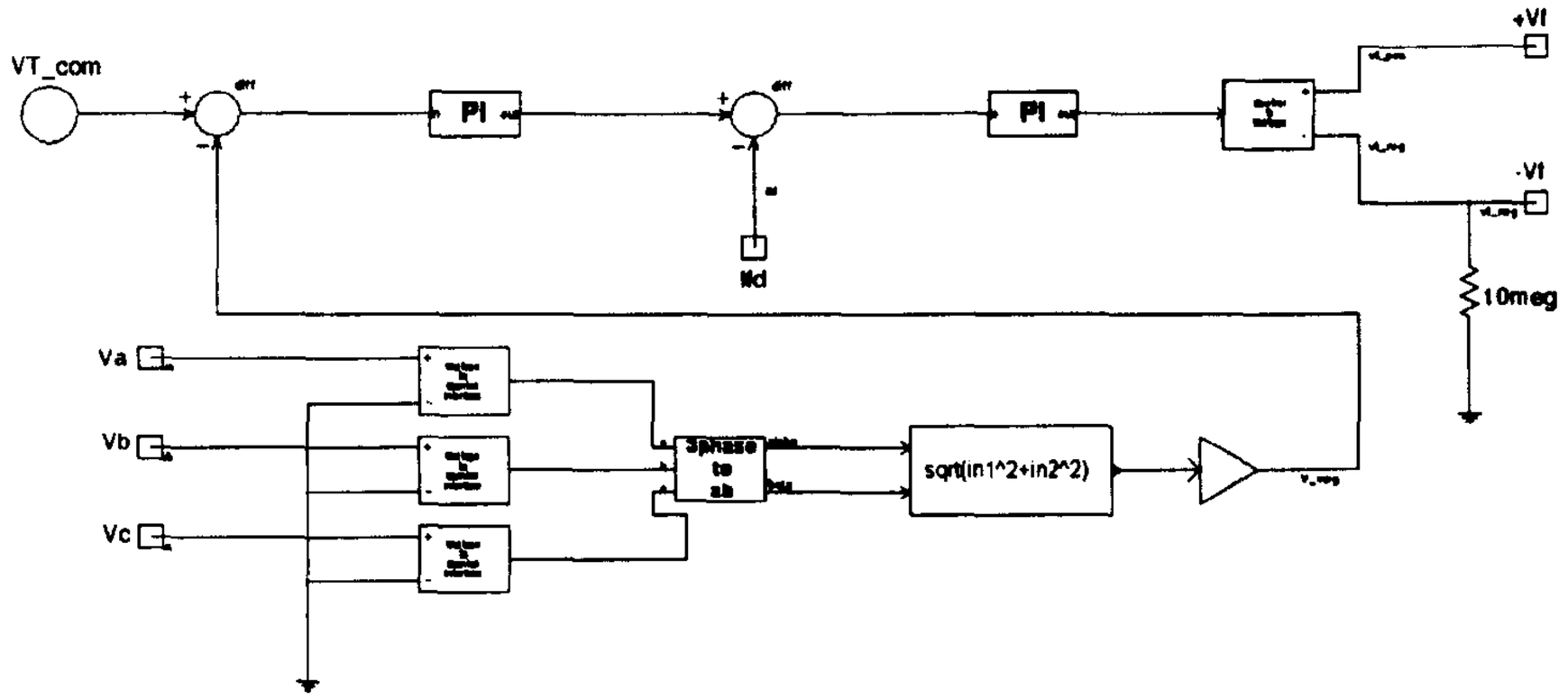

Figure D.15: AVR block

D.9 The Benchmark Model for the System of Figure 7.2

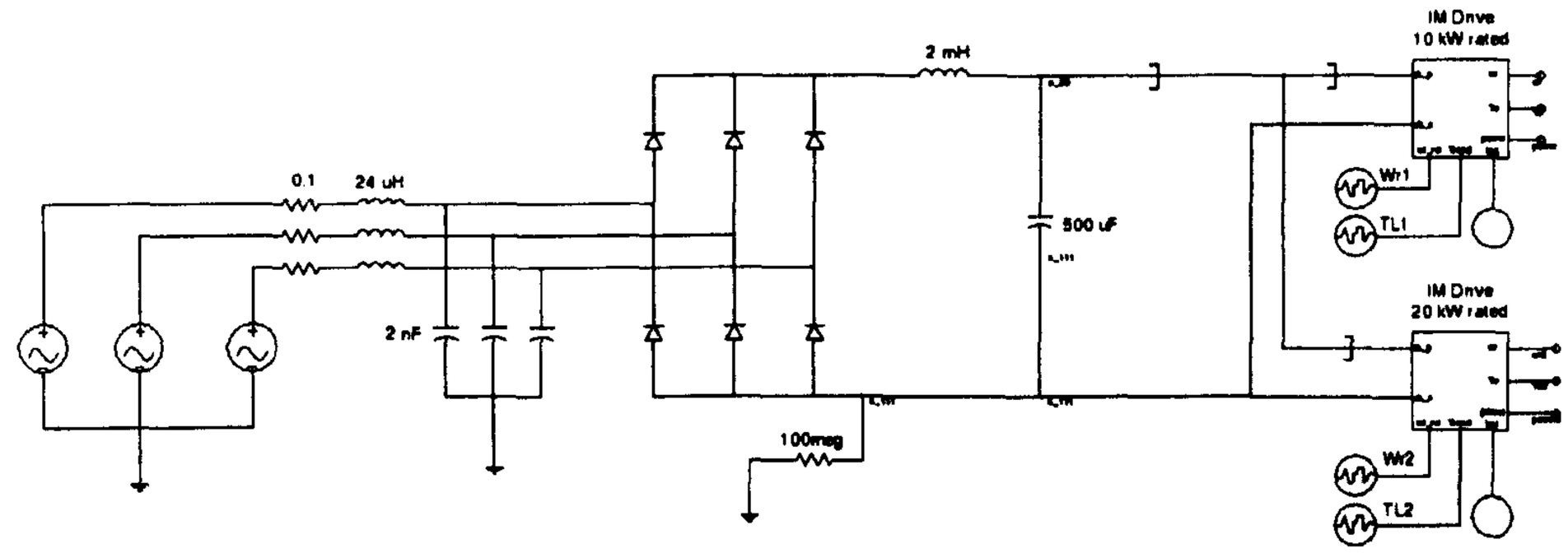

Figure D.16: The Benchmark Model for the System of Figure 7.2

D.10 The Benchmark Model for the System of Figure 7.8

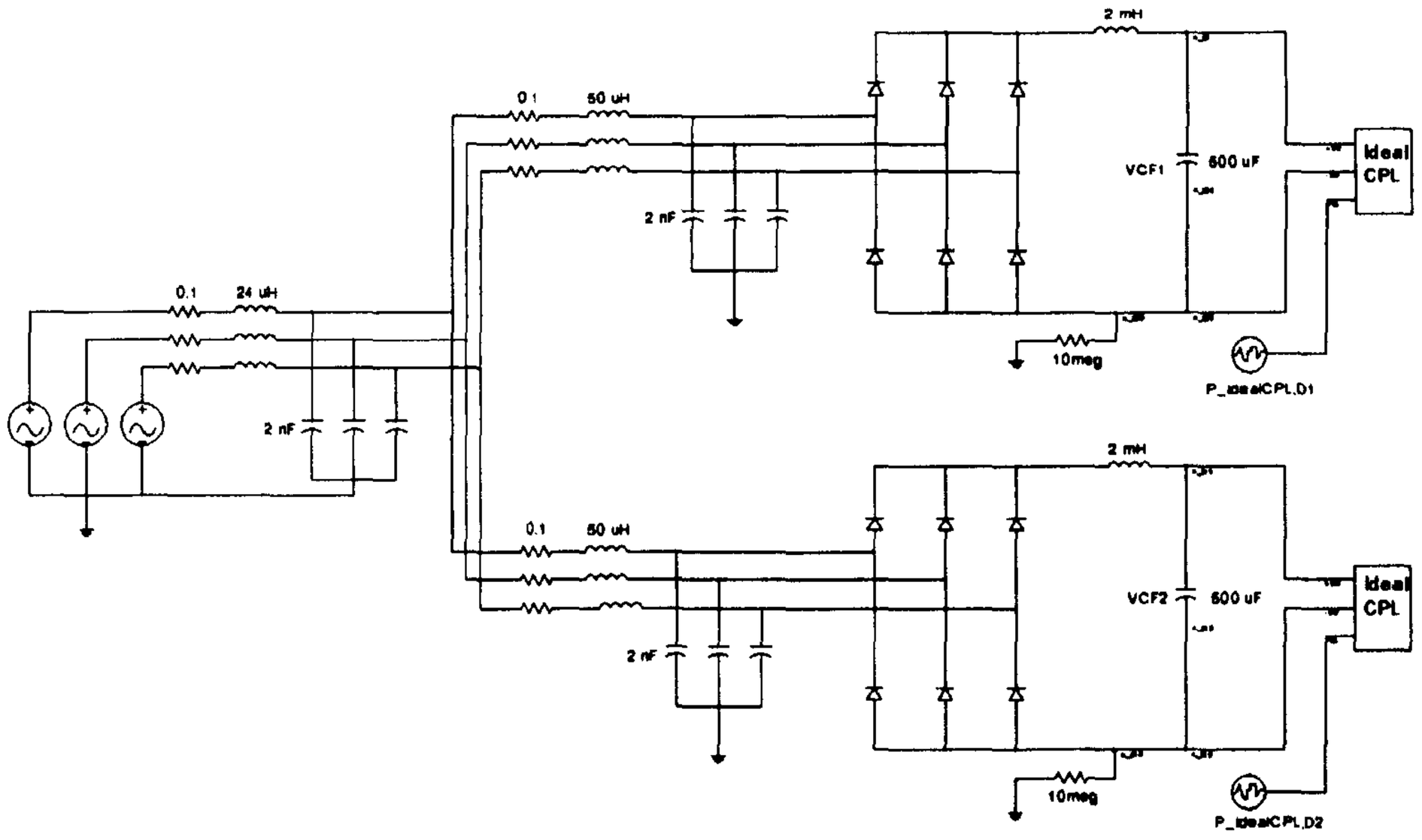

Figure D.17: The Benchmark Model for the System of Figure 7.8

D.11 The Benchmark Model for the System of Figure 7.15

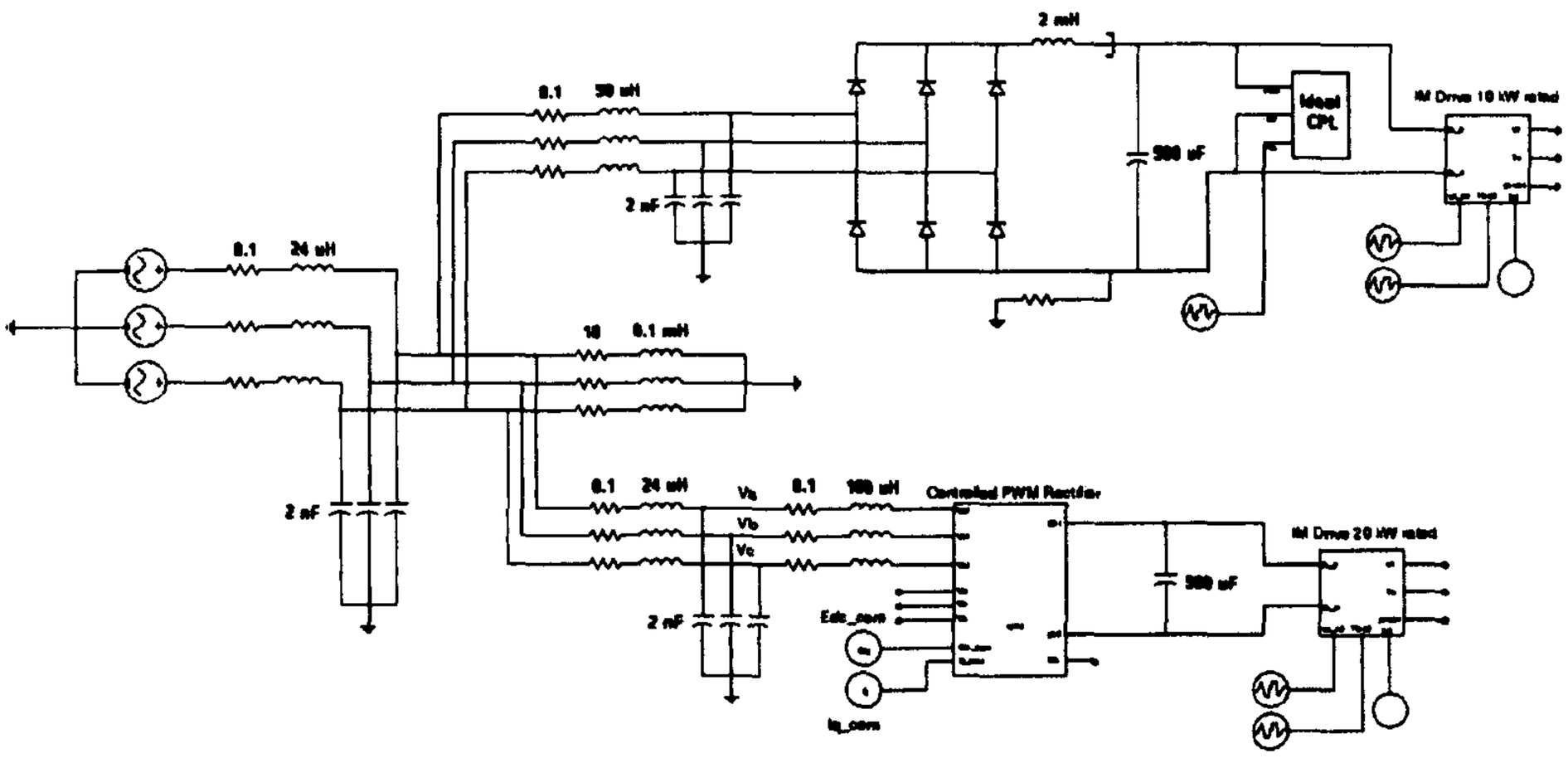

Figure D.18: The Benchmark Model for the System of Figure 7.15

Appendix E

The Details of the Element Matrices of the Generalized Model

E.1 The Details of the Element Matrices of the Generalized Model

The details of the element matrices inside the matrices $\mathbf{H}$, $\mathbf{A}_1(\mathbf{x}_o,\mathbf{u}_o)$, $\mathbf{B}_1(\mathbf{x}_o,\mathbf{u}_o)$, $\mathbf{C}(\mathbf{x}_o,\mathbf{u}_o)$, and $\mathbf{D}(\mathbf{x}_o,\mathbf{u}_o)$ are given below:

$\mathbf{I}_s = \mathbf{I}_{4\times4}$, $\mathbf{I}_m = \mathbf{I}_{5\times5}$, $\mathbf{I}_T = \mathbf{I}_{4\times4}$, $\mathbf{I}_P = \mathbf{I}_{6\times6}$, $\mathbf{I}_L = \mathbf{I}_{2\times2}$,

$$\mathbf{H}_{Dx} = \begin{bmatrix} 1 & 0 & 0 & 0 & 0 & 0 \\ 0 & 1 & 0 & 0 & 0 & 0 \\ 0 & 0 & 1 & 0 & 0 & 0 \\ 0 & 0 & 0 & 1 & 0 & 0 \\ 0 & 0 & 0 & 0 & 1 & r_{CFx}C_{Fx}L_{Fx}^{-1} \\ 0 & 0 & 0 & 0 & 0 & 1 \end{bmatrix}_{6\times6} \quad (x = 1,2,\ldots..,j),$$

$$\mathbf{A}_s = \begin{bmatrix} -\frac{R_{eq1}}{L_{eq1}} & \omega & -\frac{1}{L_{eq1}} & 0 \\ -\omega & -\frac{R_{eq1}}{L_{eq1}} & 0 & -\frac{1}{L_{eq1}} \\ \frac{1}{C_{eq1}} & 0 & 0 & \omega \\ 0 & \frac{1}{C_{eq1}} & -\omega & 0 \end{bmatrix}_{4\times4}$$

$$\mathbf{A}_{DUx} = \begin{bmatrix} 0 & 0 & 0 & 0 & 0 & 0 \\ 0 & 0 & 0 & 0 & 0 & 0 \\ -\frac{1}{C_{eq1}} & 0 & 0 & 0 & 0 & 0 \\ 0 & -\frac{1}{C_{eq1}} & 0 & 0 & 0 & 0 \end{bmatrix}_{4\times6} \quad (x = 1,2,\ldots,j), \quad \mathbf{A}_{DLx} = \begin{bmatrix} 0 & 0 & \frac{1}{L_{TRUx}} & 0 \\ 0 & 0 & 0 & \frac{1}{L_{TRUx}} \\ 0 & 0 & 0 & 0 \\ 0 & 0 & 0 & 0 \\ 0 & 0 & 0 & 0 \\ 0 & 0 & 0 & 0 \end{bmatrix}_{6\times4} \quad (x = 1,2,\ldots,j)$$

$$\mathbf{A_{Dx}} = \begin{bmatrix} -\frac{R_{TRUx}}{L_{TRUx}} & \omega & -\frac{1}{L_{TRUx}} & 0 & 0 & 0 \\ -\omega & -\frac{R_{TRUx}}{L_{TRUx}} & 0 & -\frac{1}{L_{TRUx}} & 0 & 0 \\ \frac{1}{C_{TRUx}} & 0 & 0 & \omega & -\frac{2\sqrt{3}}{\pi}\frac{\cos(\theta_{dx})}{C_{TRUx}} & 0 \\ 0 & \frac{1}{C_{TRUx}} & -\omega & 0 & \frac{2\sqrt{3}}{\pi}\frac{\sin(\theta_{dx})}{C_{TRUx}} & 0 \\ 0 & 0 & \frac{3}{2}\frac{2\sqrt{3}}{\pi}\frac{\cos(\theta_{dx})}{L_{Fx}} & -\frac{3}{2}\frac{2\sqrt{3}}{\pi}\frac{\sin(\theta_{dx})}{L_{Fx}} & -\frac{3\omega L_{TRUx}}{\pi L_{Fx}} - \frac{r_{LFx}}{L_{Fx}} & -\frac{1}{L_{Fx}} \\ 0 & 0 & 0 & 0 & \frac{1}{C_{Fx}} & A_{CPL,Dy} \end{bmatrix}_{6\times 6} \quad (x = 1,2,\ldots,j)$$

(θ_{dx} is the phase shift between the dq rotating frame and the input terminal voltage frame of diode rectifier unit x)

$$A_{CPL,Dy} = \begin{cases} \dfrac{P_{idealCPL,Dy}}{C_{Fx}V_{CFox}^2} & \text{, for } \textit{Ideal CPL} \\ & (x = 1,2,\ldots,j \text{ and } y = 1,2,\ldots,e) \\ 0 & \text{, for without } \textit{Ideal CPL} \end{cases}$$

$$\mathbf{A_{HmDx}} = \begin{bmatrix} \frac{3P_{Dx}\sigma_{Dx}L_{sm,Dx}I_{sqmo,Dx}I_{sdmo,Dx}}{8C_{Fy}V_{CFo,y}} & -\frac{3M_{qo,Dx}}{4C_{Fy}} + \frac{3\sigma_{Dx}L_{sm,Dx}I_{sqmo,Dx}}{4\tau_{r,Dx}C_{Fy}V_{CFo,y}} + \frac{3I_{sdmo,Dx}\sigma_{Dx}L_{sm,Dx}\omega_{eo,Dx}}{4C_{Fy}V_{CFo,y}} & \frac{3I_{sdmo,Dx}V_{sdmo,Dx}}{4C_{Fy}V_{CFo,y}^2} + \frac{3I_{sqmo,Dx}V_{sqmo,Dx}}{4C_{Fy}V_{CFo,y}^2} & -\frac{3I_{sqmo,Dx}}{4C_{Fy}V_{CFo,y}} & 0 \end{bmatrix}_{1\times 5}$$

$(x = 1,2,\ldots,n)$ and $(y = 1,2,\ldots,j)$

$$\mathbf{A_{VmDx}} = \begin{bmatrix} 0 \\ \frac{M_{qo,Dx}}{2\tau_{s,Dx}R_{sm,Dx}} \\ \frac{1}{2\tau_{F,Dx}} \\ -\frac{K_{Pim,Dx}M_{qo,Dx}}{2\tau_{s,Dx}R_{sm,Dx}} \\ 0 \end{bmatrix}_{5\times 1} \quad (x = 1,2,\ldots,n),$$

$$\mathbf{A_{mDx}} = \begin{bmatrix} 0 & \frac{K_{T,Dx}}{J_{m,Dx}} & 0 & 0 & 0 \\ -\frac{P_{Dx}K_{f,Dx}}{2\tau_{s,Dx}R_{sm,Dx}} & -\frac{1}{\tau_{s,Dx}} - \frac{K_{f,Dx}}{\tau_{s,Dx}R_{sm,Dx}\tau_{r,Dx}I_{sdmo,Dx}} & -\frac{V_{sqmo,Dx}}{\tau_{s,Dx}R_{sm,Dx}V_{CFo,y}} & \frac{1}{\tau_{s,Dx}R_{sm,Dx}} & 0 \\ 0 & 0 & -\frac{1}{\tau_{F,Dx}} & 0 & 0 \\ -K_{Pim,Dx}K_{fm,Dx} + \frac{P_{Dx}K_{Pim,Dx}K_{f,Dx}}{2\tau_{s,Dx}R_{sm,Dx}} & -K_{fim,Dx} - \frac{K_{Pim,Dx}K_{Pm,Dx}K_{T,Dx}}{J_{m,Dx}} + \frac{K_{Pim,Dx}}{\tau_{s,Dx}} + \frac{K_{Pim,Dx}K_{f,Dx}}{\tau_{s,Dx}R_{sm,Dx}\tau_{r,Dx}I_{sdmo,Dx}} & \frac{K_{Pim,Dx}V_{sqmo,Dx}}{\tau_{s,Dx}R_{sm,Dx}V_{CFo,y}} & -\frac{K_{Pim,Dx}}{\tau_{s,Dx}R_{sm,Dx}} & K_{Rm,Dx} \\ -K_{fm,Dx} & -\frac{K_{Pm,Dx}K_{T,Dx}}{J_{m,Dx}} & 0 & 0 & 0 \end{bmatrix}_{5\times 5}$$

$(x = 1,2,\ldots,n)$ and $(y = 1,2,\ldots,j)$

$$\mathbf{A_{TU}} = \begin{bmatrix} 0 & 0 & 0 & 0 \\ 0 & 0 & 0 & 0 \\ -\frac{1}{C_{eq1}} & 0 & 0 & 0 \\ 0 & -\frac{1}{C_{eq1}} & 0 & 0 \end{bmatrix}_{4\times 4}, \quad \mathbf{A_{TL}} = \begin{bmatrix} 0 & 0 & \frac{1}{L_{eq2}} & 0 \\ 0 & 0 & 0 & \frac{1}{L_{eq2}} \\ 0 & 0 & 0 & 0 \\ 0 & 0 & 0 & 0 \end{bmatrix}_{4\times 4}, \quad \mathbf{A_T} = \begin{bmatrix} -\frac{R_{eq2}}{L_{eq2}} & \omega & -\frac{1}{L_{eq2}} & 0 \\ -\omega & -\frac{R_{eq2}}{L_{eq2}} & 0 & -\frac{1}{L_{eq2}} \\ \frac{1}{C_{eq2}} & 0 & 0 & \omega \\ 0 & \frac{1}{C_{eq2}} & -\omega & 0 \end{bmatrix}_{4\times 4},$$

$$\mathbf{A_{PUx}}=\begin{bmatrix} 0 & 0 & 0 & 0 & 0 & 0 \\ 0 & 0 & 0 & 0 & 0 & 0 \\ -\dfrac{1}{C_{eq2}} & 0 & 0 & 0 & 0 & 0 \\ 0 & -\dfrac{1}{C_{eq2}} & 0 & 0 & 0 & 0 \end{bmatrix}_{4\times 6} (x=1,2,\ldots,k)\ ,\quad \mathbf{A_{PLx}}=[0]_{4\times 6}(x=1,2,\ldots,k)$$

$$\mathbf{A_{Px}}=\begin{bmatrix} -\dfrac{(R_{con,x}+K_{pd,x})}{L_{con,x}} & 0 & \dfrac{K_{ie,x}K_{pd,x}}{L_{con,x}} & \dfrac{K_{id,x}}{L_{con,x}} & 0 & -\dfrac{K_{pe,x}K_{pd,x}}{L_{con,x}} \\ 0 & -\dfrac{(R_{con,x}+K_{pq,x})}{L_{con,x}} & 0 & 0 & \dfrac{K_{iq,x}}{L_{con,x}} & 0 \\ 0 & 0 & 0 & 0 & 0 & -1 \\ -1 & 0 & K_{iv,x} & 0 & 0 & -K_{pe,x} \\ 0 & -1 & 0 & 0 & 0 & 0 \\ A_{P61,x} & A_{P62,x} & A_{P63,x} & A_{P64,x} & A_{P65,x} & A_{P66,x} \end{bmatrix}_{6\times 6}$$

$(x=1,2,\ldots,k)$

$$A_{P61,x}=\frac{3}{2}\left(\frac{V_{busdo,x}}{C_{F,conx}V_{CFo,conx}}-\frac{K_{ie,x}K_{pd,x}X_{eo,x}}{C_{F,conx}V_{CFo,conx}}+\frac{2K_{pd,x}I_{indo,x}}{C_{F,conx}V_{CFo,conx}}-\frac{K_{id,x}X_{do,x}}{C_{F,conx}V_{CFo,conx}}\right)\ (x=1,2,\ldots,k)\ ,$$

$$A_{P62,x}=\frac{3}{2}\left(\frac{V_{busqo,x}}{C_{F,conx}V_{CFo,conx}}+\frac{K_{pq,x}I_{inqo,x}}{C_{F,conx}V_{CFo,conx}}-\frac{K_{iq,x}X_{qo,x}}{C_{F,conx}V_{CFo,conx}}\right)(x=1,2,\ldots,k)\ ,$$

$$A_{P63,x}=-\frac{3}{2}\left(\frac{K_{ie,x}K_{pd,x}I_{indo,x}}{C_{F,conx}V_{CFo,conx}}\right)(x=1,2,\ldots,k)\ ,\quad A_{P64,x}=-\frac{3}{2}\left(\frac{K_{id,x}I_{indo,x}}{C_{F,conx}V_{CFo,conx}}\right)(x=1,2,\ldots,k)\ ,$$

$$A_{P65,x}=-\frac{3}{2}\left(\frac{K_{iq,x}I_{inqo,x}}{C_{F,conx}V_{CFo,conx}}\right)(x=1,2,\ldots,k)\ ,$$

$$A_{P66,x}=\left[\left(\frac{3}{2}\frac{1}{C_{F,conx}V_{CFo,conx}^2}\right)\begin{pmatrix}-V_{busdo,x}I_{indo,x}+K_{pe,x}K_{pd,x}I_{indo,x}V_{CFo,conx}+K_{ie,x}K_{pd,x}I_{indo,x}X_{eo,x}-K_{pd,x}I_{indo,x}^2\\+K_{id,x}I_{indo,x}X_{do,x}-V_{busqo,x}I_{inqo,x}+K_{iq,x}I_{inqo,x}X_{qo,x}\end{pmatrix}\right]+A_{CPL,Py}\ ,$$

$(x=1,2,\ldots,k)$ and $(y=1,2,\ldots,g)$

$$A_{CPL,Py}=\begin{cases}\dfrac{P_{idealCPL,Py}}{C_{F,conx}V_{CFo,conx}^2} & \text{, for } \textit{Ideal CPL}\\ 0 & \text{, for without } \textit{Ideal CPL}\end{cases}\quad (x=1,2,\ldots,k \text{ and } y=1,2,\ldots,g)\ ,$$

$$\mathbf{A_{HmPx}}=\begin{bmatrix}\dfrac{3P_{Px}\sigma_{Px}L_{sm,Px}I_{sqmo,Px}I_{sdmo,Px}}{8C_{F,conx}V_{CFo,conx}} & -\dfrac{3M_{qo,Px}}{4C_{F,conx}}+\dfrac{3\sigma_{Px}L_{sm,Px}I_{sqmo,Px}}{4\tau_{r,Px}C_{F,conx}V_{CFo,conx}}+\dfrac{3I_{sdmo,Px}\sigma_{Px}L_{sm,Px}\omega_{eo,Px}}{4C_{F,conx}V_{CFo,conx}} & \dfrac{3I_{sdmo,Px}V_{sdmo,Px}}{4C_{F,conx}V_{CFo,conx}^2}+\dfrac{3I_{sqmo,Px}V_{sqmo,Px}}{4C_{F,conx}V_{CFo,conx}^2} & -\dfrac{3I_{sqmo,Px}}{4C_{F,conx}V_{CFo,conx}} & 0\end{bmatrix}_{1\times 5}$$

$(x=1,2,\ldots,a)$ and $(y=1,2,\ldots,k)$

$$\mathbf{A_{VmPx}}=\begin{bmatrix}0\\ \dfrac{M_{qo,Px}}{2\tau_{s,Px}R_{sm,Px}}\\ \dfrac{1}{2\tau_{F,Px}}\\ -\dfrac{K_{Pim,Px}M_{qo,Px}}{2\tau_{s,Px}R_{sm,Px}}\\ 0\end{bmatrix}_{5\times 1}(x=1,2,\ldots,a)\ ,$$

$$\mathbf{A}_{mPx}=\begin{bmatrix} 0 & \frac{K_{T,Px}}{J_{m,Px}} & 0 & 0 & 0 \\ -\frac{P_{Px}K_{f,Px}}{2\tau_{s,Px}R_{sm,Px}} & -\frac{1}{\tau_{s,Px}}-\frac{K_{f,Px}}{\tau_{s,Px}R_{sm,Px}\tau_{r,Px}I_{admo,Px}} & -\frac{V_{sqmo,Px}}{\tau_{s,Px}R_{sm,Px}V_{CFo,conv}} & \frac{1}{\tau_{s,Px}R_{sm,Px}} & 0 \\ 0 & 0 & -\frac{1}{\tau_{F,Px}} & 0 & 0 \\ -K_{Pim,Px}K_{Iw,Px}+\frac{P_{Px}K_{Pim,Px}K_{f,Px}}{2\tau_{s,Px}R_{sm,Px}} & -K_{Iim,Px}-\frac{K_{Pim,Px}K_{Pw,Px}K_{T,Px}}{J_{m,Px}}+\frac{K_{Pim,Px}}{\tau_{s,Px}}+\frac{K_{Pim,Px}K_{f,Px}}{\tau_{s,Px}R_{sm,Px}\tau_{r,Px}I_{admo,Px}} & \frac{K_{Pim,Px}V_{sqmo,Px}}{\tau_{s,Px}R_{sm,Px}V_{CFo,conv}} & -\frac{K_{Pim,Px}}{\tau_{s,Px}R_{sm,Px}} & K_{Iim,Px} \\ -K_{Iw,Px} & -\frac{K_{Pw,Px}K_{T,Px}}{J_{m,Px}} & 0 & 0 & 0 \end{bmatrix}_{5\times 5}$$

$(x=1,2,\ldots,a)$ and $(y=1,2,\ldots,k)$

$$\mathbf{A}_{LUx}=\begin{bmatrix} 0 & 0 \\ 0 & 0 \\ -\frac{1}{C_{eq1}} & 0 \\ 0 & -\frac{1}{C_{eq1}} \end{bmatrix}_{4\times 2} (x=1,2,\ldots,b)\ ,\quad \mathbf{A}_{LLx}=\begin{bmatrix} 0 & 0 & \frac{1}{L_{Lx}} & 0 \\ 0 & 0 & 0 & \frac{1}{L_{Lx}} \end{bmatrix}_{2\times 4} (x=1,2,\ldots,b)\ ,$$

$$\mathbf{A}_{Lx}=\begin{bmatrix} -\frac{R_{Lx}}{L_{Lx}} & \omega \\ -\omega & -\frac{R_{Lx}}{L_{Lx}} \end{bmatrix}_{2\times 2} (x=1,2,\ldots,b)\ ,$$

$$\mathbf{B}_{s}=\begin{bmatrix} \frac{\cos(\theta_s)}{L_{eq1}} \\ \frac{\sin(\theta_s)}{L_{eq1}} \\ 0 \\ 0 \end{bmatrix}_{4\times 1}$$ (θ_s is the phase shift between the dq frame and the source frame)

$$\mathbf{B}_{Dx}=\begin{bmatrix} 0 \\ 0 \\ 0 \\ 0 \\ 0 \\ -\frac{1}{C_{Fx}V_{CFo,x}} \end{bmatrix}_{6\times 1} (x=1,2,\ldots,e)\ ,\quad \mathbf{B}_{Pox}=\begin{bmatrix} 0 \\ 0 \\ 0 \\ 0 \\ 0 \\ -\frac{1}{C_{F,conx}V_{CFo,conx}} \end{bmatrix}_{6\times 1} (x=1,2,\ldots,g)\ ,$$

$$\mathbf{B}_{mDx}=\begin{bmatrix} 0 & -\frac{1}{J_{m,Dx}} \\ 0 & 0 \\ 0 & 0 \\ K_{Pim,Dx}K_{Iw,Dx} & \frac{K_{Pim,Dx}K_{Pw,Dx}}{J_{m,Dx}} \\ K_{Iw,Dx} & \frac{K_{Pw,Dx}}{J_{m,Dx}} \end{bmatrix}_{5\times 2} (x=1,2,\ldots,n)\ ,\quad \mathbf{B}_{mPx}=\begin{bmatrix} 0 & -\frac{1}{J_{m,Px}} \\ 0 & 0 \\ 0 & 0 \\ K_{Pim,Px}K_{Iw,Px} & \frac{K_{Pim,Px}K_{Pw,Px}}{J_{m,Px}} \\ K_{Iw,Px} & \frac{K_{Pw,Px}}{J_{m,Px}} \end{bmatrix}_{5\times 2} (x=1,2,\ldots,a)\ ,$$

$$\mathbf{B}_{Px}=\begin{bmatrix} \frac{K_{pd,x}K_{pe,x}}{L_{con,x}} & 0 \\ 0 & \frac{K_{pq,x}}{L_{con,x}} \\ 1 & 0 \\ K_{pe,x} & 0 \\ 0 & 1 \\ -\frac{3}{2}\frac{K_{pe,x}K_{pd,x}I_{indo,x}}{C_{F,conx}V_{CFo,conx}} & -\frac{3}{2}\frac{K_{pq,x}I_{inqo,x}}{C_{F,conx}V_{CFo,conx}} \end{bmatrix}_{6\times 2} (x=1,2,\ldots,k)\ ,$$

$$\mathbf{C}_{Dx}=\begin{bmatrix}0 & 0 & 0 & 0 & 0 & 1\end{bmatrix}_{1\times 6}(x=1,2,\ldots,j)\ ,\quad \mathbf{C}_{Px}=\begin{bmatrix}0 & 0 & 0 & 0 & 0 & 1\end{bmatrix}_{1\times 6}(x=1,2,\ldots,k)$$

References:

[1] M.E. Elbuluk, and M.D. Kankam, "Potential Starter/Generator Technologies for Future Aerospace Applications," *IEEE Aerospace and Electronic Systems Magazine.*, pp.24-312, May 1997.

[2] A. Emadi, and M. Ehsani, "Aircraft Power Systems: Technology, State of the Art, and Future Trends," *IEEE Aerospace and Electronic Systems Magazine.*, pp. 28-32, January 2000.

[3] J.A. Rosero, J.A. Ortega, E. Aldabas, and L. Romeral, "Moving Towards a More Electric Aircraft," *IEEE Aerospace and Electronic Systems Magazine.*, pp. 3-9, March 2007.

[4] A. Garcia, J. Cusido, J.A. Rosero, J.A. Ortega, and L. Romeral, "Reliable Electro-Mechanical Actuators in Aircraft," *IEEE Aerospace and Electronic Systems Magazine.*, pp. 19-25, August 2008.

[5] J.A. Weimer, "The Role of Electric Machines and Drives in the More Electric Aircraft," in *Proc. IEEE International Conference on Electric Machines and Drives (IEMDC'03)*, Madison, Wisconsin, USA, 1-4 June 2003, pp.11-15.

[6] C.R. Avery, S.G. Burrow, and P.H. Mellor, "Electrical Generation and Distribution for the More Electric Aircraft," in *Proc. 42nd International Universities Power Engineering Conference (UPEC 2007),* University of Brighton, Brighton, UK, 4-6 September 2007, pp. 1007-1012.

[7] J. Chang, and A. Wang, "New VF-Power System Architecture and Evaluation for Future Aircraft," *IEEE Trans. on Aerospace and Electronic Systems.*, vol. 42, no. 2, pp.527-539, April 2006.

[8] M. Sinnett, "787 No-Bleed Systems: Saving Fuel and Enhancing Operational Efficiencies," in *Aeromagazine.*, QTR_04/07, pp.6-11.

[9] More Open Electrical Technologies (MOET project): http://www.eurtd.com/moet.

[10] R.D. Middlebrook, "Input Filter Considerations in Design and Application of Switching Regulators," in *Proc. IEEE Industry Application Society Annual Meeting*, Chicago, Illinois, October 1976, pp.366-382.

[11] A. Emadi, B. Fahimi, and M. Ehsani, "On the Concept of Negative Impedance Instability in the More Electric Aircraft Power Systems with Constant Power Loads," *Soc. Automotive Eng. J.*, pp.689-699, 1999.

[12] C. Rivetta, G.A. Williamson, and A. Emadi, "Constant Power Loads and Negative Impedance Instability in Sea and Undersea Vehicles: Statement of the Problem and Comprehensive Large-Signal Solution," in *Proc. IEEE Electric Ship Tech. Symposium.*, Philadelphia, PA USA, July 2005, pp.313-320.

[13] A. Emadi, A. Khaligh, C.H. Rivetta, and G.A. Williamson, "Constant Power Loads and Negative Impedance Instability in Automotive Systems: Definition, Modeling, Stability, and Control of Power Electronic Converters and Motor Drives," *IEEE Trans. on Vehicular Tech.*, vol. 55, no. 4, pp.1112-1125, July 2006.

[14] A. B. Jusoh, "The Instability Effect of Constant Power Loads," in *Proc. IEEE National Power & Energy Conference (PECon 2004)*, Kuala Lumpur, Malaysia, 29-30 November 2004, pp.175-179.

[15] J. Mahdavi, A. Emadi, M.D. Bellar, and M. Ehsani, "Analysis of Power Electronic Converters Using the Generalized State-Space Averaging Approach," *IEEE Trans. on Circuit and Systems.*, vol. 44, pp.767-770, August 1997.

[16] A. Emadi, "Modeling and Analysis of Multiconverter DC Power Electronic Systems Using the Generalized State-Space Averaging Method," *IEEE Trans. on Indus. Elect.*, vol. 51, no. 3, pp. 661-668, June 2004.

[17] A. Emadi, M. Ehsani, and J.M. Miller, "Vehicular Electric Power Systems: Land, Sea, Air, and Space Vehicles," Marcel Dekker, Inc, 2004.

[18] A. Emadi, "Modeling of Power Electronic Loads in AC Distribution Systems Using the Genearlized State-Space Averaging Method," *IEEE Trans. on Indus. Elect.*, vol. 51, no. 5, pp. 992-1000, October 2004.

[19] L. Han, J. Wang, and D. Howe, "State-space average modelling of 6- and 12-pulse diode rectifiers," in *Proc. The 12th European Conf. on Power Elect. and Appl.*, Aalborg, Denmark, Sep. 2007.

[20] S.F. Glover, "Modeling and stability analysis of power electronics based systems," Ph.D. dissertation., Purdue University, May 2003.

[21] A. Baghramian, and A.J. Forsyth, "Averaged-Value Models of Twelve-Pulse Rectifiers for Aerospace Applications," in *Proc. Power Electronics, Machines, and Drives (PEMD 2004)*, University of Edinburgh, UK, March-April 2004, pp.220-225.

[22] A. Uan-Zo-li, R.P. Burgos, F. Lacaux, F. Wang, and D. Boroyevich, "Assessment of Multi-Pulse Converter Average Models for Stability

Studies Using a Quasi-Stationary Small-Signal Technique," in *Power Electronics and Motion Control Conference 2004*, pp.1654-1658, 2004.

[23] S.D. Sudhoff, and O. Wasynczuk, "Analysis and Average-Value Modeling of Line-Commutated Converter-Synchronous Machine Systems," *IEEE Trans. on Energy Conversion.*, vol. 8, no. 1, pp. 92-99, March 1993.

[24] S.D. Sudhoff, "Waveform Reconstruction from the Average-Value Model of Line-Commutated Converter-Synchronous Machine Systems," *IEEE Trans. on Energy Conversion.*, vol. 8, no. 3, pp. 404-410, September 1993.

[25] S.D. Sudhoff, "Analysis and Average-Value Modeling of Dual Line-Commutated Converter-6-Phase Synchronous Machine Systems," *IEEE Trans. on Energy Conversion.*, vol. 8, no. 3, pp. 411-417, September 1993.

[26] S.D. Sudhoff, K.A. Corzine, H.J. Hegner, and D.E. Delisle, "Transient and Dynamic Average-Value Modeling of Synchronous Machine Fed Load-Commutated Converters," *IEEE Trans. on Energy Conversion.*, pp.508-514, September 1996.

[27] I. Jadric, D. Borojevic, and M. Jadric, "Modeling and Control of a Synchronous Generator with an Active DC Load," *IEEE Trans. on Power Electronics.*, vol. 15, no. 2, pp.303-311, March 2000.

[28] H. Zhu, R.P. Burgos, F. Lacaux, A. Uan-Zo-li, D.K. Lindner, F. Wang, and D. Boroyevich, "Average Modeling of Three-phase and Nine-phase Diode Rectifiers with Improved AC Current and DC Voltage Dynamics," in Proc. IEEE 31st Industrial Electronics Society

Conference (IECON 2005), Raleigh, North Carolina, USA, 6-10 November 2005, pp.1024-1029.

[29] C.T. Rim, D.Y. Hu, and G.H. Cho, "Transformers as Equivalent Circuits for Switches: General Proofs and D-Q Transformation-Based Analyses," *IEEE Trans. on Indus. Appl.*, vol. 26, no. 4, pp. 777-785., July/August 1990.

[30] C.T. Rim, N.S. Choi, G.C. Cho, and G.H. Cho, "A Complete DC and AC Analysis of Three-Phase Controlled-Current PWM Rectifier Using CircuitD-Q Transformation," *IEEE Trans. on Power Electronics,* vol. 9, no. 4, pp. 390-396., July 1994.

[31] S.B. Han, N.S. Choi, C.T. Rim, and G.H. Cho, "Modeling and Analysis of Static and Dynamic Characteristics for Buck-Type Three-Phase PWM Rectifier by Circuit DQ Transformation," *IEEE Trans. on Power Electronics*, vol. 13, no. 2, pp.323-336., March 1998.

[32] K-N. Areerak, S.V. Bozhko, G.M. Asher, and D.W.P. Thomas, "Stability Analysis and Modelling of AC-DC System with Mixed Load Using DQ-Transformation Method," in *Proc. IEEE International Symposium on Industrial Electronics (ISIE08).*, Cambridge, UK, 29 June-2 July 2008, pp. 19-24.

[33] K-N. Areerak, S.V. Bozhko, G.M. Asher, and D.W.P. Thomas, "DQ-Transformation Approach for Modelling and Stability Analysis of AC-DC Power System with Controlled PWM Rectifier and Constant Power Loads," in *Proc. 13th International Power Electronics and Motion Control Conference (EPE-PEMC 2008).*, Poznan, Poland, 1-3 September 2008.

[34] K-N. Areerak, S. Bozhko, G. Asher, L.de Lillo, A. Watson, T. Wu, and D.W.P. Thomas, "The Stability Analysis of AC-DC Systems including Actuator Dynamics for Aircraft Power Systems," *13th European Conference on Power Electronics and Applications (EPE 2009)*, Barcelona, Spain, 8-10 September 2009.

[35] A. Griffo, J. Wang, and D. Howe, "Large Signal Stability Analysis of DC Power Systems with Constant Power Loads," *IEEE Vehicle Power and Propulsion Conference (VPPC'08)*, Harbin, China, 3-5 September 2008, pp.1-6.

[36] S. Rosado, R. Burgos, F. Wang, and D. Boroyevich, "Large-Signal Stability Analysis in Power Systems with a Synchronous Generator Connected to a Large Motor Drive," *IEEE Electric Ship Technologies Symposium (ESTS'07)*, 21-23 May 2007, pp.42-47.

[37] J. Flower and C. Hodge, "Stability and transient-behavioural assessment of power-electronics-based dc-distribution systems Part I: The root-locus technique," *Journal of Marine Engineering and Technology.*, no. A5 2004, pp. 13-21.

[38] L. Ying-xi, M. Xin-hua, G. Hong-juan, and J. Hua, "Stability study and simulation analysis on aircraft transformer rectifier unit (TRU) with constant power load (CPL)," *ICEMS 2005*, vol. 3, pp.2018-2022, Sept. 2005.

[39] L. Han, J. Wang, and D. Howe, "Stability Assessment of Distributed DC Power Systems for 'More Electric' Aircraft," in *Proc. Power Electronics, Machines, and Drives (PEMD 2008)*, York St John University College, York, UK, 2-4 April 2008, pp. 661-665.

[40] L. Han, J. Wang, and D. Howe, "Small-signal Stability Studies of a 270V DC More-Electric Aircraft Power System," in *Proc. Power Electronics, Machines, and Drives (PEMD 2006)*, the Clontarf Castle, Dublin, Ireland, 4-6 April 2006, pp. 162-166.

[41] S.D. Sudhoff, S.F. Glover, P.T. Lamm, D.H. Schmucker, and D.E. Delisle, "Admittance Space Stability Analysis of Power Electronic Systems," *IEEE Trans. on Aerospace and Electronic Systems,* vol. 36, no. 3, pp.965-972, July 2000.

[42] S.D. Sudhoff, and S.F. Glover, "Three-Dimensional Stability Analysis of DC Power Electronics Based Systems," in *Power Electronics Specialists Conference (PESC 2000),* June 2000, pp.101-106.

[43] X. Feng, J. Liu, and F.C. Lee, "Impedance Specifications for Stable DC Distributed Power Systems," *IEEE Trans. on Power Electronics,* vol. 17, no. 2, pp.157-162, March 2002.

[44] X. Feng, Z. Ye, K. Xing, F.C. Lee, and D. Borojevic, "Individual Load Impedance Specification for a Stable DC Distributed Power System," in *Applied Power Electronics Conference and Exposition (APEC'99)*, 14-18 March 1999, pp.923-929.

[45] S. Roy, P. Got, and M. Ammari, "Stability Considerations for a Single Phase Generator-Rectifier Interface," in *Proc. The 20th IEEE Telecommunications Energy Conference*, October 1998, pp.151-155.

[46] F. Barruel, N. Retiere, and J.L. Schanen, "Stability Analysis for Aircraft On-Board System," in *Proc. The 3rd IET International Conference on Power Electronics, Machine, and Drives (PEMD 2006)*, Dublin, Ireland, April 2006, pp.361-367.

[47] C.M. Wildrick, F.C. Lee, B.H. Cho, and B. Choi, "A Method of Defining the Load Impedance Specification for a Stable Distributed Power System," *IEEE Trans. on Power Electronics.*, vol. 10, no. 3, pp. 280-285, May 1995.

[48] T. Wu, and X. Ruan, "Standardization of Input/Output Impedance Specifications of Buck Converters Based on the System Integration Concept," in *Proc. IEEE International Symposium on Industrial Electronics (ISIE06).*, Montreal, Quebec, Canada, 9-12 June 2006, pp. 982-987.

[49] J. Sun, "Input Impedance Analysis of Single-Phase PFC converters," *IEEE Trans. on Power Electronics.*, vol. 20, no. 2, pp. 308-314, March 2005.

[50] M. Chen, and J. Sun, "Low-Frequency Input Impedance Modeling of Boost Single-Phase PFC Converters," *IEEE Trans. on Power Electronics.*, vol. 22, no. 4, pp. 1402-1409, July 2007.

[51] J. Sun, and M. Chen, "Analysis and Mitigation of Interactions between PFC Converters and the AC source," in *Power Electronics and Motion Control Conference (IPEMC 2004).*, 14-16 August 2004, pp.99-104.

[52] S. Chandrasekaran, D. Borojevic, and D.K. Lindner, "Input filter Interaction in Three Phase AC-DC Converters," in *Power Electronics Specialists Conference (PESC'99).*, 27 June - 1 July 1999, pp. 987-992.

[53] H. Mao, D. Boroyevich, and F.C.Y. Lee, "Novel Reduced-Order Small-Signal Model of a Three-Phase PWM Rectifier and Its Application in Control Design and System Analysis," *IEEE Trans. on Power Electronics.*, vol. 13, no. 3, pp. 511-521, May 1998.

[54] J. Sun, M. Chen, and K.J. Karimi, "Aircraft Power System Harmonics Involving Single-Phase PFC Converters," *IEEE Trans. on Aerospace and Electronic Systems.*, vol. 44, no. 1, pp. 217-226, January 2008.

[55] P. Liutanakul, S. Pierfederici, A. Bilal, B. Nahid-Mobarakeh, and F. meibody-Tabar, "Stability Investigation of Inverter Motor Drive System with Input Filter-Optimisation of the DC-Link Capacitance Value," in *Proc. 39th IEEE Power Electronics Specialists Conference.(PESC08)*, Rhodes, Greece, June 2008, pp. 3728-3734.

[56] Z. Bing, K. Karimi, and J. Sun, "Input Impedance Modeling and Analysis of Line-Commutated Rectifiers," in *Proc. IEEE Power Electronic Specialist Conf. (PESC 2007)*, June 2007, pp.1981-1987.

[57] J.Sun, and J. Colon, "Input Impedance Modeling of Line-Frequency Rectifiers by the method of Impedance Mapping," in *IEEE COMPEL Workshop*, Rensselaer Polytechnic Institute, Troy, NY, USA, 16-19 July 2006, pp. 69-75.

[58] J. Sun, and K.J. Karimi, "Small-Signal Input Impedance Modeling of Line-Frequency Rectifiers," *IEEE Trans. on Aerospace and Electronic Systems*, vol. 44, no. 4, pp. 1489-1497, October 2008.

[59] A. Emadi, and M. Ehsani, "Multi-Converter Power Electronic Systems: Definition and Applications," in *Proc. 32nd IEEE Power Electronic Specialist Conf. (PESC 2001)*, Vancouver, BC, Canada, June 2001, pp. 1230-1236.

[60] R. McNeal, and M. Belkhayat, "DC link Stability Design Tool," in *Proc. Electric Ship Techmologies Symposium (ESTS'07)*, Arlington, VA, USA, 21-23 May 2007, pp.288-293.

[61] S.D. Sudhoff, K.A. Corzine, S.F. Glover, H.J. Hegner, and H.N. Robey, "DC link Stabilized Field Oriented Control of Electric Propulsion Systems," *IEEE Trans. on Energy Conversion.*, vol. 13, no. 1, pp.27-33, March 1998.

[62] X.Y. Wang, D.M. Vilathgamuwa, and S.S. Choi, "Decoupling Load and Power System Dynamics to Improve System Stability," in *Proc. The IEEE International Conference on Power Electronics and Drives Systems (PEDS 2005)*, Kuala Lumpur, Malaysia, 28 November – 1 December, pp.268-273.

[63] A. Emadi, and M. Ehsani, "Negative Impedance Stabilizing Controls for PWM DC/DC Converters using Feedback Linearization Techniques," in *Proc. 35th Intersociety Energy Conversion Engineering Conference and Exhibit (IECEC 2000)*, 24-28 July 2000, pp.613-620.

[64] X. Liu, A.J. Forsyth, and A.M. Cross, "Negative Input-Resistance Compensator for a Constant Power Load," *IEEE Trans. on Industrial Electronics.*, vol. 54, no. 6, pp. 3188-3196, December 2007.

[65] A.M. Rahimi, and A. Emadi, "Active Damping in DC/DC Power Electronic Converters: A Novel Method to Overcome the Problems of Constant Power Loads," *IEEE Trans. on Industrial Electronics.*, vol. 56, no. 5, pp. 1428-1439, May 2009.

[66] P.C. Krause, O. Wasynczuk, and S.D. Sudhoff, "Analysis of Electric Machinery and Drive Systems," John Wiley & Son, Inc, 2002.

[67] N. Mohan, T.M. Underland, and W.P. Robbins, *Power Electronics: Converters, Applications, and Design,* John Wiley & Son, USA, 2003, pp. 106-108.

[68] M. Sakui, H. Fujita, and M. Shioya, "A Method for Calculating Harmonic Currents of a Three-Phase Bridge Uncontrilled Rectifier with DC Filter," *IEEE Trans. on Indus. Elect.*, vol. 36, no. 3, pp. 434-440, August 1989.

[69] S. Hansen, L. Asiminoaei, and F. Blaabjerg, "Simple and Advanced Methods for Calculating Six-Pulse Diode Rectifier Line-Side Harmonics," in *Proc. The 38th IAS Annual Meeting Conf.*, vol. 3, pp.2056-2062., Oct. 2003.

[70] N. S. Nise, "Control Systems Engineering," Fifth Edition, John Wiley & Son, 2008, pp.85-93.

[71] R.C. Dorf, and R. H. Bishop, *Modern Control Systems,* Tenth Edition, Prentice Hall, USA, 2005, pp. 43-45.

[72] J. D. Glover, and M. Sarma, *Power System Analysis & Design,* Second Edition, PWS Publishing Company, USA, 1994, pp. 266-280.

[73] J. Wang, L. Han, A. Griffo and D. Howe, "Input admittance characteristics of permanent-magnet brushless AC motor drive systems," *IEEE Vehicle Power and Propulsion Conference (VPPC'07)*, Arlington, USA, 9-12 September 2007, pp. 191-196.

[74] USA Department of Defense, "MIL-STD 704F Aircraft electric power characteristics," March 2004.

[75] T. Wu, S.V. Bozhko, G.M. Asher, and D.W.P. Thomas, "A Fast Dynamic Phasor Model of Autotransformer Rectifier Unit for More Electric Aircraft," *35th Annual Conference of the IEEE Industrial Electronics Society (IECON'09)*, Porto, Portugal, 3-5 November 2009.

[76] A. Griffo, and J. Wang, "Stability Assessment of Electric Power Systems for 'More Electric' Aircraft," *13th European Conference on Power Electronics and Applications (EPE 2009)*, Barcelona, Spain, 8-10 September 2009.

[77] L. Han, J. Wang, A. Griffo, and D. Howe, "Stability Assessment of AC Hybrid Power Systems for 'More Electric' Aircraft," *IEEE Vehicle Power and Propulsion Conference (VPPC'08)*, Harbin, China, September 2009.

[78] J. R. Neuenswander, "Modern Power Systems," International textbook, 1973.

[79] T.W. Gamelin, "Complex Analysis," Springer-Verlag, 2000.

[80] S. Choi, P.N. Enjeti, and I.J. Pitel, "Polyphase Transformer Arrangements with Reduced kVA Capacities for Harmonic Current Reduction in Rectifier-Type Utility Interface," *IEEE Trans. on Power Electronics.*, vol. 11, no. 5, September 1996.

[81] R. Pena, J.C. Clare, and G.M. Asher, "Doubly fed induction generator using back-to-back PWM converters and its application to variable-speed wind-energy generation," *IEE Proc.-Electr. Power Appl.*, vol. 143, no. 3, pp.231-241., May 1996.

[82] T. Wu, S. Bozhko, G.Asher, P. Wheeler, and D. Thomas, "Fast Reduced Functional Models of Electromechanical Actuators for More-Electric Aircraft Power System Study," *SAE International Conference 2008*, Washington, USA, November 2008.

[83] B.K. Bose, "Modern Power Electronics and AC Drives", Prentice Hall, 2002.

[84] C-M Ong, "Dynamic Simulation of Electric Machinery using MATLAB/Simulink," Prentice Hall, 1998.

[85] L. de Lillo, P. Wheeler, L. Empringham, C. Gerada, and X. Huang, "A Power Converter for Fault Tolerant Machine Development in Aerospace Applications," in *Proc. 13th International Power Electronics and Motion Control Conference (EPE-PEMC 2008).*, Poznan, Poland, 1-3 September 2008, pp. 388-392.